Acoustical Identification of Sea-Mines (A Coherent, very high Frequency Sonar Model).

Wendelboe, Gorm; Jacobsen, Finn; Sørensen, Helge Bjarup Dissing

Publication date:
2007

Document Version
Publisher's PDF, also known as Version of record

Citation (APA):
Wendelboe, G., Jacobsen, F., & Sørensen, H. B. D. (2007). Acoustical Identification of Sea-Mines (A Coherent, very high Frequency Sonar Model).

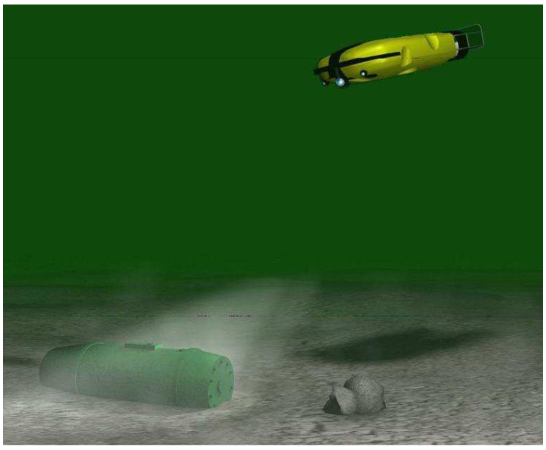

Acoustical Identification of Sea-Mines
(A Coherent Very High Frequency Sonar Model)

By Gorm Wendelboe

Danish Defence Research Establishment (DDRE)
and Technical University of Denmark (DTU)
Ørsted·DTU

29th March 2007

Abstract

This work concerns the development of a model to generate artificial very high frequency (>100 kHz) sonar images for the development and training of future detection and identification algorithms.

The model coherently computes the backscattered pressure from an arbitrarily shaped object lying on a rough seabed with a roughness power spectrum that follows one or several power laws obtained from the literature. The surface of the object is represented by numerous plane triangular facets, and the surface is smooth compared to the acoustic wavelength. The seabed is approximated by several 1D height profiles interpolated from the 2D height field in directions that correspond to the sonar beams. Thus, the 3D backscattered field from the seabed is approximated by several 2D fields computed from the height profiles. The total pressure is given as the sum of the backscattered field from the object and the seabed. The Kirchhoff approximation has been applied to predict the scattered field from both the object and seabed. When the incoming field has a near-normal incidence with respect to the broad side of a cylinder the artificial images agree reasonably well with the real images, but for angles away from normal incidence the highlight disappears in the artificial image. Hence, wave field interaction between the seabed and object is believed to be a significant contributor to the backscattered field and it should be included in the model.

The expression for scattering from the plane triangular facet, which is applicable for the time domain, causes numerical problems at certain angles, and that may yield fatal computational errors. To solve this problem the expression has been rewritten in terms of sinc-functions and a robust and numerically accurate frequency domain response has been obtained.

Ray tracing is a classical approach to predicting a second order field, but it fails to include the total amount of acoustic energy involved. A numerical method that identifies the essential seabed regions ensonified by object reflected sound has been developed. The identified regions will form the basis for a coherent computation of the second order field, and hence, by this approach almost the entire acoustic energy involved in the second order scattering process can be included.

The Kirchhoff approximation applied for seabed interface roughness scattering fails except near normal incidence; additionally, recent experiments have shown that for frequencies above 100 kHz sediment volume scattering is a significant contributor to the scattered field. Recent experiments in sandy sediments have also shown that the sediment density exhibit high variations. To overcome this problem a scattering model that by approximate means translates the sediment density variations into an equivalent roughness has been developed; furthermore, the equivalent roughness model is combined with an integral equation method, where the scattering matrix is reduced to a band matrix that allows computation of long height profiles.

Preface

This thesis describes the work carried out during the Ph.D. project "Acoustical Identification of the Sea mines". It should be treated as a supplementary note to the four papers produced.

At an early stage of the project it was realized that an understanding of acoustic processes was required before any advanced and robust signal processing algorithm could be developed. Experiments at the beginning of the project supported this conclusion; the sonar image quality varied significantly depending on the environment it was acquired in. Hence, the work of this project has been aimed at the development of a coherent sonar model for very high frequencies. The complete model has not yet fulfilled the ambitions; however, the architecture of the model has been established, sub-models have been modified and verified, and it has been necessary to develop new sub-models.

The appendices contain some fundamental issues for acoustic modeling such as the wave equation and the Kirchhoff Helmholtz integral equation; however, the appendices also contain mathematical expressions, derivations, and Benchmark solutions applied for the papers. There is no strict consistency regarding the mathematical symbols; symbols may differ from appendix to appendix, and they are introduced in each chapter, or reintroduced if the symbols have been applied in previous chapters. However, several standard symbols within acoustics are maintained such as, for example the wavenumber k, the wavelength λ, the density ρ, and the speed of sound c. A strict consistency of symbols was not possible within the time schedule in the writing process.

The author gratefully acknowledges support from Finn Jacobsen, Acoustic Technology, Ørsted·DTU for discussion and advice regarding general acoustical topics and advice concerning paper writing, Judith M. Bell, School of Engineering and Physical Sciences, Heriot Watt University, Edinburgh, for advice related to sonar-modeling, Rich Lear, Reson A/S, for carrying out the sonar experiment in Korsor 2001, Anders Villum Clausen, DDRE, for contributing with photos from the RDN demonstration at Sjællands Odde, Dr. Thomas Wever at FWG in Kiel, Germany, for photos and the mine-burial results, Bjarne Stage, DDRE, for the image on the thesis-title page and constructive discussions. Thanks to Bjarne Damsgaard, DDRE, and for constructive discussions. Thanks to supervisor Helge B.D. Sørensen, Ørsted·DTU, for pushing me to make publications. Thanks to

Chris Lee Ramsden for proofreading, and Jesper Munk for the nice office in Copenhagen where the final thesis writing was made. Finally, thanks to my wife Winnie Malling for patience and understanding during the project, and thanks to my two daughters (5 and 3 years old) for reminding me that there is a world outside underwater acoustics.

List of publications

1. G. Wendelboe, J.M. Bell, H. B. D. Soerensen, and B. Damsgaard, "Simulation of sector sonar images," Proceedings of the seventh European Conference on underwater Acoustics, ECUA 2004 Delft, The Netherlands, 5-8 July, 2004 (Ref. [1]).
2. G. Wendelboe, J. M. Bell, and F. Jacobsen, “Localization of seabed domains ensonified by object reflected sound at very high frequencies,” Proceedings of Boundary influences in high frequency, shallow water acoustics, September 2005, Bath, UK (Ref. [2]).
3. G. Wendelboe, J.M. Bell, and F. Jacobsen, "A numerically accurate and robust expression for bistatic scattering from a plane triangular facet," J. Acoust. Soc. Am **119**, 701-704 (2006). (Ref. [3]).
4. G. Wendelboe, F. Jacobsen, and J. M. Bell, “An equivalent roughness model for seabed backscattering at very high frequencies using a band-matrix,” accepted for publication to J. Acoust. Soc. Am. in October 2006. (Ref. [4]).

DTU-report (No publication):

1. G. Wendelboe “2D Signal processing for synthetic seafloor generation,” Report Individual Course, April 2005, Oersted·DTU, DK. (Ref. [5])

Contents

Chapter 1

Introduction

In 2001 the Danish Defence Research Establishment (DDRE) initiated the Ph.D.-project, Acoustical Identification of Sea Mines. The goal was to attain a method for automatic identification of naval mines located on the seabed, i.e., proud objects, by application of a very high frequency (> 100 kHz) image generating sonar.

During military conflicts naval mines pose a major threat to civilian ships as well as naval ships. The naval mines may be found at the sea-surface, in the water column (moored mines) and they can be lie on the seabed. This Ph.D. project was initiated in 2001 within the framework of a classical military conflict, with two nearly symmetric opponents represented by states of alliances. After the 9/11, 2001, a new security problem is apparent to almost anyone. The new situation requires advanced new sensor and surveillance systems, and this includes the underwater environment. Harbours in particular can be targeted and there is an urgent need to develop systems that can monitor the harbor water volume, the bottom and the sub-bottom for mines or similar threats.

In this chapter a very brief presentation of the acoustical mechanisms of the seabed sediment, and the very high frequency acoustic response from different mine shapes are given. The issues are fundamental for the development of a sonar model.

1.1 Acoustic response from the seabed

The seabed may consist of rocks, stones, sand, mud, plants, different animal species, such as shells, or a mixture of all these components. The specific acoustic impedance, Z_w, in water is defined as the product of the water density, ρ_w, and the speed of sound in water c_w, that is,

$$Z_w = \rho_w \, c_w, \tag{1.1}$$

see, e.g., Ref. [6]. In water the propagating acoustic waves are compressional waves, i.e. , the waves propagate through the medium in wave fronts exhibiting compression and rarefaction with a frequency that corresponds to the frequency of the transmitted wave. Any change in the specific acoustic impedance of the medium will affect the wave front. In the deep sea, for example, the speed of sound often varies with depth, where, for example, a downward propagating wavefront will bend upwards if the speed of sound increases with depth. In this work the water medium is assumed homogeneous as considerations are limited to shallow water areas where the maximum range of propagation does not exceed, say, 100 meters. The ambient density in water is throughout this work set equal to $\rho_w = 1000$ kg/m^3 and the speed of sound is $c_w = 1500$ m/s. For thorough expressions of the density and speed of sound in sea-water that include temperature, salinity, and ambient pressure in sea-water, see, e.g., Ref. [7] (Section 1-9, pp. 28-36). It is to be borne in mind that absorption is a significant limitation for very high frequency propagation as absorption increases with frequency; however, absorption will not be considered further in this work, but see, e.g., Ref. [8](pp. 1907).

The specific impedance given in Eq. (1.1) is the basis of the fluid-fluid model, see, e.g., Ref. [9], where the sediment is characterized as fluid; hence, the wave equation holds also in the sediment[1]. This assumption has been proven to fail in some cases, for example, when the seabed is porous. For porous materials the wave equation fails and the basic linear equations, i.e., the conservation of mass, Euler's equation and the pressure density relations must be re-examined. Sound propagation in porous materials can described in Biot models, see, e.g., Ref. [10] for a well-written introduction to Biot models, and Ref. [11] when the theory is applied to seabeds. However, Biot models are complicated and require numerous geo-acoustical parameters that are difficult to obtain. In addition, the use of a complex model may lead to more confusion than clarity; for example, data from sound field experiments within seabed sediments has lead one author to conclude the presence of a slow Biot wave, but another author suggests, by using the simple fluid-fluid approach, that the observed field might as well be the surface roughness that causes penetration into the sediment and thereby produces an apparent wave speed, or slowly propagating wavefront, see Ref. [12]. Hence, in order to reduce complexity, the sediment is characterized as fluid, and therefore, wave interaction with the seabed will be discussed in terms of a fluid-fluid assumption. In Appendix G reflection of a plane wave from an infinite smooth interface is described; the derivation is based on two key conditions; the first is that of normal displacement: At the interface the velocity of the fluid particles normal interface must be the same above and below the interface; and the second condition states that the pressure on each side of the interface must be equal. When the impedance contrast is high, most of the energy is reflected back to the medium and only a small part of energy is transmitted; when the impedance

---

[1] See, e.g., Appendix E for the derivation of and validity of the wave-equation

contrast is low[2] the main part of the energy is transmitted into the new medium. Figure (1.1a) illustrates the reflection mechanism from a long smooth surface in terms of Huygen's wavelets in the case of a incoming plane wave, and where the acoustic signal is a Delta function; each secondary wavelet propagates spherically back into the water and the main part of the acoustic energy is reflected into the specular direction, see Fig. (1.1b). For a rough surface the Huygen's wavelets construction in Fig. (1.2a) results in a field which is scattered in all directions; an analysis of the field scattered from a any rough surface with the same statistical properties as the surface in Fig. (1.2a) may lead to an expected spatial energy distribution given in Fig. (1.2b). Note here that the energy distribution in the specular direction, the coherent field, is higher than in the other directions, the diffuse field, see, e.g., Ogilvy [13]. For a very rough surface the coherent contribution vanishes and the field is scattered equally in all directions according to Lambert's law, see, e.g., Urick [14]. Wave scattering from a rough surface

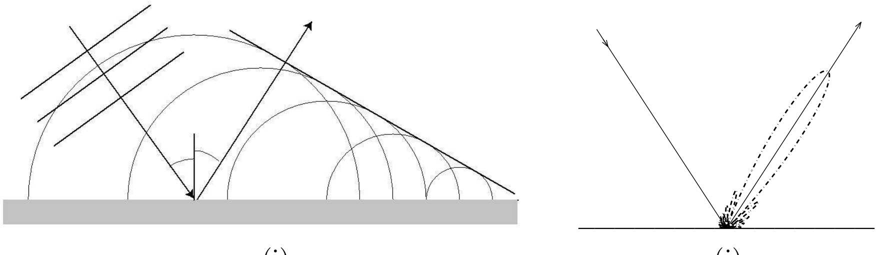
(i) (j)

Figure 1.1: Smooth surface reflection; (a) reflection illustrated by Huygens wavelets, and (b) the corresponding directional energy distribution.

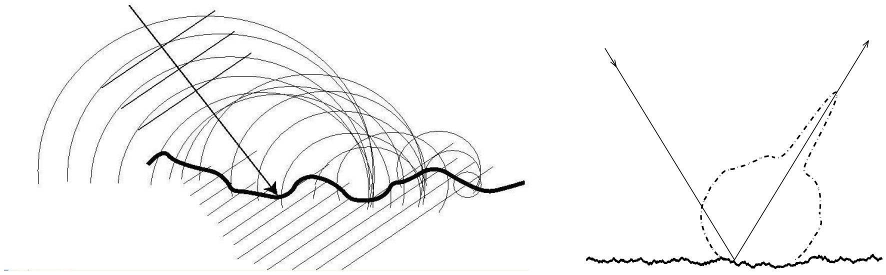
(a) (b)

Figure 1.2: Rough surface scattering illustrated by Huygens wavelets (a) and the corresponding directional energy distribution (b).

---

[2] That is, the impedance ratio between the two media is close to unity.

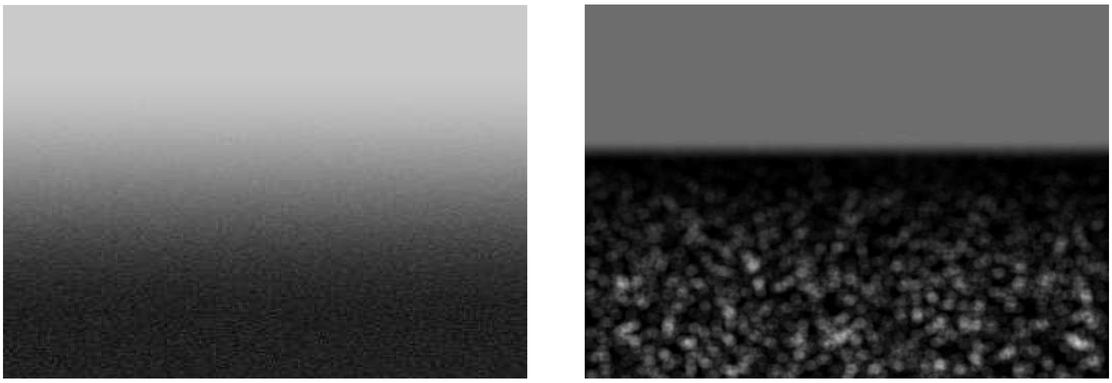
(a) An unconsolidated muddy sediment
(b) A muddy sediment with gas-bubbles

Figure 1.3: Two examples of a muddy seabed.

into a homogeneous medium (the water) is posed as a boundary value problem, where the Kirchhoff-Helmholtz integral equations are the basic equations; see, e.g., appendix F for the derivation of the Kirchhoff-Helmholtz integral equations. Figures (1.3-1.5) show different examples of sediment types. Figure (1.3a) illustrates an extremely unconsolidated, and muddy sediment, with a large transition layer; the impedance contrast is very low, and the all energy is transmitted into the sediment; hence, the backscattered energy is vanishing. Figure (1.3b) illustrates a muddy sediment containing gas bubbles. Although the mud has a weak impedance contrast with respect to the water the gas bubbles exhibit a high impedance contrast that may yield a significant amount of backscattered energy to back to the sonar depending on the spatial bubble distribution and the average bubble size. Especially, if the bubbles are excited at their resonance frequencies backscattering will be enhanced, see, e.g., Ref. [14]. A profile of a rough, sandy sediment is illustrated in Fig. (1.4). This is the type of seabed that will be treated in this work; sandy seabeds may contain ripples and may change topography due to tidal currents, storms, and seasonal variations. Animal species may also change the topography. These time varying effects can have a significant influence on the acoustic response, see, e.g., Pouliquen [15]. Figure. (1.5) shows a

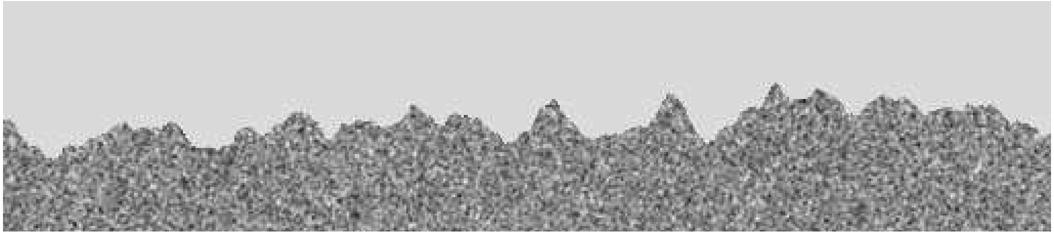
Figure 1.4: A profile of a rough sandy seabed

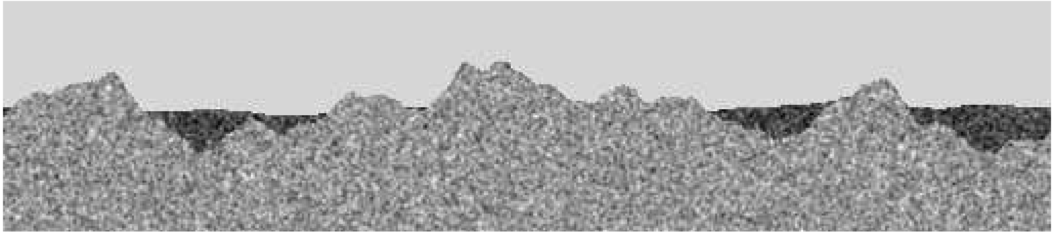

Figure 1.5: A profile of a rough sandy seabed with small muddy areas.

rough sandy sediment with pockets of mud on the sand that may yield an acoustic response different from that of pure sand or pure mud. Finally, seabed areas may be covered with stones which will lead to yet another type of acoustic response.

Appendix G addresses some basic issues related to acoustic wave interaction with the seabed. Appendix G.1 presents the basic principles of reflection, transmission and the subcritical penetration of a plane wave on a smooth interface between two homogeneous fluids. In Appendix G.2 a sediment with a depth varying density that follows an average curve obtained at the Sediment Acoustic Experiment in 1999 (SAX99) is considered, see Ref. [16]; in the unconsolidated upper part of the sediment, approximately within the first few centimetres, the density increases significantly as a function of depth, but below this the density approaches a constant value. A simple model of a normal incident plane wave onto a smooth seabed shows that the sediment reflection coefficient is frequency dependent; for low frequencies it has approximately the same magnitude as the interface reflection coefficient, but it decreases rapidly with increasing frequency. This result might indicate that the high frequency waves are absorbed in the sediment and that low frequency waves are reflected significantly. However, recent experiments have shown that volume scattering in very inhomogeneous sediments can be the dominating scattering mechanism for frequencies above 100 kHz, see, e.g., Refs. [17] and [18]. According to Ref. [16] the density exhibits high spatial variations, especially in the upper part of the sediment; therefore, the backscattered energy at high frequencies is much higher than that which this small, and simplistic, investigation proposes to cover. Appendix G.3 briefly presents the classical rough surface scattering models such as the Kirchhoff approximation and the small roughness perturbation approximation. Appendix G.4 addresses Jackson's model for high frequency seabed scattering and based on Ref. [19] the model's predictions at four different sites at different frequencies have been reconstructed. Jackson's model uses the composite roughness approximation to predict the interface scattering cross section and the small perturbation approximation to predict the volume scattering cross section. The model is incoherent and only valid up to 100 kHz.

1.2 Acoustic response from naval mines

There are a variety of different naval mines in exsistence, and here attention has only been given to mines lying on the seabed. In this work the acoustic interaction with naval mines is concentrated on very high frequency signals (>100 kHz), that is, signals with wavelengths that are much smaller than the characteristic lengths of the objects. Hence, the wave field description approaches the optical regime.


(a) (b)

Figure 1.6: A cylinder-shaped mine

Figure (1.6a) and Fig. (1.6b) show a test mine applied to the NATO Expert System Test 2005 (NEST06) which was carried out in February-March 2006 in the Baltic Sea; note, the cylindrical geometry and the smooth surface. The reflection property for a smooth surface is illustrated in Fig. (1.1) indicates that for normal incidence onto the broad side of the cylinder the backscattered wave field contains a high amount of energy, but for other angles the direct backscattered field is very weak. However, a highlight may still exist as the signal of an object reflecting sound directed toward the seabed will be scattered back to the receiver depending on the roughness and impedance characteristics of the seabed. In any case, a shadow will be present in the final sonar image. A completely different result is obtained if the mine has been lying on the seabed for a long time. In this case, plants and animal species may cover the mine. In Fig. (1.7) the surface is covered with shells, which makes the acoustic response resemble the surrounding seabed also covered with shells, and the highlight is absent, but a shadow will still exist in the sonar image. Finally, the stealthy mines are addressed. The Swedish Rockan, see Fig. (1.8a), and the Italian Manta mine, see Fig. (1.8b) are examples of mines that have a surface geometry that minimizes backscattering; a stealthy mine can be very difficult to detect as the surface shape minimizes the backscattered field. The Rockan is well-suited to environments with stones and rocks; the Manta mine is suited to sandy seabeds, and the shape even makes it

Figure 1.7: A cylinder mine covered with shells.

possible to become buried in the sand in a relatively short time.

(a) Rockan.

(b) Manta.

Figure 1.8: Stealth mines

Chapter 2

Sensing naval mines

In this chapter general underwater sensors and systems for detection and identification of naval mines on the seabed are addressed, but focus is mainly concentrated on very high frequency (> 100 kHz).

2.1 Sensors applied in the Danish Navy

The Mine Counter Measure (MCM) concept applied by the Danish Navy is illustrated in Fig. (2.1). Unmanned drones perform large seabed area survey by

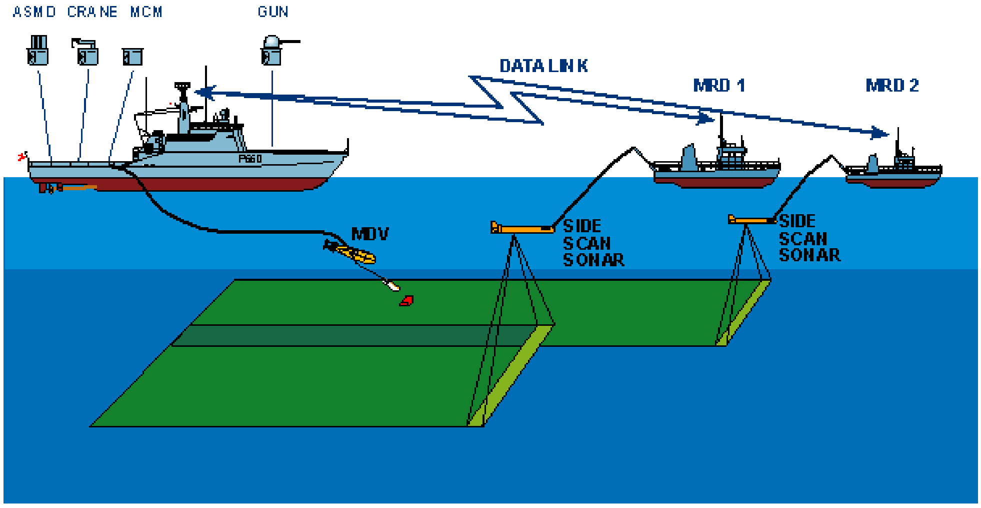

Figure 2.1: MCM concept of the Danish Navy (Year 2003; the figure is taken from Ref. [20]) .

applying very high frequency side scan sonars[1]; the side scan sonar images are transmitted to the mother ship via a radio link, where a human operator evaluates the images by detection of potential mines, see Fig. (2.2). A Remotely Operated Vehicle (ROV) is equipped with a very high frequency forward looking sonar [2], a video camera, and an explosive device; it is sent down to the location of the object. If the object is identified as a mine the explosive device is detonated. The ROV is controlled by a human operator who navigates and identifies the object by the aid of the forward looking sonar and a video camera. A cable is connected between the ROV and mother ship, and it provides the ROV with electrical power and transmits sensor data up to the operator, see Figs. (2.3) and (2.4). However, this type of mine hunting operation is time consuming and the cable is constantly at high risk of being cut. Underwater communication is

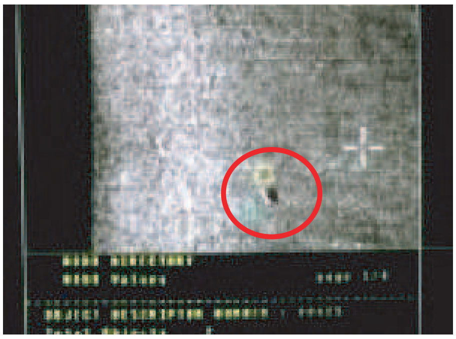

Figure 2.2: Sidescan image containing a mine (Photo: AVC, DDRE)

(a) A crane lifts the vehicle off-board.

(b) The engines are activated and the ROV descends.

Figure 2.3: ROV deployment (Photo: AVC, DDRE)

---

[1] Type: Thomson TSM2054

[2] A Reson 6012

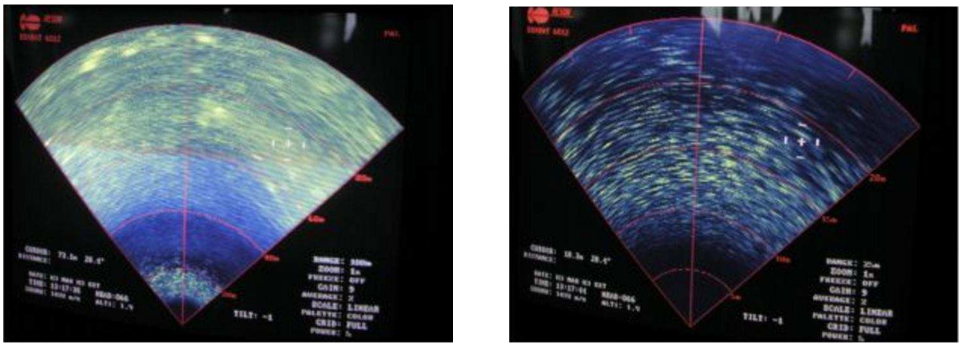

(a) No target detected

(b) No target detected

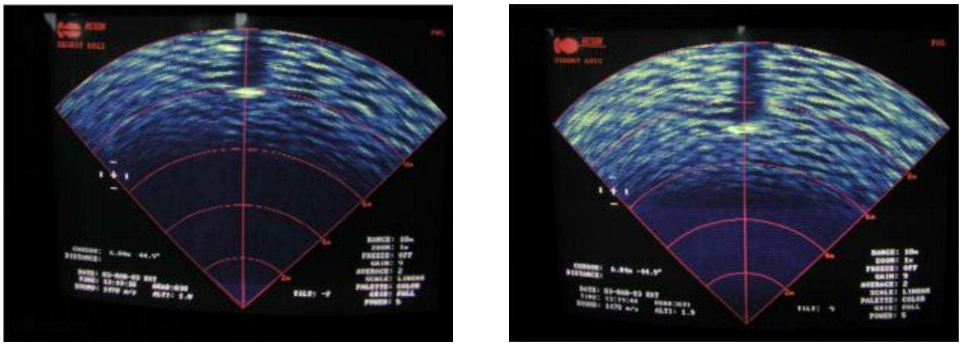

(c) Mine detected

(d) Mine detected

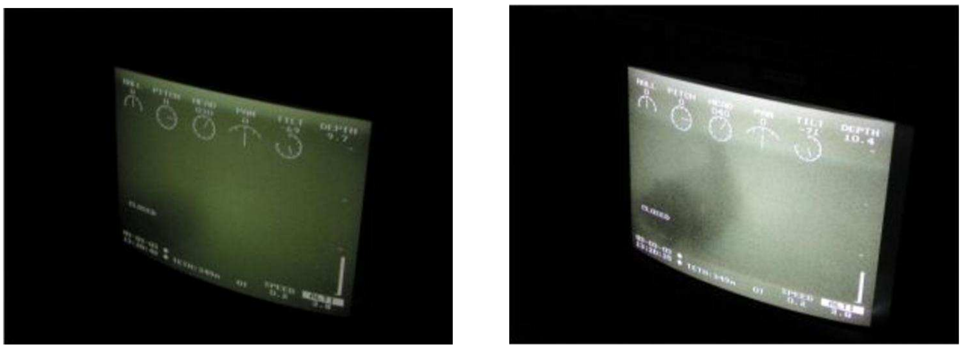

(e) Video image at low visibility range

(f) Video image acquired close to the mine

Figure 2.4: Sector sonar images acquired from the ROV. The sonar is the Reson 6012 type. The bottom images are obtained by a video camera (Photo: AVC, DDRE).

limited by a significant delay of the transmission as the speed of sound in water is low compared to the speed of light. The absorption increases with frequency, thus, in order to transmit the signals over a suitable distance the carrier frequency cannot be very high; on the other hand, a low carrier frequency will result in a low bit-rate for, say, a coherent phase shift keying modulation. Additionally, the communication channel is time varying, dispersive, and highly reverberant. Thus, it is not possible in real time to transmit images for manoeuvring the vehicle back to the operator. For more information on this topic, see, e.g., Refs. [21] and [22]. Since then, the concept of using a wireless ROV has been dropped in favour of developing autonomous underwater vehicles (AUVs). AUVs are used by several Naval forces in the NATO-countries today. Because an AUV is not able to acquire GPS-position data in the underwater environment it must rely on the position data before descending into the water and subsequently use motion sensors combined with Kalman filters in order to navigate. Artificial intelligence (AI) algorithms are used for decision management, navigation and the processing of sensor data. For issues related to AUV-systems, see, e.g., Refs. [23],[24] and [25]. The RDN images in Figs. (2.2),(2.3), and (2.4), are obtained from a demonstration in a near- coastal area at Sjællands Odde, Denmark.

2.2 Optical devices

Although optical sensors from a relatively simple video camera to a more advanced gated viewing system can deliver very good underwater images they are all limited by extremely high absorption and scattering, and thus, they can only be applied to short ranges. Figure (2.5) clearly demonstrates this; it shows images produced by the Swedish Defence Research Agency (FOI), where the performance of a modern optical gated view system is compared to a conventional camera; the images originate from a relatively polluted underwater environment. Although the gated viewing system has a better performance it is however also strongly limited by its range to the target, but it may be combined with sonar at short ranges.

2.3 Sonars

The optical images in Fig. (2.5) demonstrate, that a SOund NAvigation and Ranging (SONAR) system is still the most suitable technology for underwater imaging applications. There are a variety of different sonar types designed for different applications, but it is mainly the frequency of the applied acoustic signal that distinguishes them. Sonars are typically divided into 3 categories; first, the low frequency sonar that covers the frequency range from $1 - 10$ kHz; secondly, the high frequency sonar that covers the frequency range from $10 - 100$ kHz; and

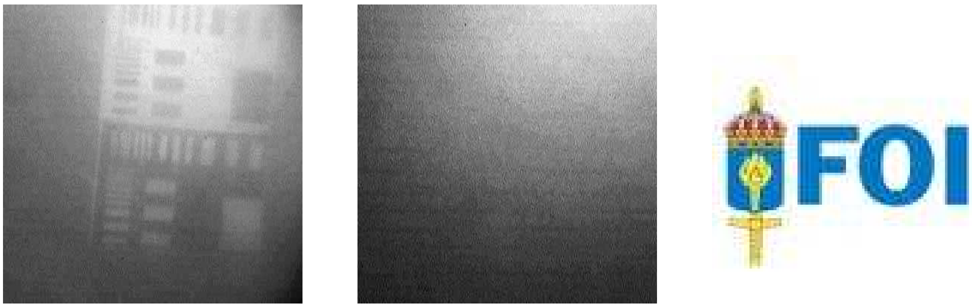

(a) Non-gated 1.45 m (b) Non-gated 2.45 m

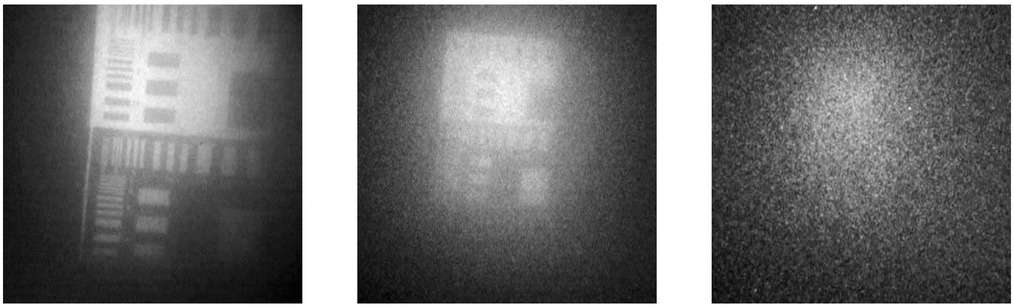

(d) Gated 1.45 m (e) Gated 2.45 m (f) Gated 3.83 m

Figure 2.5: The limitation of optical devices in an underwater environment. Gated versus non-gated viewing images measured by the Swedish Defence Research Agency (FOI); the images originates from Djupviken, a relatively polluted river.

finally, the third class, the very high frequency sonar, that operate at frequencies above 100 kHz. The low frequency sonar can be a parametric sonar; it emits two high frequency waves that due to a non-linear parametric effect transforms into a narrow beam low frequency wave, see, e.g., Ref. [9](Ch.5). The low frequency wave penetrates deep into the sediment and the backscattered signal can reveal layers in the sediment; consequently, a sub-bottom profile in along-track direction is generated, see Fig. 2.6. The parametric sonar can detect buried objects. It does, however, have a poor spatial resolution which makes it difficult to detect small objects. In addition, the received sonar data cannot be represented as an image because of the low resolution; instead the signal can be analyzed in terms of frequencies that could represent resonance frequencies from which the object can be identified. For high frequency waves ($10 < f < 100$ kHz, i.e., wavelengths from approximately $15 - 1.5$ cm) the penetration is weaker, but it is still significant. For frequencies above, approximately 20 kHz, images with a reasonable resolution can be produced. These sonars are well suited for seabeds with layered sediments, especially if the top layer is soft and if one the adjacent layers below is hard and causes a significant amount of backscattering. In these situations waves

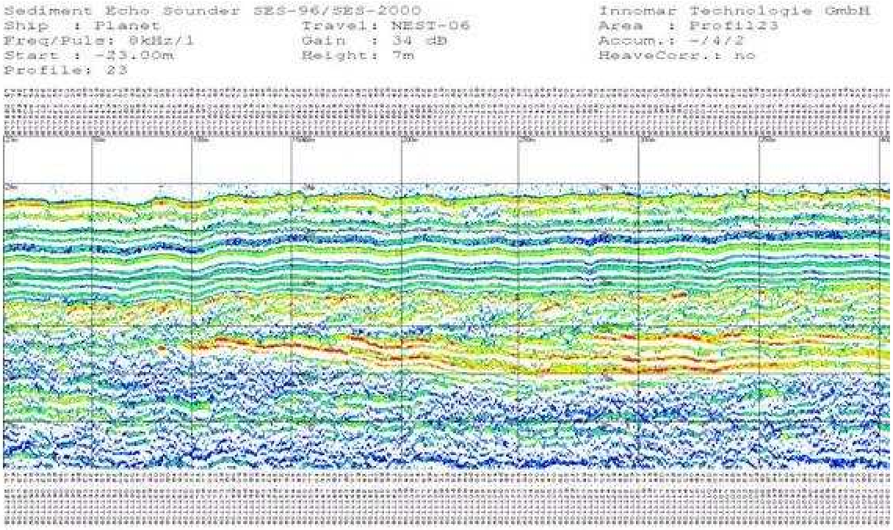

Figure 2.6: A sub-bottom profile generated by a parametric sonar. The horizontal direction is the along track, the vertical direction the subbottom depth, and the colors show acoustic impedance (The figure has been obtained from Ref. [26])

from the very high frequency (> 100 kHz) sonars will most likely be absorbed, and consequently, the backscattered pressure vanishes.

Recent experiments have shown that a high frequency (11 kHz to 50 kHz) synthetic aperture sonar (SAS) can produce an image of a buried object when the incoming field penetrates at a subcritical angle into a rough, sandy sediment, see, e.g., Refs. [27] and [28], and Fig. (2.7) (taken from Ref. [28]); however, sub-critical penetration of high frequency waves is, probably, still at a research stage.

The very high frequency sonar (> 100 kHz) has a high resolution and it produces detailed images of proud objects and the seabed. For imaging purposes very high frequency sonars are well suited for sandy sediments, but as already stated, in muddy unconsolidated sediments, the high frequency signal may be absorbed by the sediment. For objects completely buried in sand the very high frequency sonars are not very useful as the field only penetrates a couple of millimeters into the sediment.

In this thesis only very high frequency sonar is considered. Regarding buried mines the very high frequency sonar still offers good chances of detection. Experiments indicate that in only a very few cases is mine burial complete. Fig. (2.8) shows 377 cases of different burials of a cylinder mine on a muddy sediment, where data is obtained from FWG[3]. In only 10 cases, i.e., approximately 3% of the cases, was a complete burial measured. This result suggests that high resolution sonar is able to detect mines in 97% of the cases given here, but of course, a

---

[3] Forschungsanstalt der Bundeswehr für Wasserschall und Geophysik, Kiel, Germany.

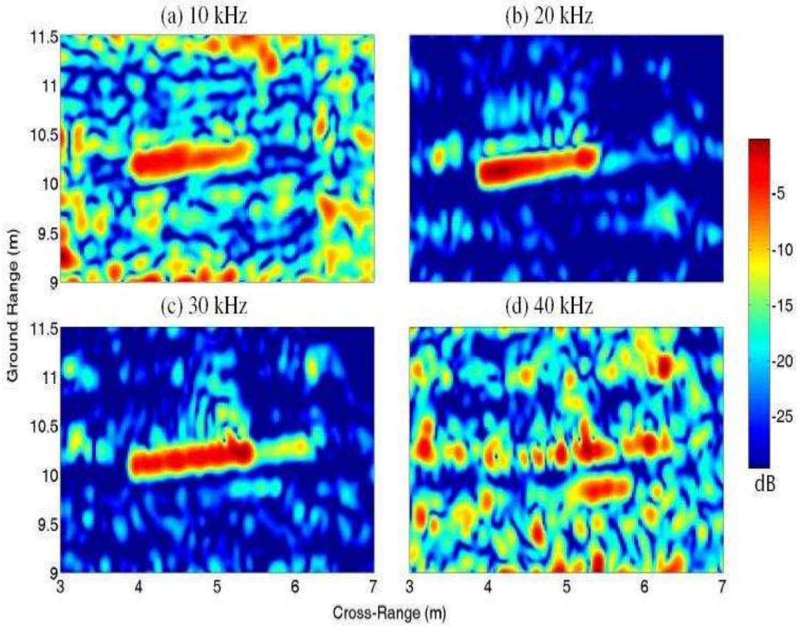

Figure 2.7: SAS intensity images (Ref. [28], pp. 150, Fig. 2), of a buried cylinder acquired by subcritical penetration into the sediment.

high degree of burial weakens the chances of detection. However, this conclusion is based on a cylindrical shaped mine on muddy sediment. Self-burying mines exist; for example, the Manta mine may be buried within a relatively short period of time in areas where strong currents produce a significant sediment transport.

Figures (2.9a-c)show images from three different types of sonars operating in the very high frequency range; Fig. (2.9a) is a Reson Seabat 8128 (445 KHz) sector sonar image of several cylindrical shaped objects (lobster pots); Fig. (2.9b) shows three examples of the low-weight Didson dual frequency (1.8 and 1.1 MHz) sonar; and it delivers video-like images and can be used by divers; and finally, a Marine Sonic sidescan (900 kHz) sonar [4] All three images are selected by the manufactures for commercial presentation.

---

[4] This sonar is applied on the Belgian REMUS-AUV.

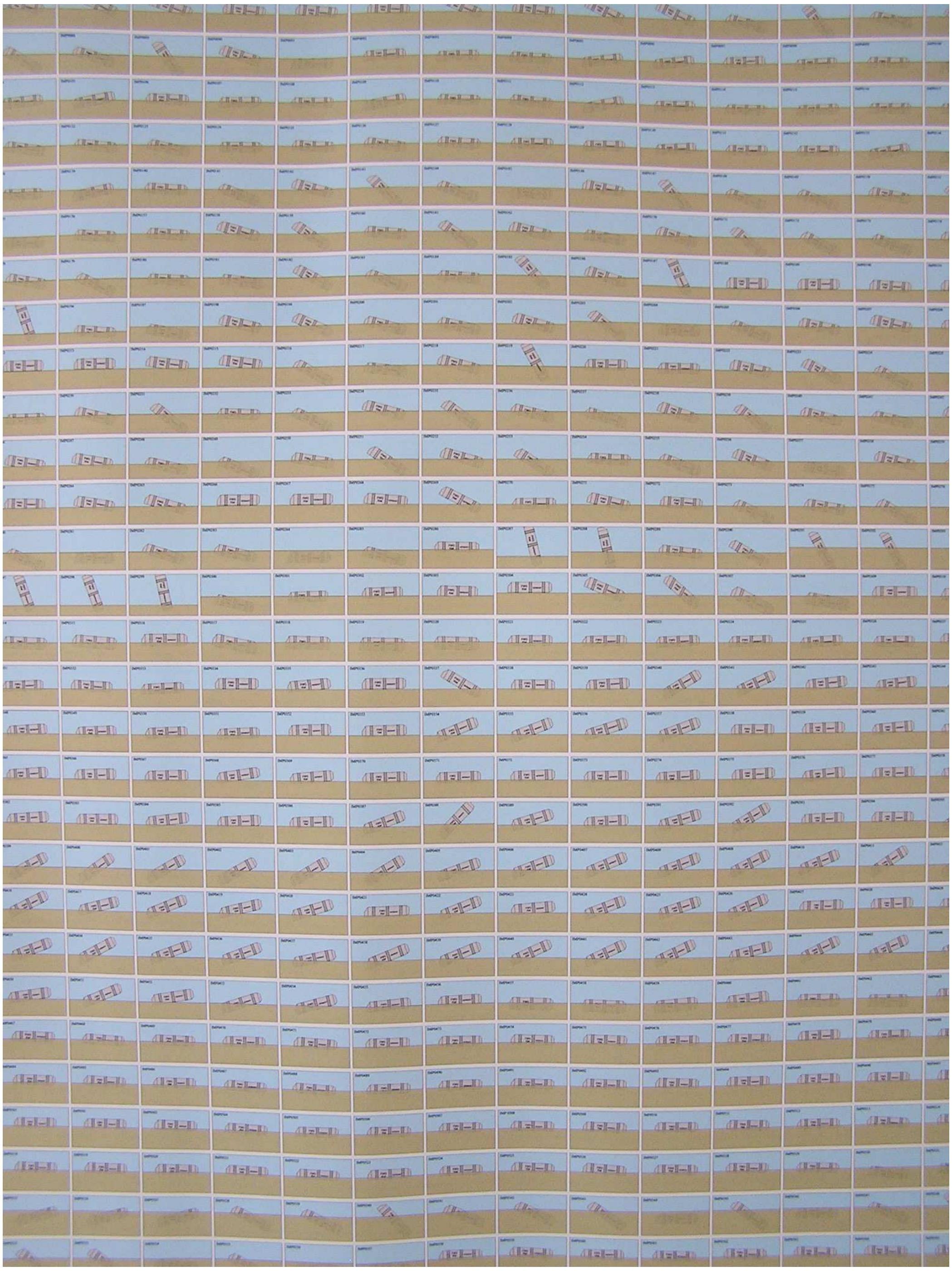

Figure 2.8: Results of experiments on mine-burial from FWG in Kiel, Germany. The figure shows $29 \times 13 = 377$ cases, and only 10 of them result in complete mine burial. The experiments have been carried out in a muddy sediment.

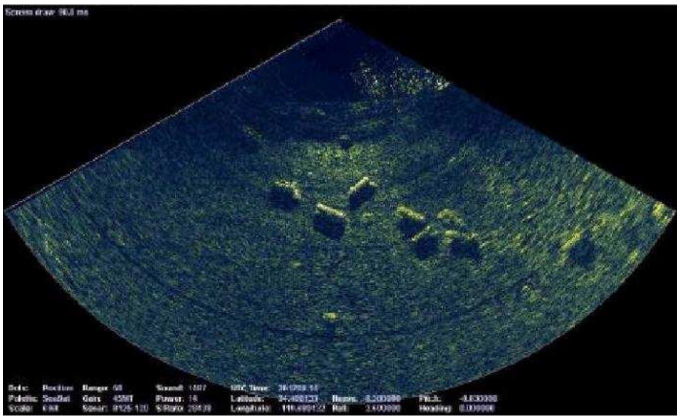

(a) Seabat 8128 sectorscan (445 kHz) image (www.reson. com)

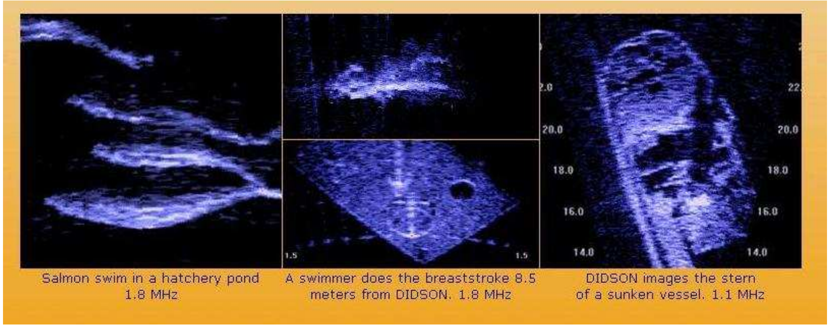

(b) Didson dual frequency (1.8 and 1.1 MHz) image (www. didson. com)

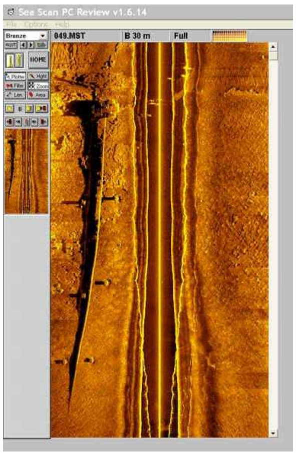

(c) Marine Sonic 900 kHz sidescan sonar image (www.marinesonic.com)

Figure 2.9: Three commercial sonar images.

2.4 DDRE/Reson sonar experiment

The images presented in Figs. (2.9a-c) are all images that the sonar manufactures have selected for commercial presentations. However, in other scenarios the images are not always as impressive. For example, the Didson sonar was applied on REMUS missions at NEST06, see Ref. [26], as a forward looking obstacle avoiding sonar and the images were distorted if the vehicle moved too fast; consequently, the sonar was taken out of the program.
DDRE experiments with a Reson 8128 sector sonar was carried out in May 2002, see Refs. [29] and [30]. The sonar was attached to a pole mounted on a naval vessel and the sonar had a grazing angle of 15° with respect to the horizontal direction. Images have been generated from 16-Bit raw-data, see, e.g., Ref. [31], that gives a dynamic range of 96 dB. The test-site was the old Ferry harbour in Korsør, Denmark, where cylindrical shaped mines had been deployed for the experiment. Images were also acquired on the near-coastal route between the Ferry Harbor and the naval harbor; here, the seabed was populated with stones which the obtained images clearly indicate, see, e.g., Fig. (2.10). A mosaic of the seabed along the route was created as a part of a Bsc. project at the DDRE [32]. The images were generated according to Ref. [33] using a grey-level 8-Bit representation, and where peak values originating from strong reflections from an object or receiver noise would be truncated by, say a factor 4, in order to enhance the background. During data acquisition in the harbour the receiver gain had a constant value of 23 dB. The images obtained in the ferry harbour with no objects included are uniform and non-featured except for a change in the harbour-seabed depth between the outer and inner harbour, see, e.g., Fig. (2.11). Figure (2.12) shows an image acquired at near normal incidence onto the broadside of a cylinder shaped mine, and the image has been truncated by a factor 24. The seabed

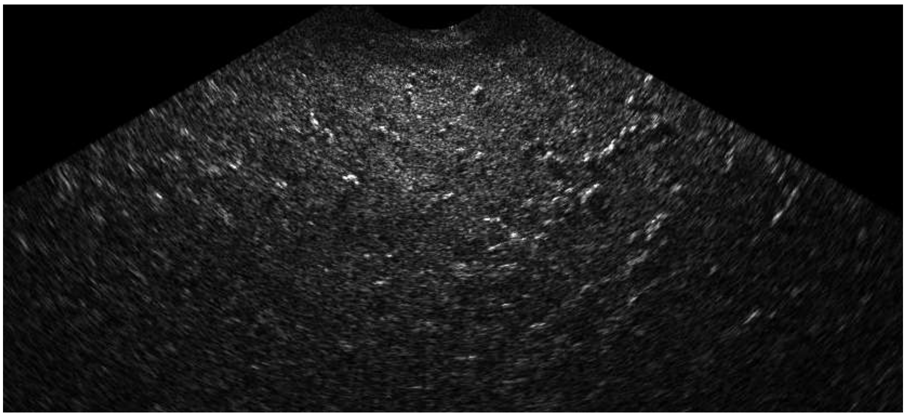

Figure 2.10: Image acquired from the stony seabed between the Ferry harbor and Naval harbor; the maximum value has been truncated by a factor 2.

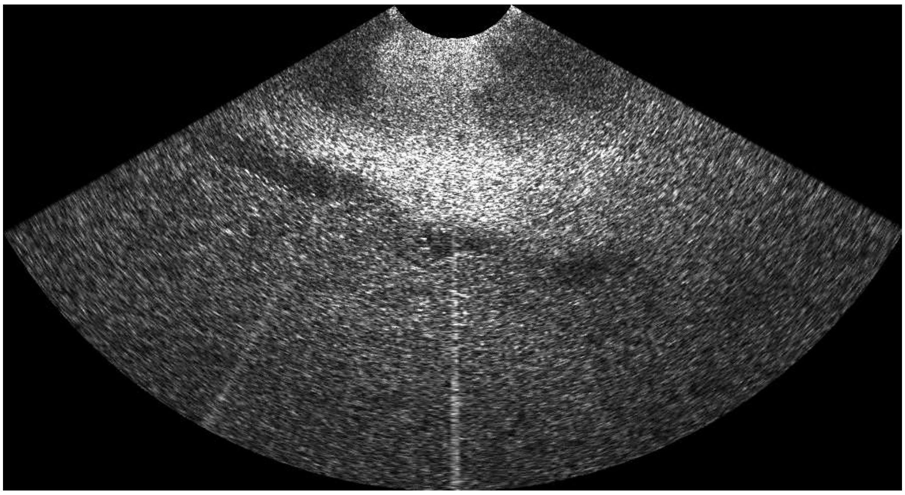

Figure 2.11: Image acquired from the Ferry harbour where the seabed is mixture of sand and mud; the maximum value has been truncated by a factor 4

properties were unknown, but it is believed to be a mixture of sand and mud; the backscattered field from the seabed was very weak compared to backscattered field from the target. Prior to truncation of the image the maximum pressure envelope difference reached 42 dB. A zoom into the mine has been made by four different approaches, see Fig. (2.13); Fig. 2.13(a) is the (R, θ), that is, the beam responses, with no truncation of the amplitude; Fig. 2.13(b) is the xy-image with no truncation of the amplitude; Fig. 2.13(c) is the xy-image with a truncation of a factor 24; and, Fig. 2.13(d) is the xy-image Log-compressed. Figure (2.14)

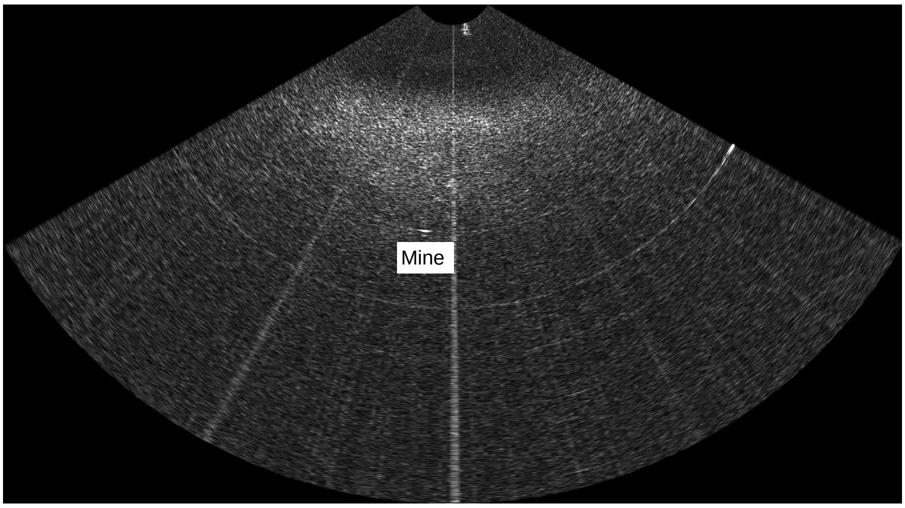

Figure 2.12: Image acquired from the Ferry harbour with a mine; the maximum value has been truncated by a factor 24

originates from the same snapshot as the images shown in Figs. (2.12) and (2.13); it has been truncated by a factor 24 and shows a larger area around the mine. The shadow is very weak, if not vanishing. Thus, the seabed response must be relatively weak, and the receiver gain is not adjusted to a sensitivity that is necessary to separate the shadow from the seabed backscattered field. Meanwhile, if the sensitivity was increased the snapshot would probably be distorted by the object reflected signal. Finally, even if the object reflected field was significantly weaker the receivers would maybe not have the required sensitivity to separate the shadow from the surrounding area.
The harbour images were used as a part of a Bsc.-project that concerned object tracking [20], where classical image processing methods were applied. Here, the harbour images, Figs. (2.11)-(2.12), have white strips caused by noise in the receiver. The three images, Figs. (2.10)-(2.12) have not, except for the truncation operation, been subject to any further processing; the Korsør images reveal that sonar images are often not as clear as the ones shown in commercial presentations.

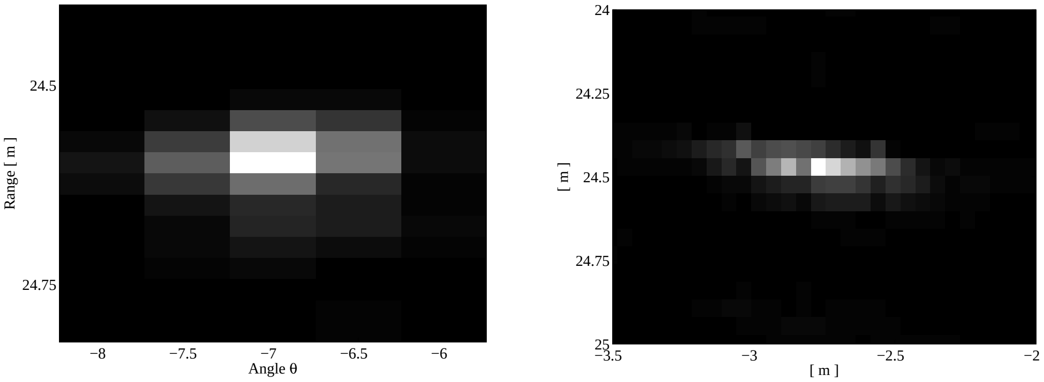

(a) R-θ image (no truncation)

(b) xy image (no truncation)

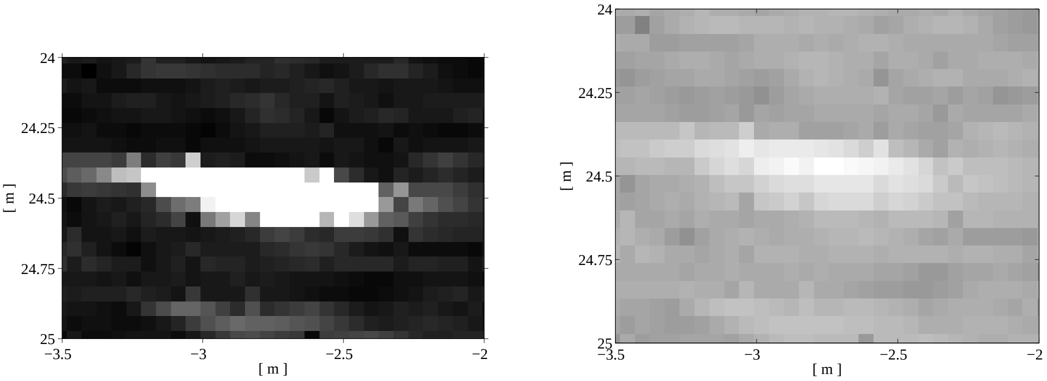

(c) xy image. Truncation by a factor 24

(d) xy image. Log-compressed

Figure 2.13: The highlight from the mine (same snapshot as Fig. (2.12)).

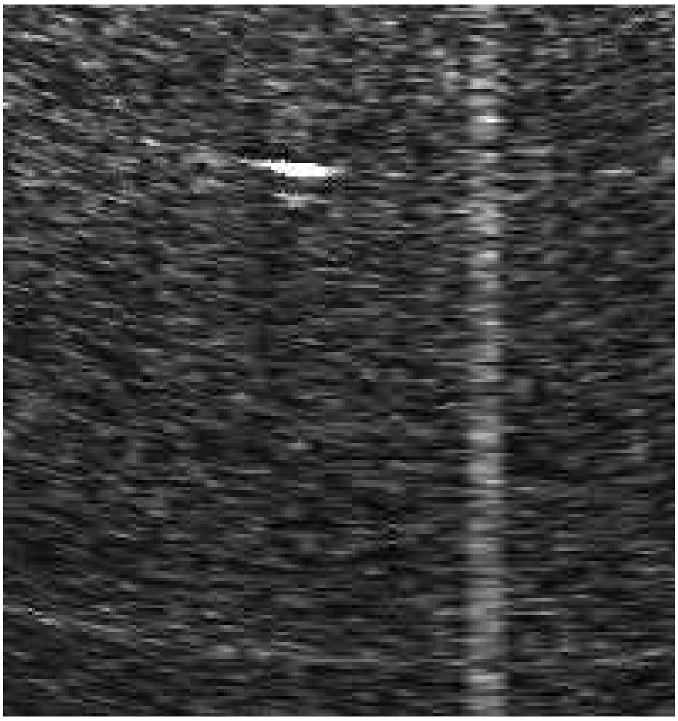

Figure 2.14: The highlight from Fig. (2.13(c)) zoomed out (it is the same snapshot as Fig. (2.12)). Note, the shadow is absent.

In this chapter the MCM concept of the Danish Navy has been presented with emphasis on the applied sensors. A brief presentation of different sonar types and their applications has been made. For the very high frequency sonars images from commercial presentations have been presented. Subsequently, images obtained from the Korsør experiment have been presented. The images obtained from the experiment reveal that successful acoustic image generation strongly depends on the environmental conditions and that commercial presentations should be viewed with this in mind.

Chapter 3

Sonar data interpretation

In this chapter small samples of the literature that concerns algorithms for detection (for example, "there is an object" or "there is no object") and identification (for example, "the object is a mine" or "the object is stone") of naval mines from sonar images and the concept of an image quality metric are addressed.

3.1 Detection/identification algorithms

Systems for automatic naval mine detection and classification from side scan sonar images have been developed by various authors, see Refs. [34], [35], [36], and [37]; generally, sonar data is processed by a time varying gain (TVG), see, e.g., Ref. [9](pp.124), and then filtered to reduce clutter[1]. Subsequently, image segmentation and feature extraction is carried out, and finally, the processed data will be subject to advanced statistical signal processing methods, such as e.g., neural networks, Bayesian filtering, or principal components analysis (PCA). The main goal in the development of computer aided detection/classification (CAD/CAC) methods is to maximize the detection and classification probability (PdPc) while maintaining a low false alarm rate. Unfortunately, an increased PdPc may often lead to an increased false alarm rate too, and that is of course inappropriate. The problem has been successfully solved, see Ref. [35], by fusing different CAD/CAC algorithms with very different strategies; the false alarm rate has decreased, and the PdPc has maintained a a constant value. There are numerous methods for classification and identification. In Ref. [38] classification of a man made object is carried out by a so called super-ellipse procedure. An automatic mine detection algorithm based on an unsupervised Markov random field model, and a classification algorithm based on a co-operating statistical snake model which extract highlights and shadows from an object has been presented by Ref. [39]; the model does not require large training data sets. Methods ap-

---

[1] Clutter is a term which is frequently used by the image/signal processing community; it refers to the highly oscillating pressure signal received from the seabed.

plied for automatic object detection from sequences of sector sonar images are presented in Refs. [40] [41] and [42]. Within this field only a very few physical conditions are included or considered; consequently, that raises the question to which extent the algorithms are robust to changes in the environmental conditions; for example, it is unclear how an algorithm based on shadow detection and classification will work when the shadow is vanishing as it is the case in Fig. 2.14.

3.2 The image quality metric

A concept of semi-automatic detection and identification of naval mines based on AUVs has been suggested by DDRE [43]: An AUV at the sea surface is (via a radio link) able to communicate the to mother ship. The AUV receives instruction to descend down to a specified position on the sea bed where an object has been detected with the side-scan sonars from the unmanned drones, see Fig. (2.1). The AUV sonar will acquire the sonar images and return back to the sea surface and transmit the images back to the mother ship. Subsequently, an operator will study the images and perhaps identify a mine. It is important that the AUV acquires images of the best possible quality. Hence, there is a need for an image quality metric - a measure that describes the quality of the sonar image to be applied by the decision algorithms on the AUV. If the metric has values that indicate high quality images, the AUV can ascend to the sea-surface and transmit the image-data. But how should this metric be defined and which properties should govern its functionality? A possible approach is to develop the metric on the basis of human perception. This concept was initiated in 1958 by Johnson [44], where target resolution, i.e., the number of pixels or resolution cells the target consists of, was compared with a human observer's capability to detect and identify the target. Later Schmieder [45] showed that background clutter in infra red images significantly reduces the observer's detection probability. Finally, Aviram [46] proposes different image quality metrics, based on estimated global clutter levels and local contrast levels in infrared images, and correlates them with detection probabilities estimated from experiments with human observers. The metrics selected were those with the strongest correlation with the human detection probabilities. All the metrics were based on infra-images or video images, and it is not clear how the methods will function on sonar images where the physics behind the image generation process is quite different.

3.3 Why a model?

A sonar image of a mine on the seabed depends significantly on the sonar's orientation with respect to the object, the shape of the object, the seabed characteristics, and the distance from the sonar to the object[2], and all these factors have an influence on the human perception and automatic algorithms for detection and identification. Hence, there is a need to understand and test the physical circumstances of sonar image acquisition in a controlled environment in order to develop algorithms for detection/identification, as well as for the development of an image quality metric. Hence, this project is aimed at developing synthetic sonar images for very high frequency sonars. A sonar simulation tool can act as a test environment for new algorithms and provide an understanding of how different seabed properties, object shapes and their orientations affect the final sonar image.

An optimal approach is to combine the model with experiments. Thus, significant inconsistencies between the model and the experiments have to be considered and explained. Perhaps the model will have to be revised and modified or new elements be included; alternatively, the experiments may be subjected to mechanical or electronic failures in the equipment; errors in the software or in the calibration will also lead to erroneous results. A sonar model can also reduce the cost and time spent on the development of detection and identification algorithms as different scenarios can be tested without necessarily involving experiments in the first stages of the algorithm development.

---

[2] For sector sonar the size of a resolution cell, i.e., pixel in an image, increases with $R\theta_b$, where R is the range and θ_b is the beamwidth in radians. Hence, the lateral resolution becomes finer as the sonar approaches the object.

Chapter 4

Summary of chpts. 1-3 and the advantage of a model

In this chapter the content of the previous three chapters is summarized, in which the problem of mine detection and identification is considered mainly within the framework of a very high frequency sonar. The summary is as follows

- In the classical defence scenario defined during the cold-war MCM was limited to selected routes where Naval ships could go pass. Typically, areas with stones and soft mud were avoided since mines are more difficult to detect there, and sandy seabeds were preferred as the acoustic response yielded shadows from the objects and reasonable highlights. Today, however, the demand for mine clearance has been extended to all types of environments, and the technological challenges in MCM have been increased.

- The acoustic response from the seabed strongly depends not only on the sediment type, that is, whether the seabed is soft (mud) or hard (stones or consolidated sand), but also on the roughness of the seabed with respect to the acoustic wavelength. The physical description of the acoustic wave interaction with the seabed is based on the assumption that the sediment is a fluid; Biot-models that include porosity will not be considered in this work as they are considered to be quite complex, and additionally, they require numerous input parameters that are difficult to obtain.

- The acoustic interaction with objects for wavelengths much smaller than the characteristic object length approaches the optical regime; a smooth surfaced object may return a large amount of acoustic energy at normal incidence onto the surface of the object, that leads to a significant highlight in a sonar image, but for other angles most of the energy is reflected in other directions. A mine whose surface is rough, for example a mine covered with shells, yields an acoustic response that consists of diffuse and coherent components, and the highlight may be absent or it will contain less energy.

For both smooth and rough surfaced objects a shadow may appear in a sonar image provided the backscattered acoustic energy from the seabed does not vanish. Stealthy mines, like the Manta and Rockan mines, are characterized by their ability to minimize acoustic backscattering; the Manta mine has additionally a shape that allows self-burial in areas with strong sediment transport.

- The Performance of optical systems are range limited because of absorption and a high degree of scattering within the water-volume; although advanced new optical systems, such as gated viewing, has been introduced, they are in most cases limited to operate at very short distances or under conditions in which the water has a high visibility. Thus, sonar is still the leading tool for underwater sensing, but the optical system may be combined with the acoustic sensor close to the object.

- Sonars are most easily distinguished with respect to frequency. Here, sonars are divided into three classes:

    1. The low frequency (< 10 kHz) ground penetrating sonar such as, for example, a parametric sonar for sub-bottom profiling. It has a poor resolution, but can reveal buried objects.
    2. The high frequency sonar for the range between 10 kHz and 100 kHz; this is applied to acoustic imaging, and recent experiments on rippled sandy seabeds have shown that the sub-critical penetration of the acoustic field into the sediment may yield images of buried objects. The resolution is moderate. For uncritical penetration the waves penetrate a couple of centimetres (depending on frequency) into the sediment. Consequently, for thin-layered and soft sediments the acoustic absorption is less significant than for very high frequency sonar (next item).
    3. The very high frequency sonar, i.e., a sonar that operates at a frequency above 100 kHz, and it is applied for acoustic imaging. Recent advances in computer-hardware have lead to high resolution multibeam sonars and sector sonar, sidescan sonar, and synthetic aperture sonar (SAS) [1]. The waves only penetrate a couple of millimetres into the sediment depending on the wavelength. Thus, even thin and soft sediments can absorb the acoustic energy and hence dramatically decrease the amount of backscattered energy.

- Experiments carried out by FWG in Germany have shown that mines dropped from ships or aeroplanes only exhibit a complete burial in muddy

---

[1] However, the resolution does also depend on signal bandwidth.

sediments. Consequently, very high frequency sonars have a reasonable chance of detection in , say, 90% of all cases on a muddy seabed.

- Sonar manufactures naturally tend to give the best impression of their products. The Reson Seabat 8128 image in Fig. (2.9a) clearly visualizes the lobster pots with highlights and shadows, and additionally, the seabed has a clear appearance; the image has been acquired under conditions where the backscattering strengths from the lobster pots and the seabed lie within the same dynamic range interval that enables raw data to be transformed into an image understandable for the humans. The Didson images and the image from the REMUS sidescan sonar (Fig. 2.9a and 2.9b respectively) are probably also acquired under best conditions. The RDN images have been acquired under a demonstration of the RDN-MCM concept, that is, a proud mine on a sandy seabed. Meanwhile, the experiments from Korsør harbour have shown that near normal incidence onto a smooth cylinder lying a soft bottom yield an image with a strong highlight with a the seabed response that vanishes together with the object shadow, but the seabed response may be enhanced if the object highlight is truncated or if the entire image is compressed.

- It is unclear how robust image processing algorithms for automatic detection and identification are to environmental changes. There is no doubt that several algorithms may be very efficient, but the absence of physical considerations should be considered with a fair amount of scepticism; after all it may have fatal consequences on their performance.

- The image quality metric based on pixel statistics used for example in infra imaging is believed to be a doubtful way to obtain an image quality metric; a metric should be combined with other, more physics based, measures.

There is a need to understand and test the physical circumstances of sonar image acquisition in a controlled environment in order to develop means for detection and identification. Hence, this project is aimed at the development of synthetic sonar images for very high frequency sonars. A sonar simulation tool can be a test environment for new algorithms and provide an understanding of how different seabed properties and object shapes and their orientations affect the final sonar image. A model that is verified with experimental data is probably the best basis for developing for algorithms for automatic MCM; it is believed that development of computer vision models, or an image quality metric, will benefit from tests in a reliable synthetic test environment before real experiments are carried out.

Chapter 5

Existing sonar models for frequencies above 100 kHz

In this chapter existing sonar models will be presented; they form the basis for some of the considerations and decisions that have been made during the development of the DDRE model. Meanwhile, the work has also been inspired by other references that are not directly related to the development of a complete sonar model; these references are related to more specific issues such as seabed scattering or object scattering, and some of them are listed in this thesis and some them are listed in the thesis papers.

A sonar simulation tool includes various sub-models and the requested simulation scenario governs which sub-models must be included, or at least how detailed these sub-models must be. Here, focus is maintained on a model that generates artificial very high frequency sonar images of arbitrarily shaped man made objects lying on the seabed. Figure (5.1) illustrates which sub-models could be included for a sonar simulation tool; source, receiver, object and seabed geometry, for example, are necessary elements for the model, but they can be modelled by different approaches. Although the elements are presented as independent building blocks, a mutual dependency exists, for example, for the object/seabed interaction. In this chapter focus is maintained on existing sonar simulation models that can generate synthetic images, and the primary focus is maintained on how the sub-models are built together. A general condition in this work is that the wavelength is much smaller than the considered environment; hence, the acoustical wave field propagation and interaction with objects, seabed, and sea-surface approaches the optical regime. The small wavelength condition implies that the seabed roughness, as well as sea-surface roughness, cannot be neglected; in fact seabed roughness is the essential source for sonar images. Low frequency models for shallow water acoustic propagation such as the Normal mode approach, see, e.g., Ref. [9], can be applied in order to describe scattering from objects and propagation in the water column; however, the short wavelength condition is not suited to normal modes since the number of modes will become extremely high

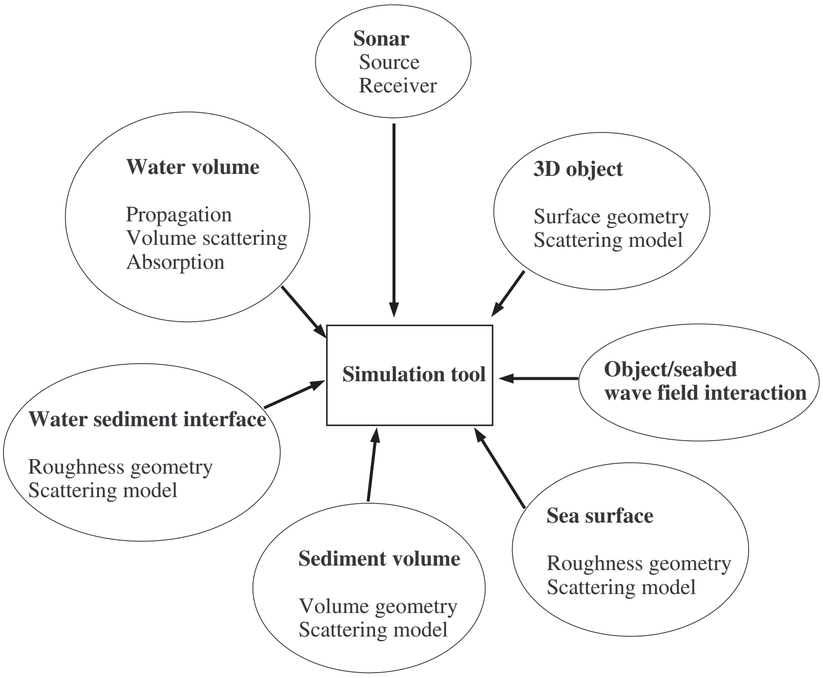

Figure 5.1: Building blocks that may be included in a sonar model. The building blocks can be mutual dependent.

and therefore computationally very demanding and not necessarily very accurate. Another approach based on parabolic equations, see, e.g., Ref. [9], is a low frequency model, but it cannot deal with a backscattering problem. For the current problem the water medium is, except for one model, assumed silent and isotropic so the acoustic field is assumed to propagate undisturbed in the medium; hence, focus is put on wave interaction with the boundaries. As a result, the study of sonar simulation models has been constrained to high frequency models that describe the propagating field by rays. It is to be borne in mind that focus is maintained on models that can generate artificial images of a man made object lying on the seabed.

J.M. Bell has developed a non-coherent model that generates synthetic sidescan sonar images, see Refs. [47], [48] and [49]. The model has been analyzed and verified by statistical analysis of the synthetic sea-floor compared with statistical results from real sidescan images. The model uses the ray tracing and includes the effects of refraction due to vertical speed of sound variations by assuming the media is horizontally stratified. Rays are emitted at preset angles from the transducer position in the 3D space and their trajectories are traced until they interact with the bottom. For each ray traced, two values are returned: the two-way travel time and the intensity. The seafloor is modelled as a height field with or without ripples and it is generated from power law spectra estimated from measurements of the seabed topography, see, e.g., Refs. [50] and [51]. The height field is represented by triangular facets to ensure the points describing each facet of the surface are coplanar. A ray that intersects the facet with a certain scattered acoustic intensity is estimated by Jackson's bistatic scattering model, see, e.g., Ref. [52]; the bistatic model is an extension of the monostatic model, see, e.g., Ref. [19] or appendix G.4. Hence, multiple scattering, typically caused by object/seabed wave interaction, is included. Only mathematically defined objects can be applied, i.e., there is no meshing involved in the object considerations; the field scattered from the object is found by application of the Kirchhoff approximation. Beam patterns for the side scan transducer as well as receiver are weighted toward the ray's intensity. Also included is the motion of the towfish, which alters the position from which the rays are traced. All the rays that return to the sonar make up a reflectogram, that is convolved with a 100 kHz pulse. Jackson's model is only verified up to 100 kHz; however, the model may use Lambert's law for higher frequencies. Refraction caused by the horizontally stratified water column has shown only to have an insignificant influence on the artificial images because the relative short-range sonar images are acquired from [53].

The Shallow Water Acoustic Toolset (SWAT) generate synthetic images of proud targets lying on the seafloor; the sonar system under consideration is a synthetic aperture sonar operating at 600 kHz, see Refs. [54] and [55]. The surface of an arbitrarily shaped object is represented by numerous rectangular facets, where the Kirchhoff approximation is applied to the computation of the scattered field. The field diffracted from edges are computed by Keller's geometric theory of diffraction and the diffracted field from bolts and small protrusions are modeled by placing point scatters at these locations. A Gaussian beam ray model for a 3D environment is applied to determine the field scattered from the seabed in which multipath contributions from the seabed, the object, and the sea-surface are also included; the rays are straight lines which correspond to a constant sound velocity in the water column. The bottom - and sea surface backscattering process are modeled as isotropic distributed point scatters, where the target strength's are treated as zero mean Gaussian random processes. Hence, topographical variations, such as directional sand ripples and a sloping bottom, are not included in the model. Shadowing caused by the target is calculated by tracing rays that intersect the object before the sea bottom. In very shallow water environments, multipath contributions from sea-bottom as well as sea surface can add highlights to the shadow zone of the sonar image. The SWAT also includes a synthetic realization of a Pierson Moskowitz surface and it's time evolution as well as bubble clouds in the surf zone. All contributions are summed coherently in order to obtain the total pressure field. A 3D coherent beam pattern represents each element of the array. It integrates the Kirchhoff-Helmholtz integral equation over the surface of the array to generate 3D coherent beam pattern for the array. Verification has been made with scale models.

The model by Caperon *et al.* [56] uses a Finite Element (FEM) method to predict the radiated field from a variety of transducer configurations. Additionally, the FEM model is applied to the modeling of receiver configurations like the degradation of a beam profile caused by, e.g., electronic failures and inter-element cross coupling. Jackson's model for high frequency bistatic scattering is applied to compute the scattered intensity from the sea bed. Recursive ray tracing is combined with the impulse response method, i.e., the model is incoherent. Three dimensional objects are composed of primitives (spheres, cones, and cylinders etc.) and the Kirchhoff approximation is applied. Synthetic images are not compared to real images and that makes evaluation difficult.

The Universal High Resolution Imaging Sonar Simulation Toolkit (UHRSST) [57] simulates backscattering of acoustic signals above 100 kHz. Data acquisition can by simulated by either a sidescan or a sector scan sonar type. The target strengths from arbitrarily shaped three dimensional objects are also computed by the Kirchhoff approximation from numerous small facets that represent the surface geometry. The seabed scattering model applied here uses seabed facets that consist of numerous sub- sand grain grids, where porosity is included. The model is coherent.

Chapter 6

The DDRE sonar model for frequencies above 100 kHz

In this chapter the DDRE model is presented. The model consists of several sub-models, or components. The artificial images obtained so far have shown, when viewed from a qualitatively point of view, to deliver good results at near normal incidence onto a cylindrical shaped target on a rough seabed. Subsequently, verifications and modifications of some of the sub-models have been carried out and shortcomings of the model have led to the introduction of new sub-models. Improvements to the sub-models and new sub-models were not implemented in the model before the end of this Ph.D.-project.

6.1 Model requirements

The Korsør experiments have shown that sonar data may exhibit large dynamic variations; it has been observed that the pressure amplitude from objects can exceed the pressure amplitude obtained from the seabed by up to 42 dB at near normal incidence onto the broad side from a cylindrical shaped object with a smooth surface. Thus, in order to model the scattered pressure from the environment in a realistic way one has to include the phase into the calculations, and therefore, the model needs to be coherent. A coherent model is a more challenging task than an incoherent model, but it is believed to be worth the effort as the modeled data will have a closer resemblance to real data, which is a key requirement. The difference between coherent and non-coherent modeling is illustrated in the following; a plane monochromatic plane wave with wavelength λ has an angle of incidence of $-30°$ onto a rough surface of length 20λ. The surface roughness has a Gaussian distribution with correlation length 0.9λ and a RMS height of 0.32λ. The scattered pressure is calculated from different stochastic surface realizations by application of Eq.(8.42) in Ref. [13], where the Kirchhoff approximation is applied. The results of 500 Monte Carlo simulations can be seen in Fig. (6.1), which shows the average scattered pressure from all 500 simulations. Figure (6.2) shows separately the scattered pressure from 8 simulations. In a coherent model the scattered pressure is calculated from a stochastic realization and the pressure amplitude scattered in a given direction depends strongly on the surface realization. For the incoherent model the scattered pressure from a rough surface is found analytically as the average or expected field contribution given some pre-specified statistical values such as, e.g., the correlation length and height RMS-value. The scattering characteristics shown in Fig. (6.1) will approach a smooth bell shaped curve if the calculations of the averages are carried out over an even larger number of surface realizations. The incoherent sonar models, presented in the previous chapter, apply Jackson's model or Lambert's law to obtain the expected field value on the surface facets that are intersected by the emitted rays; the surface facets have been generated from a stochastic realization, that is, a Monte Carlo realization. The outcome is an energy based reflectogram which is subsequently convolved with a waveform that resembles the emitted signal from the transducer. Hence, the method employs a pseudo Monte Carlo approach, and the resulting phase modulation will not yield the highly oscillating pressure envelope obtained from real sonar data. From the discussion here it has been decided that the primary requirement to the DDRE-thesis model will be coherency.

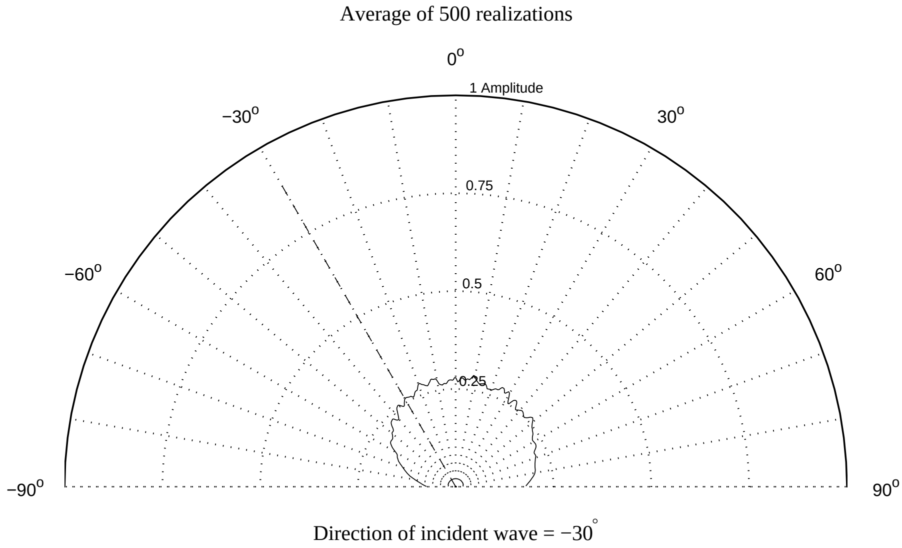

Figure 6.1: Scattering characteristics from the Gaussian surface.

Concerning accuracy and reliability, it is the intention to prioritize the seabed response and object response equally; they are mutually dependent, especially with regard to the higher order field. The seabed should be modeled as realistically as possible by adopting data acquired from *in-situ* experiments on the seabed. It must be possible to deal with, at least to some extent, arbitrarily shaped objects;

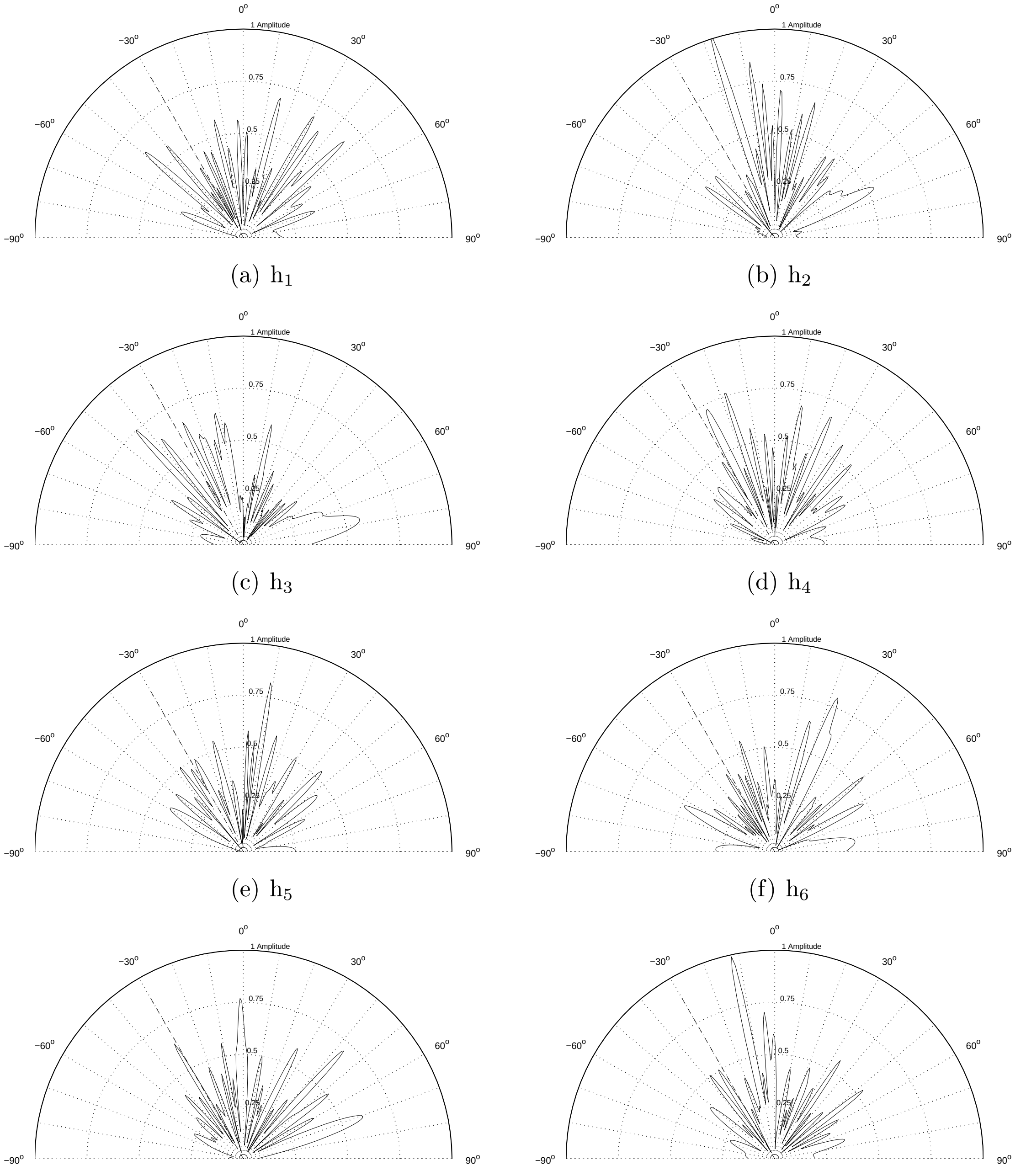

(a) h_1 (b) h_2

(c) h_3 (d) h_4

(e) h_5 (f) h_6

(g) h_7 (h) h_8

Figure 6.2: The scattered pressure calculated from 8 different surfaces realizations with the same correlation length and RMS-height value.

meanwhile, the model is limited to smooth surfaced objects. Finally, the model should be computationally efficient in the sense that images can be computed by a modern PC (year 2005 or later).

6.2 The DDRE coherent model

Among the existing sonar models the Shallow Water Acoustic Toolset (SWAT) and the Universal High Resolution Imaging Sonar Simulation Toolkit (UHRSST) compute the scattered field coherently, see Chapter 5.

The DDRE model provides a coherent computation of the scattered field from an object and the seabed. In the DDRE model the object is assumed to be rigid and smooth compared to the acoustic wavelength and the surface is numerically represented by numerous plane triangular facets; thus, the object can be arbitrarily shaped. The triangular facet is co-planar, and hence, all three grid points lie in the same plane, whereas the rectangular facet, used in the SWAT model, may fail to represent the surface correctly. The scattered field from each facet is computed by the Kirchhoff approximation. However, the expression for the field scattered from a triangular facet adopted from Fawcett [59] experiences numerical problems at certain angles, which may result in fatal errors. Hence, a new robust expression based on sinc-functions has been developed; the work has been published as a letter to The Journal of the Acoustical Society of America under the title "A numerically accurate and robust expression for bistatic scattering from a plane triangular facet", see Ref. [3], where the expression is presented and verified. A detailed derivation of the robust expression is given in Appendix K, and the Benchmark solution for the sphere applied for the verification is given in Appendix H.

The seabed is, as in the models of J.M Bell and Caperon, modeled as a 2D height field with a spatial roughness power spectrum that follows a power law found from stereo-photogrammetric experiments. The seabed is generated as a stochastic realization and frequency domain 2D overlap add filtering method enables the generation of large continuous areas, see, e.g., Ref. [5]. The 2D height field is only applied to form the large scale part of the seabed. The seabed response is calculated from several height profiles, height profiles that are interpolated from the height field that lie in planes similar to the sonar beams. Small scale roughness with a resolution finer than at least 1/5 of a wavelength is subsequently superimposed onto each height profile. Hence, the seabed response is calculated from several 2D field approximations.

The application of the Kirchhoff approximation to both the object and the seabed allows a computational efficient time domain model suitable for broad band pulses; the synthetic images have been compared with real images acquired in Korsør. The work is presented in the conference paper "Simulation of sector sonar images" at the 7^{th} European Conference in Underwater Acoustics, in Delft, The

Netherlands, 2004. Regarding the artificial beam generation Appendix I describes how the beam forming process of the Seabat 8128 has been approximated by a simple uniform linear array with 229 sensors weighted with a Hamming window, and a sensor-spacing equal to half a wavelength.

The Kirchhoff approximation is only valid for near-normal incidence on a rough surface, and consequently another seabed scattering model must be applied. Appendix G presents the basis principles of reflection, transmission and subcritical penetration of a smooth interface between two fluids; these principles form the basis for an understanding of the complex scattering mechanisms on the seabed. Suppose the seabed density increases smoothly with depth in way that resembles the average density profile found in experiments; two reflection contributions will appear, namely, the water/seabed interface reflection coefficient and the sediment reflection coefficient. The sediment reflection coefficient for normal incidence onto the sediment will become frequency dependent, with maximum values at the low frequencies. Hence, the seabed scattering computation is carried by an integral equation method for a rough interface that divides two homogeneous media and where the seabed is represented as a fluid. However, recent experiments have shown that volume scattering is a significant contributor to the total scattered field; in order to solve this problem a new method has been developed: The height field is modified to an equivalent roughness profile as the height values are altered from stochastic realizations of the density variations in the upper unconsolidated part of the sediment. Finally, as is shown here, that the scattering matrix can be approximated by a band matrix with 20 non-zero diagonals above and below the main diagonal, which allows computations of height profile lengths up to 25 metres at 300 kHz. The work has been conditionally accepted for publication on October 8th (2006) to The Journal of the Acoustical Society of America under the title "An equivalent roughness approximation for scattering at very high frequencies using a band matrix approach".

As the backscattered field is approximated by a distinct number of 2D fields in order to reduce the computational workload, an energy correction to 3D waves scattered from the seabed must be included. Appendix J addresses the expected pressure envelope as a function of range; it is shown, that the pressure envelope decays with $R^{-3/2}$, where R is the range. This relationship is based on the assumptions that the large scale height variations of seabed are small and that the seabed scatters the field according to Lambert's law.

Finally, the smooth surface assumption on the object has been exploited to detect the essential areas on the seabed ensonified by the object reflected sound. The field that propagates from the sonar to an object facet is considered; on the facet the main part of the energy is scattered into the specular direction. For a downward pointing facet the scattered field will interact with the rough seabed, where it will be scattered diffusely into all directions; however, it is only the field that points toward the receiver that is of interest, see Fig (6.3). At this stage of the project at method for localizing the seabed areas ensonified by object re-

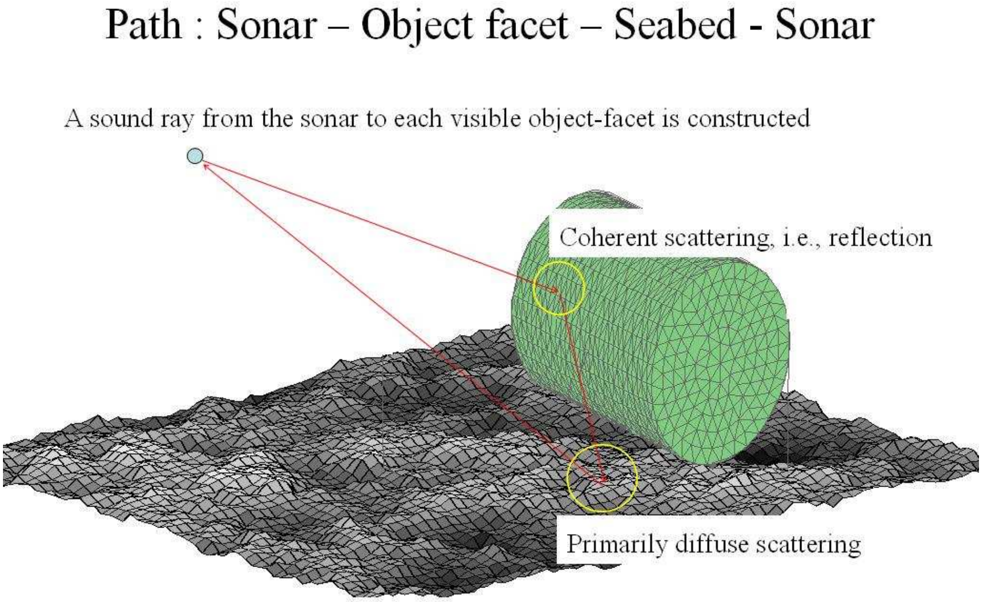

Figure 6.3: The object with a smooth surface can be applied for the localization of the seabed domains ensonified by object reflected sound.

flect sound has been developed; it has been presented in the conference paper ”Localization of seabed domains ensonified by object reflected sound at very high frequencies,” presented at "Boundary influences in high frequency, shallow water acoustics" (2005), see Ref. [2]. The regions will, for future work, be applied to approximately predict, coherently, the second order field produced by the field interaction between object and seabed; it is considered to be more reliable than a ray-tracing technique by which the full second order field is difficult to acquire. It is believed that the second order field is the dominant contributor to a highlight when sonar data is acquired from, say, a cylindrical shaped target, at angles away from near normal incidence.

6.3 Discussion and future work

The representation of an object's surface by plane triangular facets requires numerous facets especially for regions on the surface that have small radii of curvature. For example, the impulse response of the sphere represented by the plane triangular facets, see, Ref. [3] [Fig. 3, pp. 704], exhibits significant oscillations after the specular reflection that are not part of the Benchmark solutions (see

Appendix H for the Benchmark solutions). The oscillations are a result of the surface discretization and smaller facets will reduce the artifacts, but then the computational workload will increase drastically. Alternatively, one could apply a mesh-generator that combine plane triangular facets with other fundamental shapes, such as, spherical triangles, or cylindrical triangles. The curved facets would reduce the computational workload significantly, but it may not be possible to derive the expression for the scattered field analytically. This is the case when the Kirchhoff integral contains non-linear phase terms that result from a curved patch or an incoming field whose spherical shape cannot be neglected. In these cases the field integral will include quadratic phase terms and the field integral turns into a Fresnel integral, which must be solved numerically, or by the use of a look-up table. Alternatively, the field integral may be approximated by the method of stationary phase for highly oscillating integrals, see, e.g., Refs. [60] and [61]. However, for a spherical sector, at least, there is an analytical solution to the Kirchhoff approximation for a plane wave incidence, see, e.g., Appendix (H.7) where the solution is derived. Finally, recent developments within the field of graphical models and surface meshing software have introduced new sophisticated methods, for example, the so called Non-Uniform-Rational-B-Splines (NURBS) by which the surface is divided into large sub-surfaces; each sub-surface is characterized by a simple mathematical function. NURBS has been applied by Pérez *et al.* [62], where the Kirchhoff integral is evaluated over a parametric space of Bezier surfaces by application of the method of stationary phase. Radar cross sections for airplanes can be computed by the method.

Edge-diffraction has not been included in this model so far. Fawcett [59] presented a time domain expression for the edge-diffracted waves, and his work was based on the work by Van Thieu [63]. The Kircchoff approximation over-predicts the field contribution from edge diffracted waves, see, e.g., Ref. [64]. In order to avoid an implementation of an edge-diffraction model it is recognized that the definition of an edge is a mathematical idealization; regarding the edges on naval mines they are in reality rounded corners, but whether one can speak of an edge or rounded corner depends on the acoustic wavelength. For a wavelength of, say, 15 cm (10 kHz) an edge with a radius of curvature of say 0.5 cm can reasonably well be considered as an edge in its literal sense; however, for a wavelength of, say, 0.5 cm (300 kHz) the edge will rather appear as a rounded corner. Since the sonar model is aimed at frequencies above 300 kHz, for future versions it has been decided to round the corners with cylindrical or spherical triangles and apply the Kirchhoff approximation in the field integral. In Appendix H.9 it is shown that the Kirchhoff approximation performs reasonably well for a sphere with a radius of curvature down to 1/4 of a wavelength. Rounded edges will not remove the error from the Kirchhoff approximation completely; in Appendix H.7 it is shown that the analytical Kirchhoff approximation for the sphere generates an artificial back diffracted wave at the circumference between the ensonified and shadowed part of a sphere, a contribution that is not existent in the harmonic series solution solution. However, the error is believed to be reduced considerably when it is compared to the sharp edge.

The contribution from the second order field produced by the wave field interaction between the object and the seabed will have the highest priority for future work on the model. For a finite cylinder, for example, this field is believed to contribute significantly to the highlight in the case in which the sonar image has been acquired at an oblique angle with respect to the broad side of the cylinder. So far a method to estimate of the essential areas on the seabed ensonified by object reflected sound has been developed. The next step is the computation of the second order field based on these areas. For each facet on the object, an ensonified area of seabed has been found. From the seabed area the scattered field received at the sonar must be computed. The equivalent roughness approximation is planned to be used, but since the computation must be carried out on a 2D height field and not on a 1D height profile as it is done for the prediction of the seabed response, the amount of data points will increase dramatically. For example, for a 300 kHz wave, the spatial resolution must be 1 mm; it has been shown that with 20 non-zero sub-diagonals above and below the main diagonal of the scattering matrix it is possible to compute height profiles with lengths of up to 25 metres, that is, 25000 data points. However, an ensonified seabed segment of 1 m^2 will require 1000.000 data points, which of course is a problem that must be solved by reasonable approximations and/or alternative numerical techniques.

Chapter 7

Conclusions

This work concerns the generation of artificial very high frequency (> 100 kHz) sonar images applied for the training of future detection and identification algorithms.

The DDRE-model coherently computes the backscattered pressure from an arbitrarily shaped object lying on a rough seabed with a roughness power spectrum that follows one or several power laws obtained from the literature. The 3D backscattered field from the seabed is approximated by several 2D fields computed from height profiles. The surface of the object is represented by numerous plane triangular facets. The total pressure is given as the sum of the backscattered field from the object and the seabed. The Kirchhoff approximation has been applied to predict the scattered field from both the object and seabed. When the incoming field has a near-normal incidence with respect to the broad side of a cylinder the artificial images agree reasonably well with the real images, but for angles away from normal incidence the highlight disappears in the artificial image.

The original expression for the scattered field from a plane triangular facet has been rewritten in terms of sinc-functions and a numerical accurate and robust expression has been obtained.

The analytical Kirchhoff solution for the sphere has an acceptable agreement with the harmonic series solution down to a radius of one quarter of a wavelength. A very high frequency sonar signal has an acoustic wavelength of approximately $2-5$ millimetres. It is believed that the majority of the edges observed on naval mines have a radius of curvature larger than 1 mm. Thus, with the appropriate numerical model of the geometry, and by application of curved facets, the Kirchhoff approximation can also be applied with reasonable precision to the edges.

The Kirchhoff approximation applied to seabed interface roughness scattering fails except near normal incidence. The equivalent roughness approximation yields, when the horizontal AR(1)-parameter is $\kappa = 0.45$, backscattering strengths at 300 kHz that agree with experimental data acquired at SAX99. In the band-matrix approximation 20 non-zero sub-diagonals to each side of the main diagonal have been chosen. Sonar simulations are not expected to be carried out for grazing angles of less than 5°, and consequently, the field prediction error will be less than 1.5 dB. Computations have been carried out in Matab6.5$^{\mathrm{TM}}$ on a PC with a Windows XP$^{\mathrm{TM}}$ operating system, a 3 GHz (Pentium4$^{\mathrm{TM}}$) processor, and 512 MB RAM. The method allows computations of height profiles with 25000 elements that correspond to 25 metres when the resolution is one fifth of the wavelength and the wavelength is $\lambda = 0.5$ cm. The equivalent roughness approach combined with the band matrix method is well suited to model sandy seabed backscattering for artificial, very high frequency sonar images.

As the seabed response is composed of a distinct number of 2D field contributions, it is necessary to introduce an energy correction factor. For a sector sonar model where each height field response covers a lateral sector of width $\Delta\varphi$ radians, the pressure decay of the backscattered field must be approximately proportional to $(\Delta\varphi)^{1/2}\, R^{-3/2}$. Thus, since the 2D Green's function has been applied to compute the backscattered field the obtained pressure must be multiplied by $(\Delta\varphi)^{1/2}\, R^{-1/2}$.

A method for the localization of essential areas on the seabed ensonified by the sound reflected from a smooth object has been developed. The areas will be applied for future coherent computations of the second order field. Employing this approach, almost the entire acoustic energy involved in the second order scattering process can be included, an improvement on the ray tracing method, which fails to include the total amount of acoustic energy involved.

Appendix A

Thesis paper #1

Proceedings of the Seventh European Conference on Underwater Acoustics, ECUA 2004
Delft, The Netherlands
5-8 July, 2004

SIMULATION OF SECTOR SCAN SONAR IMAGES

G. Wendelboe[¤#]; J.M. Bell[*]; H.B.D. Sorensen[#] and B. Damsgaard[¤]

[¤]Danish Defense Research Establishment (DDRE), Ryvangs Allé 1, DK-2100 Kobenhavn.
[#]Oersted·DTU, Technical University of Denmark, DK-2800 Lyngby. e-mail: gwe@ddre.dk
* School of Engineering and Physical Sciences, Heriot-Watt University, Edinburgh

Future sea mine removal applications can include automated systems using AUV's equipped with, amongst other sensors, sonar followed by detection and decision algorithms. Development and application of these algorithms can benefit from simulated sonar images. This paper presents a simulation tool that mimics images from the high frequency sector scan sonar the Reson Seabat 8128. The simulation here is a sandy seabed on which man made objects may be present. The model is based on a time domain approximate description of the scattered field. The synthetic images are compared qualitatively with real Seabat 8128 sonar images.

1. INTRODUCTION

A synthetic environment, to which computer vision models applied in future AUV's can be tested, is desirable. This paper presents a model to create synthetic sonar images which mimic sector scan sonar looking down on a seabed on which arbitrary shaped objects may be present. The overall goal is the creation of realistic images. Existing sonar imaging models [1][2][3][4] consider monochromatic wave scattering where as the model presented here uses a time domain approach. The model uses 2D height profiles [2] combined with a time domain description of seafloor backscatter [5] but here approximated to all grazing angles. The time domain model for object backscattering is based on the work by Fawcett [6], but diffraction effects are not included here for simplicity.

2. MODEL DESCRIPTION

This section is divided into three subsections describing the model: Section 2.1 treat scattering from objects, section 2.2 sea floor scattering and section 2.3 signal processing and receiver transfer function.

2.1. A time-domain model for object scattering

Simulation tools using arbitrarily shaped objects [1][3][4] divide the surface of an object into a large number of small, smooth and rigid facets. In [1][3] rectangular facets have been used to estimate the target strength of an object. The Kirchhoff approximation is applied in order to relate the total field on the surface to the incoming field. The far field approximation, when valid, is convenient as it establishes a linear expression for the range between the receiver and any point on the facet which gives a linear dependent phase term [7][8]. The model here is based on [6] and use the same approximations described above but formulated in the time domain and additionally applied on triangular facets to ensure the facet points are coplanar. Hence the time domain contribution to the scattered field from a single smooth and inelastic object facet (*of*) is:

$$p_{sc}^{(of)}(t,\mathbf{x}) = \frac{p_0\ c\cos(\psi)}{8\pi\ R^2}\left[k_1\bar{e}(t-\Omega_1)+k_2\bar{e}(t-\Omega_2)+k_3\bar{e}(t-\Omega_3)\right] \tag{1}$$

p_0 is the source level, ψ the angle of incidence, c the speed of sound in the water (iso-velocity conditions are assumed) , $R = |\ \mathbf{x}\text{-}\mathbf{x}_0\ |$ is the distance from the sonar at point $\mathbf{x}$ to the facet at $\mathbf{x}_0$, k_j is a constant related to the j'th vertex and depends upon the geometry of the triangle and its orientation relative to the receiver, $\bar{e}(t)$ is the time integral of the transmitted pulse and Ω_j is the travel time between the sonar and the j'th vertex of the triangle.

2.2. A time-domain model for seafloor scattering

Analytical expressions for the average scattered intensity based on statistical descriptions of the random rough surfaces and sediment inhomogeneities are based on monochromatic wave scattering [8][9]. A time domain model of the sea floor backscattering at normal incidence has been presented in [5]. This model will use the Kirchhoff approximation for the seafloor roughness scattering and neglect volume backscattering from the sediment. Using equation (25) in [5] and assuming the emitter and receiver gain is frequency independent and equal to one, the time domain far field scattered pressure from a non-infinitesimal seabed facet (*sf*) with area ΔS is given by equation (2), where p_0 is the source level, ψ the angle of incidence, $e(t)$ the transmitted pulse, R the distance between the scattering surface and the sonar, and $\Re_{01}$ the constant water-sediment reflection at normal incidence [9] , $\Gamma = 2\sigma k\cos(\psi)$ is the Rayleigh roughness parameter, k the acoustic centre frequency wave number and σ rms roughness:

$$p_{sc}^{(sf)}(t,\mathbf{x}) = \frac{p_0\ \cos(\psi)\ \Re_{01}\ e^{-0.5\Gamma^2}}{2\pi\ c\ R^2}\frac{\partial}{\partial t}e(t-2R/c)\,\Delta S \tag{2}$$

A fractal height field [2] is interpolated into 2D height profiles where the number of profiles corresponds to the number of sonar beams, see Figure 1a. A facet is visible when the dot product between the unit normal vector and the direction vector is positive, but it also requires a slope magnitude of the line between the sonar and facet that is less than all the previous facets, see Figure 1b. A small scale roughness function with sub facets of length λ/5 and zero mean Gaussian height distribution (σ= λ/5) is superimposed around the plane of each profile facet, see Figure 1c.

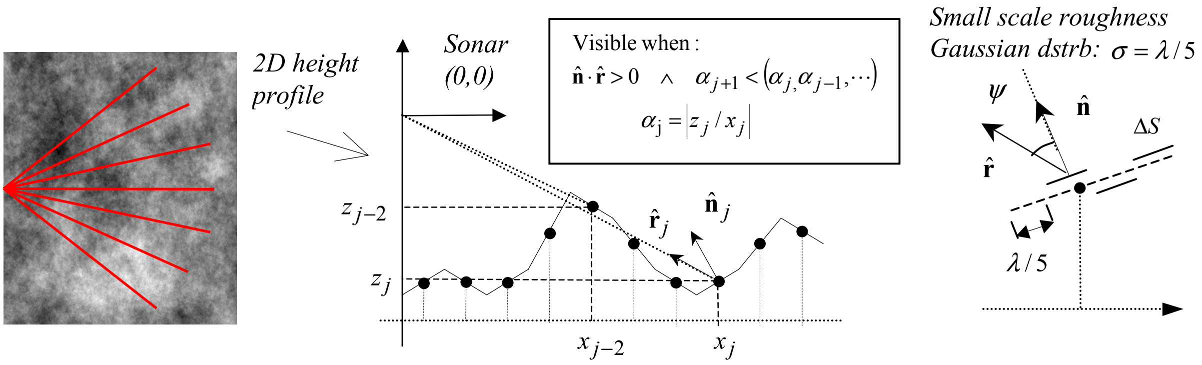

(1a) Height Field interpolation ***(1b) Shadow determination*** ***(1c) Sub facets***

Figure 1: Seabed backscattering. (a) Height field interpolation resulting in 2D height field profiles (b) Shadow determination; (x_j, z_j) is shadowed here (c) Sub facets on which equation (2) is applied.

Shadows cast by an object resulting in zero pressure return from the seabed are detected by interpolating 2D polygons of the object in the utilized beam planes; see Figure 2(a). In each shadowed beam, see Figure 2(b), the intersection of the upper and lower tangent lines with the seabed is found in a way similar to the shadow detection in Figure 1(b).

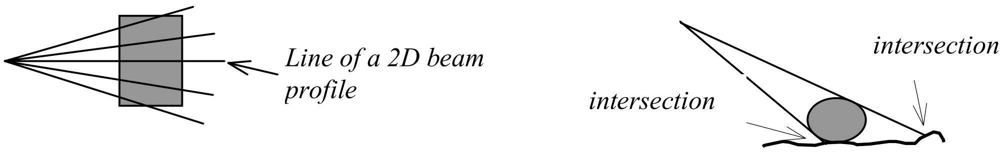

(a) 2D polygons sliced through the object ***(b) Points of intersection with the seabed***

Figure 2: Detection of shadows cast by an object.

2.3. Receiver model and signal processing

Seabat 8182 operates at 455 kHz with the horizontal beam width of 0.5° and a vertical beam width of 17°. The specific design of the sonar system is proprietary but the manufacture has stated that the system is equivalent to a uniform linear array with a 3 dB beam width equal to $\theta_{3dB} \approx 0.5°/\cos(\theta_{sta})$, where θ_{sta} is the steering angle. The frequency response of a Hanning weighted uniform linear array with 330 sensors will represent the receiver. The frequency response is considered constant for all frequencies contained in the transmitted narrowband signal. Hence it is sufficient to multiply the complex waveform with the receiver response for the centre frequency ω_0 [11]. Equation (1) and (2) are valid in far field, but the sonar will frequently operate in the near field. Fortunately, the receive beams of the 8182 are dynamically focused and the sonar system is performing as a system operating in the far field [12]. The time integral of the emitted waveform is convolved with the impulse response of the each surface patch of an object according to equation (1) and the time derivative of the emitted waveform is convolved with the impulse response of the each beam profile of the seabed according to equation (2). For each separate signal, the analytical signal is extracted using a Hilbert transform. The complex representation of the backscattered waveform is weighted with the receiver transfer function for all steering angles with respect to the facets horizontal angle relative to the receiver. Subsequently, for each beam the complex waveform is added to contributions from other surface facets as well as the contributions from the seafloor profiles.

3. RESULTS

This paper present three authentic and three synthetic images. The authentic images were acquired at Korsor Ferry Harbour in DK, May 2002. Technicians from Reson Inc. supplied Seabat 8182 and auxiliary equipment. Korsor Naval station supplied a ship and the personal to mount the sonar on the end of a pole fixed on the ships aport side. During trials the sonar head was positioned 1.5 meters below the sea surface and the depression angle was 15 degrees. The depth was approximately four meters over the entire trial area. A cylinder of length 1 meter and 35 cm in diameter with handles at both side ends had been dropped on the bottom of the harbour – the precise location and orientation unknown. The emitted sinusoid had duration equal to 29 cycles. The sonar images are represented as unsigned 8-bit (uint8) images by

$$I_{8Bit}(x,y) = \mathrm{uint8}\left(\gamma \cdot I(x,y)/I_{\max} \cdot 255\right) \quad , \quad I(x,y) \geq 0 \tag{3}$$

$I(x,y)$ is the pixel intensity value of the slant range image converted into Cartesian coordinates (x,y), γ is a scaling factor applied for enhancing the background but truncating the highlights. Figure 3 show three different snapshots acquired from experiments; each column represents a snapshot. The images on the top row have a horizontal field of view equal to 60° (half of the beams have been discarded); the mid row images have been zoomed into object highlights and shadows and the bottom row shows un-truncated images zoomed further into object highlights. The image in the first column is probably close to the normal incidence along the broadside of the cylinder as object to seabed ratio $OSR = 20 \cdot \log_{10}(|p_{obpeak}|/|p_{sbmean}|)$ is about 40 dB and the highlight extends approximately over one meter. In the two other cases OSR is about 25 dB and the highlight extends over a broader area. Figure 4 shows three synthetic snapshots. The cylinder model is represented by facets whose average side length is approx. two times the wavelength. The handles are not included in the geometry. Parameters chosen: $\Re_{01} = 0.4$ and $c = 1500\ m/s$. The images shown are normal and near normal incidence cases and appear reasonable compared to the first column in Figure 3. For angles away from normal incidence (not demonstrated here) the highlights disappear; at these angles diffraction and higher order reflections are the main contributors to the backscattered field. Shadows appear more clearly in the synthetic images probably because higher order reflections, volume scattering and receiver noise not have been taken into account. The rough shadow edges are in accordance with real images. Finally the background, i.e. the seabed, appears realistic when compared to the real images.

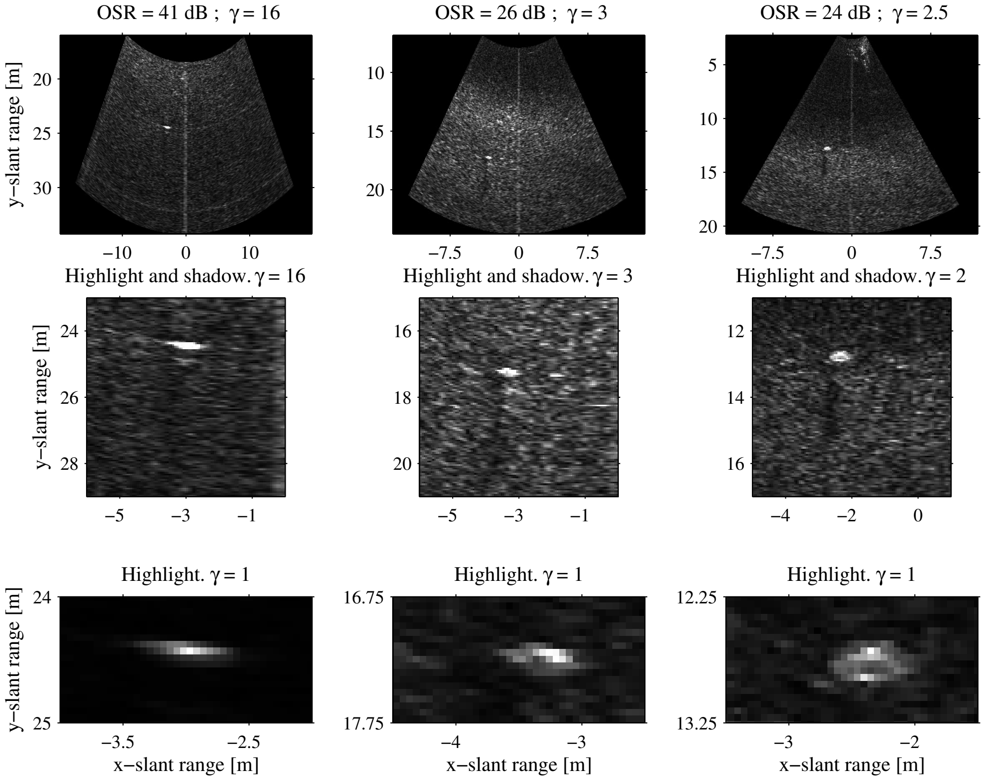

Figure 3: Images from three authentic snapshots.

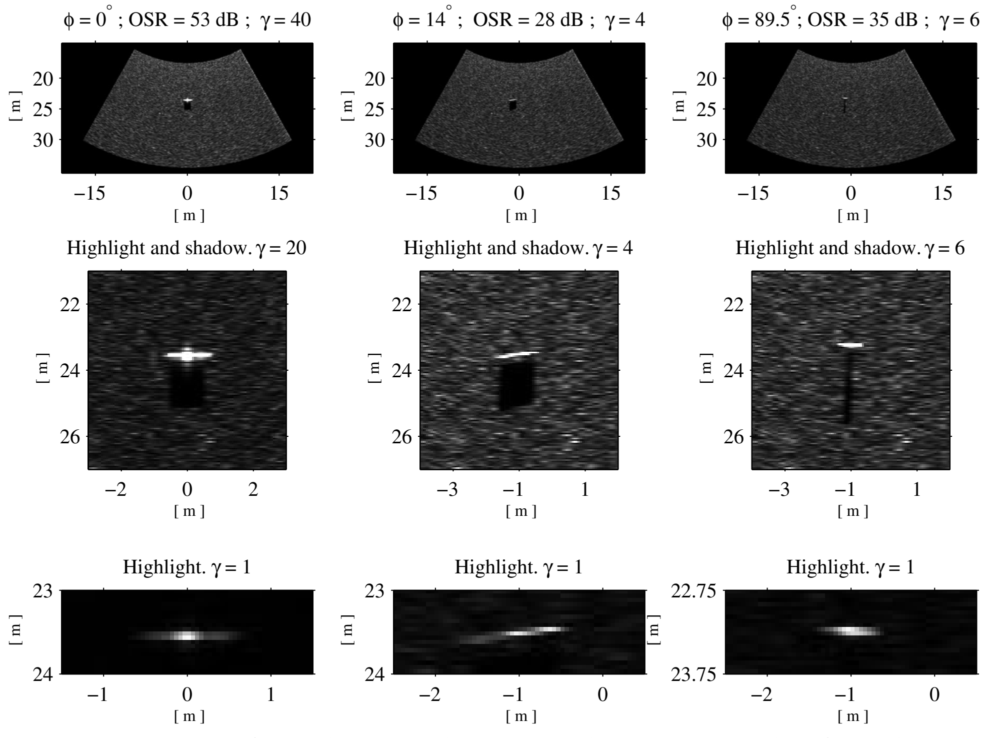

Figure 4 : Images from three synthetic snapshots. ϕ is angle of incidence with respect to the midpoint of the cylinder.

4. SUMMARY AND CONCLUSION

Synthetic sector sonar images of a rigid cylinder located on a fractal seabed have been created from a time domain model where the emitted waveform is convolved with all visible seabed and object facets. The synthetic images have been compared qualitatively to authentic images and the resemblance is reasonable concerning shadows and background. Object highlights appear realistic near normal incidence. The work will continue by introducing diffraction and higher order reflections into the model.

5. ACKNOWLEDGEMENTS

The authors are grateful to Reson A/S for supplying the necessary equipment and expertise during the Korsor experiments 2002. The authors are grateful to Rich Lear for managing the equipment during the experiments and for good communication, as well as to C.D. Cappeln for questions concerning the receiver aperture. The authors benefited greatly from O.H. Jensen and K. Tornslev at DDRE for developing software to read sonar raw-data and for their practical help during the experiment. The author benefited greatly from discussions with Finn Jacobsen at Acoustic Technology, Oersted DTU, concerning general acoustic issues. The author gratefully acknowledges the research supervision and placement provided by the School Engineering and Physical Sciences at Heriot Watt University, Edinburgh.

REFERENCES

[1] **O. George & R. Bahl**, Simulation of High frequency Sound from Complex objects and Sand Sea-Bottom, *IEEE J. Oceanic Eng.*, vol. 20 (2), pp. 119-130, 1995.

[2] **J.M. Bell**, Application of optical ray tracing techniques to the simulation of sonar images, *Optical Engineering*, vol. 36 (6), pp. 1806-1813, 1997.

[3] **G. Sammelmann**, Propagation and Scattering in Very Shallow Water, IEEE *Oceans*, pp. 337-344, 2001.

[4] **T. Capéron, G.Hayward & .Chapman**, A 3D simulator for the design and evaluation of sonar system instrumentation, *Meas. Sci. Technol*, vol. 10, pp. 1116-1126, 1999.

[5] **E. Pouliquen, O. Bergem, and N.G. Pace**, Time-evolution of seafloor scatter. I. Concept, *J. Acoust. Soc. Am.*, vol. 105 (6), pp. 3136-3141, 1999.

[6] **J.A. Fawcett**, Modelling of high frequency scattering from objects using a hybrid Kirchhoff/diffraction approach, *J. Acoust. Soc. Am.*, vol. 109 (4), pp. 1312-1319, 2001

[7] **H. Medwin C.S. Clay**, *Fundamentals of Acoustical Oceanography* , Academic Press, 1997.

[8] **J. A. Ogilvy**, *Theory of Wave Scattering from Random Rough Surfaces*, IOP Pub. Ltd, 1991.

[9] **K. L. Williams and D. R. Jackson**, Bistatic bottom scattering: Model, experiments, and model/data comparison, *J. Acoust. Soc. Am.*, vol. 103 (1), pp. 169-181, 1998.

[10] **F. Jensen, W.Kuperman, M. Porter & H. Scmidt**, *Computational Ocean Acoustics*, AIP Press, pp. 54-55, 1994.

[11] **Prabhakar S. Naidu**, *Sensor Array Signal Processing*, CRC Press LLC, pp. 87-89, 2001.

[12] **V. Muriono & A. Trucco**, Three-dimensional image generation and processing in underwater acoustic vision, *Proc. of the IEEE*, vol. 88 (12), pp. 1903-1945, 2000.

Appendix B

Thesis paper #2

LOCALIZATION OF SEABED DOMAINS ENSONIFIED BY OBJECT-REFLECTED SOUND AT VERY HIGH FREQUENCIES

G. WENDELBOE[¤#] AND [#]F. JACOBSEN

[¤]*Danish Defense Research Establishment (DDRE) , Ryvangs Allé 1, DK-2100 København. E-mail:*
gwe@ddre.dk. [#]Oersted DTU, Technical University of Denmark, DK-2800 Lyngby. E-mail:
gw@oersted.dtu.dk & fja@oersted.dtu.dk

J. M. BELL

School of Engineering and Physical Sciences, Heriot-Watt University, Edinburgh
E-mail: j.bell@hw.ac.uk

The ability to detect and identify an object located on the seafloor by application of images acquired from monostatic sonar depends on the shape and orientation of the object with respect to the sonar. For example, on-axis incidence on a cylinder results in a strong reflected wave, but with a few degrees of rotation, the only contribution to the direct backscattered signal may be diffracted waves. Sound interaction with the seabed, however, may contribute significantly to the backscattered signal. In this paper, domains on the seabed ensonified by reflected sound from a smooth arbitrarily shaped object are localized. These domains can be applied for computing the second order scattered field relevant for a sonar model. Analysis has been carried out in two and three dimensions. In two dimensions, object reflected rays are visualized for a sphere/cylinder and a truncated cone (Manta-mine) together with their estimated ensonified seabed domains. In three dimensions the estimated ensonified seabed domains are visualized for a sphere and a cylinder.

1 Introduction

This work is related to the generation of synthetic sector sonar images, that is, images acquired with high frequency (>100 kHz) sonar systems. The interest is focused on images of naval mines, but also man made objects in general, located on a sandy seabed. The model developed so far computes, coherently, the scattered field from the object and the seabed separately and finally the contributions are summed to give the total field. The Kirchhoff approximation or the physical optics solution [1-4] is the basis of the model. The model has been presented in Ref. [5], where synthetic images were compared qualitatively with authentic images of a finite cylinder on a sandy seabed. At angles close to normal incidence, i.e., normal incidence with respect to the cylinders axis, the resemblance was found to be reasonable, but away from the normal incidence the only contribution to the backscattered field may be diffracted waves and higher order reflections, features that are not implemented in the model at this stage. In the off-normal

N.G.Pace and P Blondel, (Eds), Boundary Influences In High Frequency, Shallow Water Acoustics Pages 391-398, University of Bath, UK 5th-9th September 2005

incidence cases the synthetic images only include seabed backscattered pressure and a shadow cast by the object, whereas pressure contributions caused by the sound interaction between the seabed and object are absent. If a model based on the boundary element method was employed instead higher order reflections would be an inherent part of results obtained. In the scenario under consideration the dominant wavelength is equal to approximately three millimeters and the object has, say, a length of 1 m and it is located on a rough seabed covering several square meters. Hence, a boundary element model would require an excessive computational capability. Instead, the Kirchhoff approximation will continue to be the fundamental building block in the model and it will also be used to model the seabed object sound interaction.

Sound field interaction between the seabed and a proud object has been analyzed by Fawcett [6-7] who applies an image source method because the dominant wavelength is large compared to the roughness heights, i.e., the seabed interface can be described as perfectly flat. Bell [8] has developed an incoherent sonar model for high frequency sound propagation in a refracting medium. The model is based on optical ray tracing with higher order reflections being an inherent part of the method. The incoherent model by Capéron [9] only applies straight line rays, but likewise, higher order reflections are also an inherent part of the sound propagation model. The coherent model by G.S. Sammelmann [10] only uses ray tracing to estimate the sound field interaction between the seabed (consisting of randomly distributed point scatters) and an object, whereas object backscattering is based on the physical optics solution.

In the model presented here, a ray - or wavefront component is intended to be assigned to each visible facet on the object, and, by application of the physical optics solution, the coherent field reflected down toward the seabed from the object will be computed. The next step will be to calculate the field scattered back to the sonar. However, in order to reduce the computational load it is necessary to include only seabed areas ensonified by a suitable amount of energy. This paper describes how essential areas on the seabed ensonified by object reflected sound are found.

In section 2 the second order field caused by the object-seabed interaction is considered. It is argued how the sonar-object-seabed-sonar paths can be found relatively easy, and additionally, when these paths are estimated they can – approximately - describe the full second order field. In section 3 the method to localize essential areas on the seabed ensonified by object reflected sound is described. In section 4 results are presented for two- and three-dimensional simulations. Finally in section 5 a discussion and conclusions are presented.

2 Second order scattering caused by object-seabed wave interaction

The basic assumption for the work presented here is that the surface of the object is smooth, i.e., the radius of curvature on any point on the surface is much greater than the dominant wavelength. In other words, nearly anywhere on the surface the field is scattered coherently, i.e. reflected, and the Kirchhoff approximation works very well.

Consider the field emitted from a sonar incident onto an object. On the surface of the object the field scattered from a surface element with dimensions larger than, say, three wavelengths will be concentrated in the specular direction, see Fig. 1A. Hence, each

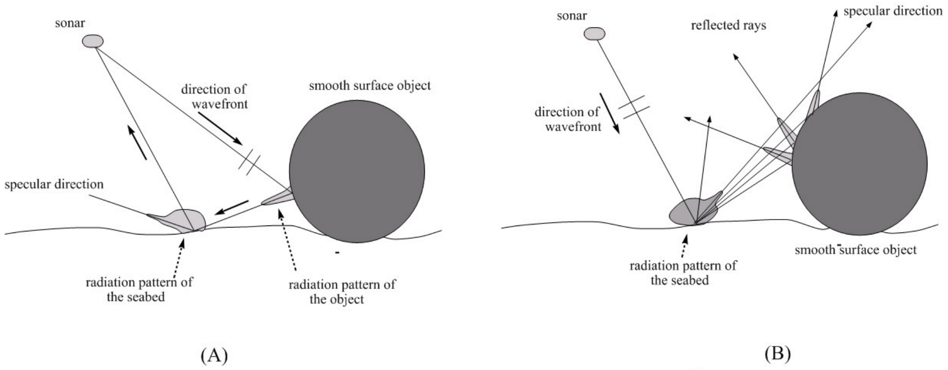

Figure 1: High frequency sound interaction between an object and the seabed for mono static sonar. Figure (A) shows the sonar-object-seabed-sonar path and Figure (B) shows the ray when the direction has been reversed, i.e., when the sonar-seabed-object-sonar path is considered.

surface element acts as local mirror, which, when directed down toward the seabed, only ensonifies a limited area. From the limited region on the seabed ensonified by the small reflector on the object the sound is scattered diffusely (but it may also contain relatively weak coherent components, depending on the roughness characteristics of the seabed). There are no ambiguities associated with the direction of the wave field scattered from seabed since interest only is on the part of the wave field received by the sonar. The seabed topography, or roughness, governs the resulting wave interference generated here. Hence, the sonar-object–seabed-sonar path, see Fig. 1A, appears with the assumption of a smooth object, to be unambiguous. The opposite sonar–seabed-object-sonar path, see Fig. 1B, is far more difficult to estimate, because here it is necessary to search for the point on the sphere where the seabed scattered sound will be reflected up to the sonar. In any other direction the field is reflected away. However, the full second order field, i.e. the field that experiences a single bounce on the object and a single bounce on the seabed is assumed to be approximately provided by multiplying the results obtained from the sonar-object–seabed-sonar path by 2, and hence, the interference between different wave paths is neglected.

In order to reduce the computational workload for second order scattering a preliminary wave field calculation for the estimation of the most important ensonified seabed areas is carried out. The method is described in the next section.

3 Method for localizing of the essential ensonified seabed regions

In the sonar model, the surface of three-dimensional objects and the seabed roughness interface, a height field, are represented by plane triangular facets. The scattered field is computed coherently in the pressure domain by application of the Kirchhoff approximation, which relates the incoming field to the total field on a surface. The Kirchhoff approximation reduces the Kirchhoff-Helmholtz integral equation to an integral. Consider an arbitrary facet in the numerical representation of the geometry, say, the m’th facet. Let p_0 be the peak pressure 1 meter from the source, $\boldsymbol{r}_0$ the vector from the facet to the sonar with the length $|\boldsymbol{r}_0| = r_0$, $\boldsymbol{r}_1$ the vector from the facet to the observation point with the length $|\boldsymbol{r}_1| = r_1$, and $\boldsymbol{n}_s$ the normal vector of the facet surface, S. If k denotes the wavenumber and $\boldsymbol{x}_s$ the integration variable over S, then the bistatic expression for the scattered pressure from any plane facet in the numerical representation of the geometry is

$$p_{sc}^{(m)}(\boldsymbol{x}) = \frac{p_0\, (\hat{\boldsymbol{r}}_1 \cdot \hat{\boldsymbol{n}}_s)\, e^{ik(r_0+r_1)}}{2\pi\, r_0\, r_1} \int_{S_m} e^{-ik(\hat{r}_0+\hat{r}_1)\cdot x_s}\, dS_m \ , \tag{1}$$

where a vector with a superscripted hat (^) corresponds to a unit length vector. For each facet on the object surface, the specular direction corresponds to the stationary point of (1) where the complex exponential phase term vanishes, and the pressure is

$$p_{sc}^{(m)}(\boldsymbol{x}_{sp}) = \frac{p_0\, e^{ik(r_0+r_1)}}{2\pi\, r_0\, r_1}\, \hat{\boldsymbol{r}}_1 \cdot \hat{\boldsymbol{n}}_s\, S_m \, , \tag{2}$$

where, $\mathbf{x}_{sp}$, corresponds to any point on the line that originates from the facet and points in the specular direction down toward the seabed. A cone around the specular ray is constructed. The cone width shall resemble, say, the 3 dB width of the radiation pattern in the specular direction from the object facet. The cone intersects the average seabed level, a perfect plane, as an ellipse. The area of the ellipse depends on the location and orientation on the facet, and the perimeter will be found numerically. The analysis is aimed at the localization of seabed areas essential for second order field computation, that is, areas on the seabed where the incoming object-reflected field is concentrated. In the analysis the field is regarded as incoherent and the total sum of all time averaged intensity contributions from all facets on the mean seabed plane is calculated. A coherent summation would result in a misleading interference pattern for energy on the flat seabed, because, the real interference pattern caused by the seabed most likely would differ significantly. An incoherent summation, on the other hand, will give a smoothly distributed intensity map independent of the seabed roughness interface. Hence, the time averaged intensity [11] received at the average seabed plane and radiated by, say, the m'th object facet is given by

$$I_{av}^{(m)} = \frac{|p_0|^2}{4\pi\rho c r_0^2} \frac{\left|\cos(\theta_1)\ S_{obj}^{(m)}\right|^2}{r_1^2} \approx \xi\, \frac{\left|\cos(\theta_1)\ S_{obj}^{(m)}\right|^2}{S_{ellipse}} \ , \tag{3}$$

where ξ is a proportionality constant. The area of the ellipse, $S_{ellipse}$, is approximately proportional to the square of the range, r_1, i.e., the range from the facet to the intersection point on the smooth seabed plane. Only when the ellipse is very large compared to the object, that is, when the centerline of the cone intersects the seabed far from the object, the approximation is invalid. A cone with an axis that intersects the seabed a distance larger than, say, five times the characteristic length of the object, is discarded. Hence, the average intensity of the incoming field is assumed constant over the elliptical shaped area. Additionally, the variation of r_0 when considering different object facets is neglected, and consequently, ξ is constant for all ellipses and is set equal to 1.

A mesh grid in the seabed plane is generated, and for each object facet the points within the seabed ellipse are found. For all of these points the magnitude of the intensity given by Eq. (3) is added to previous values assigned from other facets. Finally, an intensity matrix for the incoming field onto the seabed around the object is obtained. The essential ensonified area is found by using a threshold value which is a certain fraction of the maximum intensity value in the intensity matrix. Hence, all values larger than the threshold value are considered within the region of ensonification.

4 Numerical models

Simulations have been carried out in two and three dimensions. The threshold value has been set to 10% in all cases. The radiation cone in the specular direction has an angle of 12º.

In the two dimensional case the scattered field from the cross the section of a cylinder and a Manta-mine is analyzed. In both cases the sonar is 3 m above the seabed and the ground range distance to the object is 9 m. The cylinder has a radius of 0.35 m and its cross section is numerically represented by 1D facets, i.e., line segments of 3 mm length. In Fig. 2 (top) rays outgoing from some of the facets are shown. The major part of the ensonified energy is concentrated in front of the cylinder. Behind the cylinder seabed areas are also ensonified, but the incoming intensity there is weak as the effective reflection area on the object is small. In Fig. 2 (bottom) the object reflected area has been estimated and the ensonified area covers approximately 1 m. The Manta mine, see Fig. (3), is located at the same position as the cylinder, it has a bottom radius equal to 0.35m, its slope is 50º, and its height is 0.42m. As can be seen the stealthy Manta mine does not reflect any sound onto the seabed and the top-surface reflected sound is directed away from the sonar. The incoming field will be perpendicular to the object surface and a reflected wave is generated only in very exceptional cases. However, roughness on the surface of the object might produce a backscattered wave, but this topic is not treated here.

Three-dimensional simulations have been carried out for a sphere and a finite cylinder. In both cases the sonar is located 3 m above the seabed with a ground range distance to the object equal to 6 m. The plane triangular facets had a maximum side length of 14 mm. Figure 4 shows the estimated ensonified area by a sphere with radius 0.2 m. The sphere ensonifies an area approximately equal to 0.4 m^2. The cylinder has a length of 1 m, radius of 0.2 m, and the cylinder axis is rotated 30º with respect to the y-axis of the seabed plane, see Fig. 5. The cylinder ensonifies an area on seabed along the cylinder axis which is approximately equal to 0.5 m^2. Additionally, an area of 0.2 m^2 is ensonified by the endcaps.

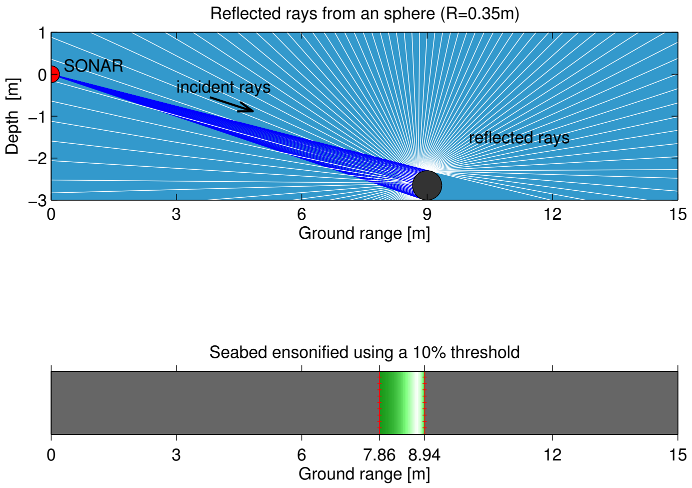

Figure 2: Reflections from a sphere/cylinder (2D). (Top) shows incident rays and some of the reflected rays from the object and (Bottom) the area of seabed ensonified by object reflected sound assuming a threshold value of 10%

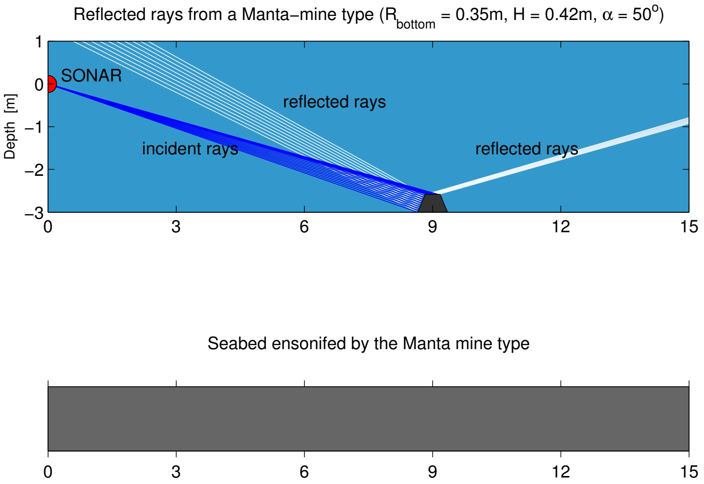

Figure 3: A Manta mine on a flat seabed. (Top) shows incident rays and reflected rays from the object and (Bottom) the stealthy properties of the mine are revealed as no seabed is ensonified by object reflected rays.

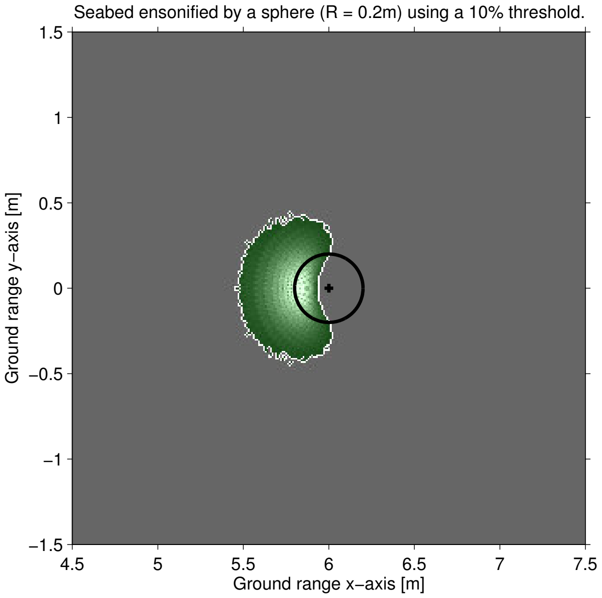

Figure 4: Estimated seabed domains ensonified by a sphere of radius 0.2 m and positioned 6 ground range meters from the sonar. The sonar is located at $x = 0$, $y = 0$, and it is elevated 3 m above the seabed. The applied threshold value is 10%.

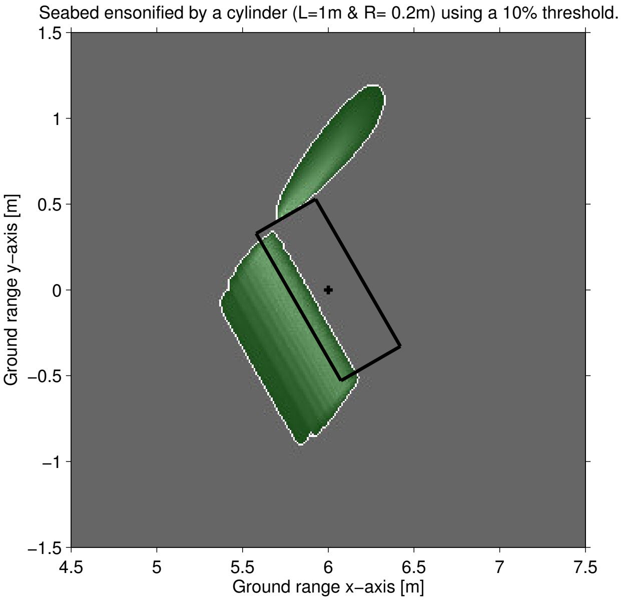

Figure 5: Estimated seabed domains ensonified by a cylinder of radius 0.2 m and length 1 m. The cylinder is 6 ground range meters from the sonar and its axis is rotated 30º with respect to the y-axis. The sonar is located at $x = 0$, $y = 0$, and it is elevated 3 m above the seabed. The applied threshold value is 10%.

5 Discussion and conclusion

A numerical method that estimates domains on the seabed ensonified by object reflected sound has been developed. The method assumes that the objects are smooth and that nearly anywhere on the surface of the object the field is scattered coherently. The assumption of smooth surfaces may only hold in certain cases, since at other times, an object can be covered with plants and different species, and consequently, it will scatter more or less diffusely. In the very rough cases the idea presented in this paper becomes irrelevant, and the object might as well be considered as a part of the seabed, where only the shadow can reveal any presence of a man made object. Scattering of orders higher than two, e.g., third order sonar-seabed-object-seabed-sonar or sonar-object-seabed-object-sonar paths, may also have a significant influence on the total field. The influence of higher order scattering primarily depends on the loss of sound energy per bottom bounce.

Results showing the ensonified area of seabed have been presented in two- and three dimensions for cylindrical, spherical and truncated cone (Manta) shaped objects, illustrating some of the stealth properties of the Manta compared to the other shapes. The three-dimensional results have a direct application as the method in three dimensions will be applied to compute the second order field using physical optics solution and will be the topic of the future work.

References

1. Medwin H., Clay C.S, *Fundamentals of Acoustical Oceanography*, Academic Press (1998)
2. Ogilvy J.A., *Theory of wave scattering from random rough surfaces*, IOP Publishing Ltd. (1991)
3. Fawcett J.A., Modeling of high frequency scattering from objects using a hybrid Kirchhoff/diffraction approach, *J.Acoust. Soc. Am.*, **109** (4), pp. 1312-1319, (2001)
4. Pouliquen E., Bergem O., and Pace N.G., Time evolution of seafloor scatter. I. Concept, *J.Acoust. Soc. Am.*, **105** (6), pp. 3136-3141 (1999)
5. Wendelboe G., Bell J.M., Sorensen H.B.D. and Damsgaard B., Simulation of Sector Scan Sonar Images. *Proc. of the Seventh European Conference on Underwater Acoustics, ECUA 2004, Delft, The Netherlands*, pp. 842-853 (2004)
6. Fawcett J.A., Fox W.L.J., and Maguer A., Modeling of scattering by objects on the seabed, *J.Acoust. Soc. Am.* **104** (6), pp. 3296-3304 (1998)
7. Fawcett J.A., L. Raymond, Evaluation of the integrals of target/seabed scattering using the method of complex images, *J.Acoust. Soc. Am.* **114** (3), pp. 1406-1415, (2003)
8. Bell J.M., Application of optical ray tracing techniques to the simulation of sonar images, *Optical Engineering,* vol **36** (6), pp. 1806–1813 (1997).
9. Capéron T., Hayward G. and Chapman R., A 3D simulator for the design and evaluation of sonar system instrumentation, *Meas. Sci. Technol.*, vol. 10, pp. 1116-1126 (1999).
10. Sammelmann G.S., Propagation and Scattering in Very Shallow Water, *IEEE Oceans*, pp. 337-344 (2001).
11. Pierce A.D., *Acoustics. An introduction to its physical principles and applications*, Acoustical Society of America (1991)

Appendix C

Thesis paper #3

LETTERS TO THE EDITOR

This Letters section is for publishing (a) brief acoustical research or applied acoustical reports, (b) comments on articles or letters previously published in this Journal, and (c) a reply by the article author to criticism by the Letter author in (b). Extensive reports should be submitted as articles, not in a letter series. Letters are peer-reviewed on the same basis as articles, but usually require less review time before acceptance. Letters cannot exceed four printed pages (approximately 3000–4000 words) including figures, tables, references, and a required abstract of about 100 words.

A numerically accurate and robust expression for bistatic scattering from a plane triangular facet (L)

Gorm Wendelboe[a]
Danish Defense Research Establishment (DDRE), Ryvangs Allé 1, DK-2100 Copenhagen
and Ørsted-DTU, Technical University of Denmark, Ørsteds Plads, Building 348, DK-2800 Kgs. Lyngby, Denmark

Finn Jacobsen[b]
Ørsted-DTU, Technical University of Denmark, Ørsteds Plads, Building 348, DK-2800 Kgs. Lyngby, Denmark

Judith M. Bell[c]
School of Engineering and Physical Sciences, Heriot-Watt University, Edinburgh, United Kingdom

(Received 18 March 2005; revised 22 July 2005; accepted 16 November 2005)

This work is related to modeling of synthetic sonar images of naval mines or other objects. Considered here is the computation of high frequency scattering from the surface of a rigid 3D-object numerically represented by plane triangular facets. The far field scattered pressure from each facet is found by application of the Kirchhoff approximation. Fawcett [J. Acoust. Soc. Am. **109**, 1319–1320 (2001)] derived a time domain expression for the backscattered pressure from a triangular facet, but the expression encountered numerical problems at certain angles, and therefore, the effective ensonified area was applied instead. The effective ensonified area solution is exact at normal incidence, but at other angles, where singularities also exist, the scattered pressure will be incorrect. This paper presents a frequency domain expression generalized to bistatic scattering written in terms of sinc functions; it is shown that the expression improves the computational accuracy without loss of robustness. *© 2006 Acoustical Society of America.*

[DOI: 10.1121/1.2149842]

PACS number(s): 43.20.Fn, 43.20.Px [MO] Pages: 701–704

I. INTRODUCTION

In the past decade low price hardware has made high frequency sonar imagery systems widely available for naval-mine identification, harbor surveillance, and offshore industry. This work is related to the generation synthetic sonar images of naval mines and other objects.

An object will be numerically represented by elementary facets. The far field scattered pressure from each facet is found by application of the physical optics solution or Kirchhoff approximation.[1,2] The total scattered field is given as the coherent sum of pressure contributions from all nonshadowed facets.

The plane rectangular facet has been used by Sammelmann[3] and George.[4] However, for arbitrarily shaped objects the plane rectangular facet can lead to problems concerning correct surface representation. The plane triangular facet, on the other hand, is suited for all types of surfaces because of its co-planar property. Fawcett[5] derived the time domain impulse response for backscattering from a plane triangular facet. An alternative to the flat facet approach is the application of nonuniform rational B-spline surfaces (NURBS).[6] The field integral is evaluated over a parametric space of Bezier surfaces using the method of stationary phase.

The plane triangular facet is considered in this note. The expression for the scattered pressure from the plane triangular facet, first presented by Fawcett,[5] consists of three contributions corresponding to a response from each of the three vertices. However, this vertex response, which is applicable in the time domain, becomes numerically unstable at certain angles as the angle dependent coefficients get very large due to division by very small numbers. One way to deal with this is to replace the integral solution with the effective ensonified area, when the coefficients exceed, say, 1000.[5] This

---

[a] Electronic mail: gw@oersted.dtu.dk
[b] Electronic mail: fja@oersted.dtu.dk
[c] Electronic mail: j.bell@hw.ac.uk

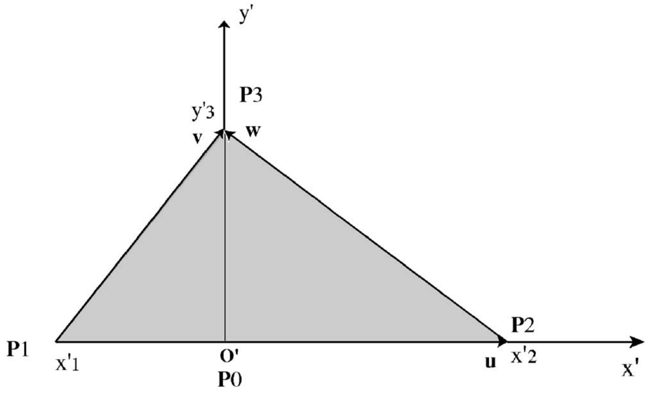

FIG. 1. Local coordinate system (′) of a plane triangular facet.

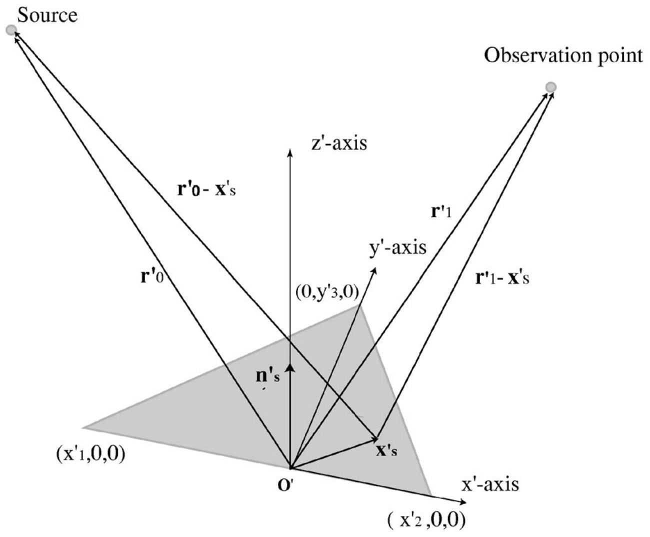

FIG. 2. Geometry applied for field integration over the surface of a triangular facet.

choice might be appropriate for near normal incidence, but for angles away from near normal incidence, where singularities also exist, the scattered pressure will be incorrect. In this note the time domain opportunity is abandoned and the frequency domain expression is rewritten in a numerically robust frame formulated additionally for bistatic scattering.

II. FACET-GEOMETRY AND FIELD APPROXIMATIONS

In this section a scattering integral for a rigid, plane and triangular facet is derived. The Kirchhoff approximation as well as the far field approximation are applied.

Suppose an arbitrarily shaped body is numerically represented by plane triangular facets. Each facet in the three-dimensional space is represented by its vertex points $\mathbf{P}_1$, $\mathbf{P}_2$, $\mathbf{P}_3$ and the unit surface normal vector, $\hat{\mathbf{n}}_s$, pointing out of the body. The vectors connecting the vertex points are defined by $\mathbf{u}=\overrightarrow{\mathbf{P}_1\mathbf{P}_2}$, $\mathbf{v}=\overrightarrow{\mathbf{P}_1\mathbf{P}_3}$, and $\mathbf{w}=\overrightarrow{\mathbf{P}_2\mathbf{P}_3}$, and they are arranged such that $\mathbf{u}$ represents the longest side of the triangle and $(\mathbf{u}\times\mathbf{v})\cdot\hat{\mathbf{n}}_s>0$; see Fig. 1.

A local coordinate system (′) is introduced. The origin $\mathbf{O}'$ has the global coordinates $\mathbf{P}_0=\mathbf{P}_1+\mathbf{v}_\mathbf{u}$, where $\mathbf{v}_\mathbf{u}$ is the projection of $\mathbf{v}$ on $\mathbf{u}$. In the local coordinate system the triangle is described by the axis-points x_1', x_2', and y_3'. The base of (′) is

$$\mathbf{e}_x'=\mathbf{u}/|\mathbf{u}|, \tag{1a}$$

$$\mathbf{e}_y'=(\mathbf{v}-\mathbf{v}_\mathbf{u})/|\mathbf{v}-\mathbf{v}_\mathbf{u}|, \tag{1b}$$

$$\mathbf{e}_z'=\mathbf{e}_x'\times\mathbf{e}_y'. \tag{1c}$$

The base given by Eqs. (1a)–(1c) establishes a coordinate transformation matrix applied on $\mathbf{r}_0$, the vector from $\mathbf{P}_0$ to the source, and on $\mathbf{r}_1$, the vector from $\mathbf{P}_0$ to the observation point. In the (′)-coordinate system $\mathbf{r}_0$ and $\mathbf{r}_1$ have been transformed into $\mathbf{r}_0'$ and $\mathbf{r}_1'$, respectively, but their (Euclidian) lengths are unchanged, i.e., $|\mathbf{r}_0'|=|\mathbf{r}_0|=r_0$ and $|\mathbf{r}_1'|=|\mathbf{r}_1|=r_1$. The unit surface normal vector has been transformed into $\hat{\mathbf{n}}_s'\equiv[001]^T$, and each point on the plane facet, S, is given by $\mathbf{x}_s'\equiv[x'y'0]^T$; see Fig. 2.

The Kirchhoff approximation is applied on the rigid surface and the total pressure field, p, is related to the incoming field, p_{inc}, through

$$p(\mathbf{x}_s')=2p_{\mathrm{inc}}(\mathbf{x}_s') \tag{2}$$

(see, e.g., Fawcett[5]). The Kirchhoff Helmholtz integral equation [see, e.g., Pierce,[7] Eq. (4-6.4)] consequently reduces to the integral

$$p_{\mathrm{sc}}(\mathbf{r}_1')=\frac{1}{2\pi}\int_S p_{\mathrm{inc}}(\mathbf{x}_s')\,\nabla G(\mathbf{x}_s'|\mathbf{r}_1')\cdot\hat{\mathbf{n}}_s'\,dS, \tag{3}$$

where $p_{\mathrm{sc}}(\mathbf{r}_1')$ is the facet-scattered pressure measured at the observation point, $\mathbf{r}_1'$, and $\nabla G(\mathbf{r}_1'|\mathbf{x}_s')$ is the gradient of the free space Green's function directed toward the observation point. The incoming field originates from a monopole source,

$$p_{\mathrm{inc}}(\mathbf{x}_s')=p_0\frac{e^{ik|\mathbf{x}_s'-\mathbf{r}_0'|}}{|\mathbf{x}_s'-\mathbf{r}_0'|}, \tag{4}$$

where p_0 is the pressure amplitude 1 meter from the source. In the far field, the range from the facet to the source by far exceeds the dimensions of the facet, and hence, a first order Taylor series expansion of $|\mathbf{x}_s'-\mathbf{r}_0'|$ with respect to $\mathbf{x}_s'/r_0$ is possible,

$$|\mathbf{x}_s'-\mathbf{r}_0'|\approx r_0-\hat{\mathbf{r}}_0'\cdot\mathbf{x}_s', \tag{5}$$

where $\hat{\mathbf{r}}_0'=\mathbf{r}_0'/r_0$ [see, e.g., Ogilvy,[1] Eq. (4.10)]. The right-hand side of Eq. (5) will be applied for the phase term of Eq. (4) whereas it is sufficient to approximate the slowly varying denominator in Eq. (4), i.e., the term that represents geometrical spreading, to zero order, that is, $|\mathbf{x}_s'-\mathbf{r}_0'|\approx r_0'$. The incoming field is

$$p_{\mathrm{inc}}(\mathbf{x}_s')=p_0\frac{e^{ikr_0}}{r_0}e^{-ik\hat{\mathbf{r}}_0'\cdot\mathbf{x}_s'}, \tag{6}$$

and hence, the part of the spherical wave that sweeps over the facet is considered locally plane. The gradient of the Green's function,

$$\nabla G(\mathbf{r}_1'|\mathbf{x}_s') = \frac{\mathbf{r}_1' - \mathbf{x}_s'}{|\mathbf{r}_1' - \mathbf{x}_s|^3}(ik|\mathbf{r}_1' - \mathbf{x}_s| - 1)e^{ik|\mathbf{r}_1' - \mathbf{x}_s'|}, \tag{7}$$

[see, e.g., Pierce,[7] Eq. (4-6.5)] is also approximated to the far field. In the phase term, $|\mathbf{r}_1' - \mathbf{x}_s'| \approx r_1 - \hat{\mathbf{r}}_1' \cdot \mathbf{x}_s'$, is applied, and in the amplitude terms, $\mathbf{r}_1' - \mathbf{x}_s' \approx \mathbf{r}_1'$ is used. The expression within the brackets of Eq. (7) is approximated to $(ik|\mathbf{r}_1' - \mathbf{x}_s'| - 1) \approx (ikr_1 - 1) \approx ikr_1$, where the second approximation is valid because $ikr_1 \gg 1$. Hence,

$$\nabla G(\mathbf{r}_1'|\mathbf{x}_s') = \hat{\mathbf{r}}_1' ik \frac{e^{ikr_1}}{r_1} e^{-ik\hat{\mathbf{r}}_1' \cdot \mathbf{x}_s'}, \tag{8}$$

where $\hat{\mathbf{r}}_1' = \mathbf{r}_1'/r_1$. Insertion of Eq. (6) and Eq. (7) into Eq. (3) leads to a scattering integral with a linear phase term

$$p_{\mathrm{sc}}(\mathbf{x}) = \frac{p_0 ike^{ik(r_0+r_1)}\hat{\mathbf{r}}_1' \cdot \hat{\mathbf{n}}_s'}{2\pi r_0 r_1} \int_S e^{-ik(\hat{\mathbf{r}}_0' + \hat{\mathbf{r}}_1') \cdot \mathbf{x}_s'}\, dS. \tag{9}$$

III. A ROBUST EXPRESSION FOR TRIANGULAR FACET SCATTERING

If the phase variation over the facet is neglected, the integral in Eq. (9) can be replaced by the facet area, S, and the approximate effective ensonified area response is

$$p_{\mathrm{sc}}(\mathbf{x}) = \frac{p_0 ike^{ik(r_0+r_1)} \cos \theta_1}{2\pi r_0 r_1} S, \tag{10}$$

where $\cos \theta_1 = \hat{\mathbf{r}}_1' \cdot \hat{\mathbf{n}}_s'$. However, this expression is only exact for normal incidence. In the general case the dot-product in the exponential term of the surface integral Eq. (9) must be considered,

$$(\hat{\mathbf{r}}_0' + \hat{\mathbf{r}}_1') \cdot \mathbf{x}_s' = ax' + by', \tag{11}$$

where the angle dependent constants are given by

$$a = \sin \theta_0 \cos \varphi_0 + \sin \theta_1 \cos \varphi_1, \tag{12a}$$

$$b = \sin \theta_0 \sin \varphi_0 + \sin \theta_1 \sin \varphi_1, \tag{12b}$$

and where the angle between $\mathbf{r}_j'$ and $\mathbf{n}_s'$ is $0 \leqslant \theta_j \leqslant \pi/2$, and the angle in the $x'y'$ plane is $0 \leqslant \varphi_j \leqslant 2\pi$, $j = 0, 1$. The solution to Eq. (9) is brought on the vertex response form

$$p_{\mathrm{sc}}(\mathbf{x}) = \frac{p_0 e^{ik(r_0+r_1)} \cos \theta_1}{ik2\pi r_0 r_1}[\kappa_1 e^{-ikax_1'} + \kappa_2 e^{-ikax_2'} + \kappa_3 e^{-ikby_3'}], \tag{13a}$$

where κ_1, κ_1, and κ_3 are the vertex coefficients given by

$$\kappa_1 = \frac{-y_3'}{a(ax_1' - by_3')}, \tag{13b}$$

$$\kappa_2 = \frac{y_3'}{a(ax_2' - by_3')}, \tag{13c}$$

$$\kappa_3 = \frac{y_3'(x_2' - x_1')}{(ax_2' - by_3')(ax_1' - by_3')}. \tag{13d}$$

The vertex response can be transformed into the time domain to obtain the impulse response (see, e.g., Fawcett[5]). As can be observed from Eqs. (13b)–(13d) three singularities are present, $a=0$, $ax_1' - by_3' = 0$, and $ax_2' - by_3' = 0$. For backscattering these singularities correspond to incident directions normal to the three sides of the triangle, i.e., normal to **u**, **w** or **v**. From an analytical point of view, large values of κ_j will cancel each other in Eq. (13a). However, in a numerical implementation the cancellation tends to fail because of truncation errors obtained near the working precision of the computer. In what follows the time domain approach is abandoned and a numerically robust expression is derived. The angle dependent terms a, $(ax_1' - by_3')$, and $(ax_2' - by_3')$ are separated and expressed in terms of the well-behaved sinc function. Hence, the solution to Eq. (9) is written

$$\begin{aligned} p_{\mathrm{sc}}(\mathbf{x}) = {} & \frac{p_0 e^{ik(r_0+r_1)} \cos \theta_1}{2\pi r_0 r_1}\left(\frac{1}{ikb}\right) \\ & \times \left[x_1' e^{-ik(ax_1'+by_3')/2} \frac{\sin(k[ax_1' - by_3']/2)}{k[ax_1' - by_3']/2} \right. \\ & - x_2' e^{-ik(ax_2'+by_3')/2} \frac{\sin(k[ax_2' - by_3']/2)}{k[ax_2' - by_3']/2} \\ & \left. + (x_2' - x_1') e^{-ika(x_1'+x_2')/2} \frac{\sin(ka[x_2' - x_1']/2)}{ka[x_2' - x_1']/2} \right]. \end{aligned} \tag{14a}$$

When $b \rightarrow 0$, Eq. (14a) becomes numerically unstable, and is replaced by the limit value, $p_{\mathrm{sc}}(\mathbf{x})$ for $b \rightarrow 0$, found by using the rule of L'Hospital,

$$\begin{aligned} p_{\mathrm{sc}}(\mathbf{x}) = {} & \frac{p_0 e^{ik(r_0+r_1)} \cos \theta_1 y_3'}{4\pi i r_0 r_1} \times [g(kax_1'/2) x_1' e^{-ikax_1'/2} \\ & - g(kax_2'/2) x_2' e^{-ikax_2'/2}], \end{aligned} \tag{14b}$$

where

$$g(x) = \frac{-\cos(x) + \sin(x)/x}{x} - i\frac{\sin(x)}{x}. \tag{14c}$$

IV. RESULTS

Validation is carried out by considering the canonical problem of backscattering of a plane wave of unit amplitude from a rigid sphere. The infinite harmonic series solution[8] is the Benchmark solution. The sphere is a good test case because sharp edges, where the Kirchhoff approximation fails, are absent. The time domain response of a 445 kHz Ricker pulse incident on a sphere with a radius equal to 10 centimeters measured at a range of 10 meters is determined. In the numerical model the surface of the sphere is represented by iso-sized facets with areas of 11 mm^2. Results from three different numerical Kirchhoff approaches are considered. The first approach is the vertex response given by Eqs. (13) where no numerical precautions are taken. In the second approach the vertex response is combined with the effective area response given by Eq. (10) according to Fawcett.[5] The vertex response is switched "off" and the effective area response "on" when the magnitude of one of the coefficients in Eqs. (13) exceed 1000. Finally, the third ap-

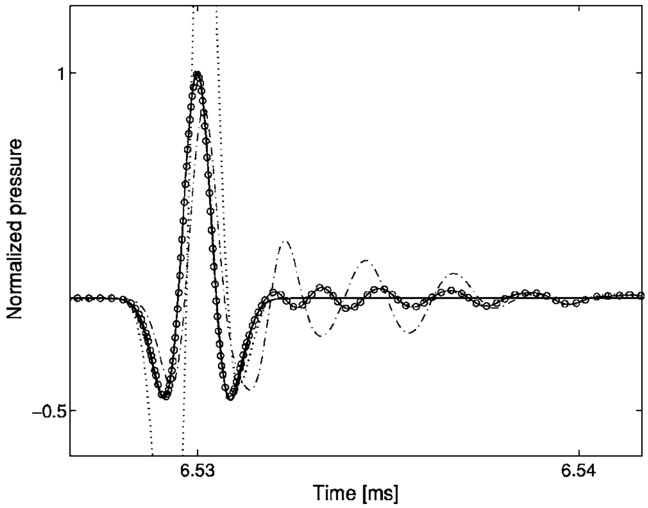

FIG. 3. Backscattering from a rigid sphere. The thick solid line is the benchmark solution; the dotted line is the vertex response [Eq. (13)] the dashed-dotted line is the vertex response, [Eq. (13)], combined with the effective area response [Eq. (10)]; and the solid line with circles is the robust response [Eq. (14)].

proach is the robust response given by Eq. (14). Fourier synthesis has been carried out on the benchmark solution as well as on the three different numerical Kirchhoff approaches.

The results are given in Fig. 3. The robust response given by Eq. (14) matches the analytic solution very well except after the specular reflection where oscillations occur. These oscillations are related to the numerical surface discretization of the sphere and not the scattering formulas. The result from the pure vertex response, Eqs. (13), clearly diverges from the analytical solution at the specular reflection, but after that, it quickly approaches the robust response. Hence, the pure vertex response is accurate as long as the critical angles are not encountered; if this happens, erroneous results orders of magnitudes from the actual response will occur. The combined solution is significantly closer to the analytical result at the specular reflection, but exhibits stronger oscillations after the specular reflection, indicating that the combined approach is a robust, but not very accurate, numerical approach when singularities are encountered. The robust response expressed in terms of sinc functions has proven to be the most numerically reliable expression.

V. CONCLUSION

A numerically robust expression for the far field bistatic scattered pressure from a plane triangular facet written in terms of sinc functions, Eq. (14), has been presented. The expression is applied for the computation of high frequency scattering from arbitrarily shaped objects. Equation (14) has been compared with two solutions based on the vertex response expression, Eq. (13). The first solution is the pure vertex response which is numerically unstable at certain angles. The second solution, presented by Fawcett,[5] combines Eq. (13) with the effective ensonified area, Eq. (10), in the case where one of the coefficients of the vertex response, Eqs. (13b)–(13d), exceeds a threshold value equal to 1000. Comparisons have been carried out by considering the canonical problem of backscattering of a plane wave from a rigid sphere, and the expression written in terms of sinc functions has been shown to be the most reliable solution in terms of accuracy.

ACKNOWLEDGMENT

The authors gratefully acknowledge communication with John Fawcett at DRDC, Atlantic.

[1] J. A. Ogilvy, *Theory of Wave Scattering from Random Rough Surfaces* (IOP, London, 1991), Chap. 4.1.

[2] H. Medwin and C. S. Clay, *Fundamentals of Acoustical Oceanography* (Academic Press, London, 1998), Chap. 7.2.3.

[3] G. S. Sammelman, “Propagation and scattering in very shallow water,” Proc. IEEE Oceans **1**, 337–344 (2001).

[4] O. George and R. Bahl, “Simulation of backscattering of high frequency sound from complex objects and sand sea-bottom,” IEEE J. Ocean. Eng. **20**, 119–130 (1995).

[5] J. A. Fawcett, “Modeling of high-frequency scattering from objects using a hybrid Kirchhoff/diffraction approach,” J. Acoust. Soc. Am. **109**, 1312–1319 (2001).

[6] J. Perez and M. F. Catedra, “Application of physical optics to the RCS computation of bodies modeled with NURBS surfaces,” IEEE Trans. Antennas Propag. **42**, 1404–1411 (1994).

[7] A. D. Pierce, *Acoustics. An Introduction to its Physical Principles and Applications* (Acoustical Society of America, New York, 1991), second printing.

[8] E. G. Williams, *Fourier Acoustics. Sound Radiation and Nearfield Acoustical Holography* (Academic Press, London, 1999), Eq. (6.185).

Appendix D

Thesis paper #4

An equivalent roughness model for seabed backscattering at very high frequencies using a band-matrix approach

Gorm Wendelboe[a]
Danish Defense Research Establishment (DDRE), Ryvangs Allé 1, DK-2100 Copenhagen and Ørsted-DTU, Technical University of Denmark, Ørsteds Plads, Building 348, DK-2800 Kgs. Lyngby, Denmark

Finn Jacobsen[b]
Ørsted-DTU, Technical University of Denmark, Ørsteds Plads, Building 348, DK-2800 Kgs. Lyngby, Denmark

Judith M. Bell[c]
School of Engineering and Physical Sciences, Heriot-Watt University, Edinburgh, Scotland

(Received 10 August 2006; revised 28 November 2006; accepted 5 December 2006)

This work concerns modeling of very high frequency (>100 kHz) sonar images obtained from a sandy seabed. The seabed is divided into a discrete number of 1D height profiles. For each height profile the backscattered pressure is computed by an integral equation method for interface scattering between two homogeneous media as formulated by Chan [IEEE Trans. Antennas Propag. **46**, 142–149 (1998)]. However, the seabed is inhomogeneous, and volume scattering is a major contributor to backscattering. The SAX99 experiments revealed that the density in the unconsolidated sediment within the first 5 mm exhibits a high spatial variation. For that reason, additional roughness is introduced: For each surface point a stochastic realization of the density along the vertical is generated, and the sediment depth at which the density has its maximum value will constitute the new height field value. The matrix of the full integral equation is reduced to a band matrix as the interaction between the point sources on the seabed is neglected from a certain range; this allows computations on long height profiles with lengths up to approximately 25 m (at 300 kHz). The equivalent roughness approach, combined with the band-matrix approach, agrees with SAX99 data at 300 kHz. *© 2007 Acoustical Society of America.* [DOI: 10.1121/1.2427127]

PACS number(s): 43.30.Gv, 43.30.Hw, 43.30.Ft [SLB] Pages: 814–823

I. INTRODUCTION

Very high frequency (>100 kHz) sonar plays a key role for naval mine detection and identification. This work is related to mines lying on the seabed, i.e., proud mines, and the goal is modeling of high frequency sonar images. Sonar images of a sandy seabed are contaminated with clutter, a term that refers to the noisy, or unwanted, component of the received sonar signal; its strength governs the detection performance of the backscattered pressure from an object, or, say, the signal-to-reverberation ratio. Hence, clutter has a key role in manually controlled as well as automated mine detection/identification systems since it can affect the false alarm rates.[1] Clutter is the result of an oscillating pressure signal scattered back from the seabed, where a complex wave interference on the water/sediment interface and in the sediment volume occur.

Wave scattering from random rough surfaces can be modeled by a field average over an ensemble of random surfaces where the scattered acoustic power is derived analytically (see, e.g., Ref. 2 and Ref. 3, Chap. 9.3). Alternatively, the scattered pressure can be computed numerically from a stochastic realization of the rough surface, that is, a Monte Carlo approach (see e.g., Ref. 4). A combination of the average field method and the Monte Carlo approach has been applied in some sonar simulation models.[5,6] However, such models generate energy-based reflectograms that do not represent the rapid phase variations obtained from real signals. The field scattered from a rough interface can be computed by the classical composite model,[2,3] a combination of the Kirchhoff approximation and the small perturbation approximation, but the small slope approximation, a relatively new model, is valid for a broader range of surfaces (see, e.g., Ref. 3, Chap. 9.14 and Refs. 7 and 8). The full integral equation solution and approximate integral equation methods have been applied on 1D surfaces, see, e.g., Refs. 9–11. Meanwhile, models for interface scattering are not sufficient for acoustic field interaction with the seabed; acoustic waves penetrate into the sediment and inhomogeneities induce a scattered field. Jackson[12–16] applied the small perturbation approximation for frequencies below 100 kHz, that is, for wavelengths greater than approximately 1.5 cm; for smaller wavelengths the model can fail.[17] At 140 kHz, volume scattering from strongly inhomogeneous sediments can be the dominating scattering mechanism,[18] a conclusion that also may be valid for the backscattering experiment at 300 kHz conducted at the Sediment Acoustic Experiment in 1999 (SAX99).[19] Small scale measurements of the density and sound speed variability conducted at SAX99 tend to confirm that;[20] within the first centimeter the sediment is unconsoli-

---

[a] Electronic mail: gw@oersted.dtu.dk
[b] Electronic mail: fja@oersted.dtu.dk
[c] Electronic mail: j.bell@hw.ac.uk

dated and the geoacoustical parameters exhibit a significantly higher spatial variability than in the deeper parts of the sediment.

In the model presented here the rapid phase variations are required, and a stochastic seabed realization that covers all roughness scales, i.e., a full Monte Carlo approach, will be applied. The sandy seabed is approximated by a discrete number of 1D height profiles in planes similar to the sonar beams. The height profiles are synthesized by application of seabed roughness parameters acquired from stereo-photogrammetric measurements at SAX99. The scattering problem is solved by using the formulation by Chan,[11] where a rough interface divides two homogeneous fluids. Volume scattering is taken into account by introducing the equivalent roughness approximation: For each surface point a stochastic realization of the density along the vertical is generated and the sediment depth at which the density has its maximum value will constitute the new height profile value. The new height profile is subsequently filtered by an AR(1)-filter in order to generate correlation along the horizontal direction. The scattering matrix is reduced to a band matrix as interactions between point sources on the seabed are neglected from a certain range, and the reduction will allow computations of long height profiles. The number of nonzero diagonals are evaluated in terms of a tradeoff between accuracy and required height profile lengths. The equivalent roughness approach combined with the band-matrix approximation is compared with SAX99 data at 300 kHz (see Ref. 21).

All simulations are carried out with a 300-kHz sinusoid and the speed of sound in water is assumed to be $c_1 = 1500\ \mathrm{m/s}$, thus the acoustic wavelength in water is $\lambda = 0.5$ cm.

II. SEABED MODELING

In this section modeling of the rough water-sediment interface as well as modeling of the density variations in the upper sediment are described. The seabed is considered as a height field; hence, the height, h, is a function of the ground plane coordinates, x and y, i.e., $h=h(x,y)$. In this work, the sandy seabed is approximated by a discrete number of 1D height profiles in planes similar to the sonar beams. Thus, each height profile is given as

$$h = h(x), \tag{1}$$

where x is the ground range coordinate along the height profile. Simulations by George[22] indicate that the backscattering characteristics are independent of sonar beam width, a result that supports the height profiles approximation.

A. Interface roughness

The seabed roughness is characterized in terms of its power spectrum, which according to, e.g., Briggs *et al.*,[23] is given by

$$P(f_s) = \frac{\phi}{f_s^{\gamma}}, \tag{2}$$

where f_s is the spatial frequency measured in cycles/cm, ϕ is the *spectral intercept* measured in cm^3, and γ is the *spectral exponent*, which is dimensionless. Taking the logarithm on each side of Eq. (2) yields

$$\log_{10} P(f_s) = \log_{10}(\phi) - \gamma \log_{10}(f_s), \tag{3}$$

where the spectral intercept is found at $f_s=1$, i.e., at one cycle per centimeter. The power spectrum parameters are estimated by *in situ* experiments with stereo-photogrammetric equipment.[1,23–25] The seabed may contain several power laws distributed over the different spatial frequencies. Here, a two-power-law spectrum is used,

$$P(f_s) = \begin{cases} \phi_1 f_s^{-\gamma_1}, & f_s^{(\mathrm{min})} < f_s < f_s^{(\mathrm{tr})}, \\ \phi_2 f_s^{-\gamma_2}, & f_s^{(\mathrm{tr})} < f_s < f_s^{(\mathrm{max})}, \\ 0, & \text{elsewhere}, \end{cases} \tag{4}$$

where ϕ_1, γ_1, and ϕ_2, γ_2 are the spectral intercept and spectral exponent for the the first and second power laws, respectively. The minimum spatial frequency, $f_s^{(\mathrm{min})}$, is governed by the size of the experimental area; $f_s^{(\mathrm{tr})}$ is the transition frequency between the two power laws; and the maximum spatial frequency, $f_s^{(\mathrm{max})}$, is related to the resolution of the stereo-photogrammetric system.

Throughout this work ϕ_1, γ_1, ϕ_2, and γ_2 are based on data presented in Ref. 23 (BAMS, 5 Oct. N, Table II, p. 511). The parameters are listed in Table I. Note, the maximum spatial frequency is chosen to be $f_s^{(\mathrm{max})}=4$ cycles/cm, although the value is 5 cycles/cm in Ref. 23. This choice will become clear in the following.

TABLE I. Applied interface roughness parameters.

Two-power law	f_s (cm^{-1})	γ	ϕ (cm^3)
Large scale	0.02–2.0	3.00	0.000 75
Small scale	2.0–4.0	3.81	0.001 31

The height profiles are synthesized in the frequency domain. Equation (4) is realized by suppressing frequencies below $f_s^{(\mathrm{min})}$ by application of a tapered cosine window,

$$W_1(f_s) = \begin{cases} \frac{1}{2}[1 - \cos(\pi f_s / f_s^{(\mathrm{min})})], & |f_s| < f_s^{(\mathrm{min})}, \\ 1, & \text{elsewhere}, \end{cases} \tag{5}$$

and, additionally, by suppressing frequencies above $f_s^{(\mathrm{max})}$ by application of the following tapered cosine window,

$$W_2(f_s) = \begin{cases} \frac{1}{2}\left[1 - \cos\left(\pi \frac{f_g - f_s}{f_g - f_s^{(\mathrm{max})}}\right)\right], & |f_s| > f_s^{(\mathrm{max})}, \\ 1, & \text{elsewhere}, \end{cases} \tag{6}$$

where f_g is the Nyquist frequency. The Fourier transform of the synthetic height profile, $h(x)$, is

$$H(f_s) = N(f_s) W_1(f_s) W_2(f_s) \sqrt{P(f_s)}, \tag{7}$$

where $N(f_s)$ is the Fourier transform of a random Gaussian variable with unit variance. The first and second order de-

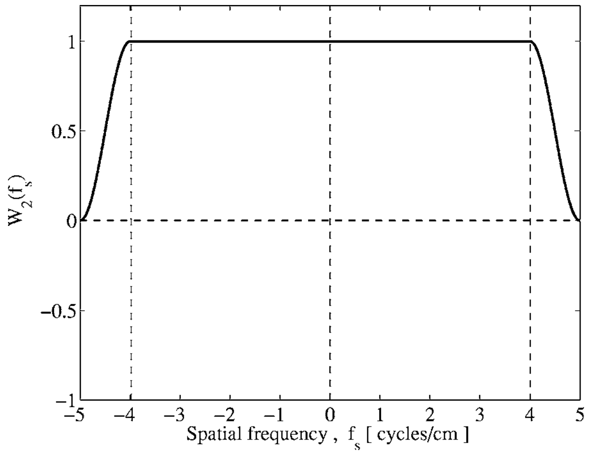

FIG. 1. The tapered cosine, frequency domain window, $W_2(f_s)$, see Eq. (6). It is applied on the surface, h, its derivative, dh/dx, and the second order derivative, d^2h/dx^2.

rivatives of the height profile are required in the scattering formulation presented in Sec. III. Since

$$h(x) \leftrightarrow H(f_s), \tag{8}$$

the surface derivatives are given by

$$\frac{dh}{dx} \leftrightarrow 2\pi i f_s H(f_s), \tag{9}$$

$$\frac{d^2h}{dx^2} \leftrightarrow -4\pi^2 f_s^2 H(f_s). \tag{10}$$

If the equidistant step range along the ground range axis (the x axis) is equal to

$$\Delta x = 0.2\lambda = 0.1 \text{ cm}, \tag{11}$$

the spatial Nyquist frequency is

$$f_s^{(\text{Nyquist})} = 5 \text{ cycles/cm}. \tag{12}$$

The Bragg spatial frequency (or wave number) for back-scattering at zero grazing angle is

$$f_s^{(\text{Bragg})} = 4 \text{ cycles/cm} \tag{13}$$

(see the Appendix); it is the maximum spatial frequency of the rough surface where reinforcement of the backscattered signal can occur. For a sonar model the grazing angle may vary between, say, $\theta=10°$ and $\theta=75°$, and consequently, the Bragg wave numbers will approximately lie between 1 to 3.9 cycle/cm.

Figures 1–3 show $W_2(f_s)$, $2\pi i f_s W_2(f_s)$, and $-4\pi^2 f_s^2 W_2(f_s)$, respectively. The tapered cosine window, $W_2(f_s)$, suppresses undesired high frequency content in $h(x_n)$ and its the first and second order derivative. The ground range resolution, specified in Eq. (11), has been selected such that $W_2(f_s)$ tapers off between the maximum Bragg wave number and the Nyquist frequency, and that explains why the implementation uses $f_s^{(\text{max})}=f_s^{(\text{Bragg})}=4$ cycles/cm and not 5 cycles/cm as in Ref. 23.

In the literature Δx may vary from 0.2λ down to 0.05λ [see, e.g., Ref. 4 (Appendix 1, Table 1]. Here, an analysis of convergence has shown that a resolution of 0.2λ yields backscattering strengths that nearly coincide with backscattering strengths obtained at a resolution of 0.1λ. Thus, a resolution of $\Delta x=0.2\lambda$ is applied. The distance between adjacent points on the rough surface, i.e., the arc-length of the nth height profile sample, $\Delta s(x_n)$, depends on the magnitude of the surface derivative, $\gamma(x_n)$, by[9]

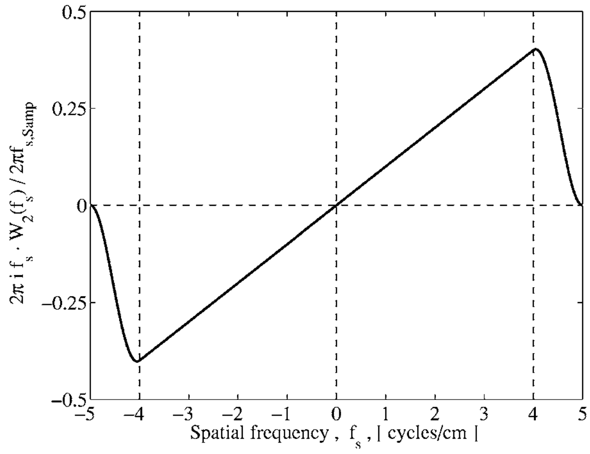

FIG. 2. Frequency domain window applied to obtain the surface first order derivative, dh/dx.

$$\Delta s(x_n) = \gamma(x_n)\Delta x, \tag{14}$$

where x_n is nth ground range sample, and where the magnitude of the surface derivative is given by

$$\gamma^2(x_n) = \left. 1 + \left(\frac{dh}{dx}\right)^2 \right|_{x=x_n}. \tag{15}$$

For very steep height variations in the profile the arc lengths become large. The simplest way to decrease Δs is by reducing Δx, but that will increase the computational workload drastically and include a large number of redundant or unnecessary surface points. Instead, extra points are inserted between points in the height profile when $\Delta s > \lambda/4$ (see, e.g., Ref. 26). The extra points are found by cubic spline interpolations and, consequently, Δx is no longer constant and Eq. (14) yields

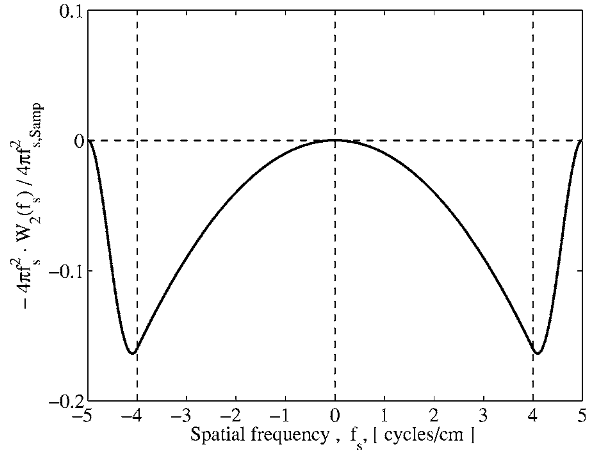

FIG. 3. Frequency domain window applied to obtain the surface second order derivative, d^2h/dx^2.

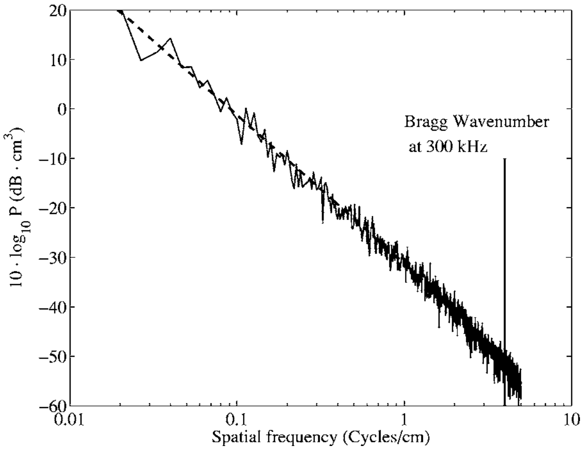

FIG. 4. Power spectrum of the interface roughness between the water and sediment; the spectrum has been acquired by optical means, i.e., stereophotogrammetric equipment. The dotted line represents the two-power law power spectrum according to Eq. (4) with the parameters listed in Table I. The solid, noisy, line is an average of five realizations.

$$\Delta s(x_n) = \gamma(x_n)\Delta x(x_n). \tag{16}$$

The number of extra points required depends inversely on minimum spatial frequency. If $f_s^{(\min)}$ decreases, the height profile will contain larger height values and arc lengths will increase. However, the minimum spatial frequency applied here only results in a few percent extra surface points. Equation (16) is applied in the implementation described in Sec. III.

Figure 4 shows the roughness power spectrum of the modeled interface; the spectrum shows an average of 5 roughness power spectra, and the maximum Bragg-wavenumber for backscattering at 300 kHz (=4 cycles/cm) is indicated by the solid vertical line.

B. Sediment density variations

The seabed may typically consist of sand, mud, stones, plants, and different animal species, but in this work only a sandy seabed sediment is considered. Experiments of the vertical and horizontal density variations have been carried out at the SAX99, and this section is solely based on results obtained by Tang *et al.*[20] The experiments showed that the density variations are strongest within the first 5 mm of the sediment, that is, the transition layer or unconsolidated sediment. For frequencies below 100 kHz, i.e., wavelengths above approximately 1.5 cm, the density inhomogeneities do not contribute to the scattering as the wavelength is greater than the thickness of the transition layer. At frequencies above 100 kHz inhomogeneities are believed to affect scattering significantly.

The 3D spatial variations in the upper sediment layer, that is, 0 to 6 cm, have been measured with an *in situ* measurement of porosity (IMP) system that measures the variability of the electrical conductivity within the sediment. The vertical density variations are considered in the following; Eqs. (17)–(21) are taken from Ref. 20 [Eqs. (11)–(15)]. For a sandy sediment the mean density as a function of depth is

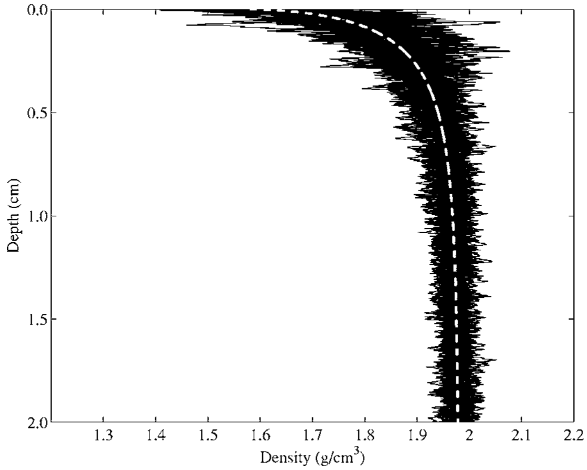

FIG. 5. A total of 32 synthetic density profiles based on density parameters listed in Table II and adopted from Ref. 20. The white dotted line represents the mean density profile, $\rho_m(z)$, given in Eq. (17).

$$\rho_m(z) = 1.98 - 0.4e^{-3.5z^{0.6}}, \tag{17}$$

where ρ is measured in g/cm^3 and the depth z in cm. The relative density variability,

$$\epsilon = \frac{\rho(x,y,z) - \rho_m(z)}{\rho_m(z)}, \tag{18}$$

is spatially nonstationary and follows the trend

$$\epsilon_m = 0.0152 - 0.096e^{-3.7z^{0.82}}. \tag{19}$$

The relative density variation is normalized by its trend profile, Eq. (19),

$$\eta = \frac{\epsilon(x,y,z)}{\epsilon_m(z)}, \tag{20}$$

where η is assumed to be a spatial stationary process. In the vertical direction the power law spectrum yields

$$P_z(f_s) = \frac{w}{f_s^{\gamma_\rho}}, \tag{21}$$

where w=6.76×10^{-2} cm$^{1-\gamma_\rho}$ and γ_ρ=2.17. The power law has been verified up to a spatial frequency of approximately f_s=20 cycles/cm, which corresponds to a spatial resolution of 0.5 mm [see Ref. 20 (Fig. 14)]; above this frequency the noise floor of the IMP is reached. From these relations stochastic realizations of the sediment density are generated as a function of depth (see Fig. 5).

C. The equivalent roughness profile

The high density variations in the first millimeters below the water-sediment interface, i.e., the unconsolidated sediment, are believed to contribute significantly to the backscattered field. In order to include density variations in a model that only accounts for interface roughness scattering, an equivalent roughness approach is presented here. Considered from an acoustic point of view, there are numerous interfaces, or spatially distributed impedance contrasts, within the first 5 mm that contribute to the wave interaction. Here, the interface is redefined in terms of the density variations: For

TABLE II. Applied sediment density parameters.

Direction	Type	Parameters
Vertical	Power law	$\gamma_\rho=2.17$ $w=0.0676\ \mathrm{cm}^{1-\gamma_\rho}$ $(f_s=0.3-30\ \mathrm{cm}^{-1})$
Horzontal	AR(1)	$\kappa=0.45$

each point along the height profile a Monte Carlo realization like the ones shown in Fig. 5 is carried out, and the depth where the maximum density is found, $z(x_n,\rho_{\max})$, forms the new height profile value. At the present stage the equivalent roughness is defined as

$$h_{\mathrm{eq}}(x_n)=h(x_n)-z(x_n,\rho_{\max}). \tag{22}$$

Along the horizontal direction the density variations also follow a power spectrum [see Ref. 20 (Fig. 15)], but experimental data are only provided in the frequency range 0.06 to 2 cycles/cm, and at a minimum depth of 1 cm. Here, we are interested in wave numbers up to 4 cycles/cm at sediment depths from 0 to 1 cm. Because $z(x_n,\rho_{\max})$ tends to be white noise along the horizontal direction, $h_{\mathrm{eq}}(x_n)$ is filtered with an AR(1) low-pass filter (see, e.g., Ref. 27) with coefficient κ, that is,

$$h_{\mathrm{eqft}}(x_n)=\kappa h_{\mathrm{eqft}}(x_{n-1})+(\kappa-1)h_{\mathrm{eq}}(x_n). \tag{23}$$

A single part of the results presented in Sec. IV is given in advance by anticipating that $\kappa=0.45$; this value gives an equivalent roughness profile, $h_{\mathrm{eqft}}(x_n)$, that results in modeled backscattering strengths that approach experimental data. The parameters applied for the generation of equivalent roughness profiles are listed in Table II.

Figure 6 shows the spatial power spectra of the equivalent roughness profile together with the equivalent roughness interface in the case where the interface acquired by optical means is perfectly flat, that is, $h(x_n)\equiv x_0$. The optically acquired two-power law, i.e., Eq. (4), is also shown. The power spectra of the equivalent roughness profiles exhibit higher levels for large wave numbers, i.e., from 0.4 to 4 cycles/cm, than the optically acquired two-power law. Hence, an increase in the backscattering level is expected there.

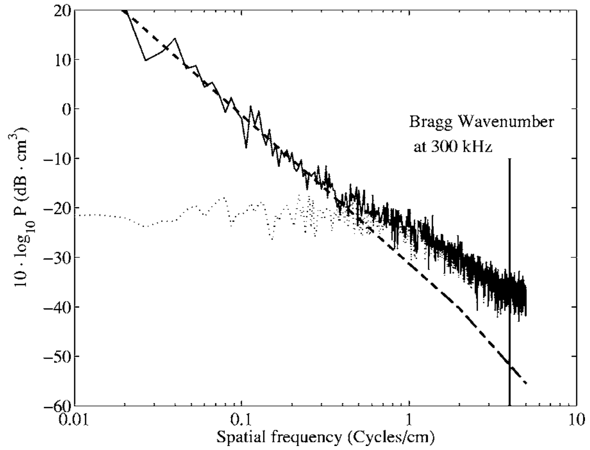

FIG. 6. Spatial power spectra obtained as an average of five equivalent roughness realizations based on spatial density parameters given in Table II. The solid line (———) is the equivalent roughness according to Eq. (23). The thin dotted line (:) is the roughness solely estimated from the density variations. The dashed line (– –) is the two-power law, see Eq. (4), based on parameters listed in Table I.

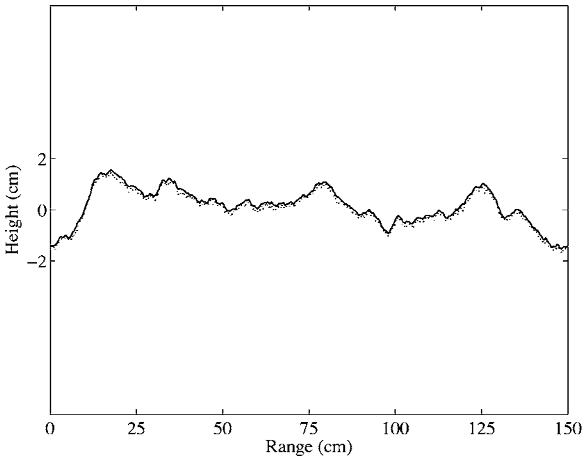

FIG. 7. Stochastic realizations of height profiles. The solid line (———) represents the interface roughness and the dotted line (:) the equivalent roughness.

Figure 7 is an example of a 1.5-m-long height profile based on optical data only, together with the corresponding equivalent roughness profile. Figure 8 is Fig. 7 zoomed to the range between 10 and 30 cm.

In the next section the field equations and the method applied to calculate the scattered field from the interface are presented.

III. FIELD EQUATIONS

In this work wave field propagation and scattering is considered in two dimensions, a consequence of the height-field to height-profiles approximation presented in beginning of Sec. II. The $e^{-i\omega t}$ time dependence is assumed. Hence, a two-dimensional diverging outgoing wave is described in terms of the Hankel function of the first kind, $H_0^{(1)}(z)$. A plane wave incident on the water-sediment interface on the

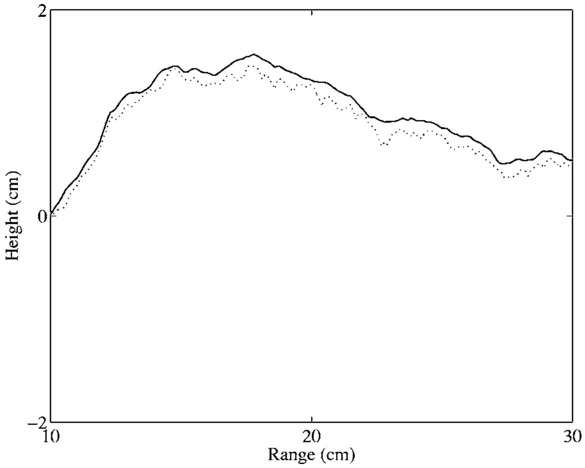

FIG. 8. The height profile realization from Fig. 7 zoomed. The solid line (———) represents the interface roughness and the dotted line (:) the equivalent roughness. Note, the equivalent roughness exhibits higher small scale variations.

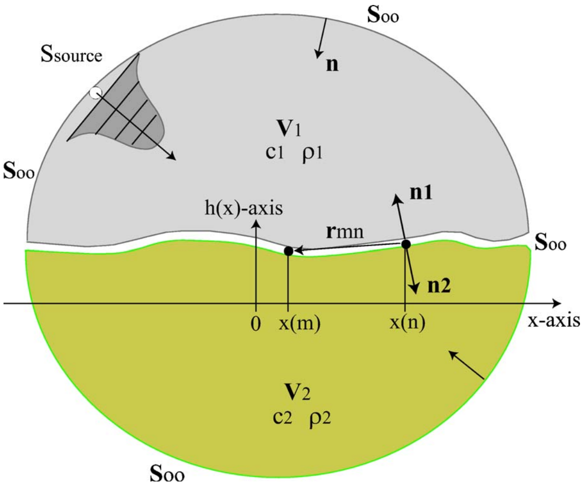

FIG. 9. The geometry applied for the fluid-fluid model represented by the coupled integral equations, Eqs. (24)–(26). In the water, i.e., medium 1, a tapered plane wave is incident from the infinity. Medium 2 represents the homogeneous sediment.

seabed is considered. The sediment is modeled as a fluid, i.e., the acoustic properties are fully described in terms of the mass density and sound speed. The backscattered pressure from the interface is the subject here. In Fig. 9 V_1 represents the water medium, with density ρ_1 and sound speed c_1, and V_2 represents the sediment with density ρ_2 and sound speed c_2. Within V_1 a source at infinity generates a plane wave incident on the interface between the water and sediment; the plane wave is tapered, i.e., it is of finite extent and excites only a limited part of the seabed.

The field on the surface, S_∞, at infinity obeys Sommerfeld's radiation condition, i.e., the field vanishes here. The pressure p at an observation point $\mathbf{r}$ within or on the boundary of V_1 can be expressed in terms of the Kirchhoff Helmholtz integral equation (see, e.g., Ref. 28):

$$\alpha_1 p(\mathbf{r}) = p^i(\mathbf{r}) + \frac{1}{4i}\int_{-\infty}^{\infty}\left(p(\mathbf{r}')\frac{\partial H_0^{(1)}(k_1|\mathbf{r}-\mathbf{r}'|)}{\partial n'} - H_0^{(1)}(k_1|\mathbf{r}-\mathbf{r}'|)\frac{\partial p(\mathbf{r}')}{\partial n'}\right) ds', \tag{24}$$

where the integral represents the field scattered from the interface s', p^i is the incoming field, $\mathbf{r}'$ is a point on s' and serves as an integration variable, $k_1=\omega/c_1$ is the acoustic wave number in the water, and $\partial/\partial n' = \nabla\cdot\hat{\mathbf{n}}'$ is the gradient projected onto the surface normal vector $\hat{\mathbf{n}}'$ of unit length on s'. Finally, the constant α_1 on the left hand side of Eq. (24) is, for $j=1$, given by

$$\alpha_j = \begin{cases} 1, & \text{if } \mathbf{r} \text{ is inside } V_j, \\ \frac{1}{2}, & \text{if } \mathbf{r} \text{ is on the boundary of } V_j, \\ 0, & \text{if } \mathbf{r} \text{ is outside } V_j. \end{cases} \tag{25}$$

In the sediment, i.e., in V_2, the integral equation becomes

$$-\alpha_2 p(\mathbf{r}) = \frac{1}{4i}\int_{-\infty}^{\infty}\left(p(\mathbf{r}')\frac{\partial H_0^{(1)}(k_2|\mathbf{r}-\mathbf{r}'|)}{\partial n'} - H_0^{(1)}(k_2|\mathbf{r}-\mathbf{r}'|)\frac{\partial p(\mathbf{r}')}{\partial n'}\right) ds', \tag{26}$$

where there is no incoming field from within V_2, α_2 is defined in Eq. (25) with $j=2$, and the sign of the integral has been reversed due to a 180° reversal of the normal vector, $\hat{\mathbf{n}}'$ (see Fig. 9). The two integral equations, Eqs. (24) and (26), are coupled through the boundary conditions at the water-sediment interface as

$$p_1(\mathbf{r}') = p_2(\mathbf{r}'), \tag{27}$$

$$\frac{\partial p_1(\mathbf{r}')}{\partial n'} = \frac{1}{\mu}\frac{\partial p_2(\mathbf{r}')}{\partial n'}, \tag{28}$$

where $\mu=\rho_2/\rho_1$.

The gradient of the Hankel function projected onto the surface normal [the left term inside the integral of Eq. (24) and Eq. (26)] is considered next. The surface derivative of the zeroth-order Hankel function of the first kind projected onto the surface normal is

$$\frac{H_0^{(1)}(k|\mathbf{r}-\mathbf{r}'|)}{\partial n'} = kH_1^{(1)}(k|\mathbf{r}-\mathbf{r}'|)(\hat{\mathbf{r}}'\cdot\hat{\mathbf{n}}'), \tag{29}$$

where $\hat{\mathbf{r}}'=(\mathbf{r}-\mathbf{r}')/|\mathbf{r}-\mathbf{r}'|$.

In the following, the position variables are written in terms of a discrete surface and, thus, the observation point vector $\mathbf{r}$ is given by $(x_m, h(x_m))$, where $m=1,2,\ldots,N$; the integration variable $\mathbf{r}'$ is given by $(x_n, h(x_n))$, where $n=1,2,\ldots,N$. The distance between the observation point m and integration point n is

$$r_{mn} = \sqrt{(x_m - x_n)^2 + [h(x_m) - h(x_n)]^2}, \tag{30}$$

and the unit vector pointing from n to m is

$$\hat{\mathbf{r}}_{mn} = \frac{1}{r_{mn}}\begin{bmatrix} x_m - x_n \\ h(x_m) - h(x_n) \end{bmatrix}. \tag{31}$$

The unit surface normal vector is given by

$$\hat{\mathbf{n}}(x_n) = \frac{1}{\gamma(x_n)}\begin{bmatrix} -(dh/dx)|_{x=x_n} \\ 1 \end{bmatrix}, \tag{32}$$

where $\gamma(x_n)$ is defined in Eq. (15). The nth line segment that points towards the mth observation point has an effective length of

$$\kappa_{mn} = \Delta s(n)\hat{\mathbf{n}}(x_n)\cdot\hat{\mathbf{r}}_{mn}, \tag{33}$$

and combining Eqs. (14), (31), and (32) in Eq. (33) yields

$$\kappa_{mn} = \Delta x(n)\frac{-(x_m - x_n)\,(dh/dx)|_{x=x_n} + [h(x_m) - h(x_n)]}{r_{mn}}, \tag{34}$$

a factor applied in the discretization of the first integrand in Eq. (26). In order to find the scattered pressure the pressure and pressure gradient on rough interface must be determined. The establishment of the matrix equations for the coupled problem follows Chan,[11] who used the collocation method to obtain the following set of equations,

$$p^{(\mathrm{inc})}(x_m) = \sum_{n=1}^{N} a_{mn}F_1(x_n) + \sum_{n=1}^{N} b_{mn}F_2(x_n), \tag{35}$$

$$0 = \sum_{n=1}^{N} c_{mn}F_1(x_n) + \sum_{n=1}^{N} d_{mn}F_2(x_n), \tag{36}$$

where $F_1(x)=p(x)$ and $F_2(x)=\gamma(x_n)\partial p(x)/\partial n$. For $m \neq n$,

$$a_{mn} = -\frac{ik_1}{4}\kappa_{mn}H_1^{(1)}(k_1 r_{mn}), \tag{37}$$

$$b_{mn} = \Delta x(n)\frac{i}{4}H_0^{(1)}(k_1 r_{mn}), \tag{38}$$

$$c_{mn} = \frac{ik_1}{4}\kappa_{mn}H_1^{(1)}(k_2 r_{mn}), \tag{39}$$

$$d_{mn} = -\mu\Delta x(n)\frac{i}{4}H_0^{(1)}(k_2 r_{mn}), \tag{40}$$

where κ_{mn} is defined by Eq. (34). For $m=n$ the coefficients become

$$a_{mm} = \frac{1}{2} - \frac{h''(x)\Delta x(m)}{4\pi\gamma_m^2}, \tag{41}$$

$$b_{mm} = \Delta x\frac{i}{4}H_0^{(1)}[k_1\Delta x(m)\gamma_m/(2e)], \tag{42}$$

$$c_{mm} = \frac{1}{2} + \frac{h''(x)\Delta x(m)}{4\pi\gamma_m^2}, \tag{43}$$

$$d_{mm} = -\mu\Delta x(m)\frac{i}{4}H_0^{(1)}[k_1\Delta x(m)\gamma_m/(2e)]. \tag{44}$$

In matrix form the following is obtained,

$$\begin{bmatrix} a_{11} & b_{11} & a_{12} & \cdots & a_{1N} & b_{1N} \\ c_{11} & d_{11} & c_{12} & \cdots & c_{1N} & d_{1N} \\ \vdots & \vdots & \ddots & \ddots & b_{2N} & b_{2N} \\ \vdots & \vdots & \cdots & \cdots & \cdots & \cdots \\ a_{N1} & b_{N1} & a_{N2} & \cdots & a_{NN} & b_{NN} \\ c_{N1} & d_{N1} & c_{N2} & \cdots & c_{NN} & d_{NN} \end{bmatrix} \begin{bmatrix} F_1(x_1) \\ F_2(x_1) \\ \vdots \\ \vdots \\ F_1(x_N) \\ F_2(x_N) \end{bmatrix} = \begin{bmatrix} p^i(x_1) \\ 0 \\ \vdots \\ \vdots \\ p^i(x_N) \\ 0 \end{bmatrix}. \tag{45}$$

When the pressure and the pressure gradient on the interface have been determined the resulting field at any observation point in the water column can be determined. The far field expression for the scattered field is

$$p_{sc}(\mathbf{r}) = \frac{1}{4i}\sum_{n=1}^{N} \sqrt{\frac{2}{\pi k_1 r_n}}e^{ikr_n}e^{-i\pi/4}\left[ip(x_n) - \frac{\partial p}{\partial n}(x_n)\right] \times \Delta x(n), \tag{46}$$

where $r_n=|\mathbf{r}-\mathbf{r}_n|$.

IV. APPROXIMATIVE SOLUTION FOR LARGE SURFACES

For very long height profiles the matrix in Eq. (45) becomes extremely large since a sonar's field of view may cover several square meters. Suppose a height profile of length 20 m is required for modeling the sonar beam; a scattering computation of a 300-kHz wave requires a height field resolution equal to 1 mm, which yields a matrix of size $20\,000^2$ or 2.3 Gigabytes. Iterative solutions to Eq. (45) can be applied such as the conjugant gradient method (see Ref. 11) or the forward-backward method, similar to the Gauss-Seidel procedure (see Ref. 10). Here the direct method is maintained, but the matrix is reduced to a sparse band matrix by the insertion of zeros outside a certain number of diagonals,

$$\begin{bmatrix} a_{11} & b_{11} & \cdots & b_{1M} & a_{1,M+1} & 0 & & \cdots & & 0 \\ c_{11} & d_{11} & & & & & \ddots & & & \vdots \\ \vdots & & & & & & & \ddots & & \\ c_{K1} & & & & & & & & 0 & \\ a_{M+1,1} & & & & & & & & & 0 \\ 0 & \ddots & & & & & & & & \\ & 0 & & & & & & & & \vdots \\ \vdots & & \ddots & & & & & & & \\ & \vdots & & \ddots & & & & & & b_{NN} \\ 0 & 0 & 0 & 0 & 0 & \ddots & \cdots & c_{NN} & & d_{NN} \end{bmatrix}, \tag{47}$$

with M diagonals below and M diagonals above the main diagonal. This choice is based on the fact that the Hankel function decays with range or, expressed in physical terms, the pressure at a given observation point on the surface mainly depends on the nearest neighbor points due to the geometrical spreading of the scattered waves.

V. RESULTS

The incoming field is formed as a tapered plane wave according to Ref. 9 [Eq. (11)], where the tapering parameter, g, of the incoming plane wave is equal to $L/4$, and L is the height profile length. Results are presented in terms of the scattering strength,

$$\mathrm{SS} = 10\log_{10}\sigma(\theta,\theta_s), \tag{48}$$

where $\sigma(\theta,\theta_s)$ is the dimensionless scattering cross section. For 2D wave propagation it is given by [see, e.g., Ref. 9, Eq. (13)]

$$\sigma(\theta,\theta_s) = \langle I_s(\theta_s)\rangle r/I_{\mathrm{inc}}L, \tag{49}$$

where I_{inc} is the incident intensity and $\langle I_s(\theta_s)\rangle$ is the scattered intensity in the far field range r and averaged over numerous surface realizations in the direction θ_s. Finally, L is the profile length. Thus, σ is the *ratio* of the acoustic power scattered in direction θ_s to the power of the incoming field with grazing angle θ, and, hence, it is comparable with the scattering cross section applied for 3D scattering problems.

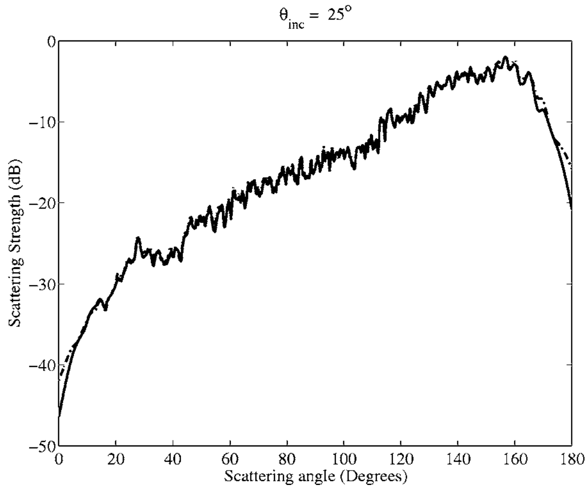

FIG. 10. Bistatic scattering strength for the equivalent roughness surface subject to a pressure release boundary condition. The incoming wave has a grazing angle of 25°. The solid line (———) is the full matrix solution and the dash-dot line (–·–) is the band-matrix solution with $M=80$.

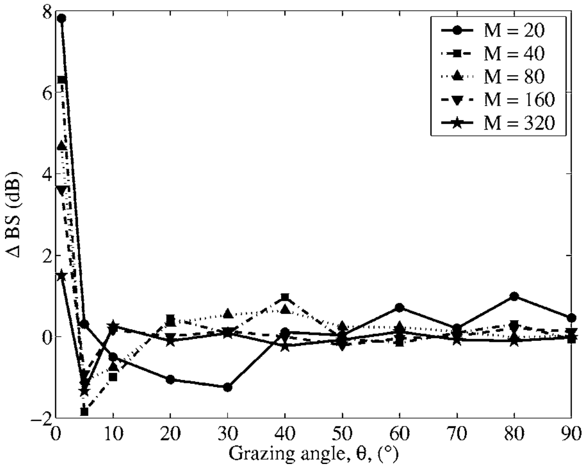

FIG. 11. Backscattering difference in dB between the full matrix solution and the band matrix solution for different values of M as a function of grazing angle. The curves are averages of 20 surface realizations of length 200λ.

The equivalent roughness profiles applied in the following correspond to the type of realizations shown in Figs. 7 and 8; the seabed parameters are depicted in Tables I and II. The AR(1)-parameter value, $\kappa=0.45$ [see Eq. (23)] is found to be an acceptable choice since the modeled backscattering strengths match the experimental data reasonably well (see below). The spatial ground range resolution of a height profile is $\lambda/5=1$ mm, and the acoustic parameters used in the simulations are, unless anything else is specified, as follows: the speed of sound in water $c_1=1500$ m/s, the sound speed ratio $\delta=c_2/c_1=1.165$, the water density $\rho_1=1$ g/cm^3, and the homogeneous sediment density $\rho_1=1.8$ g/cm^3.

Figure 10 shows the bistatic scattering strength for an incident field with a grazing angle, $\theta_i=25°$, and a height profile length of 120λ. The interface has a pressure-release boundary condition, which is established by setting $\rho_2=10^{-5}$ g/cm^3. For the scattering problem on a pressure release surface the Kirchoff-Helmholtz integral equation reduces to

$$p^i(\mathbf{r})=\frac{1}{4i}\int_{-\infty}^{\infty}H_0^{(1)}(k_1|\mathbf{r}-\mathbf{r}'|)\frac{\partial p(\mathbf{r}')}{\partial n'}\,ds', \tag{50}$$

and the solution, given by Eqs. (4), (5), and (8) in Ref. 9, is applied as a first validation of the model presented here.

In Fig. 10 the full matrix solution based on Thorsos's solution is shown together with the solution provided by the band-matrix method, with $M=80$, where M is the number of nonzero diagonals to each side of the main diagonal. For the scattering angles in the range from 0° to 10° the error decreases from 5 dB down to approximately 1 dB. From 10° up to approximately 160° the solutions continue to coincide within 1 dB.

Figure 11 shows the backscattering error between the full matrix solution and the band matrix solution for different values of M, i.e., $M=20,40,80,160,320$. The grazing angles under consideration are $\theta=1°$, 5°, 10°, 20°, 30°,…, 90°, and each point is an average of 20 surface realizations of length 200λ=1 m. The errors increase dramatically for grazing angles below 5°, where the most sparse matrix solution, i.e., $M=20$, has a maximum error of approximately 8 dB at $\theta=1°$. The smallest error, at $\theta=1°$, is 1.8 dB for $M=320$. For grazing angles above 5° the error for $M=20$ is within 1.5 dB, 1 dB for $M=40$, and for higher values of M below 0.5 dB. Apart from computational accuracy, the computational efficiency is another aspect that must be taken into account: The capability of estimating the backscattered pressure from long height profiles is needed. Therefore, a band matrix with $M=20$ is chosen. It is unlikely that a sonar is directed toward the seabed with a grazing angle of less than 5° and, therefore, with $M=20$, an expected error of 1.5 dB is considered to be acceptable.

The required CPU time as a function of height profile length has been invested on a 3 GHz Pentium4™ processor with 512 MB RAM, and computations have been made in Matlab™ on a Windows-XP™ operating system. The maximum profile length that can be computed on the current platform is $N=25\,000$, which takes approximately 95 s; larger matrices result in lack of workspace memory and cannot be carried out. The applied incremental ground range resolution is 1 mm, which yields a profile length of 25 m. The interpolation that is carried out when the distances between adjacent points on the height profile are larger that λ/4 typically increases the number of elements, N, by 3%, thus the actual matrix length is $N=25\,750$. Computation of a matrix of length $N=15\,000$, i.e., a profile length of 15 m, takes approximately 40 s, and a matrix with $N=5000$, i.e., a profile length of 5 m, takes approximately 15 s.

Figure 12 shows different backscattering strengths computed from equivalent roughness profiles; the grazing angle resolution is 0.5°, and each curve represents an average of 50 surface realizations. All band matrix solutions use $M=20$, i.e., 20 nonzero diagonals below and above the main diagonal of Eq. (47). The backscattering strengths from the equivalent roughness profiles of length $L_x=200\lambda$, i.e., 1 m, have been computed by the full matrix solution and the band matrix solution. Additionally, backscattering strengths from equivalent roughness profiles of length $L_x=2000\lambda$, i.e.,

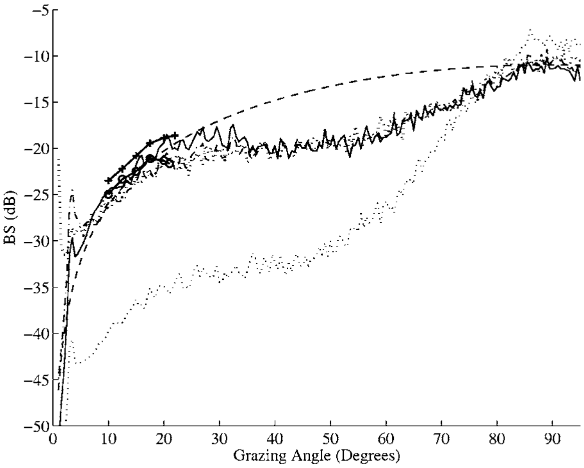

FIG. 12. Backscattering strength as a function of θ with $\Delta\theta = 0.5°$. All band matrix solutions (BMS) use $M = 20$. The solid line (———) is the full matrix solution, the dash-dot line (–·–) is the BMS, and both curves are based on the equivalent roughness profile (ERP). The thin dotted line (:) is the BMS from a height profile only based on stereo photogrammetry. The ERPs explained so far have a length of 200λ. The thick dotted line (:) is BMS, with an ERP length of 2000λ; the cross and circle marked lines, i.e., (–+–), and (–o–), represent the SAX99 data; finally, the thin dashed line (– –) is Lamberts law.

10 m, have been computed with the band matrix solution. The three solutions coincide within a few decibels with the SAX99 data, i.e., XBAMS and BAMS presented in Ref. 21 (Fig. 5, p. 10) for grazing angles between 10° and 22°. The backscattering strengths calculated from the interface found by optical means, i.e., the stereo-photogrammetric equipment, are for $\theta = 5°$ to 50°, approximately 15 dB weaker than the strengths found from the equivalent roughness profiles. For grazing angles between approximately 50° up to normal incidence, i.e., 90°, this difference decreases gradually. The model follows Lambert's law for small grazing angles as well as angles near normal incidence, i.e., for $\theta < 30°$ and $\theta > 80°$, respectively.

VI. DISCUSSION

Apart from a strong spatial variability of the density, experiments have also revealed a high spatial variability of the sediment sound speed (see, for example, Refs. 20 and 25), but sound speed variability is not included in the equivalent roughness approximation.

The scattering model presented in Sec. III is adopted from radar theory, where the interface between air and ground has a significant impedance contrast, which consequently yields a weak wave penetration into the ground. Hence, interface scattering is the dominant scattering mechanism, and the air and ground can be considered as homogeneous media. Prior to the development of the equivalent roughness approach it was attempted to vary the sediment density along each discrete surface point; that is, the density ratio μ, in Eqs. (40) and (44), was replaced by μ_n, with $n = 1, 2, \ldots, N$, where N represents the total number of surface points. The same principle was applied by varying k_2, i.e., the sediment sound speed, along the height profile. However, simulations did not show any change in the shape of the backscattering curve, probably because the equations formulated in Sec. III are formulated strictly for interface roughness variations.

Another approach to compute the scattered field could be a finite element model, also for 1D height profiles, of the upper part of the sediment combined with a boundary value formulation for the interface. However, the method would probably become very computationally demanding and yet suffer from the lack of precise information regarding small scale density and sound speed variations in the upper part of the sediment.

It has also been attempted to apply the method presented by D. Kapp *et al.*,[10] but it yields more inaccurate results for the zeroth-order Born term than the band matrix approximation applied here, and it does not converge for higher order iterations.

It is important to emphasize that the optically acquired roughness parameters, shown in Table I, probably not are measured at the same date and time as the acoustic data. Except for the fact that BAMS is the correct site, it is not quite clear which set of parameters in Ref. 23 must be applied. However, it does not change the fact that the equivalent roughness approach lifts the backscattering level up to the levels obtained from experiments.

VII. CONCLUSION

The equivalent roughness approximation yields, when $\kappa = 0.45$, backscattering strengths at 300 kHz that agree with experimental data acquired at SAX99. The band-matrix approximation, with $M = 20$, yields backscattering errors of 8 dB for $\theta = 1°$; for grazing angles above 5° backscattering errors are less that 1.5 dB. Sonar simulations are not expected to be carried out for grazing angles of less than 5°, and, hence, the model is considered to have a sufficient accuracy for $M = 20$. Computations have been carried out in Matlab6.5™ on a PC with a Windows XP™ operating system, a 3 GHz (Pentium4™) processor, and 512 MB RAM. The method allows computations of height profiles with 25 000 elements that correspond to 25 m when the resolution is one-fifth of the wavelength and the wavelength is $\lambda = 0.5$ cm. The equivalent roughness approach combined with the band matrix method is well suited to model sandy seabed backscattering for artificially very high frequency sonar images.

ACKNOWLEDGMENTS

The authors are grateful to Dajun Tang at Applied Physics Laboratory, University of Washington, for answers related to the seabed model, and to Eric Thorsos, Applied Physics Laboratory, University of Washington, for general advice regarding the scattering problem. The authors also gratefully acknowledge advice from Per Christian Hansen, Informatics and Mathematical Modeling (IMM), Technical University of Denmark, regarding the band matrix solution.

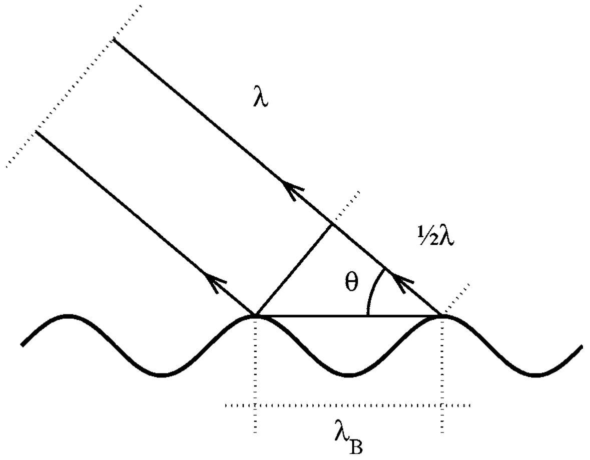

FIG. 13. Geometry applied to derive the Bragg wavelength.

APPENDIX: THE BRAGG WAVELENGTH

The Bragg wavelength, λ_B, for a rough interface is defined in terms of an incoming, monochromatic plane wave with wavelength, λ, and a grazing angle of incidence, θ, that is,

$$\lambda_B = \frac{\lambda}{2\cos\theta} \tag{A1}$$

(see Fig. 13). Equation (A1) is equivalent to the reinforcement criterion for backscattering described by Urick.[29] The Bragg frequency of the seabed roughness is

$$f_B = \frac{2\cos\theta}{\lambda}. \tag{A2}$$

At 300 kHz the wavelength is $\lambda = 0.5$ cm when it is assumed that the sound speed is $c = 1500$ m/s; thus at zero grazing angle, i.e., $\theta = 0$, one has $f_B = 4$ cycles/cm, which corresponds to the vertical lines indicated in Figs. 1–3.

[1] E. Pouliquen, G. Canepa, L. Pautet, and A. P. Lyons, "Temporal variability of seafloor roughness and its impact on acoustic scattering," in Proceedings of the Seventh European Conference in Underwater Acoustics (ECUA2004), Delft, The Netherlands, 5–8 July 2004.

[2] J. A. Ogilvy, *Theory of Wave Scattering from Random Rough Surfaces* (IOP, London, 1991), Chap. 4.1.2.

[3] L. M. Brekhovskikh and Yu. P. Lysanov, *Fundamentals of Ocean Acoustics*. Third edition (AIP, Springer-Verlag, New York, 2003).

[4] E. I. Thorsos and D. R. Jackson, "Studies of scattering using numerical methods," Waves Random Media **3**, S165–S190 (1991).

[5] J. M. Bell, "Application of optical ray tracing techniques to the simulation of sonar images," Opt. Eng. (Bellingham) **36**, 1806–1813 (1997).

[6] T. Capron, G. Hayward, and R. Chapmann, "A 3D simulator for the design and evaluation of sonar system instrumentation," Meas. Sci. Technol. **10**, 1116–1126 (1999).

[7] E. I. Thorsos and S. L. Broschat, "An investigation of the small slope approximation for scattering from rough surfaces. Part I. Theory," J. Acoust. Soc. Am. **97**, 2082–2093 (1995).

[8] S. L. Broschat and E. I. Thorsos, "An investigation of the small slope approximation for scattering from rough surfaces. Part II. Numerical studies," J. Acoust. Soc. Am. **101**, 2615–2625 (1997).

[9] E. I. Thorsos, "The validity of the Kirchhoff approximation for rough surface scattering using a Gaussian roughness spectrum," J. Acoust. Soc. Am. **83**, 78–92 (1988).

[10] D. A. Kapp and G. S. Brown, "A new numerical method for rough surface scattering calculations," IEEE Trans. Antennas Propag. **44**, 711–721 (1996).

[11] C. H. Chan, L. Tsang, and Q. Li, "Monte Carlo simulations of large scale one-dimensional random rough surface scattering at near-grazing incidence: Penetrable case," IEEE Trans. Antennas Propag. **46**, 142–149 (1998).

[12] D. R. Jackson, D. P. Winebrenner, and A. Ishmaru, "Application of the composite roughness model to high frequency bottom backscattering," J. Acoust. Soc. Am. **79**, 1410–1422 (1986).

[13] D. R. Jackson and K. B. Briggs, "High frequency bottom backscattering: Roughness versus sediment volume scattering," J. Acoust. Soc. Am. **92**, 962–977 (1992).

[14] P. D. Mourad and D. R. Jackson, "High-frequency sonar equation models for bottom backscatter and forward loss," in *Proceedings of OCEANS'89* (1989), pp. 1168–1175.

[15] D. R. Jackson, "Models for scattering from the sea bed," Proc. IOA, Vol. **16**, Part 6 (1994).

[16] K. L. Williams and D. R. Jackson, "Bistatic bottom scattering: Model, experiments, and model/data comparison," J. Acoust. Soc. Am. **103**, 169–181 (1998).

[17] S. Stanic, R. R. Goodman, K. B. Briggs, N. P. Chotiros, and E. T. Kennedy, "Shallow-water bottom reverberation measurements," IEEE J. Ocean. Eng. **23**, 203–210 (1998).

[18] E. Pouligen and A. P. Lyons, "Backscattering from Bioturbated sediments at very high frequency," IEEE J. Ocean. Eng. **27**, 388–402 (2002).

[19] K. L. Williams, D. R. Jackson, E. I. Thorsos, D. Tang, and K. B. Briggs, "Acoustic backscattering experiments in a well characterized sand sediment: Data/model comparisons using sediment fluid and Biot models," IEEE J. Ocean. Eng. **27**, 376–387 (1998).

[20] D. Tang, K. B. Briggs, K. L. Williams, D. R. Jackson, E. I. Thorsos, and D. B. Percival, "Fine scale volume heterogeneity measurments in sand," IEEE J. Ocean. Eng. **27**, 546–560 (2002).

[21] E. I. Thorsos, K. L. Williams, N. P. Chotiros, J. T. Christoff, K. W. Commander, C. F. Greenlaw, D. V. Holliday, D. R. Jackson, J. L. Lopes, D. E. McGehee, J. E. Piper, M. D. Richardson, and D. Tang, "An overview of SAX99: Acoustic measurements," IEEE J. Ocean. Eng. **26**, 4–25 (2001).

[22] O. George and R. Bahl, "Simulation of backscattering of high frequency sound from complex objects and sand sea-bottom," IEEE J. Ocean. Eng. **20**, 119–130 (1995).

[23] K. B. Briggs, D. Tang, and K. L. Williams, "Characterisation of interface roughness of rippled sand off Fort Walton Beach, Florida," IEEE J. Ocean. Eng. **27**, 505–514 (2002).

[24] K. B. Briggs, "Microtopographical roughness of shallow-water continental shelves," IEEE J. Ocean. Eng. **14**, 360–367 (1989).

[25] K. B. Briggs, M. Zimmer, and M. D. Richarson, "Spatial and temporal variations in sediment compressional wave speed and attenuation measured at 400 kHz for SAX04," in Proceedings of Boundary Influences in High Frequency, Shallow Water Acoustics, Bath, UK, September 2005.

[26] E. I. Thorsos and M. D. Richardson, "GuestEditorial," IEEE J. Ocean. Eng. **27**, 341–345 (2002), p. 342, first column, lines 27–31.

[27] J. G. Proakis and D. G. Manolakis, *Digital Signal Processing. Principles, Algorithms, and Applications*. Third edition (Prentice-Hall, Englewood Cliffs, NJ, 1996), Chap. 11.1.1.

[28] E. G. Williams, *Fourier Acoustics. Sound Radiation and Nearfield Acoustical Holography* (Academic, London, 1999), Chap. 8.5, pp. 262–264.

[29] R. J. Urick, *Principles of Underwater Sound*. Third edition (Peninsula, Los Altos, CA, 1983), Chap. 8.13.

Appendix E

The wave equation

In this chapter the wave equation is derived together with the Helmholtz equation. The derivation is followed by a brief discussion of the validity of the wave equation in terms of the fundamental assumptions. The limits of the wave equation are relevant for acoustic waves that have penetrated into the seabed sediment. The content of this appendix is based on Ref. [7].

Acoustic waves propagate by a compression and rarefaction of the medium; compression and rarefaction is perpendicular to the propagating wavefront. Compared to air the amount of compression and rarefaction in water is very small. Let p_0, ρ_0 denote the ambient, or undisturbed, pressure and density respectively for a homogeneous and quiescent medium, that is, a medium with zero particle velocity, i.e., $\mathbf{v}_0 = \mathbf{0}$. The pressure p, density ρ, and particle velocity are expressed by first order Taylor series by

$$p = p_0 + p', \tag{E.1}$$

$$\rho = \rho_0 + \rho', \tag{E.2}$$

$$\mathbf{v} = \mathbf{v}', \tag{E.3}$$

where $\mathbf{v}$ represents the particle velocity, and where p', ρ', and $\mathbf{v}'$ are the acoustic contributions to, or perturbations of, the pressure, density, and particle velocity respectively, see, e.g., Ref. [7]. When deriving the wave equation Eqs. (E.1) and (E.2) will be substituted into the equation of mass conservation, Euler's equation of motion for an inviscid fluid, and the pressure density relations.

We begin by the conservation of mass which is expressed by

$$\frac{\partial \rho}{\partial t} + \boldsymbol{\nabla} \cdot (\rho \mathbf{v}) = 0, \tag{E.4}$$

where t represents time, see, e.g., Ref. [7] (Eq. 1-2.4). Eulers equation of motion for an inviscid fluid is

$$\rho \frac{\partial \mathbf{v}}{\partial t} + (\mathbf{v} \cdot \nabla)\mathbf{v} = -\nabla p, \tag{E.5}$$

see, e.g., Ref. [7] (Eq. 1-3.7). Finally, the pressure density relation must be introduced,

$$p = p(\rho, s), \tag{E.6}$$

that is, the acoustic pressure depends on the density and specific entropy s of the fluid. Acoustic propagation is assumed to have constant entropy, i.e., $s = s_0$. Consequently, the pressure density relation can be expressed by the following Taylor series expansion, see, e.g., Ref. [7] (Eq. 1-5.2c'),

$$p' = \Big(\frac{\partial p}{\partial \rho}\Big)_0 \rho' + \frac{1}{2}\Big(\frac{\partial^2 p}{\partial \rho^2}\Big)_0 (\rho')^2 + ... \tag{E.7}$$

Insertion of Eqs (E.2) and (E.3) into the equation of conservation of mass, Eq. (E.4), yields

$$\frac{\partial(\rho_0 + \rho')}{\partial t} + \boldsymbol{\nabla} \cdot ([\rho_0 + \rho']\mathbf{v}') = 0, \tag{E.8}$$

and similarly, insertion of Eqs (E.1) and (E.3) into Euler's equation, Eq. (E.5), yields

$$[\rho_0 + \rho']\frac{\partial \mathbf{v}'}{\partial t} + (\mathbf{v}' \cdot \nabla)\mathbf{v}' = -\nabla[p_0 + p'], \tag{E.9}$$

By neglecting second order terms, i.e., terms containing factors of two primed variables Eqs. (E.7), (E.8), and (E.9) yields,

$$\frac{\partial \rho'}{\partial t} + \rho_0 \boldsymbol{\nabla} \cdot \mathbf{v}' = 0, \tag{E.10}$$

$$\rho_0 \frac{\partial \mathbf{v}'}{\partial t} = -\nabla p', \tag{E.11}$$

$$p' = \Big(\frac{\partial p}{\partial \rho}\Big)_0 \rho' \tag{E.12}$$

Note, the assumption of a homogeneous medium yields

$$\begin{aligned} p_0(x, y, x) &\equiv p_0\,, \\ \rho_0(x, y, x) &\equiv \rho_0\,, \end{aligned} \tag{E.13}$$

and consequently

$$\boldsymbol{\nabla}\rho_0 = 0\,, \tag{E.14}$$

$$\boldsymbol{\nabla}p_0 = 0, \tag{E.15}$$

and these properties are also includes in the transformations from Eq. (E.8) to Eq. (E.10) and from Eq. (E.9) to Eq. (E.11). The speed of sound is related to the ratio of the ambient pressure and density by

$$c^2 = \Big(\frac{\partial p}{\partial \rho}\Big)_0\,, \tag{E.16}$$

and Eq. (E.12) becomes

$$p' = c^2\rho'. \tag{E.17}$$

Thus, in Eq. (E.10) the density disturbance ρ' is substituted by p'/c^2 which yields,

$$\frac{1}{c^2}\frac{\partial p'}{\partial t} + \rho_0 \boldsymbol{\nabla} \cdot \mathbf{v}' = 0, \tag{E.18}$$

and subsequently, by taking the time derivative of Eq. (E.18) one obtains,

$$\frac{1}{c^2}\frac{\partial^2 p'}{\partial t^2} + \boldsymbol{\nabla} \cdot (\rho_0 \frac{\partial \mathbf{v}'}{\partial t}) = 0. \tag{E.19}$$

Substitution of Eulers linearized equation, Eq. (E.11), into Eq. (E.19) yields,

$$\frac{1}{c^2}\frac{\partial^2 p'}{\partial t^2} + \boldsymbol{\nabla} \cdot (-\nabla p') = 0. \tag{E.20}$$

and

$$\frac{1}{c^2}\frac{\partial^2 p'}{\partial t^2} - \boldsymbol{\nabla}^2 p' = 0. \tag{E.21}$$

A substitution of p' with p leads to the wave equation

$$\nabla^2 p - \frac{1}{c^2}\frac{\partial^2 p}{\partial t^2} = 0. \tag{E.22}$$

The Fourier transform of wave equation lead to the Helmholtz equation; the Fourier transform relationship for differentiation in the time domain is

$$\frac{\partial}{\partial t} \leftrightarrow -i\omega\,, \tag{E.23}$$

is applied in Eq. (F.2) and the Helmholtz equation yields

$$\nabla^2 \widehat{p} + k^2 \widehat{p} = 0, \tag{E.24}$$

where $\widehat{p}$ represents the Fourier transform of p. Suppose the medium is inhomogeneous, but still quiescent, then the last term on the left side of Eq.(E.8) would become

$$\boldsymbol{\nabla} \cdot ([\rho_0 + \rho']\mathbf{v}') = \boldsymbol{\nabla} \cdot (\rho_0 \mathbf{v}') \tag{E.25}$$

where higher order terms still are neglected; the right hand side of Eq. (E.25) is considered

$$\begin{aligned}\boldsymbol{\nabla} \cdot (\rho_0 \mathbf{v}') &= \frac{\partial}{\partial x}(\rho_0 v'_x) + \frac{\partial}{\partial y}(\rho_0 v'_y) + \frac{\partial}{\partial z}(\rho_0 v'_z) \\ &= \rho_0 \boldsymbol{\nabla} \cdot \mathbf{v}' + \mathbf{v}' \cdot \boldsymbol{\nabla} \rho_0 \end{aligned} \tag{E.26}$$

An inhomogeneous medium will also require that the pressure-density relation is re-examined, see, e.g., Ref. [7](pp. 15). In the study of acoustic penetration into the seabed sediment the fundamental assumptions that the wave equation is based on must be reconsidered; the seabed may be porous and a Biot model should be applied, or for a fluid model, the density and sound speed variations cannot be neglected below a certain wavelength.

Appendix F

The Kirchhoff Helmholtz Integral Equation (KHIE)

This appendix is based on text-book material.

In this appendix nearly all equations are considered in the frequency domain; p will represent the Fourier transform of the acoustic pressure; when the pressure is expressed in the time domain it will be written as $p(t)$, where t represents time, and the same praxis will be applied for other variables. An $e^{-i\omega t}$ time dependence is applied (ω represents the radial frequency); consequently a spherically diverging wave is expressed as e^{ikR}/R, where k is the wavenumber, and R is the distance to the source. The Kirchhoff-Helmholtz integral equations are the fundamental equations for general boundary value problems that concerns radiation and scattering, and they are derived here and the derivation is based on Ref. [65]. Other derivations are presented in, for example, Refs. [60],[9], and [7].

Sound fields are generated by acoustic sources that excite the surrounding medium. The simplest source is a harmonic oscillating rigid sphere that periodically compresses and rare facts the fluid around it. This disturbance then propagates spherically away from the sphere with the speed of sound c that depends on the ratio between the fluids pressure and density. The sphere can be idealized as a point, which this leads to the concept of a point source, or monopole source, where its spatial description is formed by Dirac's delta function. Sources that emit more complicated waveforms can be modeled as composition of several monopole sources. The dipole source, for example, is constructed by locating two opposite phase monopole sources sufficiently close to each other. The quadrupole is a combination of two dipole sources. In this way one can compose a source that exhibit a specified radiation or directivity pattern needed for a specific problem. In order to determine the free field pressure generated by several sources the superposition generalized to a continuum of sources is

$$p = \iiint_{V_s} G_k(\mathbf{x}|\mathbf{x}_s)\, q(\mathbf{x})\, dV_s \tag{F.1}$$

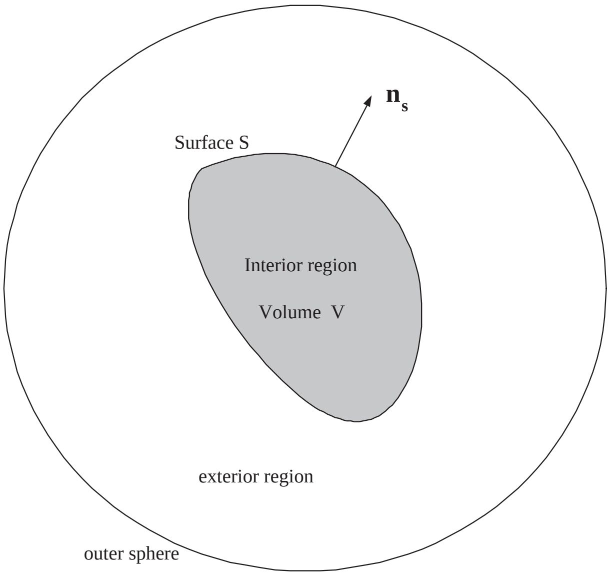

Figure F.1: Geometry applied to derive the KHIE equations. The interior region is within the volume V and the exterior region is between the surface of S of the volume and an outer sphere that goes to infinity. The normal derivative of the surface points out of the volume into the exterior region

where $G_k(\mathbf{x}|\mathbf{x}_s)$ is the free space Green's function for the wavenumber k, and q represents the volume velocity of the source. When the sound wave interacts with a wall, the ground, or a sea surface it is scattered back in many directions dependent on the shape and the material property of the boundary. In the following the general integral equations that formally represent this phenomenon are derived, that is, the Kirchhoff-Helmholtz theorem.

The Kirchhoff-Helmholtz theorem is derived for an isolated vibrating body in an unbounded fluid where each body on the surface vibrates with the same frequency; it also applies for a fixed surface enclosing a source. The situation is depicted in Fig. (F.1). The starting point of the derivation is the inhomogeneous Helmholtz equation

$$\nabla^2 p \ + \ k^2 p = -f(\mathbf{x}_0), \tag{F.2}$$

where $k = \omega/c$ is the wavenumber, p is the acoustic pressure and f is the source centered at $\mathbf{x}_0$. The solution to this problem can be divided into an *interior* or *exterior* problem. For the *interior volume* problem values of p at points in the interior region satisfy the homogeneous Helmholtz equation, i.e., no sources are present here, and the boundary conditions are specified via the normal outward derivative of $\widehat{p}$ at the surface S. For the *exterior* problem the homogeneous Helmholtz equation is satisfied in the *exterior volume*, and again no sources are present here. The boundary conditions are specified via the normal outward derivative along the surface S and Sommerfeld's radiation condition

$$r(\frac{p_{ext}}{\partial r} - ik\,p_{ext}) \rightarrow 0\ , \quad r \rightarrow 0 \tag{F.3}$$

at the outer sphere, see, e.g., Ref. [7] ().
Equation (F.2) is proportional to

$$\nabla^2\Psi \ + \ k^2\Psi = \ -4\pi\,\delta(\mathbf{x}-\mathbf{x}_0)\,, \tag{F.4}$$

where the right hand side, the source term, $-\widehat{f}(\mathbf{x}_0)$, has been replaced by an equivalent monopole source, and where Ψ is represents the field function. The solution to (F.4) can be expressed as a sum of the homogeneous solution Ψ_h and the particular solution Ψ_p:

$$\Psi = \Psi_h + \Psi_p. \tag{F.5}$$

The particular solution is the free space solution to the inhomogeneous wave equation and is given by the free space Green's function

$$G(\mathbf{x}|\mathbf{x}_0) = \frac{e^{ik|\mathbf{x}-\mathbf{x}_0|}}{|\mathbf{x}-\mathbf{x}_0|}\,, \tag{F.6}$$

which will be treated in the next section.

F.1 The free space Greens function

Time and space dependency of an acoustic signal $s(t)$ radiated from a monopole source at position $\mathbf{x}_0$ can be expressed by the acoustic pressure

$$p(R,t) = q(t - R/c)/R \tag{F.7}$$

where $R = |\,\mathbf{x}-\mathbf{x}_0\,|$ is the distance between source at $\mathbf{x}_0$ and receiver at $\mathbf{x}$; this monopole source radiates a spherical wave. By using the Fourier transform relationship $f(t-t_0) \leftrightarrow f e^{i\omega t_0}$ one obtains

$$p = q\,\frac{e^{i\omega R/c}}{R} = q\,\frac{e^{ikR}}{R}, \tag{F.8}$$

and hence, the free space Greens' function is given by

$$G(\mathbf{x}|\mathbf{x}_0) = \frac{e^{ikR}}{R}. \tag{F.9}$$

The gradient of the free space Green function is given by

$$\begin{aligned}\nabla G &= \frac{\mathbf{x}-\mathbf{x}_0}{R}\frac{\partial}{\partial R}(\frac{e^{ikR}}{R}) \\ &= \frac{\mathbf{x}-\mathbf{x}_0}{R}(-\frac{1}{R^2}+\frac{ik}{R})e^{ikR} \\ &= \frac{\mathbf{x}-\mathbf{x}_0}{R^3}(ikR-1)e^{ikR}\,, \end{aligned} \tag{F.10}$$

and

$$\nabla G = \frac{\mathbf{x}-\mathbf{x}_0}{R^3}(ikR-1)e^{ikR} \tag{F.11}$$

For large wavenumbers $kR >> 1$ and Eq. (F.11) reduces to

$$\nabla G = \frac{\mathbf{x}-\mathbf{x}_0}{R^2}\, ik\, e^{ikR} \tag{F.12}$$

Spherical symmetry has been assumed such that $\nabla = \widehat{r}\frac{\partial}{\partial R} + \widehat{\phi}\frac{1}{R}\frac{\partial}{\partial \phi} + \widehat{\theta}\frac{1}{R\cdot sin(\phi)}\frac{\partial}{\partial \theta} = \widehat{r}\frac{\partial}{\partial R}$. Note that the normalized vector from the source to the receiver, $\widehat{\mathbf{r}}$, is given by

$$\widehat{\mathbf{r}} = \frac{\mathbf{x}-\mathbf{x}_0}{R}\,, \tag{F.13}$$

and Eq. (F.12) yields

$$\nabla G = ik\,\frac{e^{ikR}}{R}\,\widehat{\mathbf{r}}. \tag{F.14}$$

F.2 Derivation of KHIE

This section is based on Ref. [65]. Two homogeneous Helmholtz equations with respectively the acoustic pressure field and the Greens function are:

$$\nabla^2 p + k^2 p = 0 \tag{F.15}$$

$$\nabla^2 G + k^2 G = 0 \tag{F.16}$$

If one multiplies Eq. (F.15) by G, and multiplies Eq. (F.16) by p, and subsequently subtracts Eq. (F.16) from Eq. (F.15) one obtains:

$$G(\nabla^2 + \ k^2)p - p(\nabla^2 + \ k^2)G = 0, \tag{F.17}$$

which is equivalent to

$$G(\nabla^2)p - p(\nabla^2)G = G(\nabla\cdot\nabla)\widehat{p} - p(\nabla\cdot\nabla)G. \tag{F.18}$$

Green's theorem states that

$$\nabla\cdot(u\nabla v) = u\nabla\cdot\nabla v + (\nabla u)\cdot(\nabla v), \tag{F.19}$$

$$\nabla\cdot(v\nabla u) = v\nabla\cdot\nabla u + (\nabla v)\cdot(\nabla u), \tag{F.20}$$

where u and v are two scalar functions; see, e.g., Ref. [66] (Eqs. (1.101) and (1.102), pp. 62). Subtraction of Eq. (F.20) from Eq. (F.19) yields

$$\nabla\cdot(u\nabla v) - \nabla\cdot(v\nabla u) = u\nabla\cdot\nabla v - v\nabla\cdot\nabla u, \tag{F.21}$$

and the right hand side of (F.21) is equivalent to the right hand side of (F.18). Since the left hand side of Eq. (F.21) is $\nabla\cdot(u\nabla v)-\nabla\cdot(v\nabla u)=\nabla\cdot(u\nabla v-v\nabla u)$ equation (F.17) can be expressed as

$$G(\nabla^2+\ k^2)p-p(\nabla^2+\ k^2)G=\nabla\cdot(G\nabla p-p\nabla G) \tag{F.22}$$

This is the vector identity that is the starting point for deriving the Kirchhoff-Helmholtz integral.

In the following this equation is integrated over either the *interior* or *exterior* volume, see figure (F.1). Before analyzing the specific cases Eq. (F.22) is integrated over an unspecified volume

$$\iiint_V \Big(G(\nabla^2+\ k^2)p-p(\nabla^2+\ k^2)G\Big)dV=\iiint_V \nabla\cdot(G\nabla p-p\nabla G)\,dV. \tag{F.23}$$

Gauss theorem states that the volume integral of the divergence of a vector, $\nabla\cdot\mathbf{V}$, is equal to the surface integral of the vector over the surface that encloses the specific volume

$$\int_V \nabla\cdot\mathbf{V}\,dV=\int_S \mathbf{V}\cdot\hat{\mathbf{n}}\,dS, \tag{F.24}$$

where $\hat{\mathbf{n}}$ is the unit-outward-normal vector of the surface S that encloses the volume V, see, for example, Ref. [66] (Eq. (101a), pp. 61). Gauss theorem is applied on the right hand side of equation (F.23) and we obtain

$$\iiint_V \Big(G(\nabla^2+\ k^2)p-p(\nabla^2+\ k^2)G\Big)\,dV=\iint_S (G\nabla p-p\nabla G)\cdot\hat{\mathbf{n}}\,dS. \tag{F.25}$$

The left hand side of equation (F.25) is an integral of the field equations and the right hand side is an integral of the acoustic boundary conditions at the surface of the volume. The field equations are represented by the Helmholtz equation which is the Fourier transform of the wave equation. The wave equation is derived from the linearized equation of mass conservation, Euler's linearized equation of motion of a fluid, and finally the linearized pressure density relations of the medium.

The source terms are now considered and the inhomogeneous Helmholtz equations are

$$\begin{aligned}(\nabla^2+k^2)\,p &= -f(\mathbf{x}_0), &\text{(F.26)}\\ (\nabla^2+k^2)\,G(\mathbf{x}|\,\mathbf{x}_0) &= -4\pi\,\delta(\mathbf{x}-\mathbf{x}_0), &\text{(F.27)}\end{aligned}$$

where Green's function, $G(\mathbf{x}|\,\mathbf{x}_0)$, represents the field value at $\mathbf{x}$ provided the source is located at $\mathbf{x}_0$.

For the *internal* formulation there are no sources within V, that is, $\mathbf{x}_0$ is outside V, see, e.g., Fig. (F.2). Hence, Eq. (F.26) reduces to the homogeneous Helmholtz

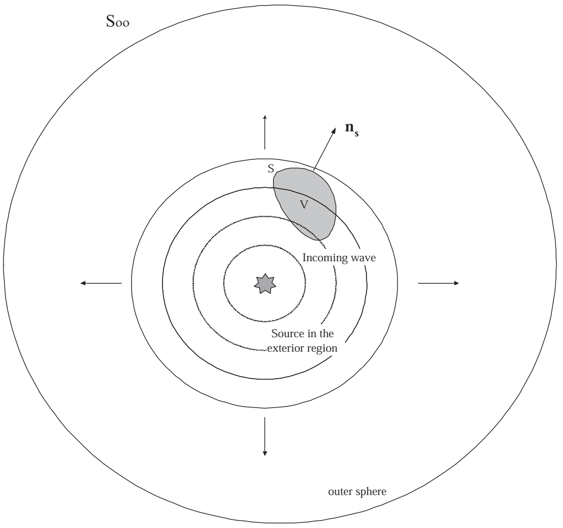

Figure F.2: The *internal* formulation, where all sources are located in the exterior region.

equation, but the observation point $\mathbf{x}$ is arbitrary, and consequently, Eq. (F.25) yields

$$-\iiint_V p_{int}(\nabla^2 + \ k^2)G\,dV_{int} = \iint_S (G\nabla p_{int} - p_{int}\nabla G)\cdot\hat{\mathbf{n}}\,dS. \tag{F.28}$$

In the *external* formulation there are no sources outside V, that is, $\mathbf{x}_0$ is inside V. Hence, in the *exterior* volume Eq. (F.26) reduces to the homogeneous Helmholtz equation, but the observation point $\mathbf{x}$ is still arbitrary, and consequently, Eq. (F.25) yields

$$-\iiint_V p_{ext}(\nabla^2 + \ k^2)G\,dV_{ext} = -\iint_S (G\nabla p_{ext} - p_{ext}\nabla G)\cdot\hat{\mathbf{n}}\,dS + I_R. \tag{F.29}$$

There is a minus sign multiplied to the first term on the right side of Eq. (F.29) because the surface normal vector points into the exterior field. I_R is the surface integral over the outer sphere and it is given by

$$I_R = R^2\int_0^{2\pi}\int_0^{\pi}(G\nabla p_{ext} - p_{ext}\nabla G)\sin\theta\,d\theta\,d\phi, \tag{F.30}$$

and according to Sommerfeld's radiation condition

$$I_R \to 0 \text{ for } R\to\infty. \tag{F.31}$$

Hence, Eq. (F.29) reduces to

$$-\iiint_V p_{ext}(\nabla^2 + \ k^2)G\,dV_{ext} = -\iint_S (G\nabla p_{ext} - p_{ext}\nabla G)\cdot\hat{\mathbf{n}}\,dS. \tag{F.32}$$

For the internal formulation Eq. (F.28) the pressure at the observation point is

$$p_{int}(\mathbf{x}) = \frac{1}{4\pi}\iint_S (G\nabla p_{int} - p_{int}\nabla G)\cdot\hat{\mathbf{n}}\,dS \;\; ; \;\; \mathbf{x}\,\text{is inside}\,V\,. \tag{F.33}$$

$$0 = \frac{1}{4\pi}\iint_S (G\nabla p_{int} - p_{int}\nabla G)\cdot\hat{\mathbf{n}}\,dS \;\; ; \;\; \mathbf{x}\,\text{is outside}\,V\,. \tag{F.34}$$

For the external formulation Eq. (F.32) the pressure at the observation point is

$$p_{ext}(\mathbf{x}) = -\frac{1}{4\pi}\iint_S (G\nabla p_{ext} - p_{ext}\nabla G)\cdot\hat{\mathbf{n}}\,dS \;\; ; \;\; \mathbf{x}\,\text{is outside}\,V\,. \tag{F.35}$$

$$0 = -\frac{1}{4\pi}\iint_S (G\nabla p_{ext} - p_{ext}\nabla G)\cdot\hat{\mathbf{n}}\,dS \;\; ; \;\; \mathbf{x}\,\text{is inside}\,V. \tag{F.36}$$

F.3 KHIE for scattering

In the following the resulting sound field from a source and reflecting boundaries is considered. In linear acoustic theory the total field can be separated into the wave field generated by the source, i.e., the incoming wave field, p_{inc}, and the wave field reflected or scattered from the surface S, that is, p_{sc}. The total pressure is given by

$$p_{tot} = p_{inc} + p_{sc}. \tag{F.37}$$

Here, the incoming field is generated by a source in the exterior region; since the Helmholtz equation is not equal to zero in the entire external region the exterior formulation does not hold; instead, the interior formulation is applied for the incoming wave

$$p_{inc}(\mathbf{x}) = \frac{1}{4\pi}\iint_S (G\nabla p_{inc} - p_{inc}\nabla G)\cdot\hat{\mathbf{n}}\,dS \;\; ; \;\; \mathbf{x}\,\text{is inside}\,V\,. \tag{F.38}$$

$$0 = \frac{1}{4\pi}\iint_S (G\nabla p_{inc} - p_{inc}\nabla G)\cdot\hat{\mathbf{n}}\,dS \;\; ; \;\; \mathbf{x}\,\text{is outside}\,V\,. \tag{F.39}$$

The scattered field within V, on the other hand, satisfies the Helmholtz equation in the exterior region and the external formulation is applied

$$p_{sc}(\mathbf{x}) = -\frac{1}{4\pi}\iint_S (G\nabla p_{sc} - p_{sc}\nabla G)\cdot\hat{\mathbf{n}}\,dS \;\; ; \;\; \mathbf{x}\,\text{is outside}\,V\,. \tag{F.40}$$

$$0 = -\frac{1}{4\pi}\iint_S (G\nabla p_{sc} - p_{sc}\nabla G)\cdot\hat{\mathbf{n}}\,dS \;\; ; \;\; \mathbf{x}\,\text{is inside}\,V\,. \tag{F.41}$$

For the region outside V, the exterior region, the combination of Eq. (F.37) with Eq. (F.40) yields

$$p_{tot} = p_{inc} - \frac{1}{4\pi}\iint_S (G\nabla p_{sc} - p_{sc}\nabla G)\cdot\hat{\mathbf{n}}\,dS. \tag{F.42}$$

The total pressure can be included inside the surface integral by adding Eq. (F.39) to Eq. (F.42)

$$p_{tot} = p_{inc} - \frac{1}{4\pi} \iint_S (G \nabla p_{tot} - p_{tot} \nabla G) \cdot \hat{\mathbf{n}} \, dS \tag{F.43}$$

This integral equation is fundamental when dealing with scattering problems and it is very often applied within the literature related to underwater scattering problems.

In this chapter the general Kirchhoff Helmholtz integral equations, that form the basis for boundary value problems, have been derived. Equation (F.43) is central for the work made in this thesis.

Appendix G

Wave scattering from the seabed

In radar applications there is a high impedance contrast between the air and ground/sea interface; consequently, the backscattered field is produced at the interface as the ground penetration is weak. However, the impedance ratio between the sediment and water is typically not greater than approximately 2.5 and there is a significant penetration in the sediment. Thus, the backscattered field from the seabed contains contributions from the water sediment interface and contributions from the sediment volume.
In this chapter the fundamental mechanisms concerning plane wave reflection and transmission at a smooth interface between two homogeneous fluids are addressed; it is followed up by a brief presentation of sub-critical sediment penetration, a mechanism that may be exploited for detection of buried objects. An inhomogeneous sediment changes the reflection and transmission mechanisms, and a simple simulation based on Mourad and Jackson, see Ref. [19], is carried out to demonstrate this: A a plane wave with normal incidence onto the interface is transmitted into a sediment with a depth vary density and it is shown that the reflection coefficient strongly depends on the frequency and the shape of the density profile. The issue of scattering from rough surfaces is considered, and the most important models for rough surface scattering are presented. A separate section is devoted to Jackson's model for high frequency backscattering, where some of the results from Ref. [19] are reconstructed.

G.1 Plane wave reflection and transmission at an infinite smooth fluid-fluid interface

The content of this section involves the fundamentals of plane wave reflection and transmission from the smooth interface between two homogeneous fluids, see, e.g., Ref. [67] (Ch. 3.1) and Ref. [9] (Ch. 2.6.1). A real water-sediment interface is of course rough, and the ratio between the coherent and the diffuse part of the transmitted field depends on the roughness characteristics and the acoustic wavelength. However, the interface may be considered smooth when

$$k \cdot h_{RMS} << 1, \tag{G.1}$$

where k is the acoustic wave number and h is the roughness height function; at least the smooth surface assumption corresponds to the zero'th order solution in the perturbation theory, where the solution is expanded in power series of kh. In the fluid model there is continuity of normal displacement at the interface, that is,

$$\mathbf{v}_i \cdot \hat{\mathbf{n}} + \mathbf{v}_r \cdot \hat{\mathbf{n}} = -\mathbf{v}_t \cdot \hat{\mathbf{n}}, \tag{G.2}$$

where $\mathbf{v}_i$, $\mathbf{v}_r$, and $\mathbf{v}_t$ are the particle velocity of the incoming field, the reflected field, and transmitted field respectively, and where $\hat{\mathbf{n}}$ is the normal vector of the interface. In addition, the acoustic pressure on each side of the interface must be equal:

$$p_i + p_r = p_t. \tag{G.3}$$

Let the water sound speed be denoted c_w, the sediment sound speed c_s, the water density ρ_w, and the sediment density ρ_s. If the sediment specific impedance differs much of that of the water, that is,

$$\rho_s c_s \gtrless \rho_w c_w, \tag{G.4}$$

the acoustic penetration into the sediment is vanishing and the sound field is scattered back into the water (This is the case at the sea surface where the density contrast is very high and the reflection coefficient magnitude approaches one). The plane wave reflection coefficient given by

$$R = \frac{\rho_s c_s \cos\theta_s - \rho_w c_w \cos\theta_w}{\rho_s c_s \cos\theta_s + \rho_w c_w \cos\theta_w}, \tag{G.5}$$

and the transmission coefficient is given by

$$T = \frac{2\rho_s c_s \cos\theta_w}{\rho_s c_s \cos\theta_w + \rho_w c_w \cos\theta_s}. \tag{G.6}$$

Figure (G.1) illustrates the reflection and transmission of a plane wave onto a perfectly smooth water/sediment fluid-fluid interface by application of Huygens principle. Here, the sound speed is higher in the sediment. In a stable geophysical environment, only considered here, the sediment density is always larger than that of the water; hence, the density ratio,

$$m = \frac{\rho_s}{\rho_w} > 1. \tag{G.7}$$

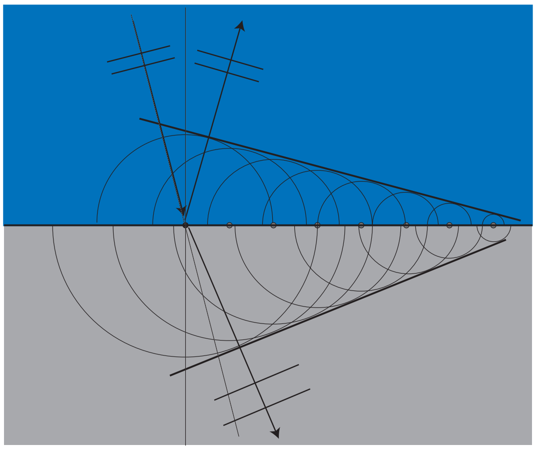

Figure G.1: Reflection and transmission, demonstrated by Huygens principle for perfectly smooth water-sediment interface with $c_s > c_w$.

If $m < 1$ the layer would be unstable and sooner or later the sediment would rise toward the sea surface.On the other hand the sound speed ratio defined by

$$\nu = \frac{c_s}{c_w}, \tag{G.8}$$

does not have this restriction. Figure G.2 shows a plane wave with an angle of incidence θ_w onto a perfectly smooth interface. During the time, Δt, the wavefront moves the distance l_w with speed c_w, i.e.,

$$\Delta t = \frac{l_w}{c_w}. \tag{G.9}$$

Meanwhile, within the same time frame, Δt, the wavefront has moved the distance l_{wy} along the y-axis and l_{wx} along the x-axis, and hence, the apparent velocities, c_{wy} and c_{wx} are give by

$$c_{wy} = \frac{l_{wy}}{\Delta t} = \frac{l_{wy}}{l_w} c_w = \frac{c_w}{\cos(\theta_w)}, \tag{G.10}$$

$$c_{wx} = \frac{l_{wx}}{\Delta t} = \frac{l_{wx}}{l_w} c_w = \frac{c_w}{\cos(\pi/2 - \theta_w)} = \frac{c_w}{\sin(\theta_w)}. \tag{G.11}$$

Similarly, the apparent velocities in the sediment, c_{sy} and c_{sx} are

$$c_{sy} = \frac{c_s}{\cos(\theta_s)}, \tag{G.12}$$

$$c_{sx} = \frac{c_s}{\sin(\theta_s)}. \tag{G.13}$$

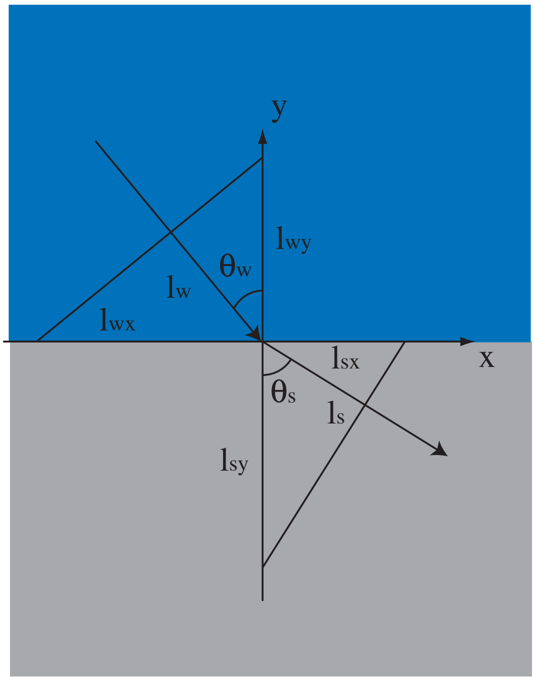

Figure G.2: Incoming plane wave in water with sound speed c_w is transmitted and refracted into the sediment with sound speed c_s.

The trace-velocity matching principle, see Ref. [7](pp.), states that the trace velocity, or the apparent velocity, c_{wx}, in the x-direction in the water equals the trace velocity in the sediment, c_{sx}; that leads to Snell's law

$$\frac{c_w}{\sin\theta_w} = \frac{c_s}{\sin\theta_s}. \tag{G.14}$$

Hence, the the angle of refraction, θ_s, is a function of the sound speed ratio and the angle of incidence, i.e.,

$$\theta_s = \arcsin\left(\frac{c_s}{c_w}\sin\theta_w\right). \tag{G.15}$$

When the expression inside the parenthesis on the right side of (G.15) equals 1 the refracted wave will propagate along the x-axis because $\theta_s = \pi/2$; in this situation the angle of the incident field θ_w corresponds to the critical angle given by

$$\theta_w^{(c)} = \arcsin\left(\frac{c_w}{c_s}\right) \tag{G.16}$$

In Table G.1 the critical grazing angles, i.e., $\gamma_c = 90° - \theta_c$, are listed for different sediment types. Note, if the sound speed ratio is less than 1, i.e., the sound speed in the water is greater than in the sediment the penetrated field is refracted

Table G.1: Density and sound speed for different sea-bed sediments

Sediment type	Density (kg/m^3)	Sound speed (m/s)	Specific imped. (Pa s/m) $\cdot 10^6$	Density ratio	Sound speed	Critical grazing angle
	ρ	c	$\rho \cdot c$	m	ν	γ_c
Kinsler [6]:						
Sea-water(13^{o}C)	1026	1500	1.48	1	1	-
Red clay	1340	1460	1.96	1.31	0.97	-
Calcareous ooze	1570	1470	2.31	1.53	0.98	-
Coarse silt	1790	1540	2.76	1.74	1.02	13^o
Coarse sand	2070	1730	3.58	2.01	1.15	29^o
Jackson [52] (Tab. I, pp. 171):						
Eckernförde, Mud	-	-	-	1.18	0.991	-
Panama City, Sand	-	-	-	1.97	1.126	28^o

downwards, and there exists no critical grazing angle. Assume the sound speed ratio is greater than one, i.e., $\nu > 1$; assume also that the angle of the incident field exceeds that of the critical angle, θ_c. In this case the refracted angle, θ_s, becomes complex and the wave number in the y-direction is

$$\begin{aligned} k_{sy}^2 &= k_s^2 - k_{sx}^2 \\ &= \left(\frac{\omega}{c_s}\right)^2 - \left(\frac{\omega \sin\theta_s}{c_s}\right)^2 \\ &= k_s^2 \left[\, 1 - \nu^2 \sin^2\theta_w \,\right] \end{aligned} \tag{G.17}$$

The transmitted - or refracted - plane wave in the sediment can be expressed

$$p_t(x_s, y_s) = e^{i[\, k_{sx}x_s + k_{sy}y_s \,]} \tag{G.18}$$

Hence, for incidence angles greater than the critical angle the pressure is written

$$p_t(x_s, y_s) = e^{i\, k_{sx}x_s} \; e^{k_s \sqrt{\nu^2 \sin^2\theta_w - 1}\; y_s}, \tag{G.19}$$

The evanescent wave in the sediment decays exponentially with depth[1]; the rate of decay depends on the sound speed ratio and angle of incidence. An evanescent

---

[1] The $e^{k_s y_s \sqrt{\nu^2 \sin^2\theta_w - 1}}$ term decays for $y_s \to -\infty$, see Fig. G.2 for the orientation of the coordinate system.

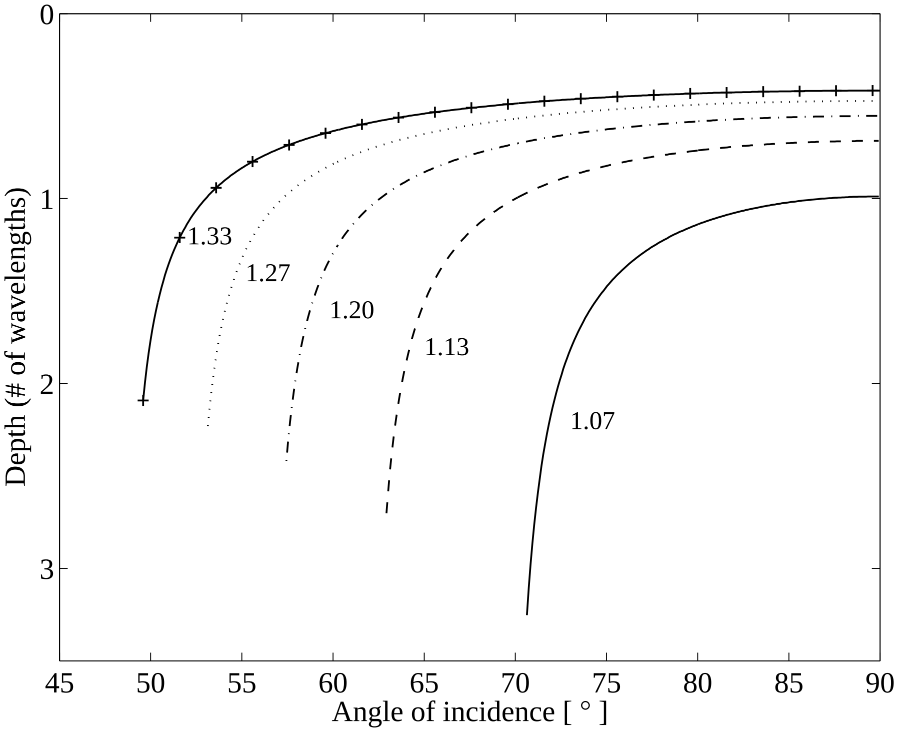

Figure G.3: Subcritical penetration depths for different values of ν.

wave propagates parallel to the interface, or along the x-axis, with a speed that corresponds to the sediment sound speed. Figure (G.3) shows the the sub-critical penetration depth, defined here as the depth where the evanescent wave has decayed 20 dB, as a function of the angle of incidence; the figure shows the relationship for 5 different sound speed ratios. Note, the sub-critical penetration depth is normalized with respect to the acoustic wavelength in the sediment. Thus, sub-critical penetration takes place at large angles of incidence, or small grazing angles, and the waves penetrate a couple of wavelengths into the sediment. Although the evanescent waves decays rapidly they can, at least for at the low frequencies, ensonify buried mines near the water and generate a backscattered wave.

G.2 Depth varying density

Consider a case of plane wave with normal incidence onto a perfectly smooth interface between the water and sediment, and, let the compressional sound speed velocity in the sediment be equal to that of the water, i.e., $c_2 = c_1$. The only variation in the sediment is the depth varying density. In the following the acoustic reflection as a function of frequency is invested; instead of addressing

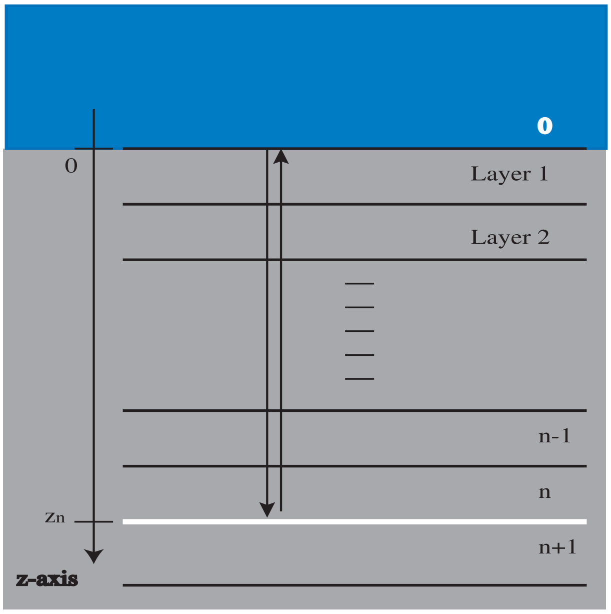

Figure G.4: Depth varying density modeled as a high number of constant density layers.

the fundamental continuity and force equilibrium equations the field is described by dividing the unconsolidated sediment into numerous constant density layers, see Fig. (G.4). Between the n'th and $n+1$'th layer the reflection coefficient is

$$R_{n,n+1} \equiv \frac{p_r}{p_i} = \frac{\rho_{n+1} - \rho_n}{\rho_{n+1} + \rho_n}. \tag{G.20}$$

The equality of the normal components of particle velocities at the interface leads to

$$\frac{p_i - p_r}{\rho_n} = \frac{p_t}{\rho_{n+1}}, \tag{G.21}$$

and a combination of Eq. (G.20) and Eq. (G.21) yields

$$p_t = \frac{\rho_{n+1}}{\rho_n} p_i \left(1 - R_{n,n+1}\right), \tag{G.22}$$

and the transmission coefficients becomes

$$T_{n,n+1} \equiv \frac{p_t}{p_i} = \frac{\rho_{n+1}}{\rho_n} \left(1 - R_{n,n+1}\right). \tag{G.23}$$

The layers are thin in order to maintain a low impedance contrast between each of them; thus, the transmission coefficients approach 1 and the reflection coefficients approach 0. With this approximate approach the contribution from the n'th hypothetical interface is modeled by a single reflection at the interface between the n'th and $n+1$'th layer; and, the total transmission loss is found as the product of all the transmission coefficients on the path down to the interface, i.e., $T_{01}T_{12}T_{13}$ .. $T_{n-1,n}$ and back again, i.e., $T_{n,n-1}$ .. $T_{32}T_{21}T_{10}$. Hence, the total, single harmonic, field reflected from the sediment is

$$p_r^{(sed)} = p_i \sum_{n=1}^{N} (T_{01}T_{12}T_{13} \;..\; T_{n-1,n})\, R_{n,n+1}\, (T_{n,n-1} \;..\; T_{32}T_{21}T_{10})\, e^{ik2z(n)}, \quad \text{(G.24)}$$

where $z(n)$ is the depth of the n'th layer, and N is the number of hypothetical layers used in the calculations. The water to interface reflected pressure,

$$R_{int} = \frac{p_r^{(int)}}{p_i}, \quad \text{(G.25)}$$

is compared to the sediment reflected pressure,

$$R_{sed} = \frac{p_r^{(sed)}}{p_i}. \quad \text{(G.26)}$$

Figure G.5a shows the density along the x-axis and the depth plotted along the negative y-axis; the relationship corresponds to the average density depth profile obtained at the SAX99, where fine scale measurements of volume heterogeneities in sand were carried out, see Ref. [16]. For depths over 1 cm the sediment is considered as consolidated, that is, the density only increases slightly with depth.

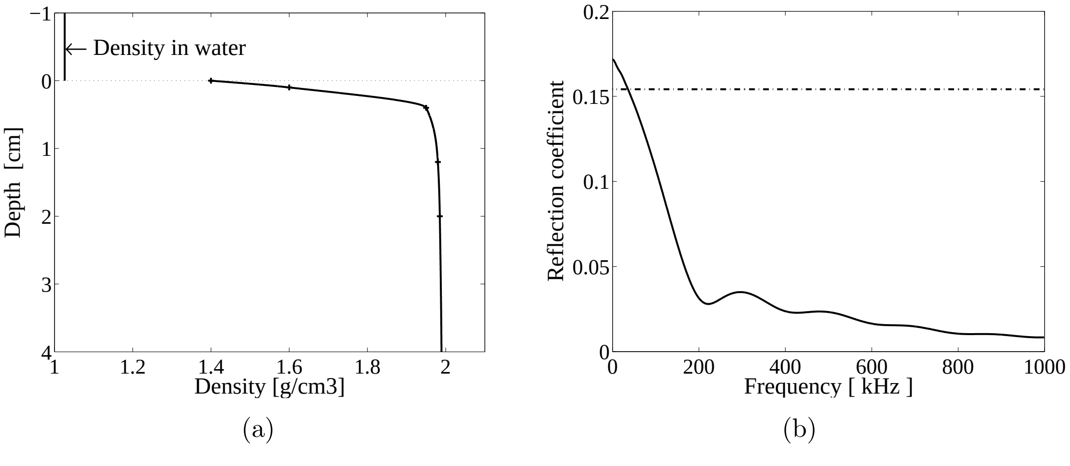

(a) (b)

Figure G.5: (a) Mean density as a function of sediment depth, and (b) the corresponding normal incidence reflection coefficient for the smooth interface, R_{int} (the dash-dot line), and the reflection coefficient for the sediment, R_{sed} (the solid line).

In Fig. G.5b R_{int} and R_{sed} are plotted as a function of frequency; R_{int} is constant, but R_{sed} decays significantly with frequency. For long wavelength signals all reflections and refractions take place within a wavelength until a depth of approximately 1 cm, where the layers reach a constant density and the reflections vanish; hence, in the unconsolidated layer all reflections are added together in phase, which leads to a sediment reflected signal that is comparable with the reflection at the interface. For small wavelength signals the reflections cancel out. Since the transition layer between the unconsolidated and consolidated layer is longer than a wavelength the wave field does not experience an abrupt change in acoustic impedance and most of the field it refracted into the sediment. A similar result has been presented in Ref. [19].

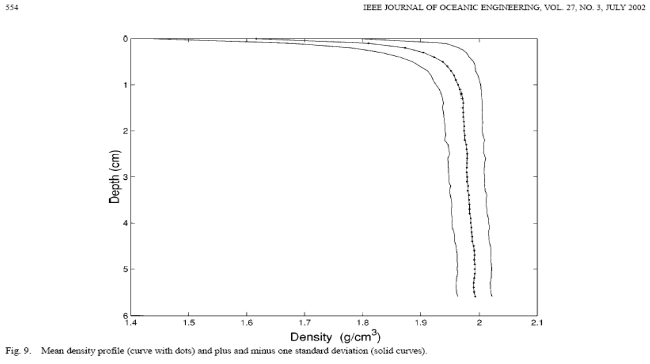
554 IEEE JOURNAL OF OCEANIC ENGINEERING, VOL. 27, NO. 3, JULY 2002

Fig. 9. Mean density profile (curve with dots) and plus and minus one standard deviation (solid curves).

(a)

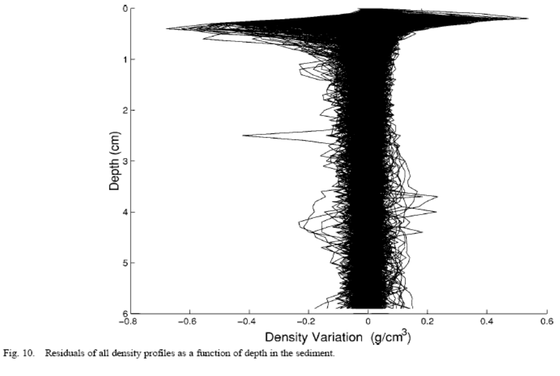

Fig. 10. Residuals of all density profiles as a function of depth in the sediment.

(b)

Figure G.6: Mean density profile (a) and average density variability (b) from a sandy sediment within the first couple of centimetres of the sediment (copied from Ref. [16], © 2002 IEEE)

Figure (G.6a) shows the original average profile which has been copied from Ref. [16] and used in the simulations. The mean density (top) increases rapidly with depth within the first centimetre, that is, from 1.4 to 1.9 g/cm^3. At the depths ranging from 2 cm to 5 cm the density is nearly constant; it only exhibits a slightly increase of approximately 0.1 g/cm^3. The average variability in Fig. (G.6b) is also a copy from Ref. [16]; the average variability is approximately 0.5 g/cm^3 within the first centimetre and it reduces to 0.1 g/cm^3 at the depths from 2 cm to 6 cm. The significant variability within the first 5 millimetres is believed to enhance the backscattering strengths for very high frequency signals and Fig. (G.6b) forms the basis for the equivalent roughness approximation applied for computation of the backscattered field.

G.3 Classical rough surface scattering models

This section treats presents in brief terms the classical rough surface scattering models which are the Kirchhoff approximation and the small roughness perturbation approximation. The small slope approximation is a new model whose range of validity extends further than the classical models presented here, see, e.g., Refs. [67](pp. 221-226.), [68] and [69]. For a list of other rough surface scattering models, see, e.g., the introduction in Ref. [68].

The Kirchhoff approximation is also denoted the physical optics solution, or the tangent plane approximation, see, e.g., Refs. [13] [67] and [9]. The Kirchhoff approximation relates the scattered field to incoming field by

$$p_{sc} \;=\; \mathcal{R}\, p_{inc}, \tag{G.27}$$

where $\mathcal{R}$ is the plane wave reflection coefficient for an infinite smooth interface; hence, locally the scattered field is related to the incoming field by assuming that the surface is infinite, smooth and plane, see Fig. (G.7). The total field on the surface is approximated by

$$p \;=\; (\,1+\mathcal{R}\,)\, p_{inc}. \tag{G.28}$$

The particle velocity of the incoming field normal to the surface points into the surface and the particle velocity of the scattered field points points out of the surface; hence

$$\begin{aligned} \nabla p \cdot \hat{\mathbf{n}}_s \;&=\; (\,1-\mathcal{R}\,)\, \nabla p_{inc} \cdot \hat{\mathbf{n}}_s, \\ &=\; (\,1-\mathcal{R}\,)\, p_n^{(inc)}. \end{aligned} \tag{G.29}$$

The Kirchhoff approximation is valid for surfaces where the local radius of curvature, r_c, is larger than three times the acoustic wavelength, i.e.,

$$r_c \geq 3\lambda, \tag{G.30}$$

see, e.g., [13] (pp. 104). For rough surfaces where the condition in Eq. (G.30) does not hold the Kirchhoff approximation is valid at normal and near normal

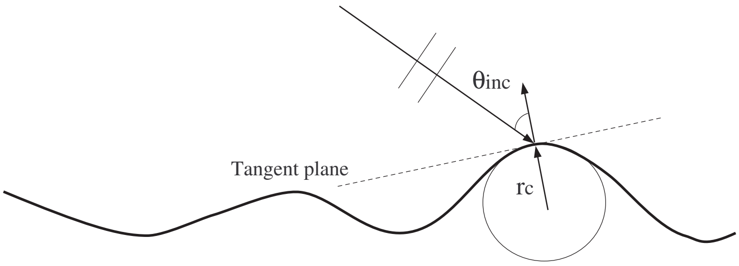

Figure G.7: In the Kirchhoff approximation each point on a rough surface is treated as if is was a part of infinite smooth plane

incidence; the exception is a Gaussian surface with a correlation length of 0.9λ and a RMS height $\sigma = 0.212\lambda$, where Thorsos [58] has shown that the range of validity extends to nearly all angles. The great advantage of the approximation is that it reduces the integral equation into an integral:

$$\begin{aligned} p(\mathbf{r_s}) &= p_{inc}(\mathbf{r}'_\mathbf{s}) + \int_S \Big[p(\mathbf{r}_s)\nabla G(\mathbf{r}'_\mathbf{s}|\mathbf{r}_s) - G(\mathbf{r}'_\mathbf{s}|\mathbf{r}_s)\nabla p(\mathbf{r}_s) \Big] \cdot \hat{\mathbf{n}}_s \, dS \\ &= p_{inc}(\mathbf{r}') \\ &\quad + \int_S \Big[(\,1 + \mathcal{R}\,) p_{inc}(\mathbf{r}_s) G_n(\mathbf{r}'_\mathbf{s}|\mathbf{r}_s) - (\,1 - \mathcal{R}\,)\, G(\mathbf{r}'_\mathbf{s}|\mathbf{r}_s) p_n^{(inc)}(\mathbf{r}_s) \Big] \, dS, \end{aligned} \tag{G.31}$$

where $G_n = \nabla G \cdot \hat{\mathbf{n}}_s$ and $p_n = \nabla p \cdot \hat{\mathbf{n}}_s$.
The small perturbation approximation, see, e.g., [13] and [67], is applied on nearly smooth (compared to the acoustic wavelength) surfaces; in other words the height variations multiplied by the acoustic wavelength must be smal and gradient of the height variations must be small. Expressed formally one have

$$\begin{aligned} k|h(x,y)| &<< 1, \\ |\nabla h(x,y)| &<< 1. \end{aligned} \tag{G.32}$$

The first restriction arises from the assumption that the acoustic pressure is a function of the roughness height function $h(x,y)$ and that it may be expanded as a Taylor series around about the value on the mean scattering surface, that is,

$$p(x,y,h) = p(x,y,0) + h\frac{\partial p(x,y,0)}{\partial z} + \frac{h^2}{2}\frac{\partial^2 p(x,y,0)}{\partial z^2} + ... \tag{G.33}$$

The simplest mean scattering surface is a plane, but other geometries are also possible. The field value on the rough surface is known but the Taylor series expansion is made in order to establish an equation that relates the field values on the mean plane to those on the surface. The total field on the smooth plane is the sum of the incoming field and the scattered field, i.e.,

$$p(x, y, z) = p_{inc}(x, y, z) + p_{sc}(x, y, z). \tag{G.34}$$

The scattered field is expressed as a power series expansion up to order n

$$p^{\,sc} = p_0^{\,sc} + p_1^{\,sc} + p_2^{\,sc} + p_3^{\,sc} + \ldots.. + p_n^{\,sc}, \tag{G.35}$$

where $p_n^{\,sc} = O(h^n)$. For expansions up to the first and second order, see, e.g., Refs. [13] and [67]. Unlike the Kirchhoff approximation the small perturbation approximation contributes significantly to the scattered field at non-specular directions. The small perturbation approximation can also be applied to model volume scattering, see, e.g. Sec. (G.4) below.
For corrections to the Kirchhoff approximation, see, e.g. Refs. [70] and [71]. For the composite roughness approximation where the Kirchhoff approximation is combined with the small perturbation approximation for a surface with two scales functions, see, e.g., Refs. [13] (Sec. 7.1), [67] (Sec. 9.11) and [72].

G.4 Jackson's model

This section presents briefly Jackson's model for seabed backscattering in the frequency range from 10 to 100 kHz. The model is estimates the expected, or average, acoustic power backscattered from different sediment types ranging from sand through clays. The model is probably the most famous and most frequently applied when it comes to the issue of high frequency seabed scattering. Jackson's model is not directly applicable for the sonar model under development here mainly because it does not include the phase, but additionally, it also fails above 100 kHz. However, Jackson's model cannot be neglected because the essential physical mechanisms that are important for the understanding of acoustic seabed scattering are included here. In this work results from the bottom backscattering model presented by Mourad and Jackson [19] are reconstructed, and contributions from the separate scattering sources, such as the rough seabed interface and inhomogeneous sediment are presented separately. For the bottom backscattering model see, e.g., Ref. [73]; for a later version that includes bistatic scattering, see, e.g., Ref. [52]. However, no detailed descriptions of the model will be given here.

Jackson's model is based on the fluid-fluid assumption, and thus, it neglects elasticity and porosity. There are no gradients in the sediment properties except for random fluctuations in the sediment volume such as the mass density the sound speed, and the acoustic absorption. These properties are all considered statistically stationary. The seabed relief is an isotropic, two-dimensional Gaussian random process completely determined by a spectral density that follows a simple power law in the wave number. The composite roughness model is applied; it uses the Kirchhoff approximation near specular normal incidence and the small roughness perturbation approximation in the other directions. The sediment volume scattering is described as a surface process and it is quantified by an interface scattering cross section; a small perturbation model of the mass density, sound speed and the acoustic absorption is applied.

The model requires 6 parameters: The sediment/water density ratio, m; the sediment/water sound speed ratio, ν; the loss tangent, δ, which is the ratio of imaginary wavenumber to real wavenumber in the sediment; the volume parameter, σ_2, which is the ratio of sediment volume scattering cross section to sediment attenuation coefficient; the spectral exponent, γ, which is the exponent of bottom roughness spectrum; and the spectral strength, w_2, which is the strength of the roughness spectrum. The density and sound speed ratios have already been defined in Eqs. (G.7) and (G.8) respectively. The loss parameter is expressed by

$$\delta = \frac{k_{2i}}{k_{2r}} = \frac{\alpha\,\nu c_1 \ln(10)}{40\pi f}, \tag{G.36}$$

where c_1 is the speed of sound in water, α is the attenuation coefficient usually measured in dB/m, and finally, f is the acoustic frequency. In Ref. [19] the volume scattering parameter, σ_2, is

$$\begin{aligned} \sigma_2 &= 0.002 \text{ for } 1 \leq M_z \leq 5, & \text{(G.37)} \\ \sigma_2 &= 0.001 \text{ for } 5 \leq M_z \leq 9, & \text{(G.38)} \end{aligned}$$

where M_z is the logarithmic grain size. The spectral exponent and spectral strength are associated to the interface roughness power spectrum as

$$w_2 K^{-\gamma}, \tag{G.39}$$

where K is the magnitude of the roughness wavenumber.

The total dimensionless backscattering cross section per unit solid angle per unit area is given by

$$\sigma = \sigma_r(\theta) + \sigma_v(\theta), \tag{G.40}$$

where θ is the grazing angle, σ_r represents the roughness cross section, and σ_v represents the volume cross section. The composite roughness approximation defines $\sigma_r(\theta)$ as

$$\sigma_r(\theta) = f(x)\sigma_{kr}(\theta) + [\,1 - f(x)\,]\,\sigma_{cr}(\theta), \tag{G.41}$$

where $\sigma_{kr}(\theta)$ is the Kirchhoff approximation cross section, $\sigma_{cr}(\theta)$ is the composite roughness cross section, and $f(x)$ is the interpolating function, where x is a variable that depends on θ; the interpolation function shifts between the Kirchhoff approximation grazing angles near 90° to the composite roughness approximation at smaller angles. In the composite roughness approximation the small-roughness perturbation is used with corrections of shadowing and large-scale bottom slope; the composite roughness cross section is given by

$$\sigma_{cr} = S(\theta, s)\, F(\theta, \sigma_{pr}, s), \tag{G.42}$$

where S is the shadowing correction that depends on the grazing angle θ, and the large scale bottom slope s; F depends on θ, s, and the small roughness perturbation cross section σ_r, see Ref. [19].
Figures (G.8), (G.9), (G.10), and (G.11) are the results from four different sites with different acoustic frequencies. Here the model outputs will not be compared with real data since it has already been done by the authors in Ref. [19]. The composite roughness cross section σ_{cr} is especially important at the low grazing angles where the Kirchhoff approximation fails in all cases, but for higher values of the grazing angle the composite roughness scattering cross section σ_{cr} may also differ significantly from σ_{kr}, see, Fig. (G.11a); on the other hand σ_{cr} overestimates the field near 90° grazing angle, see Fig. (G.8a),(G.10a), and (G.11a). Finally, volume backscattering σ_v may contribute significantly to the total field for grazing angles below 80°, see Fig. (G.9d) and (G.10d).

In this chapter the fundamental mechanisms concerning plane wave reflection and transmission at a smooth interface between two homogeneous fluids have been addressed, and a brief presentation of sub-critical sediment penetration has been made. A simple computational example with a sediment that has a depth varying density has shown, that the normal incidence reflection coefficient strongly depends on the frequency and the shape of the density profile. The issue of scattering from rough surfaces is considered, and the most important models for rough surface scattering are presented. A separate section has been devoted to Jackson's model for high frequency backscattering, where some of the results from Ref. [19] are reconstructed (see the next 4 pages).

Quinault, 35 KhZ

Density ratio:	$m = 1.93$
Volume parameter:	$\sigma_2 = 0.001$
Spectral strength:	$w_2 = 0.004225$
Loss tangent:	$\delta = 0.02601$
Velocity ratio:	$\nu = 1.08$
Spectral exponent:	$\gamma = 3.67$

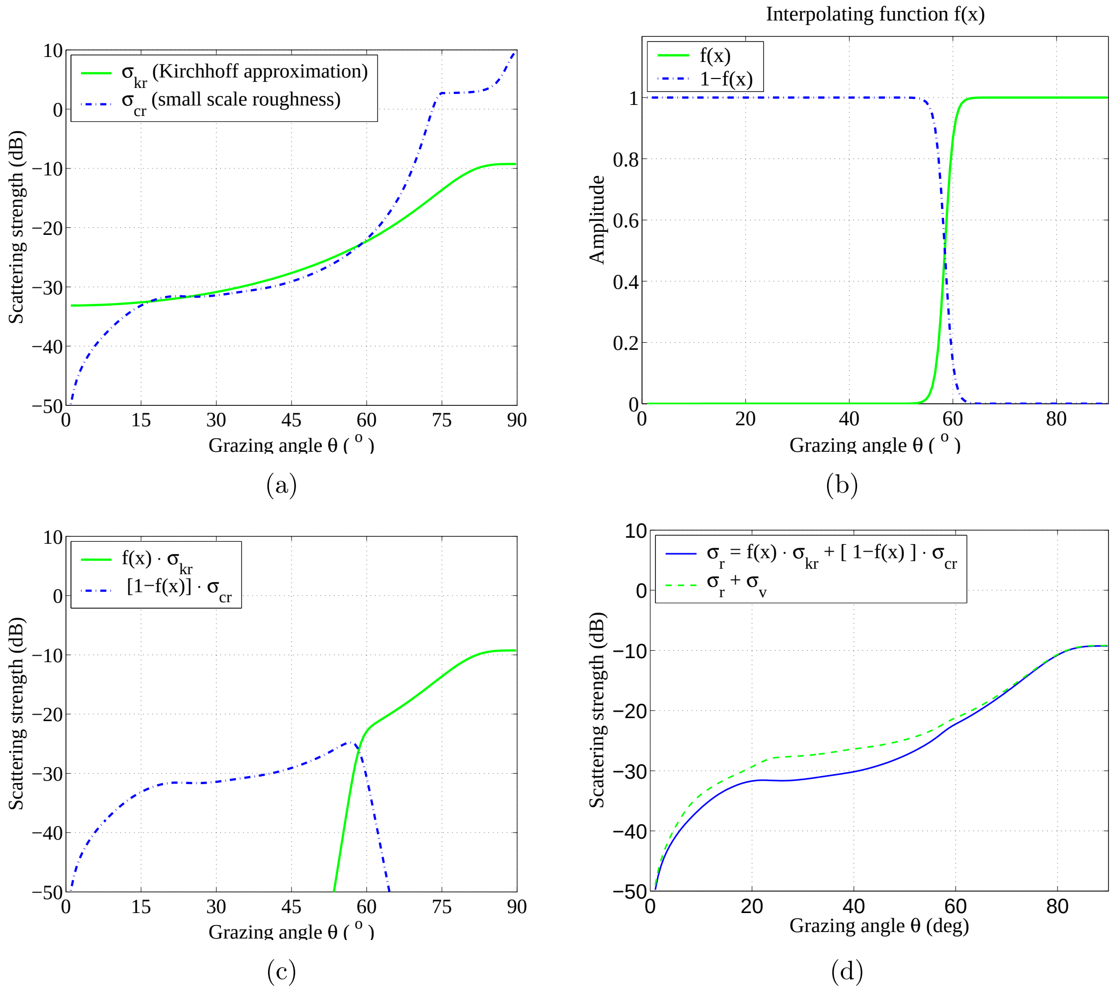

(a) (b) (c) (d)

Figure G.8: Example 1.

Puget Sound, 1.25 kHz

Density ratio:	m = 1.74
Volume parameter:	σ_2 = 0.002
Spectral strength:	w_2 = 0.0046
Loss tangent:	δ = 0.01007
Velocity ratio:	ν = 1.006
Spectral exponent:	γ = 3.5

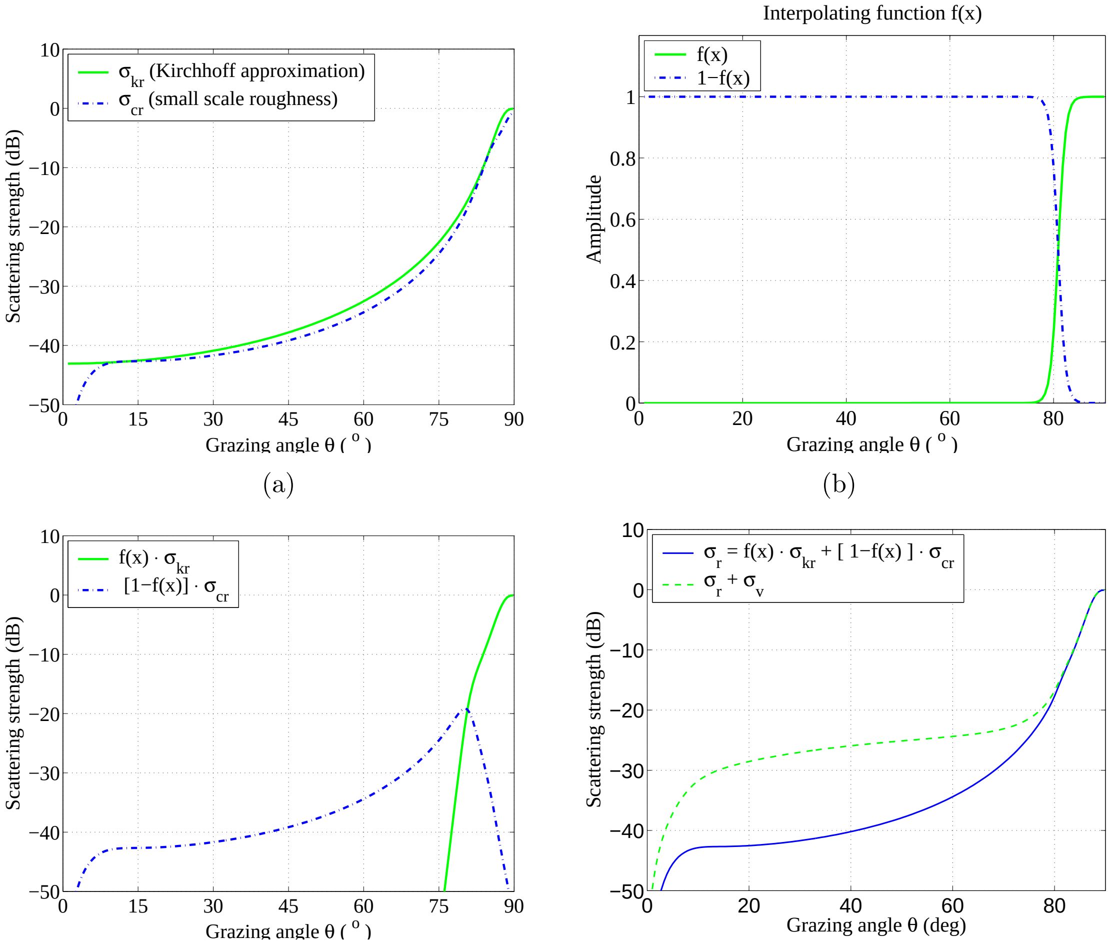

(a) (b)

(c) (d)

Figure G.9: Example 2.

Arafura Sea, 20 kHz

Density ratio:	$m = 1.49$
Volume parameter:	$\sigma_2 = 0.005$
Spectral strength:	$w_2 = 0.002166$
Loss tangent:	$\delta = 0.01007$
Velocity ratio:	$\nu = 0.989$
Spectral exponent:	$\gamma = 3.18$

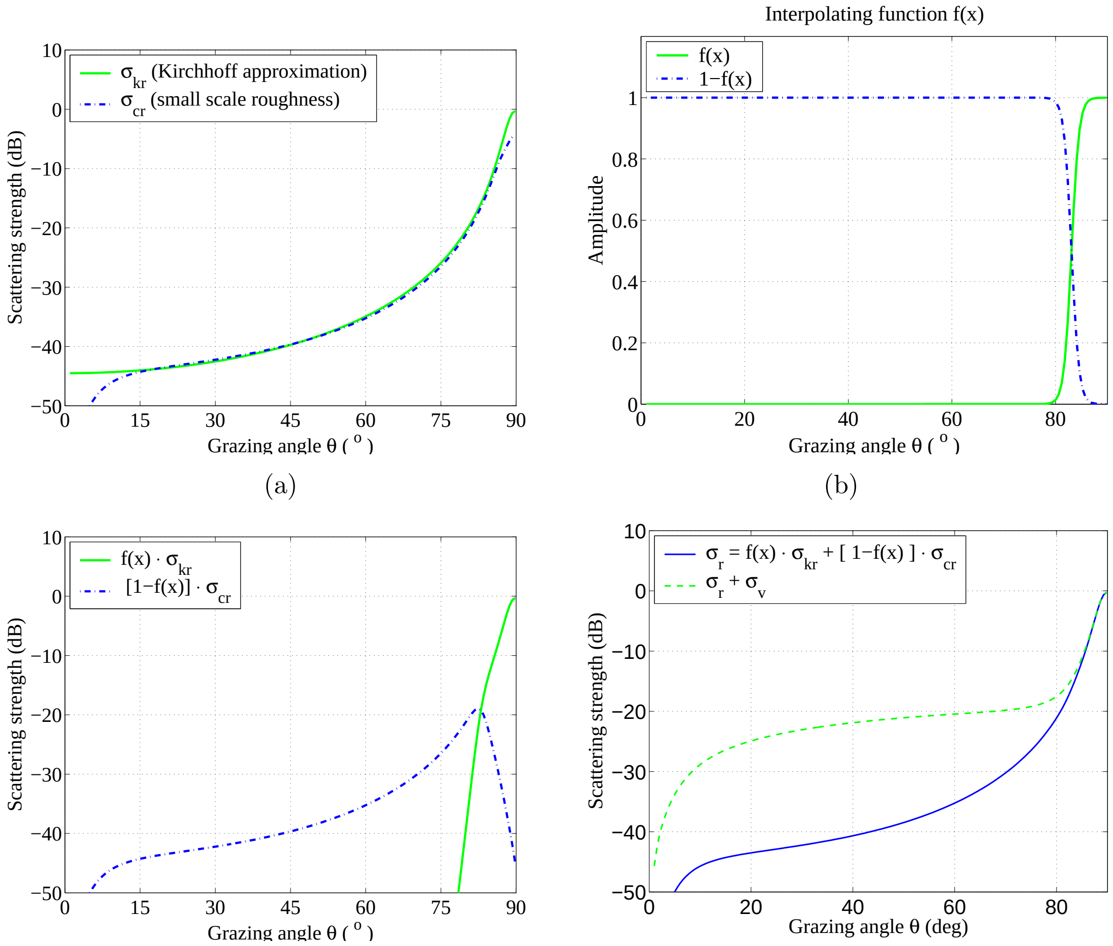

(a) (b)

(c) (d)

Figure G.10: Example 3.

Stanic, et al. 1988, 40 kHz

Density ratio: $m = 1.966$
Volume parameter: $\sigma_2 = 0.004$
Spectral strength: $w_2 = 0.006163$
Loss tangent: $\delta = 0.01856$
Velocity ratio: $\nu = 1.133$
Spectral exponent: $\gamma = 2.92$

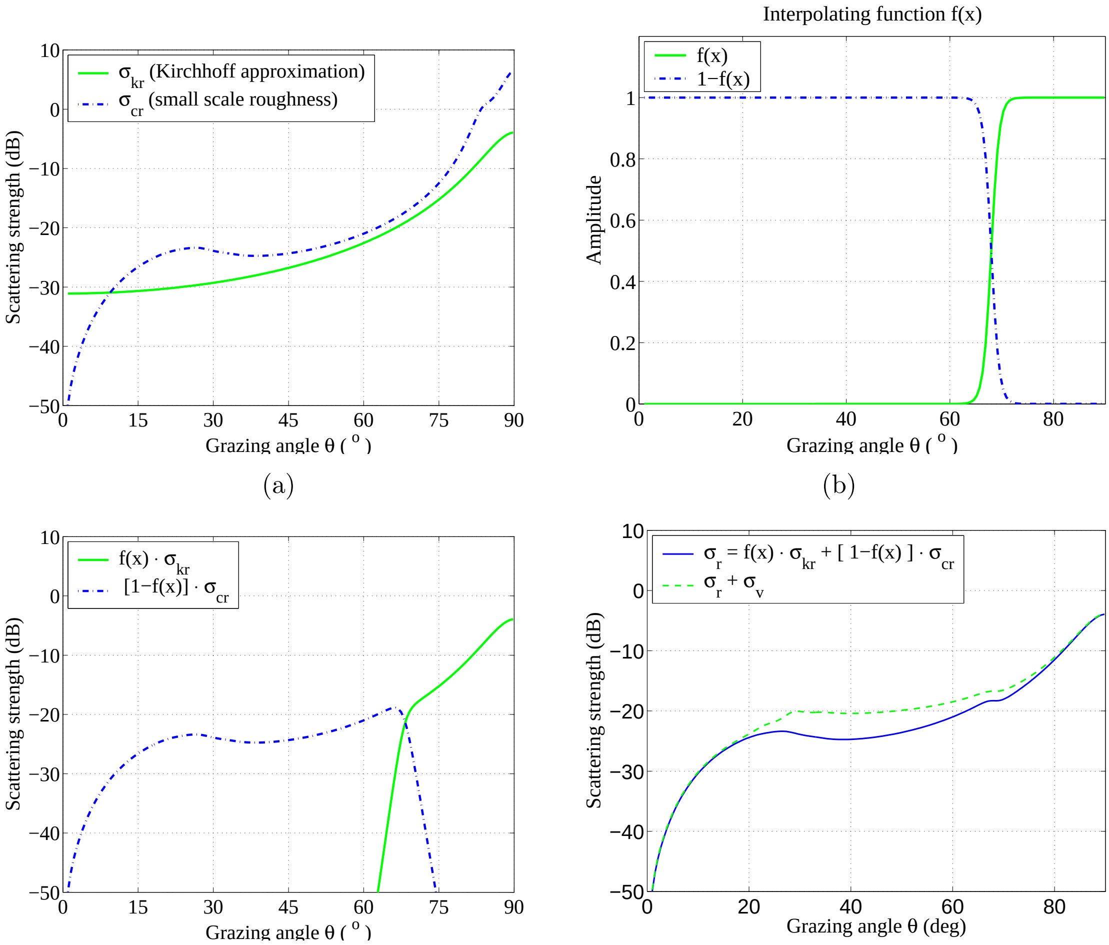

(a) (b)

(c) (d)

Figure G.11: Example 4.

Appendix H

Benchmark solutions to scattering from a sphere

This chapter is a supplement to Ref. [3](Thesis paper) and it concerns the benchmark solution required for verification of the numerical Kirchhoff model, where the harmonic series solution to the problem of high frequency scattering from a rigid sphere from an incident plane wave has been applied. The verification has been carried out in the time domain by application of a Ricker pulse, which is the second order derivative of a Gaussian pulse. Thus, this chapter concerns the generation of the Ricker-pulse response from the smooth rigid sphere by application of Fourier synthesis.
Additionally, the analytical Kirchhoff solution for a rigid sphere is derived and it is based on Ref. [74]. The analytical Kirchhoff solution is compared with the harmonic series solution solution, and the difference is analyzed. The limit of the Kirchhoff approximation is analyzed for the rigid sphere, where the Kirchhoff approximation is compared with the harmonic series solution solution for decreasing radii slightly above and below the acoustic wavelength. The analysis leads to the conclusion that the Kirchhoff approximation is applicable on edges with a radius of curvature down to 1/4 of the acoustic wavelength.

H.1 Physical problem

In this section a presentation of the physical problem is given. Figure (H.1) illustrate a perfectly plane wave incident onto a rigid sphere of radius a. A perfectly plane wave is an abstraction. Nevertheless, the abstraction is approximately valid if the ratio of the cross sectional area, A, to the applied wavelength, λ, is less than the distance R between the source and the object

$$\frac{A}{\lambda} < R. \tag{H.1}$$

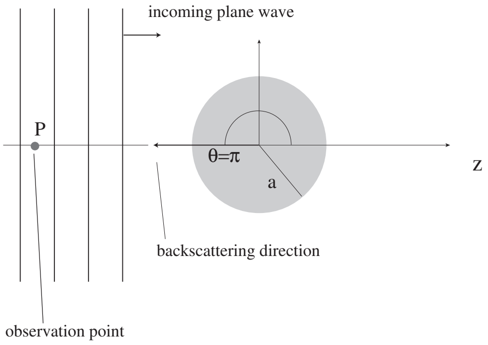

Figure H.1: Incident plane wave field onto a rigid sphere with radius a. The observation point P is in the negative z–direction, i.e. the backscattering direction.

In other words, the abstraction is valid when the part of the emitted wavefront that interacts with the sphere can be considered plane. The scattered field is measured along the negative z-axis, i.e., the field is measured in the direction back towards the source. The backscattered field may consist of three contributions, see, e.g., Ref.[9](Fig. 7.3.3), that is, the reflected wave from the front face of the sphere, the back-diffracted wave from the pressure release circumference and finally the wave diffracted around the cylinder and continues to the observation point, the so-called Franz wave, see Fig. (H.2). Since the sphere is assumed rigid reflections from within the sphere will not occur.

H.2 Geometrical considerations

The lengths of the travel-paths for the three arrivals are determined. Consider Figs. (H.3a) and (H.3b); $\mathbf{r}$ is the vector from the centre of the sphere to the observation point P and $\mathbf{r}_t$ is the vector from P to the circumferential edge that separate the visible from the invisible part of the sphere (seen from P); $\mathbf{a}_\gamma$ is the vector from the centre of the sphere to the circumferential edge, and it has the angle γ with respect to the z-axis. These vectors are given by

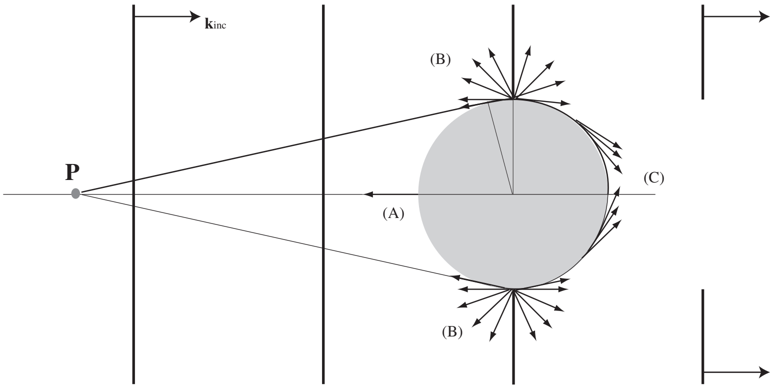

Figure H.2: Reflection and diffraction mechanisms: A) Front- face reflection; B) The back-diffracted pressure is caused by the pressure release point at the sphere's circumference that separates the ensonified field from the shadow zone; C) A diffraction mechanism generates a creeping wave around the sphere which is received at the observation point P.

$$\mathbf{a}_\gamma = \begin{pmatrix} a\cos\gamma \\ a\sin\gamma \end{pmatrix}, \tag{H.2}$$

$$\mathbf{r} = \begin{pmatrix} -R \\ 0 \end{pmatrix}, \tag{H.3}$$

$$\mathbf{r}_t = \begin{pmatrix} a\cos\gamma + R \\ a\sin\gamma \end{pmatrix}, \tag{H.4}$$

where $R = \mathbf{r}$ and $\mathbf{r}_t = \mathbf{a}_\gamma - \mathbf{r}$. The circumference of the sphere seen from the observation point P is the point, where $\mathbf{r}_t$ and $\mathbf{a}_\gamma$ are orthogonal, i.e., $\mathbf{a}_\gamma \cdot \mathbf{r}_t = 0$. Hence, γ is given by the relation

$$\cos\gamma = -\frac{a}{R}. \tag{H.5}$$

The travel times are respectively

$$\tau_A = \frac{R - a}{c}, \tag{H.6}$$

$$\tau_B = \frac{a + a(\gamma - \pi/2) + |\mathbf{r}_t|}{c}, \tag{H.7}$$

$$\tau_C = \frac{a + a\pi + a(\gamma - \pi/2) + |\mathbf{r}_t|}{c}, \tag{H.8}$$

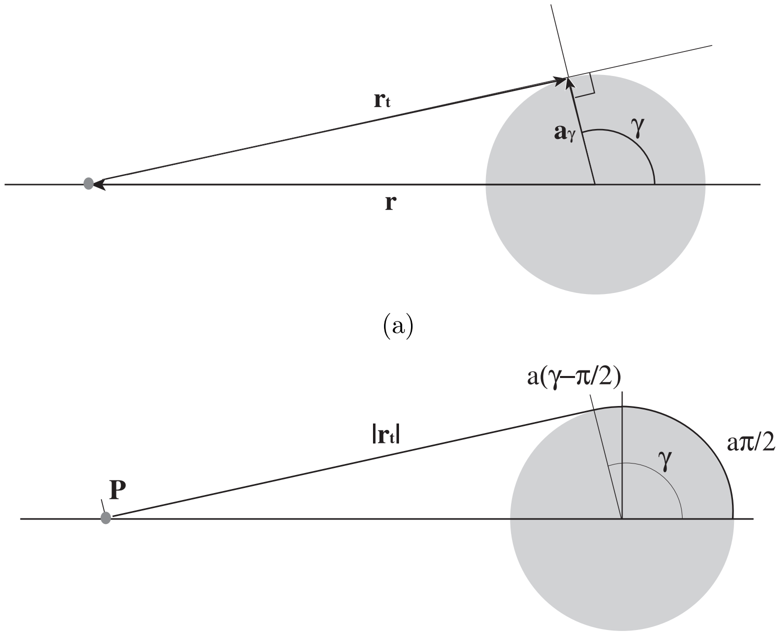

(a)

(b)

Figure H.3: Sketch of vectors and angle for determination of travel times.

where $\tau = 0$ corresponds to the time where the incoming wave is at the front face of the sphere.

H.3 Harmonic series solution

The infinite harmonic series solution is

$$p_s(k) = -P_0 \sum_{n=0}^{\infty} (2n+1)\, i^n \, \frac{j_n'(ka)}{h_n'(ka)}\, h_n(kr)\, P_n(cos(\theta)), \tag{H.9}$$

see, e.g., Ref. [60](Eq. (6.185) on page 228). P_0 is the pressure amplitude of the incoming plane wave. j_n' and h_n' are the derivative of spherical Bessel- and Hankel functions respectively, and of the first kind and of order n; h_n is the spherical Hankel function of the first kind and of order n. P_n is the Legendre polynomial of order n and θ is the scattering angle, see Fig. (H.1). For the backscattering case studied here $\theta = \pi$, and thus, $P_n(-1) = (-1)^n$.

We need to find an acceptable truncation for the infinite sum. For that purpose ka and kr are fixed and each term inside the summation is observed for increasing values of n. In other words we will study the asymptotic behaviour of the function:

$$s(n) = (2n+1)\, i^n \; (-1)^n \, \frac{j_n'(ka)}{h_n'(ka)}\; h_n(kr). \tag{H.10}$$

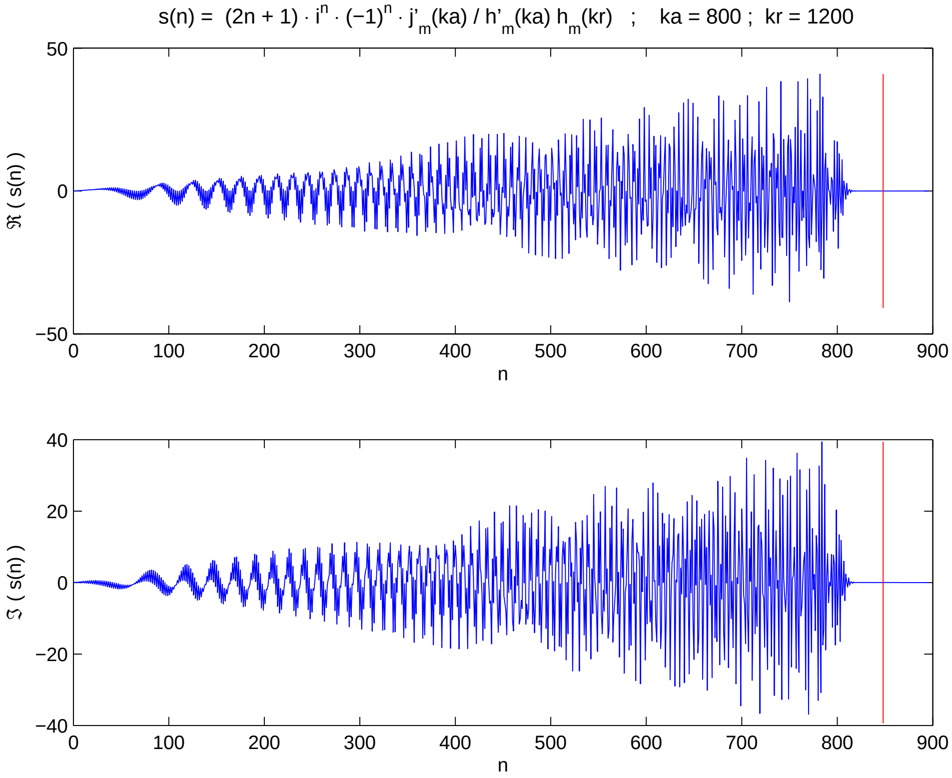

Figure H.4: Real (top) and imaginary (below) part of $s(n)$, see Eq. (H.10), as a function of n.

This work deals with acoustic signals in the lower part of the ultrasonic range (The dominant frequency is 445 kHz). The medium is water and the speed of sound is 1500 m/s, which yields a wavelength of approximately three millimetres. The geometries of interest have characteristic dimensions in the centimetre and meter scale. Hence, $ka \gg 1$ and the behaviour is often described by geometrical optics. However, the backscattered acoustic pressure will here be computed from the harmonic series solution. As a consequence it is necessary to operate with Bessel - and Hankel functions of very high orders. Figure (H.4) shows $s(n)$ for $ka = 800$ and $kr = 1200$; it is observed that $s(n)$ rapidly goes to zero when $n > ka$, and consequently, it has been chosen to truncate the infinite sum at

$$n_{max} = \lceil ka \rceil + 48. \tag{H.11}$$

Thus, the pressure backscattered along $\theta = \pi$ is approximated by

$$p_s(k,r) \approx -\sum_{n=0}^{\lceil ka \rceil + 48} (2n+1)\, i^n\, (-1)^n\, \frac{j_n'(ka)}{h_n'(ka)}\, h_n(kr). \tag{H.12}$$

This expression is used for Fourier synthesis on the emitted pulse. It is interesting to note that (H.12) is valid for all $r \geq a$, and hence, it does also describe the behaviour of the scattered pressure in the near field. Meanwhile, if the near field is approached, i.e., $kr \rightarrow ka$, one must ensure that sum still converges and a new truncation number might be selected. Here, the near field case will not be considered.

H.4 The Ricker test-pulse

The Ricker pulse is the second order time derivative of a Gaussian pulse. It has often been applied in underwater issues related to time domain modeling, see, e.g., Refs. [75] and [76]. Let $A = \pi^2 \nu_M^2$ where ν_M is the dominant frequency which in this case is 445000 kHz. Hence, the Gaussian signal is $f(t)$ and the Ricker pulse is $f''(t)$:

$$\begin{aligned} f(t) &= -\frac{1}{2A} e^{-At^2}, && \text{(H.13)} \\ f'(t) &= t e^{-At^2}, && \text{(H.14)} \\ f''(t) &= \Big(1 - 2At^2\Big) e^{-At^2}, && \text{(H.15)} \\ f'''(t) &= \Big(-6At + 4A^2 t^3\Big) e^{-At^2}. && \text{(H.16)} \end{aligned}$$

Figure (H.5) shows the time integral of the Ricker pulse, the Ricker pulse and the time derivative of the Ricker pulse.

H.5 Fourier synthesis

Fourier synthesis is frequency domain multiplication. Let $X(\omega)$ represent the Fourier transform of the Ricker pulse and $p_{sc}(\omega)$ the transfer function of the sphere. The scattered signal $Y(\omega)$ is obtained by multiplication in the frequency domain

$$Y(\omega) = X(\omega) p_{sc}(\omega). \tag{H.17}$$

The analytical signal $Z_y(\omega)$ instead of $Y(\omega)$ is given by

$$Z_y(\omega) = 2\,U(\omega)\,X(\omega)\,p_{sc}(\omega)\ ,\quad \omega > 0, \tag{H.18}$$

where $U(\omega)$ is the unit step function defined by

$$U(\omega) = \begin{cases} 1, & \omega > 0; \\ \frac{1}{2}, & \omega = 0; \\ 0, & \omega < 0; \end{cases} \tag{H.19}$$

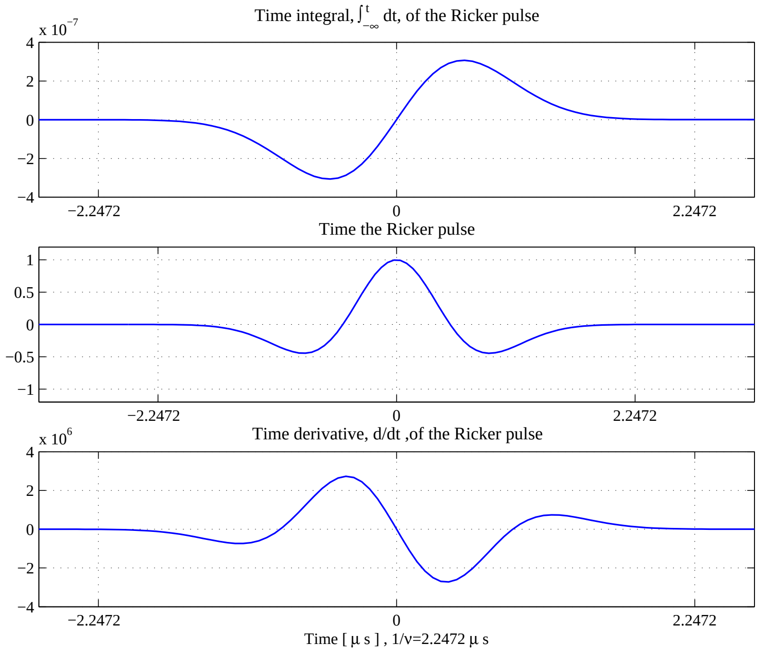

Figure H.5: The Ricker pulse (RP) is the second derivative of a Gaussian pulse. Top: The time integral of RP, mid: RP and the time derivative of RP

see, e.g., Ref. [77](pp. 118-121). The analytical signal, $z(t)$, is the inverse Fourier transform of $Z(\omega)$ and $y(t)$ is the real part of $z(t)$. Figure (H.6) is a plot of the incoming Ricker pulse and its corresponding one-sided spectrum. The spectra in the mid- and lowest plots are identical but the frequency axes are different: The mid-plot use ka with $a = 10$ cm and the spectrum in the lowest plot is plotted against the DFT-bins. Here, the incoming field is a Ricker pulse with a dominant frequency of 445 kHz sampled at 2^{25} Hz; it is padded with zeros in order to leave space for the diffraction contributions. In this case, the Fourier synthesis is only performed on the first 1500 FFT-bins; above this bin-value the spectral content of the pulse is vanishing. If the radius of the sphere is increased, the travel times of the diffracted arrivals will increase, and more zeros are needed in the zero padding; hence, the first FFT-bin number, at which no significant spectral content, will increase. For example if the radius is increased to $a = 0.25$ m the smallest FFT-bin number will be approximately to 3500.

H.6 The impulse response of the sphere. Part I

In order to compare the scattered waveform with the incoming waveform will be scaled with respect to the energy loss. Since intensity is power per unit area, the power intercepted by the sphere from the incoming wave is given as the cross sectional area of the sphere multiplied by the intensity of the incoming wave.

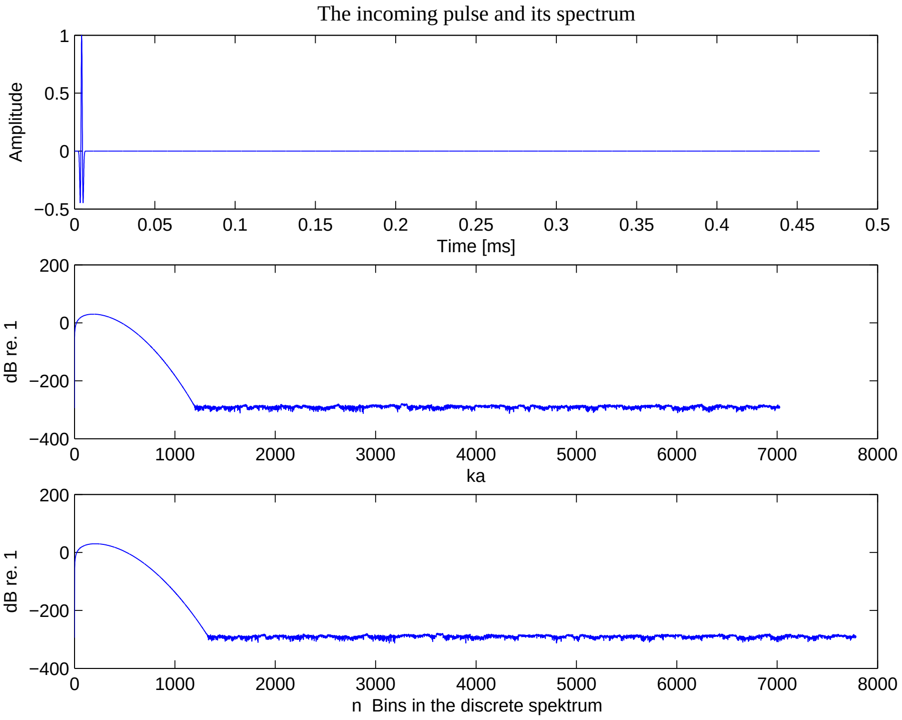

Figure H.6: The incoming pulse (top) and it's spectrum (mid and below)

If one assume that the sphere reflect the power uniformly in all directions, the intensity of the reflected wave at distance R from the sphere is

$$I_r = \frac{\pi a^2 I_{inc}}{4\pi r^2}\,, \tag{H.20}$$

see, e.g., Ref. [14](pp. 293). Let P_0 be the pressure amplitude of the incoming wave at the sphere's front face. The intensity can be expressed as

$$I_{inc} = \frac{P_0^2}{2\rho c}, \tag{H.21}$$

and

$$I_{sc} = \frac{P_{sc}^2}{2\rho c}\Big|_r. \tag{H.22}$$

Insertion of (H.21) and (H.22) into (H.20) and taking the square root yields

$$P_{sc} = \frac{a}{2r}\,P_0. \tag{H.23}$$

Backscattering of a 445000 kHz Ricker pulse from a rigid sphere of radius $a = 0.1$ is considered here. Figure (H.7) shows the scaled front-face reflected pulse together with the incoming pulse and except for a very slight deviation in the

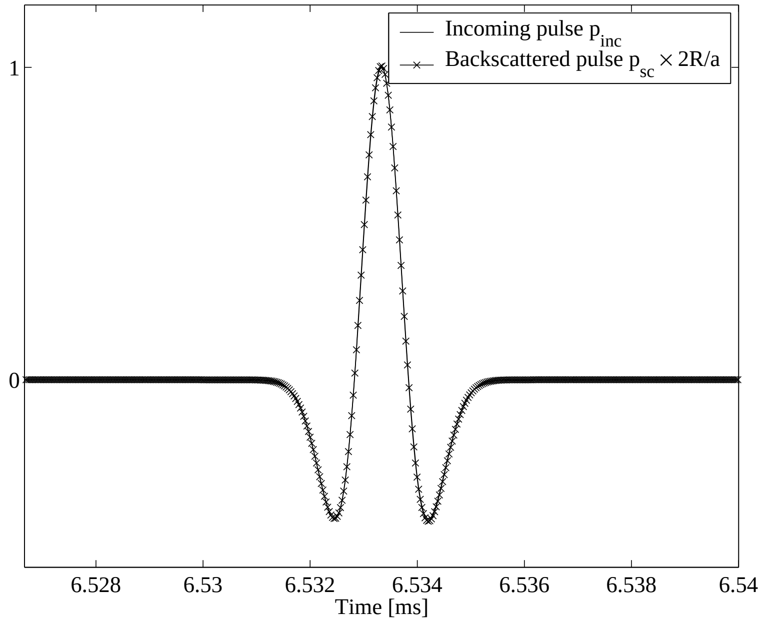

Figure H.7: Incoming and front face reflected pulse (normalized). Radius of the sphere is 10 cm and the observation point is located 10 m from the sphere's centre.

last under-slope they are identical. Thus, the sphere's impulse response is very close to be proportional to Dirac's delta function. However, as it will be shown in the next section, the harmonic series solution contains a very weak component that originates from waves diffracted around the object, the so called Franz-Wave (Ref. [9]).

H.7 The Analytical Kirchhoff model

This section derives the physics optics solution (or the Kirchhoff method) to scattering from a sphere at plane wave incidence. The solution is found by analytic integration over the ensonified part of the sphere; the computation is inspired by Ref. [74], where focus was maintained on partial ensonification of the sphere. Here, it is considered to be fully ensonified. We begin with the KHIE for a rigid body

$$p_{sc}(\mathbf{x}) = \frac{1}{4\pi} \int\!\!\int_S p(\mathbf{x}_s)\, \nabla G(\mathbf{x}_s|\mathbf{x}) \cdot \hat{\mathbf{n}}_s \, dS, \tag{H.24}$$

and apply the Kirchhoff approximation

$$p_{sc} \;=\; \mathcal{R}\, p_{inc}. \tag{H.25}$$

For the rigid sphere the pressure reflection coefficient $\mathcal{R} = 1$; a spherical coordinate system with origin in the center of the sphere is introduced, see Fig. (H.8).

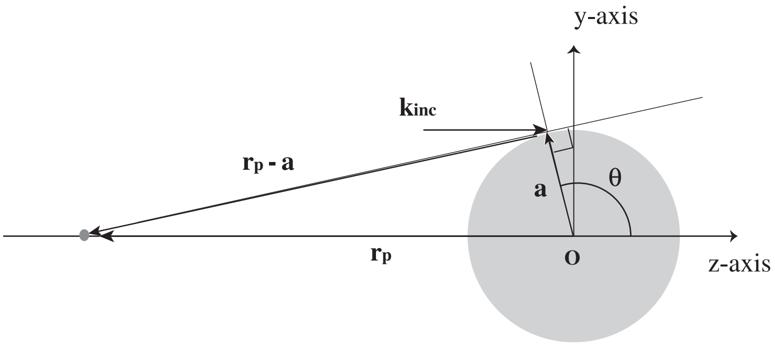

Figure H.8: Geometry applied for the analytical Kirchhoff approximation.

The scattered pressure can be expressed by

$$p_{sc}(\mathbf{r}_p) = \frac{1}{2\pi} \iint_S p_{inc} \, \nabla G(\mathbf{r}_p|\mathbf{a}) \cdot \hat{\mathbf{a}} \, dA, \tag{H.26}$$

where $\mathbf{a}$ is a point on the sphere, $\hat{\mathbf{a}} = \mathbf{a}/|\mathbf{a}|$ is the unit normal vector pointing out of the sphere, and $\mathbf{r}_p$ is an observation point along the negative z-axis. The incoming plane wave is incident from the negative z-axis, and θ is the angle with respect to the z-axis ($0 \leq \theta \leq \pi$) and ϕ is the angle in the xy-plane ($0 \leq \phi \leq 2\pi$). The incoming field is

$$p_{inc}(\mathbf{a}) = p_0 \, e^{i\mathbf{k}_{inc}\cdot\mathbf{a}}, \tag{H.27}$$

where $\mathbf{k}_{inc}$ is the wave-vector of the incoming wave and p_0 is an acoustic reference pressure. We have

$$\mathbf{k}_{inc} = \begin{pmatrix} 0 \\ 0 \\ k \end{pmatrix}, \tag{H.28}$$

$$\mathbf{a} = \begin{pmatrix} a\sin\theta \, \cos\phi \\ a\sin\theta \, \sin\phi \\ a\cos\theta \end{pmatrix},$$

and hence

$$p_{inc}(\mathbf{a}) = p_0 \, e^{ika\cos\theta}. \tag{H.29}$$

The free space Green's function is

$$G(\mathbf{r}_p \, |\mathbf{a}) = \frac{e^{ik|\mathbf{r}_p - \mathbf{a}|}}{|\mathbf{r}_p - \mathbf{a}|}. \tag{H.30}$$

By assuming $(a/r_p)^2 << 1$ the following range approximation is applied

$$|\mathbf{r}_p - \mathbf{a}| \approx r_p + a\cos\theta, \tag{H.31}$$

where the power series expansion to the first order of the square root term has been applied, i.e., $\sqrt{1+x} \approx 1 + 0.5\,x$. The gradient of the free space Green's function approximated to the far field is

$$\nabla G(\mathbf{r}_p|\mathbf{a}) \;=\; \frac{\mathbf{r}_p - \mathbf{a}}{|\mathbf{r}_p - \mathbf{a}|}\,\frac{ik}{r_p}\;e^{ikr_p}\;e^{ika\cos\theta}\;, \tag{H.32}$$

and subsequently, $\nabla G \cdot \hat{\mathbf{a}}$, must be found. Thus,

$$\begin{aligned}(\mathbf{r}_p - \mathbf{a})\cdot\hat{\mathbf{a}} &= \begin{pmatrix} 0 \\ 0 \\ -r_p \end{pmatrix} \cdot \begin{pmatrix} \sin\theta\,\cos\phi \\ \sin\theta\,\sin\phi \\ \cos\theta \end{pmatrix} - a \\ &= -r_p\cos\theta - a\;,\end{aligned} \tag{H.33}$$

and subsequently, the approximation, $|\mathbf{r}_p - \mathbf{a}| \approx r_p$, is applied in order to obtain the following quantity

$$\begin{aligned}\frac{\mathbf{r}_p - \mathbf{a}}{|\mathbf{r}_p - \mathbf{a}|}\;\cdot\hat{\mathbf{a}} &= \frac{-r_p\cos\theta - a}{r_p}\;, \\ &= -\cos\theta - \frac{a}{r_p}\;.\end{aligned} \tag{H.34}$$

Finally, the gradient of Green's function on the surface of the sphere becomes,

$$\nabla G_n(\mathbf{r}_p|\mathbf{a}) \;=\; (-\cos\theta\; - \frac{a}{r_p})\frac{ik}{r_p}\;e^{ikr_p}\;e^{ika\cos\theta}\;. \tag{H.35}$$

Since Eq. (H.35) contains two terms the integral in Eq. (H.26) is divided into two integrals represented by $p_{sc}^{(2)}(\mathbf{r}_p)$ and $p_{sc}^{(2)}(\mathbf{r}_p)$. Integration is carried out in a spherical coordinate system with the incremental area element $dA = a^2\sin\theta\,d\theta\,d\phi$, and hence

$$\begin{aligned}p_{sc}^{(1)}(\mathbf{r}_p) &= -\frac{p_0}{2\pi}\frac{ik}{r_p}\;e^{ikr_p}\iint_S \cos\theta\,e^{i2ka\cos\theta}\;\;a^2\;\sin\theta\,d\theta\,d\phi, \\ &= -\frac{p_0}{2\pi}\frac{ika^2}{r_p}\;e^{ikr_p}\int_{\phi=0}^{2\pi} d\phi\int_{\theta=\pi}^{\pi/2}\cos\theta\,e^{i2ka\cos\theta}\;\;\sin\theta\,d\theta\,, \\ &= -p_0\frac{ika^2}{r_p}\;e^{ikr_p}\int_{\theta=\pi}^{\pi/2}\cos\theta\,e^{i2ka\cos\theta}\;\;\sin\theta\,d\theta\,,\end{aligned} \tag{H.36}$$

and

$$\begin{aligned} p_{sc}^{(2)}(\mathbf{r}_p) &= -\frac{p_0}{2\pi}\frac{ik}{r_p}\, e^{ikr_p}\frac{a}{r_p}\iint_S e^{i2ka\cos\theta}\;a^2\,\sin\theta\,d\theta\,d\phi, \\ &= -\frac{p_0}{2\pi}\frac{ika^3}{r_p^2}\, e^{ikr_p}\int_{\phi=0}^{2\pi} d\phi\int_{\theta=\pi}^{\pi/2} e^{i2ka\cos\theta}\quad \sin\theta\,d\theta\,. \end{aligned} \tag{H.37}$$

There appears to be not analytical solution to Eq. (H.37), but fortunately, since the expression contains a $(a/r_p)^2$ factor the integral can be neglected, i.e., $p_{sc}^{(2)}(\mathbf{x}) \approx 0$. In order to solve Eq. (H.36) the substitution $\mu = \cos\theta$ is applied; thus,

$$d\theta = -\frac{d\mu}{sin\theta}\,, \tag{H.38}$$

and with the new limits $\cos(\pi) = -1$ and $\cos(\pi/2) = 0$ the expression changes into:

$$p_{sc}(\mathbf{x}) \;=\; p_0\frac{ika^2}{r_p}\,e^{ikr_p}\int_{-1}^{0}\mu\,e^{i2ka\mu}\quad d\mu\,. \tag{H.39}$$

The integral in Eq. (H.39) is determined:

$$\begin{aligned} \int_{-1}^{0}\mu\,e^{i2ka\mu}\quad d\mu &= \left[\frac{e^{i2ka\mu}}{(2ika)^2}\,(\,2ika\mu-1\,)\right]_{-1}^{0} \\ &= \frac{1}{(2ika)^2}\left[e^{i2ka\mu}(\,2ika\mu-1\,)\right]_{-1}^{0} \\ &= \frac{1}{(2ika)^2}\left[1(\,0-1\,)-e^{-i2ka}(\,-2ika-1\,)\right] \\ &= \frac{1}{(2ika)^2}\left[\,-1+2ika\;e^{-i2ka}+e^{-i2ka}\right], \end{aligned} \tag{H.40}$$

and one finally obtains,

$$p_{sc}(\mathbf{x}) \;=\; \frac{p_0 e^{ikr_p}}{4r_p}\;\left[\,-\frac{1}{ik}+2a\;e^{-i2ka}+\frac{1}{ik}e^{-i2ka}\right]. \tag{H.41}$$

The corresponding time domain response is

$$p_{sc}(t,\mathbf{x}) \;=\; \frac{c}{4r_p}\;\left[p_0^{-}\Big(t-\frac{r_p}{c}\Big)+\frac{2a}{c}\,p_0\Big(t-\frac{r_p-2a}{c}\Big)\;-p_0^{-}\Big(t-\frac{r_p-2a}{c}\Big)\right], \tag{H.42}$$

where the Fourier transform properties $p_0(\omega)\,e^{i\omega t_d} \leftrightarrow p_0(t-t_d)$ and $p_0(\omega)/i\omega \leftrightarrow -\int_{-\infty}^{t} p_0(\tau)d\tau$ have been applied, and where $p_0^{-}(t) = \int_{-\infty}^{t} p_0(\tau)d\tau$.

H.8 The impulse response of the sphere. Part II

The last two terms in Eq. (H.42) belong to the the front face reflection. As the expression indicate, the physical optics solution to the front facet reflection is the pulse times $2a$ plus the time-integrated pulse. Hence the magnitude of the front face reflection is almost proportional to the radius of the sphere. At first sight, the first term in Eq. (H.42) appears to be a pressure release diffracted wave, but that is not the case; the term is a result of the Kirchhoff approximation that fails at the circumferential edge; this is confirmed in Fig. (H.9), which shows the result from the harmonic series solution Fig (H.9a) and the analytical Kirchhoff solutions Fig (H.9b); the dominant frequency of the incoming field is 445 kHz, the sphere has a radius of 10 cm, and the observation point is 10 meters from the sphere. According to Eqs. (H.6),(H.7), and (H.8) the travel paths yield respectively,

$$\tau_A = 6.53\,\text{ms}, \tag{H.43}$$

$$\tau_B = 6.60\,\text{ms}, \tag{H.44}$$

$$\tau_C = 6.87\,\text{ms}. \tag{H.45}$$

Fig (H.9a)(top) and Fig (H.9b) (top) are similar; they show the full dynamic of the impuls response and the front face reflection appears to be the only component. In Fig (H.9a)(bottom) a zoom onto the y-axis has been made, and it reveals the existence of a wave field that travels around the sphere and propagates towards the observation point (creeping waves); however, it is approximately 70 dB below the front face reflection. Note, there are no contributions from the circumferential zone between the ensonified and shadowed part of the sphere. In Fig (H.9a)(bottom), i.e., the Kirchhoff solution, a zoom onto the y-axis has also been made; here, a contribution from the the circumferential zone between the ensonified and shadowed part of the sphere is present, and it is approximately 50 dB below the front face reflection. However, since this contribution is absent in the harmonic series solution, it is rather considered as an artifact caused by a breakdown of the Kirchoff approximation/assumption.

H.9 The limit of the Kirchhoff approximation

Finally, the analytical Kirchhoff approximation for the sphere is evaluated in the case where the radius of the sphere is comparable with the acoustic wavelength. Here, only the front face reflection is of interest. Figs. (H.10a-f) show that the Kirchhoff approximation performs reasonably well even with a sphere that has a radius down to one quarter of a wavelength. Provided this result can be observed on other shapes, for example, a cylinder, it may be exploited in a future model for very high frequency scattering from a 3D object. For frequencies between, say 5 kHz and 50 kHz, which corresponds to wavelengths between 30 cm down to 3 cm, an edge diffraction model is necessary on corners, edges, and protrusions of a

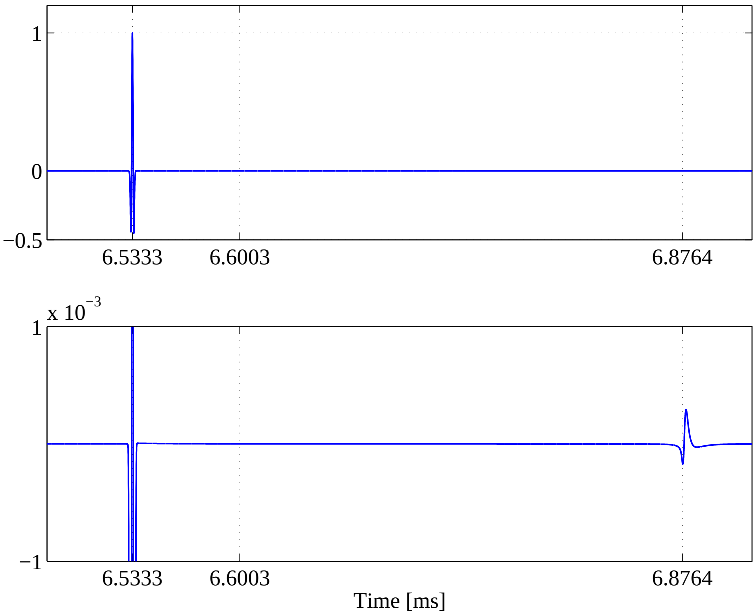

(a) Harmonic series solution

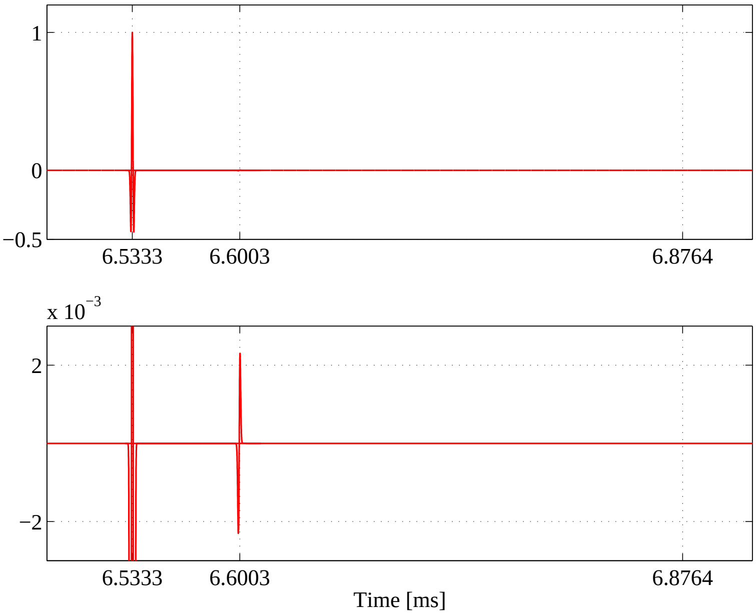

(b) Analytical Kirchhoff solution

Figure H.9: The impulse response of the sphere for wavelengths much less than the radius of the sphere.

mine, see, e.g., Refs. [59], [63],[78],[79],[80], [54],[55], and [7](Ch. 9.6). However, for wavelengths below 5 mm it may be more reasonable to consider the edges as *rounded* edges, because most Naval mines probably dont have edges whose radii of curvature are less than, say, 1 mm. Therefore, the Kirchhoff approximation is believed to be sufficient to model the scattered field from the (rounded) edges. The discussion leads to the issue of modeling the 3D surface. In this project the triangular facet has been applied as the building-block for the composition of a surface with an arbitrary shape, and although it is an improvement of the simpler rectangular facet, it not well suited for curved surfaces and rounded edges. For example, in Ref.[3] the numerical model of a sphere is composed by plane triangular facets and a high number of facets are necessary in order to suppress the artificial oscillations that occur after the front face reflection. The artifacts are a result of an inaccurate surface model. The analytical Kirchhoff solution derived in Sec. H.7 is basically a large semispherical facet. Hence, it can be concluded that the accuracy of the numerical surface representation has the dominating influence on the resulting scattered field. Therefore, a future model ought to operate with different basic facets shapes such as the spherical triangle derived in the next section (H.10), the cylindrical triangle, or even larger facets. Non-Uniform Rational B-Splines (NURBS), see, e.g., Ref. [62], can be an alternative approach; here, the field integral is evaluated over a parametric space of Bezier surfaces using the method of stationary phase, see, e.g., Ref. [60](Sec. 4.6.1).

H.10 Extension to a spherical triangle

The results from Sec. H.7 can be applied on a spherical triangle. Hence, the integration limits are only specified from ϕ_1 to ϕ_2 and from θ_1 to θ_2. Integration yields

$$\begin{aligned} p_{sc}(\mathbf{x}) &= -\frac{p_0}{2\pi}\frac{ik}{r_p}\, e^{ikr_p} \int_{\phi_1}^{\phi_2}\int_{\theta_1}^{\theta_2} \cos\theta\, e^{i2ka\cos\theta}\;\; a^2\,\sin\theta\, d\theta\, d\phi \\ &= -\frac{p_0}{2\pi}\frac{ik}{r_p}\, e^{ikr_p}\,[\,\phi_2-\phi_1\,] \int_{\theta_1}^{\theta_2} \cos\theta\, e^{i2ka\cos\theta}\;\; a^2\,\sin\theta\, d\theta\, d\phi \end{aligned} \tag{H.46}$$

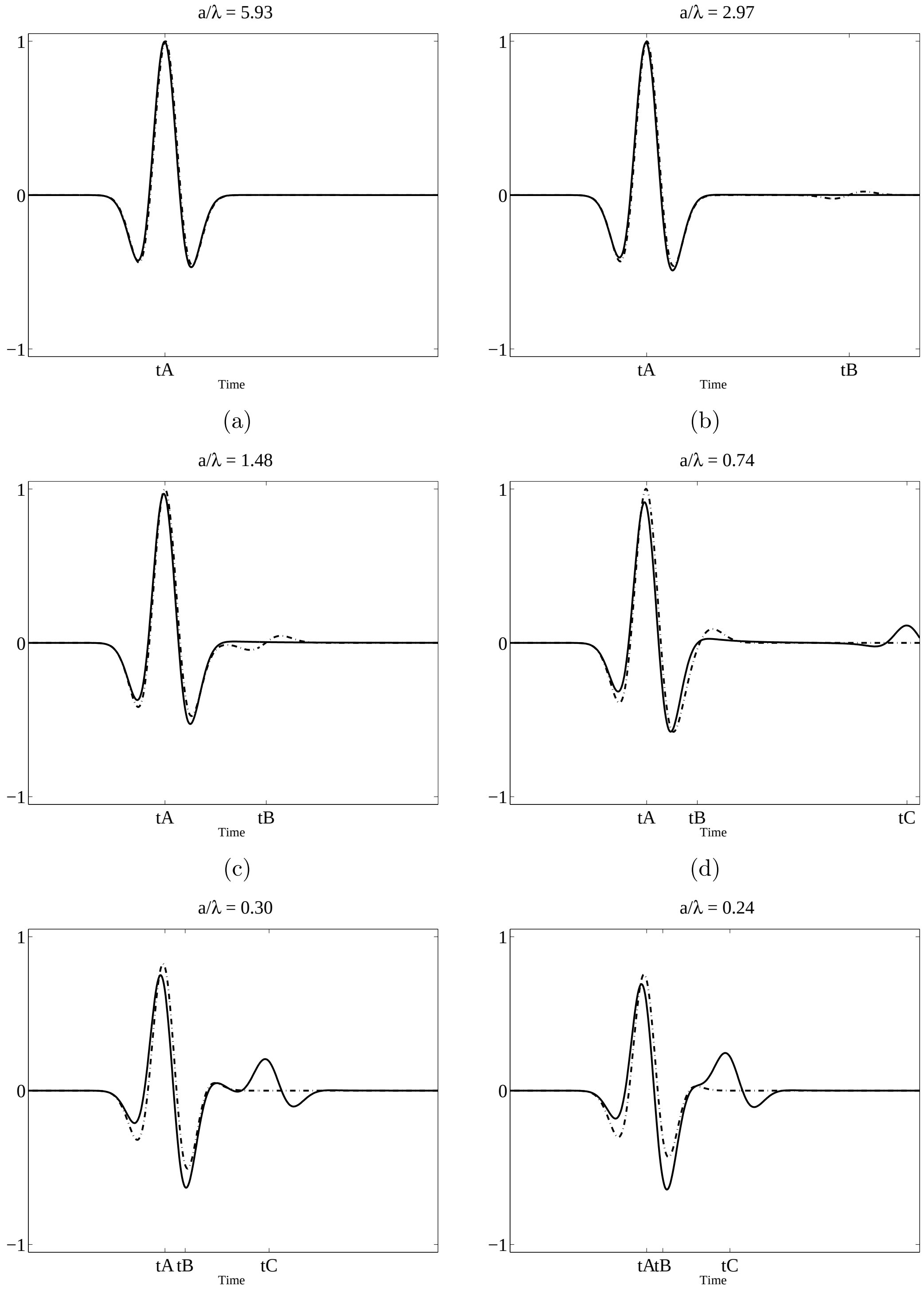

(a) (b) (c) (d) (e) (f)

Figure H.10: Kirchhoff solution (-.) versus the harmonic series solution (-) when the sphere's radius is comparable with the acoustic wavelength.

The integral in (H.46) is determined with $\mu_1 = \cos(\theta_1)$ and $\mu_2 = \cos(\theta_2)$; hence,

$$\begin{aligned}
\int_{\mu_1}^{\mu_2} \mu\, e^{i2ka\mu} \; d\mu &= \left[\frac{e^{i2ka\mu}}{(2ika)^2} \,(\, 2ika\mu - 1\,) \right]_{\mu_1}^{\mu_2} \\
&= \frac{1}{(2ika)^2} \left[\, e^{i2ka\mu_2} (\, 2ika\mu_2 - 1\,) - e^{i2ka\mu_1} (\, 2ika\mu_1 - 1\,) \right] \\
&= \frac{1}{(2ika)} \left[\left(\mu_2\, e^{i2ka\mu_2} - \mu_1\, e^{i2ka\mu_1} \right) \right] + \frac{1}{(2ika)^2} \left[e^{i2ka\mu_1} - e^{i2ka\mu_2} \right],
\end{aligned} \tag{H.47}$$

Before this expression may be applied on a spherical shaped surface it must be ensured that no numerical problems may occur.

In this chapter the benchmark solution required for verification of the numerical Kirchhoff model has been presented. The harmonic series solution to the problem of high frequency scattering from a rigid sphere from an incident plane wave has been applied, and the verification has been carried out in the time domain by application of a Ricker pulse
In addition, the analytical Kirchhoff solution for a rigid sphere has been derived. The limit of the Kirchhoff approximation is analyzed for the rigid sphere, and compared with the harmonic series solution for decreasing radii slightly above and below the acoustic wavelength. The analysis leads to the conclusion that the Kirchhoff approximation is applicable on edges with a radius of curvature down to 1/4 of the acoustic wavelength. Finally, the Kirchhoff expression for a spherical triangle has been considered briefly.

Appendix I

The receiver aperture

The synthetic sonar images presented at ECUA2004, see Ref. [1], use the Reson Seabat 8128 sector scan sonar as the reference sonar, and the the artificial images are compared with real 8128 images. In radar applications the incoming waves are most frequently received from the far field, and consequently, the incoming waves are plane as they sweep over the receiver aperture. For a sonar imaging system the distance between the sonar and the seabed is relatively close; consequently, the spherical curvature of the wavefront cannot be neglected. Hence, in order to establish a beam formation in a specific direction it is necessary to adjust the time delays so that the aperture focuses on a specific points in space. The Reson Seabat 8128 applies an auto-focusing method by which the focal range changes on a sample basis.

Here, the fundamental theory behind focused beam formation is presented. Subsequently, it is assumed that all point scatters are located in the same range as the focal distance, and as a consequence, it is possible to the consider the focusing receiver as a classical far field receiver. Reson A/S has delivered a simple formula of the beam width as a function of the steering angle for the Seabat 8182. A uniform linear array with the appropriate shading function, or sensor weighting function, which meets the sensor specification is presented. Additionally, it is assumed that the beam pattern have a constant profile over the bandwidth of the emitted signal, which leads to the final approximate expression to calculate a sonar beam response; the method avoids time domain beam-forming and it is applied for the sonar model. The content of this Appendix is based on Ref. [8].

I.1 The focused beam

The focused beam is derived for a 2D wave field, but it can without loss of generality be extended to a 3D wave field. Consider a 1D array with N point-like and omnidirectional sensors numbered by the index l, from 0 to $N-1$; N is assumed to be an unequal number. The position of the l'th sensor is denoted

$\mathbf{p}_l$ and all sensors lie in the plane $z = 0$, see Fig. I.1. The received signal at the l'th sensor, $s_l(t)$, is linearly proportional to the pressure field $q(t)$ emitted from an ideal point source located at the coordinate system's origin located at the $((N+1)/2)$'th sensor. The beam signal steered in the direction of the unit vector $\hat{\mathbf{u}}$ is found by

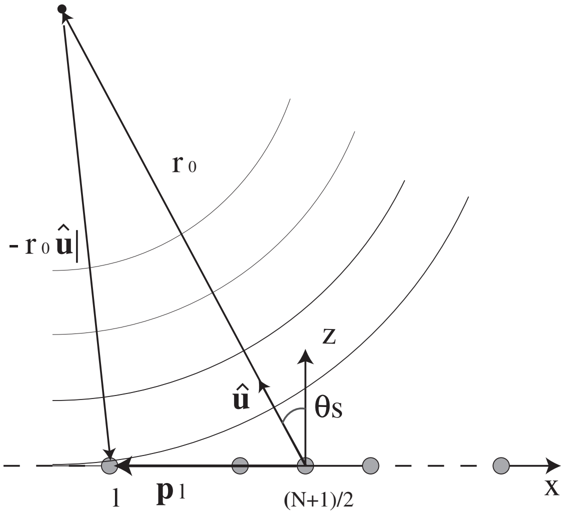

Figure I.1: Geometry applied for focused beam.

$$b(t, \hat{\mathbf{u}}) = \sum_{l=0}^{N-1} w_l s_l(t - \tau(\hat{\mathbf{u}}, r_0, l)), \tag{I.1}$$

where w_l is a weight assigned to each sensor, r_0 is the focal length, and τ is the time-delay. In the following all sensor weights are equal to one, i.e., $w_l = 1$. The time delay is given by

$$\tau(\hat{\mathbf{u}}, r_0, l) = \frac{r_0 - |\mathbf{p}_l - r_0\hat{\mathbf{u}}|}{c}, \tag{I.2}$$

and where $\tau = 0$, when $|\mathbf{p}_l - r_0\hat{\mathbf{u}}| = 0$, i.e., for the sensor with index $l = (N+1)/2$. When $\hat{\mathbf{u}}$ points into the half-plane where $x < 0$, as illustrated in Fig. I.1, the time delay τ is positive for all sensors in the left plane; the outermost left sensor, i.e., the sensor with index $l = 0$ has to be delayed the time it takes for the spherical wavefront to sweep over to the midpoint of the array. On the right part the time delay will be negative which is a violation of causality; however, this problem can in a real system be solved by application of extra buffer delays; however, this topic is not addressed here. Consider the range

$$|\mathbf{p}_l - r_0\hat{\mathbf{u}}| = \sqrt{r_0^2 + |\mathbf{p}_l|^2 - 2r_0\hat{\mathbf{u}} \cdot \mathbf{p}_l}, \tag{I.3}$$

and let $x_l = |\mathbf{p}_l|$, and θ_s be the angle between the z-axis and the steering vector $\hat{\mathbf{u}}$; hence,

$$\hat{\mathbf{u}} \cdot \mathbf{p}_l = x_l \sin\theta_s, \tag{I.4}$$

and Eq. (I.3) can now be written as

$$\begin{aligned} |\,\mathbf{p}_l - r_0\hat{\mathbf{u}}\,| &= \sqrt{r_0^2 + x_l^2 - 2r_0 x_l \sin\theta_s} \\ &= r_0\sqrt{1 + (x_l/r_0)^2 - 2(x_l/r_0)\sin\theta_s} \end{aligned} \tag{I.5}$$

Following variable is introduced

$$\varepsilon = (x_l/r_0)^2 - 2(x_l/r_0)\sin\theta_s, \tag{I.6}$$

and $\varepsilon << 1$; the square-root term is now expanded in a Taylor series to the second order

$$\sqrt{1+\varepsilon} \approx 1 + \frac{1}{2}\varepsilon - \frac{1}{8}\varepsilon^2 \tag{I.7}$$

The right side of Eq. (I.6) is inserted into the right side of Eq. (I.7) which yields,

$$\begin{gathered} 1 + \frac{1}{2}\left[\,(x_l/r_0)^2 - 2(x_l/r_0)\sin\theta_s\,\right] - \frac{1}{8}\left[\,(x_l/r_0)^2 - 2(x_l/r_0)\sin\theta_s\,\right]^2 = \\ \\ 1+\frac{1}{2}\left[\,(x_l/r_0)^2-2(x_l/r_0)\sin\theta_s\right]-\frac{1}{8}\left[(x_l/r_0)^4+4(x_l/r_0)^2\sin^2\theta_s-4(x_l/r_0)^3\sin^2\theta_s\right]^2 \end{gathered} \tag{I.8}$$

In the Fresnel approximation terms of $(x_l/r_0)^l$ where $l > 2$ are discarded; hence,

$$\sqrt{1 + (x_l/r_0)^2 - 2(x_l/r_0)\sin\theta_s} \approx 1 + \frac{1}{2}(x_l/r_0)^2 - (x_l/r_0)\sin\theta_s - \frac{1}{2}\,(x_l/r_0)^2\sin^2\theta_s \tag{I.9}$$

The second order term, $4(x_l/r_0)^2\sin^2(\theta_s)$, is not included in Ref.[8], possibly because the square root term only has been Taylor expanded up to the first order; it is not quite clear why, but as a consequence the steering angle angle must be small, say, $\theta_s < 20°$ so that $(\sin\theta_s)^2 < 0.117$ (in Ref. [8] $\theta_s < 18°$ and then $(\sin\theta_s)^2 < 0.095$). Hence,

$$\sqrt{1 + (x_l/r_0)^2 - 2(x_l/r_0)\sin\theta_s} \;\approx\; 1 + \frac{1}{2}(x_l/r_0)^2 - (x_l/r_0)\sin\theta_s\,, \tag{I.10}$$

and

$$|\,\mathbf{p}_l - r_0\hat{\mathbf{u}}\,| \;\;\approx\;\; r_0 + \frac{1}{2}(x_l^2/r_0) - x_l \sin\theta_s \tag{I.11}$$

In order to steer the receiver array in the direction corresponding to the angle θ_s the time delay required after each sensor is,

$$\begin{aligned} \tau(\hat{\mathbf{u}}, r_0, l) &= \frac{r_0 - (r_0 + \frac{1}{2}(x_l^2/r_0) - x_l \sin\theta_s)}{c} \\ &= \frac{x_l \sin\theta_s}{c} - \frac{x_l^2}{2r_0 c} \end{aligned} \tag{I.12}$$

The Fourier transform of $b(t, \theta_s)$ is

$$B(\omega, \theta_s) = \sum_{l=0}^{N-1} S_l(\omega)\, e^{i\omega(x_l \sin\theta_s/c - x_l^2/(2r_0))} \tag{I.13}$$

I.2 The field at a single receiver

Suppose each sensor receives contributions from M independent point scatters; a coordinate system similar to the one applied in Fig. (I.1) is applied, see Fig. (I.2), where the scattering surface is shown; $\mathbf{r}_m$ is the vector from the origin to the mth point scatter and $\mathbf{p}$ is the vector from the origin to the receiver. The source is assumed located in the origin where it emits a pulse $q(t)$ from an ideal point source. The Fourier transform of the received signal at $\mathbf{p}$ is

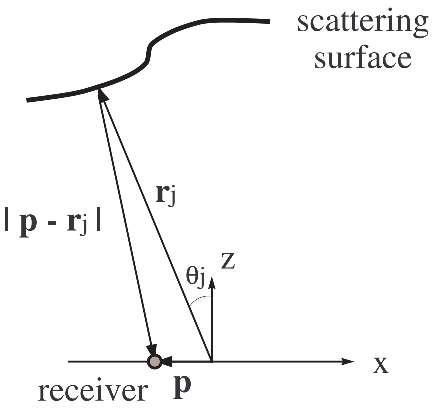

Figure I.2:

$$S(\omega, \mathbf{p}) = \sum_{j=1}^{M} C_j\, Q(\omega) e^{ik(r_j + |\mathbf{p} - \mathbf{r}_j|)}, \tag{I.14}$$

where r_j is the distance from the source to the j'th point scatter, $|\mathbf{p} - \mathbf{r}_j|$ is the distance from the j'th point scatter to the receiver $\mathbf{p}$, and C_j is the attenuation coefficient; it can include geometrical spreading, i.e., $1/r_j^2$, absorption in the medium, and other effects depending on the selected scattering model, see Ref. [8](pp. 1907). A range consideration is made again, where $|\mathbf{p}| = x$ and θ_j is the angle between the z-axis and the j'th point scatter; one obtains

$$\begin{aligned}
|\mathbf{p} - \mathbf{r}_j| &= [\, r_j^2 + x^2 - 2\,\mathbf{p}\cdot\mathbf{r}_j \,]^{1/2} \\
&= [\, r_j^2 + x^2 - 2\, r_j x \sin\theta_j \,]^{1/2} \\
&= r_j\, [\, 1 + (x/r_j)^2 - 2\, x/r_j \sin\theta_j \,]^{1/2} \\
&\approx r_j + \frac{1}{2}(x^2/r_j) - x\sin\theta_j - \frac{1}{2}x^2/r_j \sin^2\theta_j, \\
&\approx r_j + \frac{1}{2}(x^2/r_j) - x\sin\theta_j, \qquad \text{(I.15)}
\end{aligned}$$

and as in the previous section the $\frac{1}{2}x^2/r_j \sin^2\theta_j$ term has been discarded. Eq. (I.14) becomes,

$$S(\omega, \mathbf{p}) = \sum_{j=1}^{M} C_j\, Q(\omega)\, e^{ik(2r_j - x\sin\theta_j + x^2/(2r_j))}. \qquad \text{(I.16)}$$

I.3 Total field over the array - all point scatters at the focal distance.

Equation (I.16) is now expressed in terms of the array presented in section I.1; for the l'th sensor one have

$$S_l(\omega, \mathbf{p}_l) = \sum_{j=1}^{M} C_j\, Q(\omega)\, e^{ik(2r_j - x_l\sin\theta_j + x_l^2/(2r_j))}, \qquad \text{(I.17)}$$

Equation (I.17) is inserted into the Fourier transform of the beam steering function, Eq. (I.13), that is,

$$B(\omega, \theta_s) = \sum_{l=0}^{N-1}\sum_{j=1}^{M} C_j\, Q(\omega)\, e^{ik(2r_j - x_l\sin\theta_j + x_l^2/(2r_j))}\, e^{ik(x_l\sin\theta_s - x_l^2/(2r_0))} \qquad \text{(I.18)}$$

Suppose all scatters are located in the same range as the focal distance, i.e., $r_i = r_0$, then Eqs. I.18 yields

$$B(\omega, \theta_s)|_{(r_j = r_0)} \;=\; Q(\omega)\sum_{l=0}^{N-1}\sum_{j=1}^{M} C_j\, e^{ik2r_0} e^{ikx_l(\sin\theta_s - \sin\theta_j)}, \qquad \text{(I.19)}$$

and the quadratic terms in the phase function are canceled out. The origin of the coordinate system is located at the $((N+1)/2)$'th receiver, i.e., $x_{(N+1)/2} = 0$, and thus,

$$x_l = \Delta x(l - (N+1)/2), \tag{I.20}$$

so that,

$$B(\omega, \theta_s)|_{(r_j=r_0)} = Q(\omega) e^{ik2r_0} \sum_{l=0}^{N-1} \sum_{j=1}^{M} C_j \, e^{-ik\Delta x(N+1)/2(\sin\theta_s - \sin\theta_j)} e^{ik\Delta x l(\sin\theta_s - \sin\theta_j)}. \tag{I.21}$$

A substitution of the summations yields,

$$\begin{aligned} B(\omega, \theta_s)|_{(r_j=r_0)} &= Q(\omega) e^{ik2r_0} \sum_{j=1}^{M} \sum_{l=0}^{N-1} C_j \, e^{-ik\Delta x(N+1)/2(\sin\theta_s - \sin\theta_j)} e^{ik\Delta x l(\sin\theta_s - \sin\theta_j)} \\ &= Q(\omega) e^{ik2r_0} \sum_{j=1}^{M} C_j \, e^{-ik\Delta x(N+1)/2(\sin\theta_s - \sin\theta_j)} \sum_{l=0}^{N-1} e^{-ik\Delta x l(\sin\theta_j - \sin\theta_s)} \end{aligned} \tag{I.22}$$

The right sum in Eq.(I.22) is a finite sum of complex exponential functions[1], and consequently,

$$\begin{aligned} B(\omega, \theta_s)|_{(r_j=r_0)} &= Q(\omega) e^{ik2r_0} \sum_{j=1}^{M} C_j \, e^{ik\Delta x(N+1)/2(\sin\theta_j - \sin\theta_s)} \\ &\qquad \times e^{-ik\Delta x(N+1)/2(\sin\theta_j - \sin\theta_s)} \, \frac{\sin(k\Delta x[\sin\theta_j - \sin\theta_s]N/2)}{\sin(k\Delta x[\sin\theta_j - \sin\theta_s]/2)} \\ &= Q(\omega) e^{ik2r_0} \sum_{j=1}^{M} \; C_j \, \frac{\sin(k\Delta x[\sin\theta_j - \sin\theta_s]N/2)}{\sin(k\Delta x[\sin\theta_j - \sin\theta_s]/2)} \\ &= Q(\omega) e^{ik2r_0} \sum_{j=1}^{M} \; C_i \, H_l(\theta_j, \theta_s, \omega_0), \end{aligned} \tag{I.23}$$

where

$$H_l(\theta_j, \theta_s, \omega) = \frac{\sin(k\Delta x[\sin\theta_j - \sin\theta_s]N/2)}{\sin(k\Delta x[\sin\theta_j - \sin\theta_s]/2)} \tag{I.24}$$

---

[1]

$$\sum_{n=0}^{M-1} e^{-i\phi n} = \frac{1 - e^{-i\phi M}}{1 - e^{-i\phi}} = \frac{e^{-i\phi M/2}}{e^{-i\phi/2}} \, \frac{e^{i\phi M/2} - e^{-i\phi M/2}}{e^{i\phi/2} - e^{-i\phi/2}} = e^{-i\phi(M+1)/2} \, \frac{\sin(\phi M/2)}{\sin(\phi/2)},$$

see, e.g., Ref. [81](Example 3.2.4, pp. 164) is the beampattern for a uniform linear array operating in the far field. Thus by assuming that all point scatters lie in a range that corresponds to the focal distance, the receiver can be considered to work in the far field.

I.4 The shading function

The manufacturer of the Seabat 8128 has informed that the horizontal beam resolution is

$$\Delta\theta \approx 0.5^{\circ}/\theta_s. \tag{I.25}$$

Sofar, it has been assumed that contributions from all elements or hydrophones are weighted equally. In order to reduce side-lobe effects by following Eq. I.25 a shading function will be applied. The following Hamming window is selected

$$w_l = 0.54 - 0.46\cos\left(\frac{2\pi l}{N}\right) \; ; \; l = 0, 1, ..., N-1., \tag{I.26}$$

and it can also be expressed by

$$w_l = 0.54 - 0.23\Big[\, e^{i2\pi l/N} + e^{-i2\pi l/N)} \Big] \; ; \; l = 0, 1, ..., N-1. \tag{I.27}$$

Thus, the shading function is represented by the three sub-functions as

$$w_l = w_l^{(1)} + w_l^{(2)} + w_l^{(3)} \;\; ; \text{ l=0,1,....,N-1,} \tag{I.28}$$

and they are expressed in terms of the complex exponentials

$$\begin{aligned} w_1 &= \alpha_1 \, e^{i\beta_1}, \\ w_2 &= \alpha_2 \, e^{i\beta_2}, \\ w_3 &= \alpha_3 \, e^{i\beta_3}, \end{aligned} \tag{I.29}$$

where

$$\begin{aligned} \beta_1 &= 0\,, \\ \beta_2 &= 2\pi/N\,, \\ \beta_3 &= -2\pi/N\,, \end{aligned} \tag{I.30}$$

and where

$$\begin{aligned} \alpha_1 &= 0.54\,, \\ \alpha_2 &= -0.23\,, \\ \alpha_3 &= -0.23\,. \end{aligned} \tag{I.31}$$

The last sum in the last line of Eq. (I.22) is expressed in terms of a non-unitary weight function $w_l^{(n)} = \alpha_n\, e^{i\beta_n l}$, where $n = 0, 2$, and 3; hence,

$$\sum_{l=0}^{N-1} w_l^{(n)}\, e^{-ik\Delta x l(\sin\theta_i - \sin\theta_s)} = \sum_{l=0}^{N-1} \alpha_n\, e^{-i\,[\,k\Delta x(\sin\theta_i - \sin\theta_s) - \beta_n\,]\,l},$$

$$= \alpha_n\, e^{-i\,[\,k\Delta x(\sin\theta_s - \sin\theta_j) - \beta_n\,]\,(N+1)/2}\ \frac{\sin((k\Delta x\,[\,\sin\theta_s - \sin\theta_j] - \beta_n\,)\,N/2)}{\sin((k\Delta x\,[\,\sin\theta_s - \sin\theta_j] - \beta_n\,)\,/2)},$$

A derivation similar to the one that was carried out from Eq. (I.22) through Eq. (I.23) to Eq. (I.23) yields,

$$H_l^{(n)}(\theta_i, \theta_s, \omega) = \alpha_n\, e^{i\beta_n\,(N+1)/2}\ \frac{\sin((k\Delta x[\,\sin\theta_i - \sin\theta_s\,] - \beta_n)N/2)}{\sin((k\Delta x[\,\sin\theta_i - \sin\theta_s\,] - \beta_n)/2)}. \tag{I.32}$$

Hence, the receiver transfer function is expressed by its three sub-functions

$$H_{rcv}^{(0)}(\theta_i, \theta_s, \omega) \;=\; 0.54\ \frac{\sin(k\Delta x[\,\sin\theta_i - \sin\theta_s\,]N/2)}{\sin(k\Delta x[\,\sin\theta_i - \sin\theta_s\,]/2)}\,, \tag{I.33}$$

$$H_{rcv}^{(1)}(\theta_i, \theta_s, \omega) \;=\; 0.23\, e^{i\pi/N}\ \frac{\sin(k\Delta x[\,\sin\theta_i - \sin\theta_s\,]N/2 - \pi)}{\sin(k\Delta x[\,\sin\theta_i - \sin\theta_s\,]/2 - \pi/N)}\,, \tag{I.34}$$

$$H_{rcv}^{(2)}(\theta_i, \theta_s, \omega) \;=\; 0.23\, e^{-i\pi/N}\ \frac{\sin(k\Delta x[\,\sin\theta_i - \sin\theta_s\,]N/2 + \pi)}{\sin(k\Delta x[\,\sin\theta_i - \sin\theta_s\,]/2 + \pi/N)}\,. \tag{I.35}$$

Finally, the receiver transfer function for a Hamming weighted receiver array is

$$H_{rcv}(\theta_i, \theta_s, \omega) = H_{rcv}^{(1)}(\theta_i, \theta_s, \omega) + H_{rcv}^{(2)}(\theta_i, \theta_s, \omega) + H_{rcv}^{(3)}(\theta_i, \theta_s, \omega), \tag{I.36}$$

and the beamwidth specified by the manufacturer of the Seabat 8128

$$\Delta\theta_{3dB} \approx 0.5^\circ/\theta_s,$$

is accomplished by setting the number of sensors equal to $N = 229$ and use a sensor spacing of $\Delta x = \lambda/2$.

I.5 Constant beam profile over signal bandwidth

If it is assumed that the beam pattern have a constant profile over the bandwidth of the emitted signal, i.e.,

$$H_{rcv}(\theta_j, \theta_s, \omega) \approx H_{rcv}(\theta_j, \theta_s, \omega_c), \tag{I.37}$$

where ω_c is the carrier frequency.
The point scatter formulation applied presented in section (I.2) will not be applied for the sonar model presented in this work. Instead, the numerous seabed and object responses are represented in the time domain and each response originates from a specific angular direction, θ_j, in space. Let the j'th time domain response be expressed in its complex analytical form as

$$z_j(t) = f_j(t)\, e^{i\omega_c t}, \tag{I.38}$$

where $f_j(t)$ is the complex base band signal. The contribution to the beam signal at steering θ_s

$$b_j(t, \theta_s) = f_j(t) \;\; H_{rcv}(\theta_j, \theta_s, \omega_c)\, e^{i\omega_c t}. \tag{I.39}$$

Thus, the total beam signal, at a given steering angle θ_s, is the weighted sum of all waveforms backscattered from the object facets and height profiles

$$b_{tot}(t, \theta_s) = \sum_{j=1}^{M} f_j(t) \;\; H_{rcv}(\theta_j, \theta_s, \omega_c)\, e^{i\omega_c t}, \tag{I.40}$$

which is the method applied when the synthetic images are generated.

In this chapter the fundamentals of a high resolution sonar operating in the near field have been addressed. For each receiving direction the array must focus on a specific range. The Reson Seabat 8128 uses an autofocusing algorithm that increases the focal range as a function of time.
When it is assumed that all the scatters are located within the focal range it is shown that the receiver array works as if it was operating in the far field. This assumption is exploited in the DDRE-model, where the field obtained from the seabed and the object is transformed into each beam according to Eq. (I.40).

Appendix J

Energy of a sonar beam

So far the seabed scattering model has been concentrated on the phase modulation of the scattered field from the seabed. Although a reliable model for scattering from sandy sediment has been developed, the energy aspects related to a real sonar system has not been included. In the model the backscattered field from the seabed is added coherently to the object-backscattered field and their mutual acoustic energy contributions must be correct. Therefore, in this chapter the acoustic energy, or power, scattered from the seabed is examined in terms of the functional relationship between the amplitude of pressure envelope and the range R. The expression derived will be applied to correct for the range decay in the seabed scattering model; a range decay that depends on the selected Greens function.

The sonar model computes the backscattered field from several distinct 1D height profiles in directions of the sonar beams, see Fig. (J.1). In the Delft paper, see Ref. [1], wave propagation from the height profiles is assumed spherical, whereas

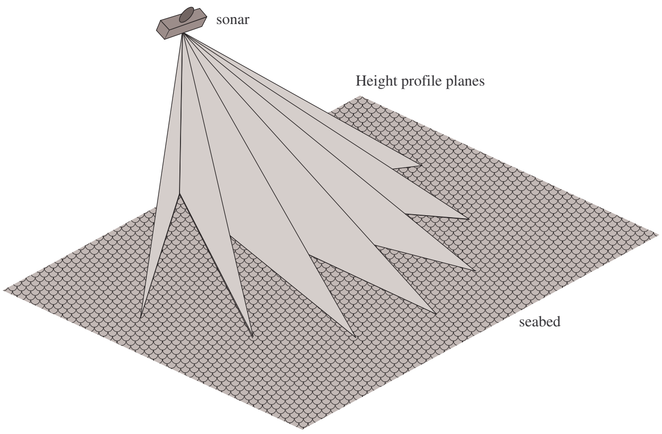

Figure J.1: The scattered pressure is calculated from numerous height profiles in planes similar to the sonar beams.

in Ref. [4], it is implicitly assumed that the scattered waves propagate cylindrically because the Hankel function of the first kind has been applied as the Green's function[1]; the reason for this choice is caused by the fact that the solution to the penetrable rough surface scattering problem adopted from Ref. [82] has been presented in terms of Hankel functions.

A high frequency sonar collects the backscattered field in narrow beams using either an acoustic linse or an electronic steered array; since, most often, the backscattered field is acquired from a distance that is smaller than, or is at least the same order of magnitude, as the water column the field is composed of spherically spreading waves. During preprocessing of sonar raw data, which is before the data are converted into an image, the time variant gain (TVG) can be applied; Medwin and Clay, see Ref. [9](pp. 416- 418), distinguish between a ($20 \cdot \log_{10}(R)$) intensity compensation for unresolved echoes, i.e., volume scatter and a ($40 \cdot \log_{10}(R)$) intensity compensation for isolated echoes. J. M. Bell [48] use the ($40 \cdot \log_{10}(R)$) compensation in a sidescan sonar model and Mansour [83] introduce a variable decay law in a sonar model. Urick [14](pp. 245) also applies the ($40 \cdot \log_{10}(R)$) range decay law and presents it together with the surface reverberation loss

$$RL_s = SL - 40 \cdot \log_{10} R + S_s + 10 \cdot \log_{10} \left(\frac{c\tau}{2} \phi R \right) \tag{J.1}$$

where SL is the source level, S_s the scattering strength for the surface reverberation and the last term is the area of the surface under consideration; c is the speed of sound, τ is the pulse duration and ϕ the beamwidth, and absorption is not included. From Eq.(J.1) it can be seen that the corresponding far field intensity has a R^{-3} dependency, and hence, the pressure envelope will fall as $R^{-3/2}$. In the following the Eq. (J.1) is re-examined.

J.1 The resolution cell

Here, the resolution cell within a sonar beam directed toward a seabed is considered. For simplicity the source is assumed to be a point source and the derivation of the expected pressure envelope will be based on the expected sound power scattered from the seabed. Consider Fig. (J.2(a)); the black circle represents the sonar; the transmitter, a point source, is located at a certain height above the seabed. The source emits a spherical wave. The mean height seabed, i.e., a perfectly flat seabed, is sketched here. The circles represent intersection of the incoming field with the mean height seabed at range R and $R + \Delta R$, and the circles are lines of constant phase. For a continuous wave (CW) pulse the in-

---

[1] The $e^{-i\omega t}$ time dependence is assumed; hence, a two-dimensional diverging wave is described in terms of the Hankel function of the first kind, $H_0^{(1)}(kR)$, and the three dimensional diverging wave is described by the complex exponential e^{ikR}/R, where k is the acoustic wave number and R is the range.

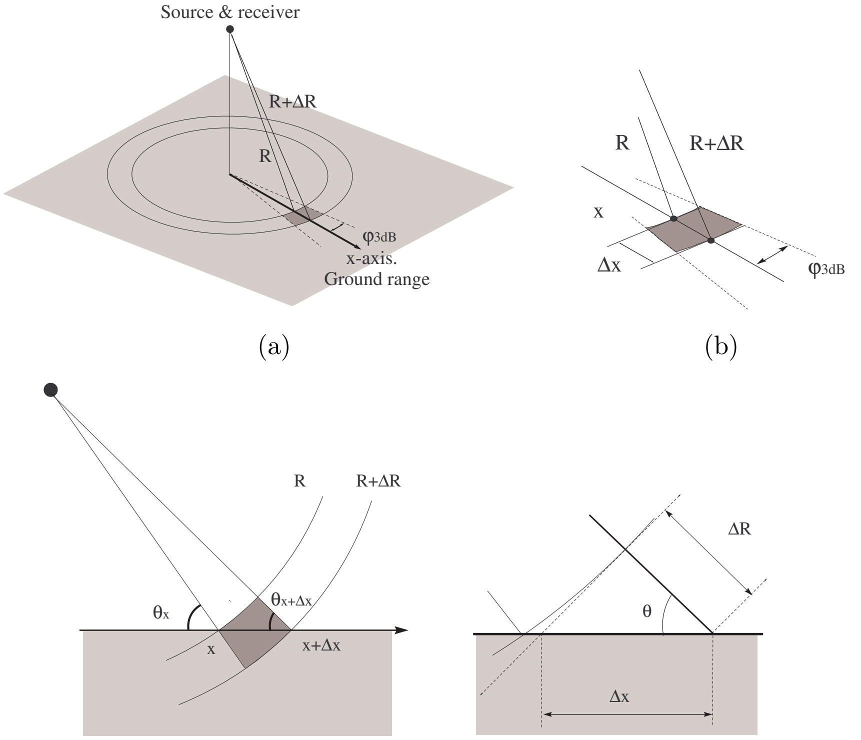

(a) (b) (c) (d)

Figure J.2: Sonar beam. (a) The resolution cell; (b) The resolution cell projected onto the flat seabed; (c) a vertical slice of the resolution cell and; (d) the relation between the slant range and ground range resolution as the incoming wave is considered locally plane.

cremental range, ΔR, is related to the sound speed, c, and pulse duration, τ_p, by

$$\Delta R \approx \frac{\tau_p c}{2}, \tag{J.2}$$

(see, e.g., Skolnik [84](Ch. 1.1)) that is, the range resolution in a sonar beam is approximately equal to half the pulse length. Let B be the pulse bandwidth and let it be assumed that the time-bandwidth of the pulse is equal to one, i.e.,

$$B\tau_p = 1. \tag{J.3}$$

In addition, it is assumed that the baseband sampling frequency, F_s, equals the bandwidth of the pulse, i.e.,

$$F_s = B. \tag{J.4}$$

A combination of equation (J.3) and (J.4) leads to, $\tau_p = 1/F_s$, which inserted into equation (J.2) yields

$$\Delta R = \frac{c}{2Fs}, \tag{J.5}$$

i.e., the range resolution corresponds to half the distance the sound moves between two samples. The dark shaded area illustrated in figure J.2(a) and J.2(b) is the part of the mean height seabed located within a particular resolution cell, which is here denoted the ground range resolution patch. The slant range, R, and slant range resolution, ΔR, can be projected into the ground range, x, and ground range resolution, Δx, on the ground range resolution patch. Each beam of the receiver array measures the backscattered field with a 3 dB bandwidthφ_{3dB}, within the main lobe; hence the angular resolution is $2\varphi_{3dB}$ radians. Figure (c) shows the resolution cell in a vertical slice. The grazing angle, θ, varies only slightly through the resolution cell, that is, from θ_x to $\theta_{x+\Delta x}$ and, consequently they are considered equal, i.e.,

$$\theta_x \approx \theta_{x+\Delta x}, \tag{J.6}$$

at the point x the grazing angle is

$$\cos\theta_x = \frac{x}{R}. \tag{J.7}$$

Figure (d) sketches the relation between the slant range resolution, ΔR, and the ground range resolution, Δx, under the assumption that the incoming wave is locally plane and, at the point $x + \Delta x$ the grazing angle is

$$\cos\theta_{x+\Delta x} = \frac{\Delta R}{\Delta x}, \tag{J.8}$$

The area of the ground range resolution patch is given by

$$A = \frac{2\varphi_{3dB}}{2\pi}\left[\pi(x+\Delta x)^2 - \pi x^2\right] \approx 2\varphi_{3dB} x \Delta x,$$

where the final approximation follows since $\Delta x << x$. Let the area be expressed as a function of R instead of x; application of (J.8) and (J.7) in (J.9) yields

$$A \approx 2\,\varphi_{3dB} R\cos\theta\left(\frac{\Delta R}{\cos\theta}\right) = 2\,\varphi_{3dB}\,R\,\Delta R, \tag{J.9}$$

and it is seen that the resolution patch area depends on the range, R.

J.2 The wave field

The strength of the backscattered field from a resolution cell depends on the impedance contrast, the interface roughness, and volume heterogeneities. Typically, the resolution cell is considered to consist of independent, randomly distributed point scatters that allows one to draw simple conclusions regarding the expected value of the backscattering strength. For example, Lambert's law may be applied on a rough sandy seabed where the scattered field does not contain any coherent contributions. However, if the seabed is covered with stones the backscattered field exhibits higher dynamic variations with strong reflections.

In the following the source is assumed to be a point source that emits a spherical wave. At the range, R, from the source the average intensity or acoustic power per unit area is,

$$I_i = \frac{p_0^2}{R^2 \rho c}, \tag{J.10}$$

where p_0 is the peak pressure amplitude one meter from the transducer, ρ the mass density of the water medium, and c the sound speed in water, see, e.g., Ref. [7](pp. 44-45). The emitted field that intercepts a small surface patch area, A, within a resolution cell is assumed plane. The power intercepted by the surface patch is

$$\mathcal{P}_i = I_i A \sin \varphi_i, \tag{J.11}$$

where $A \sin(\varphi_i)$ represents the effective area and φ_i is the *local* grazing angle of the incoming field. It is assumed, for simplicity, that the surface-patch has

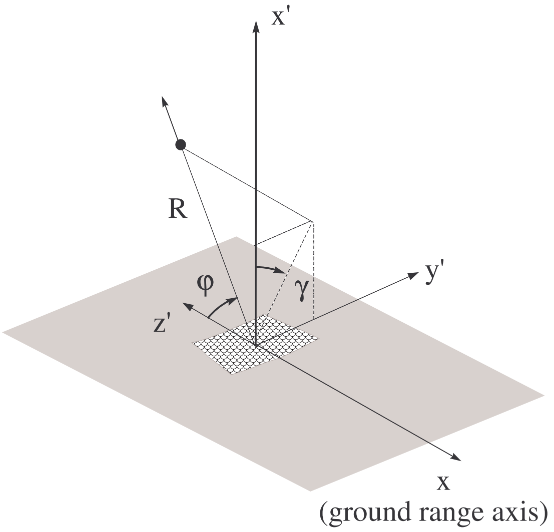

Figure J.3: A local coordinate system (') with origin at $x + \Delta x/2$ on the ground range axis. Spherical coordinates are applied: φ represents the polar angle with $0 \leq \varphi \leq \pi$ and γ the azimuthal angle with $0 \leq \gamma \leq 2\pi$.

an infinite impedance. Hence, the total power scattered back into the medium equals the incident power, i.e.,

$$\mathcal{P}_s = \mathcal{P}_i. \tag{J.12}$$

A spherical coordinate system with a polar axis (z'-axis) directed toward the sonar and an azimuthal plane (the $x'y'$-plane) orthogonal to the plane of the surface patch is introduced, see Fig. (J.3). The polar angle $0 \leq \varphi \leq \pi$, corresponds to the grazing angle with respect to the seabed and $-\pi/2 \leq \gamma \leq \pi/2$ is the azimuthal angle. The intensity of the field emitted from the surface path can expressed as

$$\mathbf{I}_s(\varphi,\gamma,R) = \frac{\mathcal{P}_i\, b(\varphi,\gamma)}{R^2}\,\mathbf{e}'_r, \tag{J.13}$$

where $\mathbf{e}'_r$ is the radial unit vector, and $b(\varphi,\gamma)$ is the radation pattern of the resolution cell, see, e.g., Ref. [7](pp. 45-47). Inserting Eq. (J.9) and Eq. (J.10) into Eq. (J.11) yields,

$$\mathcal{P}_i = \Psi\,\frac{\sin\varphi_i}{R}\,, \tag{J.14}$$

where $\Psi = (2p_0^2\varphi_{3dB}\Delta R)/(\rho c)$. Finally, the intensity magnitude of Eq. (J.13) is

$$I_s(\varphi,\gamma,R) = \Psi\,\frac{b(\varphi,\gamma)\sin\varphi_i}{R^3}. \tag{J.15}$$

Hence, the pressure envelope can be expressed as

$$p_s(\varphi,\gamma,R) = \left[\,\Psi\,b(\varphi,\gamma)\sin\varphi_i\,\right]^{1/2}R^{-3/2}, \tag{J.16}$$

where the $R^{-3/2}$ dependency is the essential conclusion drawn here. On the rough surface where Lambert's can be applied the radiation pattern is $b(\varphi,\gamma) = \mu_s\cos(\gamma)\sin(\varphi)$, where μ_s is a constant that accounts for the energy. On an infinitely high impedance surface, where the scattered field can be described by Lambert's law the radiation pattern is $b(\varphi,\gamma) = \mu_s\cos(\gamma)\sin(\varphi)$, where μ_s is a constant that must be determined. Equation (J.13) is

$$\mathbf{I}_s(\varphi,\gamma,R) = \frac{\mathcal{P}_i\, b(\varphi,\gamma)}{R^2}\,\mathbf{e}'_r, \tag{J.17}$$

for $-\pi/2 \leq \gamma \leq \pi/2$ and $\mathbf{I}_s(\varphi,\gamma,R) = \mathbf{0}$ for $\pi/2 \leq \gamma \leq 3\pi/2$. In order to determine μ_s for the the rigid rough surface the total scattered power is considered,

$$\mathcal{P}_s = \int_S \mathbf{I}_s\cdot\mathbf{e}_r\,dS, \tag{J.18}$$

where S represents the area of the hemisphere of radius R around the surface patch using an incremental area element, $dS = R^2\sin(\varphi)\,d\varphi d\gamma$. Hence,

$$\begin{aligned}
\mathcal{P}_s &= \int_{-\pi/2}^{\pi/2}\int_0^{\pi}\mathbf{I}_s\cdot\mathbf{e}_r\,R^2\,\sin(\varphi)\,d\varphi d\gamma,\\
&= \mu_s\mathcal{P}_i\int_{-\pi/2}^{\pi/2}\cos(\gamma)\,d\gamma\int_0^{\pi}\sin^2(\varphi)\,d\varphi,\\
&= \mu_s\mathcal{P}_i\,2\left[\frac{\varphi}{2}-\frac{\sin(2\varphi)}{4}\right]_0^{\pi},\\
&= \mu_s\mathcal{P}_i\,\pi,
\end{aligned} \tag{J.19}$$

and thus, $\mu_s = 1/\pi$.

In this appendix the pressure envelope within a sonar beam has been re-examined from the expression given by Urick (Ref. [14](pp. 245)). Equation (J.16) shows that the pressure decay is proportional to the range as $R^{-3/2}$. This result will be applied as a correction to the pressure computed from the 2D field, where the pressure decays as $R^{-1/2}$.

Appendix K

Field integral for the plane triangular facet

The field integral given in Eq. (9) in Ref. [3] is the starting point of the derivation of the robust expression Eq. (14a) in Ref. [3].
The integral of the left sub-triangle, I_1, is

$$\begin{aligned}
I_1 &= \int_{x'_1}^{0} \Big(\int_{0}^{\alpha x' + y'_3} e^{-ik(ax'+by')}\, dy' \Big) dx' \\
&= \int_{x'_1}^{0} e^{-ikax'} \Big(\int_{0}^{\alpha x' + y'_3} e^{-ikby'}\, dy' \Big) dx' \\
&= \int_{x'_1}^{0} e^{-ikax'} \Big(\frac{1}{-ikb} \Big[e^{-ikby'} \Big]_{0}^{\alpha x' + y'_3} \Big) dx' \\
&= \frac{-1}{ikb} \int_{x'_1}^{0} e^{-ikax'} [\, e^{-ikb(\alpha x' + y'_3)} - 1 \,]\, dx' \\
&= \frac{-1}{ikb} \Big(e^{-ikby'_3} \int_{x'_1}^{0} e^{-ik(a+b\alpha)x'} dx' - \int_{x'_1}^{0} e^{-ikax'} dx' \Big) \\
&= \frac{-1}{ikb} \Big(\frac{e^{-ikby'_3}}{-ik(a+b\alpha)} \,[\, e^{-ik(a+b\alpha)x'} \,]_{x'_1}^{0} - \frac{1}{-ika} \,[\, e^{-ikax'} \,]_{x'_1}^{0} \Big) \\
&= \frac{1}{ikb} \Big(\frac{e^{-ikby'_3}}{ik(a+b\alpha)} \,[\, e^{-ik(a+b\alpha)x'} \,]_{x'_1}^{0} - \frac{1}{ika} \,[\, e^{-ikax'} \,]_{x'_1}^{0} \Big) \\
&= \frac{1}{ikb} \Big(\frac{e^{-ikby'_3}}{ik(a+b\alpha)} \,(\, 1 - e^{-ik(a+b\alpha)x'_1} \,) - \frac{1}{ika} \,(\, 1 - e^{ikax'_1} \,) \Big).
\end{aligned} \tag{K.1}$$

The integral of the right sub-triangle, I_2, is

$$\begin{aligned}
I_2 &= \int_0^{x'_2} \Big(\int_0^{\beta x' + y'_3} e^{-ik(ax'+by')}\, dy' \Big) dx' \\
&= \int_0^{x'_2} e^{-ikax'} \Big(\int_0^{\beta x' + y'_3} e^{-ikby'}\, dy' \Big) dx' \\
&= \int_0^{x'_2} e^{-ikax'} \Big(\frac{1}{-ikb} \Big[e^{-ikby'} \Big]_0^{\beta x' + y'_3} \Big) dx' \\
&= \frac{-1}{ikb} \int_0^{x'_2} e^{-ikax'} [\, e^{-ikb(\beta x' + y'_3)} - 1 \,]\, dx' \\
&= \frac{-1}{ikb} \Big(e^{-ikby'_3} \int_0^{x'_2} e^{-ik(a+b\beta)x'} dx' - \int_0^{x'_2} e^{-ikax'} dx' \Big) \\
&= \frac{-1}{ikb} \Big(\frac{e^{-ikby'_3}}{-ik(a+b\beta)} [\, e^{-ik(a+b\beta)x'} \,]_0^{x'_2} - \frac{1}{-ika} [\, e^{-ikax'} \,]_0^{x'_2} \Big) \\
&= \frac{1}{ikb} \Big(\frac{e^{-ikby'_3}}{ik(a+b\beta)} [\, e^{-ik(a+b\beta)x'} \,]_0^{x'_2} - \frac{1}{ika} [\, e^{-ikax'} \,]_0^{x'_2} \Big) \\
&= \frac{1}{ikb} \Big(\frac{e^{-ikby'_3}}{ik(a+b\beta)} (\, e^{-ik(a+b\beta)x'_2} - 1 \,) - \frac{1}{ika} (\, e^{ikax'_2} - 1 \,) \Big).
\end{aligned} \tag{K.2}$$

Let $I = I_1 + I_2$:

$$\begin{aligned}
I = \frac{e^{-ikby'_3}}{b(ik)^2} \Big(\frac{1}{a+b\alpha} (\, 1 - e^{-ik(a+b\alpha)x'_1} \,) + \frac{1}{a+b\beta} (\, e^{-ik(a+b\beta)x'_2} - 1 \,) \Big) - \\
\frac{1}{ab(ik)^2} \Big(e^{-ikax'_2} - e^{-ikax'_1} \Big),
\end{aligned} \tag{K.3}$$

and hence,

$$\begin{aligned}
I = \frac{e^{-ikby'_3}}{b(ik)^2} \Big(\frac{e^{-ik(a+b\alpha)x'_1/2}}{a+b\alpha} [\, e^{ik(a+b\alpha)x'_1/2} - e^{-ik(a+b\alpha)x'_1/2} \,] + \\
\frac{e^{-ik(a+b\beta)x'_2/2}}{a+b\beta} [\, e^{-ik(a+b\beta)x'_2/2} - e^{ik(a+b\beta)x'_2/2} \,] \Big) - \\
\frac{e^{-ikax'_2/2} e^{-ikax'_1/2}}{ab(ik)^2} \Big(e^{-ika(x'_2 - x'_1)/2} - e^{-ika(x'_1 - x'_2)/2} \Big),
\end{aligned} \tag{K.4}$$

and subsequently,

$$
\begin{aligned}
I = \frac{e^{-ikby'_3}}{b(ik)} \Bigg(& x'_1\, e^{-ik(a+b\alpha)x'_1/2}\ \frac{e^{ik(a+b\alpha)x'_1/2} - e^{-ik(a+b\alpha)x'_1/2}}{2ik(a+b\alpha)x'_1/2} - \\
& x'_2\ e^{-ik(a+b\beta)x'_2/2}\ \frac{e^{ik(a+b\beta)x'_2/2} - e^{-ik(a+b\beta)x'_2/2}}{2ik(a+b\beta)x'_2/2} \Bigg) + \\
& (x'_2 - x'_1)\, \frac{e^{-ikax'_2/2} e^{-ikax'_1/2}}{b(ik)}\ \ \frac{e^{ika(x'_2-x'_1)/2} - e^{-ika(x'_2-x'_1)/2}}{2ika(x'_2-x'_1)/2}.
\end{aligned}
\tag{K.5}
$$

Since $\alpha x_1 = -y_3$ and $\beta x_2 = -y_3$ one get

$$
\begin{aligned}
e^{-ikb\alpha x_1/2} &= e^{ikby_3/2}, \\
e^{-ikb\beta x_2/2} &= e^{ikby_3/2},
\end{aligned}
\tag{K.6}
$$

and finally,

$$
\begin{aligned}
I = \frac{1}{b(ik)} \Bigg(& x'_1\, e^{-ik(ax'_1+by_3)/2}\ \frac{\sin(k[a+b\alpha]x'_1/2)}{k[a+b\alpha]x'_1/2} - \\
& x'_2\ e^{-ik(ax'_2+by_3)/2}\ \frac{\sin(k[a+b\beta]x'_2/2)}{k[a+b\beta]x'_2/2} + \\
& (x'_2 - x'_1)\, e^{-ika(x'_1+x'_2)/2}\ \frac{\sin(ka[x'_2 - x'_1]/2)}{ka[x'_2 - x'_1]/2} \Bigg).
\end{aligned}
\tag{K.7}
$$

Hence, Eq. (K.7) is the central factor applied for the robust expression in Ref. [3].

Appendix L

DTU Report

2D SIGNAL PROCESSING FOR SYNTHETIC SEAFLOOR GENERATION

(Report individual Course 5 ECTS Points)

Gorm Wendelboe
Supervisor: H.B.D Soerensen

October 2005

1 INTRODUCTION

The sonar model requires a model of the seabed roughness for computation of the backscattered field. Experiments with stereo-photogrammetric cameras, see e.g., Ref. [2][1][3], have shown that for sandy seabeds the roughness has a spatial power spectrum following a power law, that is,

$$S(K) = \frac{\phi}{K^{\gamma}} \tag{1}$$

where K is the wave number magnitude $K = \sqrt{k_x^2 + k_y^2}$ with k_x and k_y being the roughness wave number components in the x- and y direction respectively; γ is the spectral exponent and ϕ the spectral strength. In a 3D Cartesian coordinate system the height field value, h, is measured along the z-axis and it is a function of the ground plane coordinates x and y, that is,

$$h = h(x, y). \tag{2}$$

The synthetic height field is generated in the frequency domain as

$$H(K) = X(K)\sqrt{S(K)} \tag{3}$$

where $X(K)$ is the discrete, 2D, Fourier Transform of a unit variance 2D signal. For ripples the power spectrum takes the form

$$S(K) = \frac{\phi}{2}\left(|K - K_r|^{-\gamma} + |K + K_r|^{-\gamma}\right) \tag{4}$$

where $K_r = \sqrt{k_{xr}^2 + k_{xr}^2}$ is the ripple wave number. Figure (1) shows spectra and stochastic realizations with and without ripples.

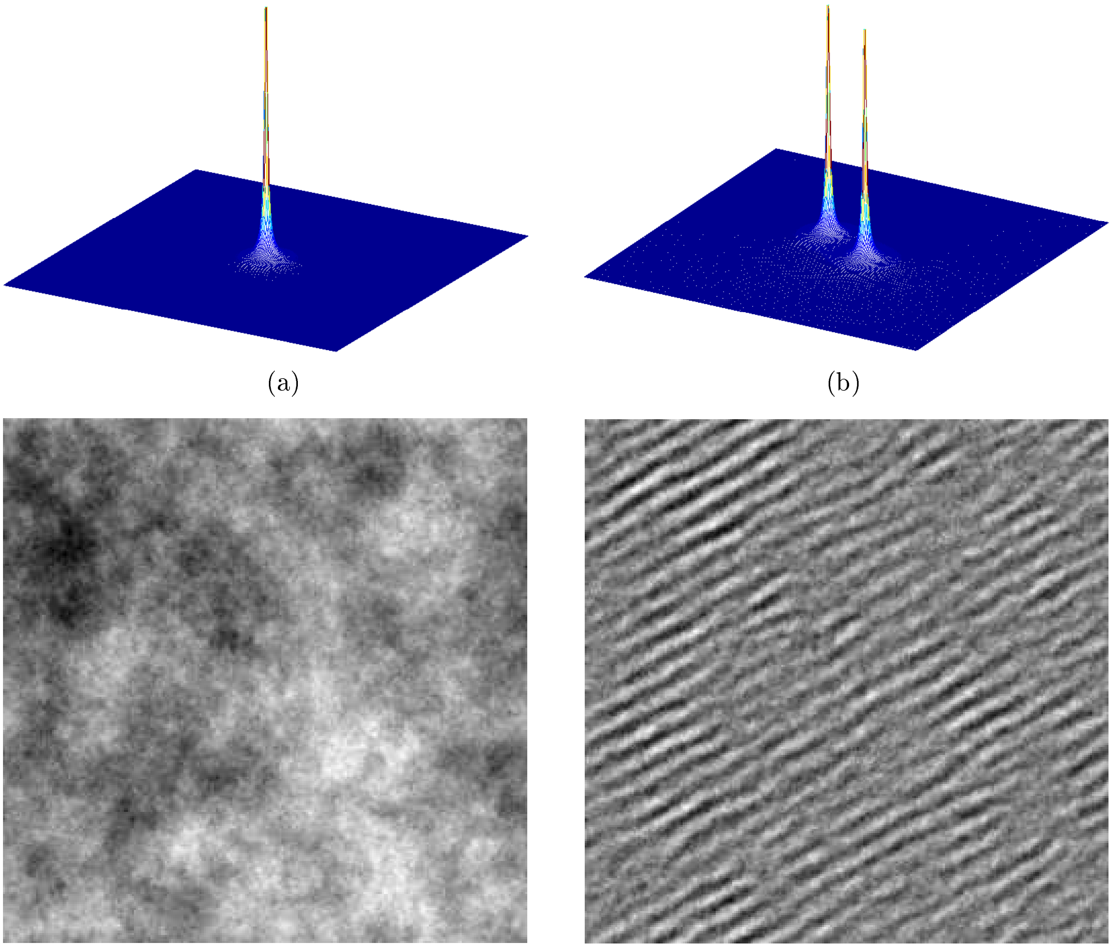

(a) (b)

(c) (d)

Figure 1: *Spectrum of the transfer-function with no ripples (a) and with ripples (b). The stochastic realizations with no ripples (c) and with ripples (d).*

2 2D OVERLAP-ADD FILTERING

Generation of a large synthetic seabed cannot be made with a single 2D-FFT unless a very low resolution is applied. The state of the art PC's anno 2006 reach their limit when a 2048×2048 matrix must be processed in the workspace. Typically, the sector sonar may ensonify an area of $50\text{m} \times 50\text{m} = 2500\text{m}^2$, and since the distance between adjacent height field points must be less than a quarter of the acoustic wavelength (≈ 3 mm) a $(50/(0.25 \times 0.003))^2 = 67000 \times 67000$ matrix is required. However, the height field will only be generated with a resolution down to, say, 1 cm, and hence, only a $(50/0.01)^2 = 5000 \times 5000$ matrix is required. The reason is that the backscattered pressure from the seabed will be computed using 2D height profiles in lines that corresponds to the directions of the sonar beams, see e.g., Ref. [5], because, a full three dimensional computation of the

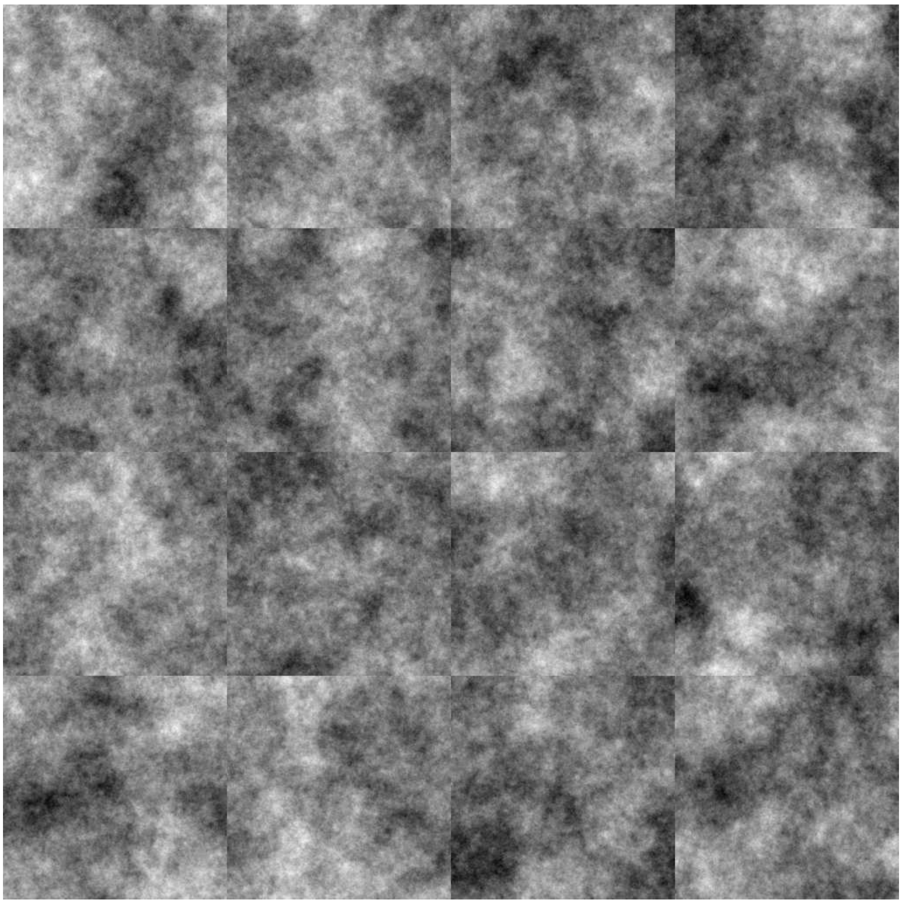

Figure 2: *The motivation for applying a 2D overlap-add method. The figure shows a synthetic seabed generated by 16 FFT's that subsequently are collected into one height field. The vertical and horizontal lines of discontinuity are artifacts that appears because the surface correlation has been neglected in the processing.*

scattered field will require an excessive computational workload, and that must be avoided (the height profiles are obtained by interpolation of the large scale roughness height field, and subsequently, a small scale roughness is superimposed on the height profile). Nevertheless, the large scale height field does still require more numbers than it is possible to process in the workspace. Therefore, the synthetic seabed will be generated using several, but smaller, matrices. Figure (2) shows an unfortunate consequence when 16 FFT's have been used to generate the height field and subsequently are collected into one height field matrix. The vertical and horizontal lines of discontinuity are artifacts that appears because the surface correlation has been neglected in the processing; in other words the convolution process has been truncated in each sub-image. The overlap-add method (see e.g. Ref. [4], pp. 430-432, for the 1D case) will instead be applied in the following. Consider the power-law filter of size (N, N); in the spatial domain its matrix is padded with N zeros in the rows and columns and transferred back to the frequency domain as a $(2N, 2N)$ filter, see figure (3). In figure (4) a synthetic seabed generated after zero-padding the spatial response is presented. In the, apparently, gray shaded frame, contours of the convolution residuals can be observed. The procedure is convenient for all PC's as a limited workspace is the main obstacle. The figures (5-8) illustrate the procedure.

```
h          = fftshift(ifft2(H));
h(2*N,2*N) = 0;
H          = fftshift(fft2(h));
```

Figure 3: *Zero-padding code*

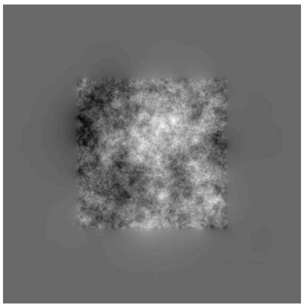

Figure 4: *The synthetic seabed matrix when the spatial response of a* $N \times N$ *power-law filter matrix has been padded with* N *zeros in the spatial domain (along the rows and columns) so that the resulting power law frequency response matrix is of size* $2N \times 2N$*. In the, apparently, gray shaded frame, contours of the convolution residuals can be observed.*

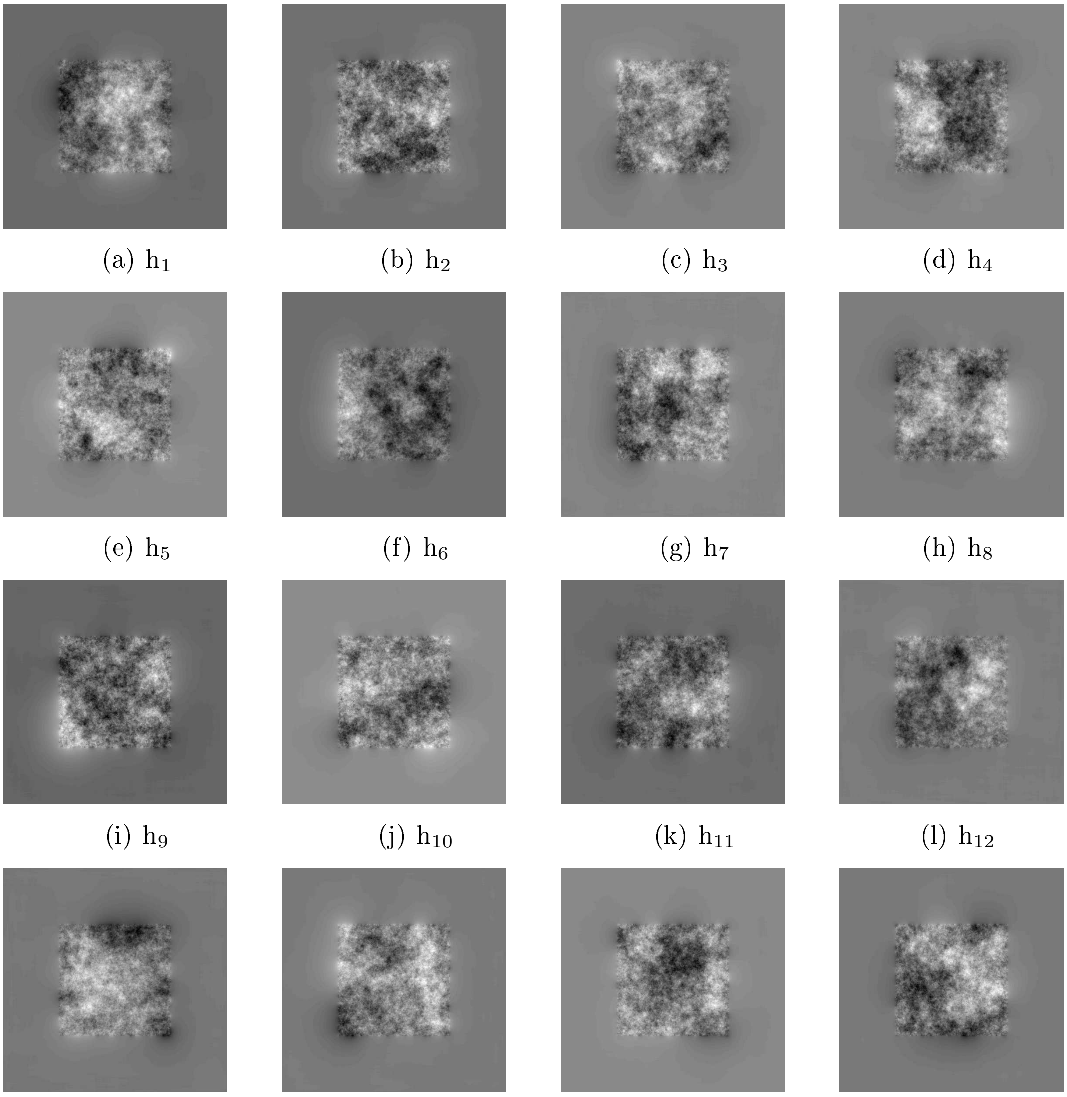

(a) h_1 (b) h_2 (c) h_3 (d) h_4

(e) h_5 (f) h_6 (g) h_7 (h) h_8

(i) h_9 (j) h_{10} (k) h_{11} (l) h_{12}

(m) h_{13} (n) h_{14} (o) h_{15} (p) h_{16}

Figure 5: *First step in the generation of a large synthetic seafloor using the overlap-add method. 16 synthetic height fields have been generated using zero padding of the power law response. Each matrix is of size* $2N \times 2N$.

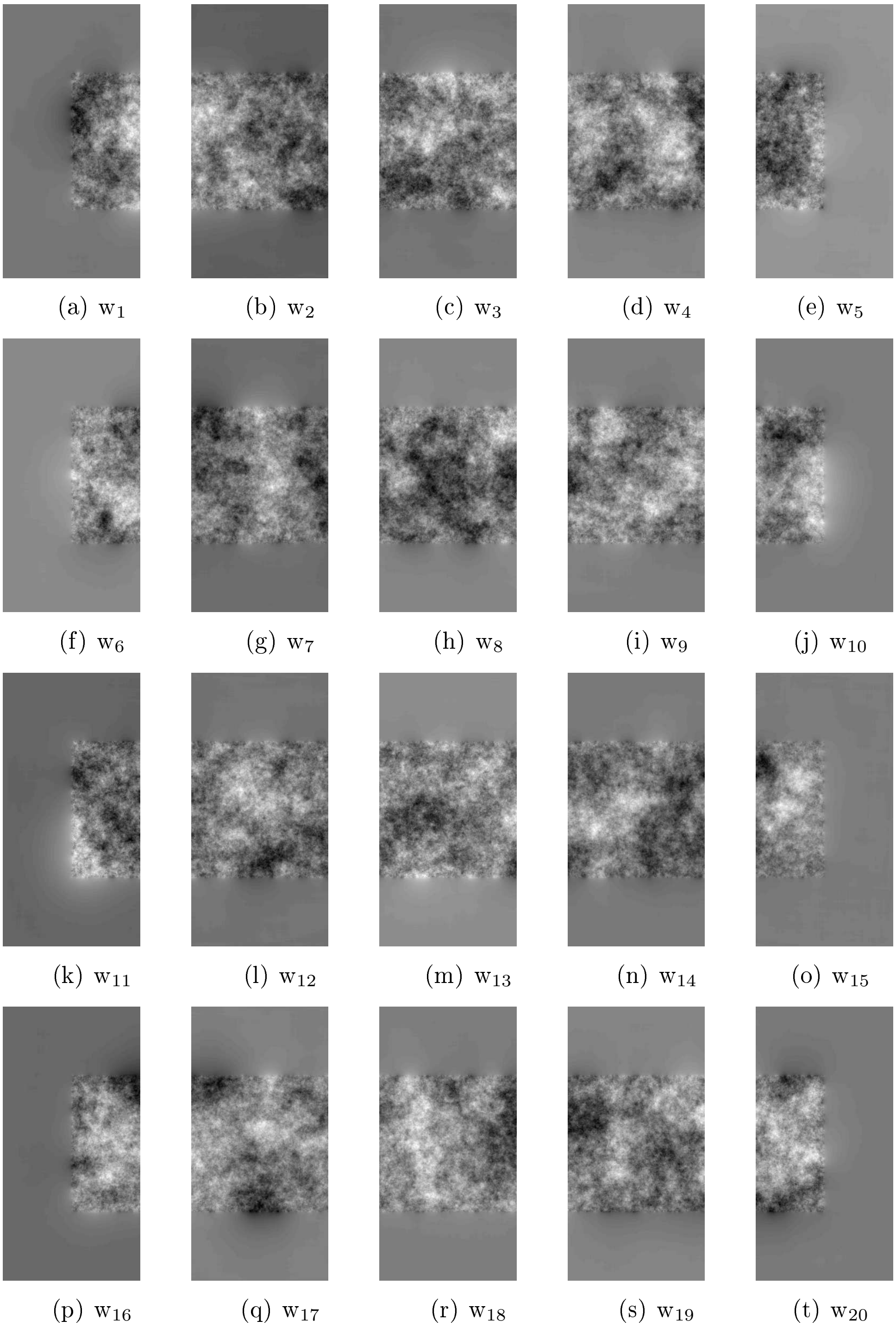

(a) w_1 (b) w_2 (c) w_3 (d) w_4 (e) w_5

(f) w_6 (g) w_7 (h) w_8 (i) w_9 (j) w_{10}

(k) w_{11} (l) w_{12} (m) w_{13} (n) w_{14} (o) w_{15}

(p) w_{16} (q) w_{17} (r) w_{18} (s) w_{19} (t) w_{20}

Figure 6: *Second step; the overlap-add procedure along the vertical direction. For example,* w_2*, see sub-figure (b), is* $w_2 = h_1(1:2N, N+1:2N) + h_2(1:2N, 1:N)$*.* h_1 *and* h_2 *are shown in the sub-figures (a) and (b) in figure (5).*

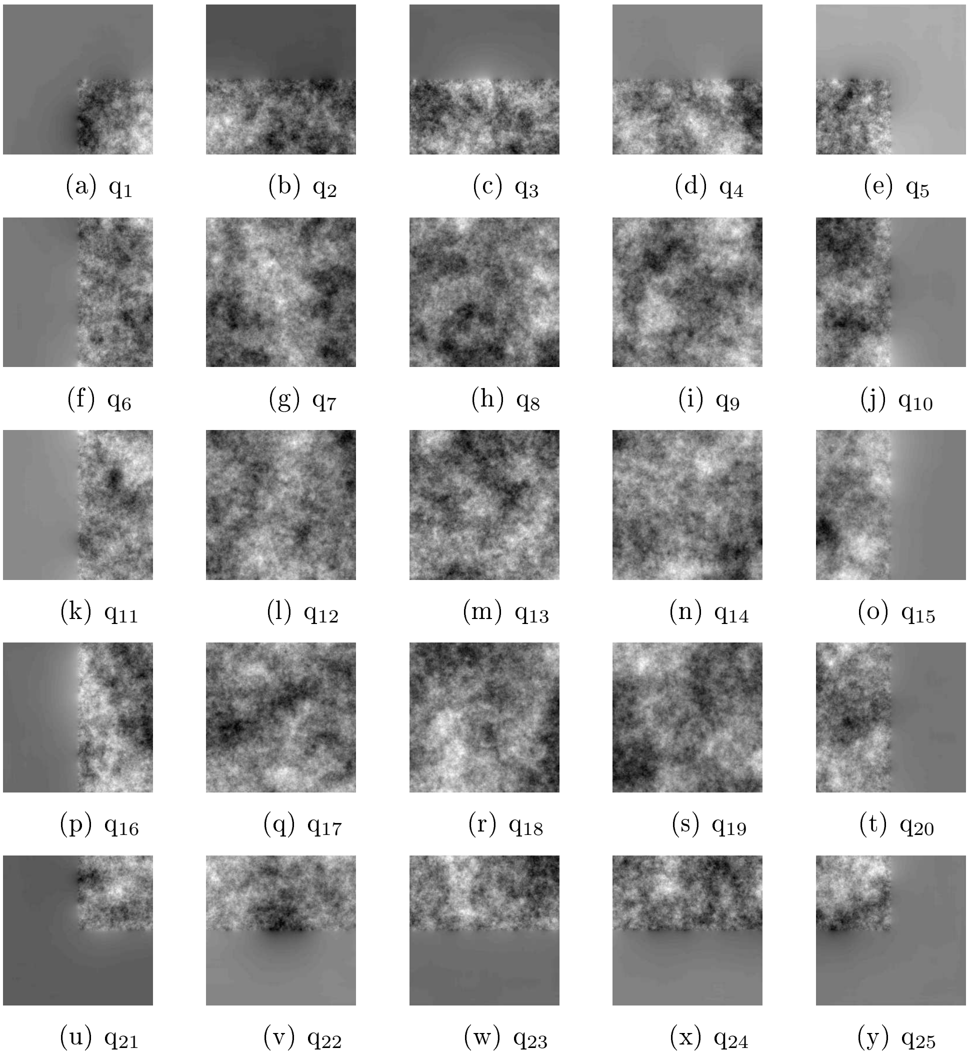

(a) q_1 (b) q_2 (c) q_3 (d) q_4 (e) q_5

(f) q_6 (g) q_7 (h) q_8 (i) q_9 (j) q_{10}

(k) q_{11} (l) q_{12} (m) q_{13} (n) q_{14} (o) q_{15}

(p) q_{16} (q) q_{17} (r) q_{18} (s) q_{19} (t) q_{20}

(u) q_{21} (v) q_{22} (w) q_{23} (x) q_{24} (y) q_{25}

Figure 7: *Third step; the overlap-add procedure along the horizontal directions. For example,* q_7*, see sub-figure (g), is* $q_7 = w_2(N+1:2N, 1:2N) + w_7(1:N, 1:2N)$*.* w_2 *and* w_7 *are shown in the sub-figures (b) and (g) in figure (6).*

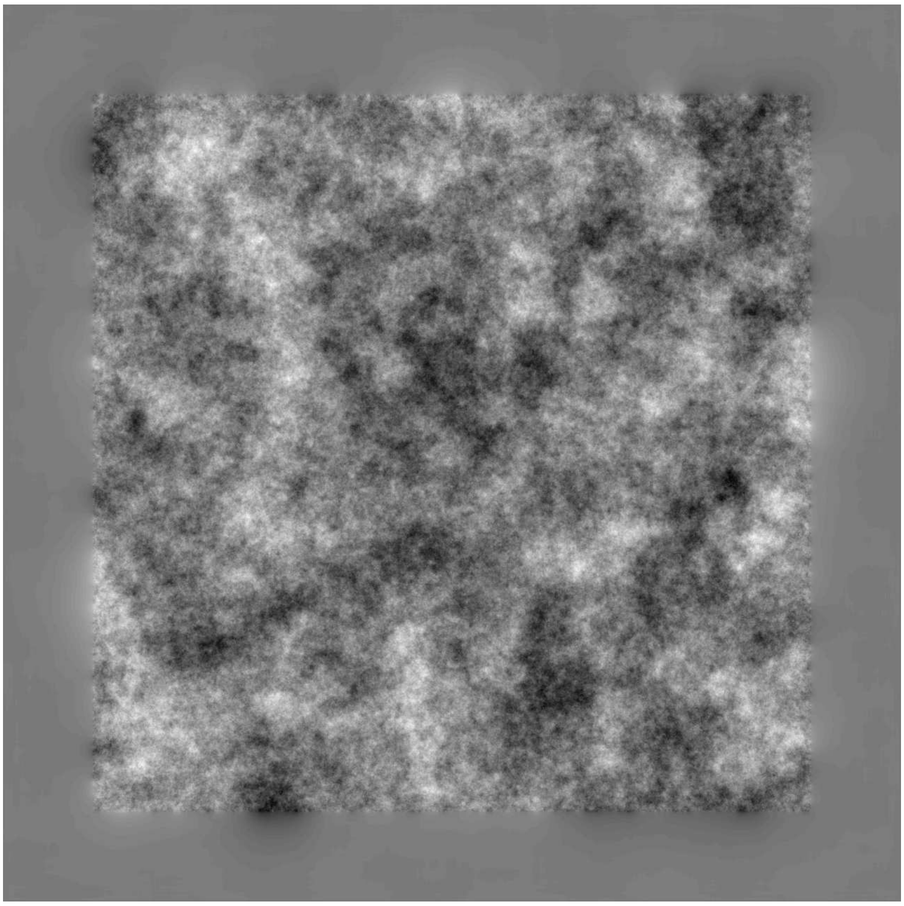

Figure 8: *Fourth and last step. All the q's from figure (7) are collected into one single matrix; the large seabed has been generated without unwanted artifact-lines, and thus, computation of the scattered field can be performed without unwanted phase-jumps.*

3 ADDITION OF SMALL SCALE ROUGHNESS

The sonar model developed so far does only include first order scattering effects, that is, the direct backscattered pressure from the seabed and the object; the pressure contributions are added to form the total backscattered field, see e.g., Ref. [5]. However, the second order field may contribute significantly to the total field, and hence, a method that localizes the essential areas on the seabed ensonified by object reflected sound has been developed, see e.g., Ref [6]. It is the intention, in future work, to compute this field, and for that purpose, the large scale height field must have superimposed small scale roughness with a resolution down to one quarter of the minimum signal wavelength. This section describe how the detected seabed areas ensonified by object reflected sound will be up-sampled and subsequently given additional, fine scale roughness. The first step is the insertion of zeros in the height field; suppose the height field must be up-sampled with an integer factor I, then $I-1$ zeros must be inserted between the values of h; this results in a 2D spectrum that is an I-fold periodic repetition of the original spectrum, see e.g. pp. $787-790$ in Proakis [4]. Figure (9) shows the

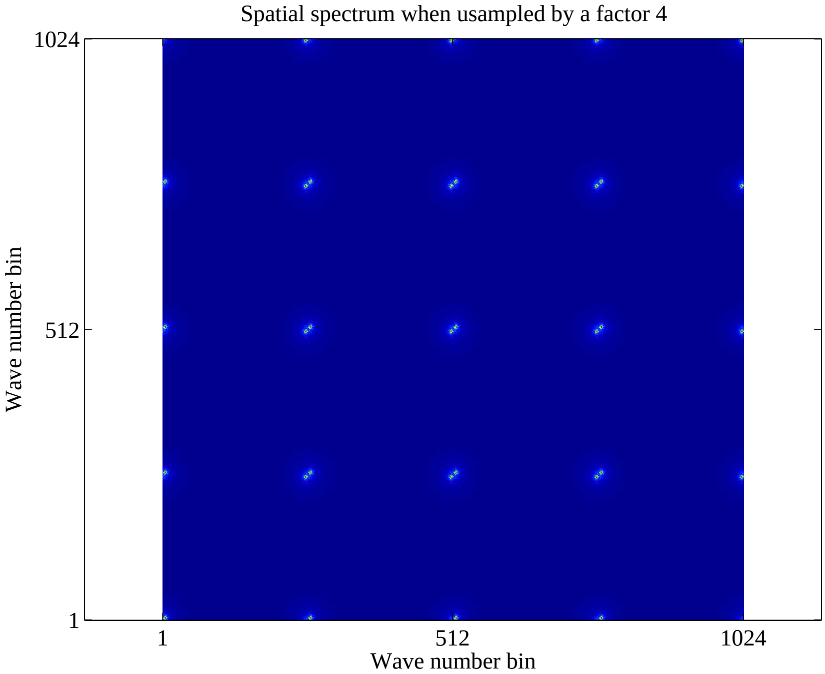

Figure 9: *Frequency spectrum of* h *after up-sampling by a factor* 4*. The spectrum is a* 4*-fold periodic repetition of the original spectrum.*

spectrum of a height field, h, up-sampled by a factor 4, i.e., 3 zero samples have been inserted between the existing height field values. The size of the height field matrix has increased from a 256×256 matrix to a 1024×1024. The next step in

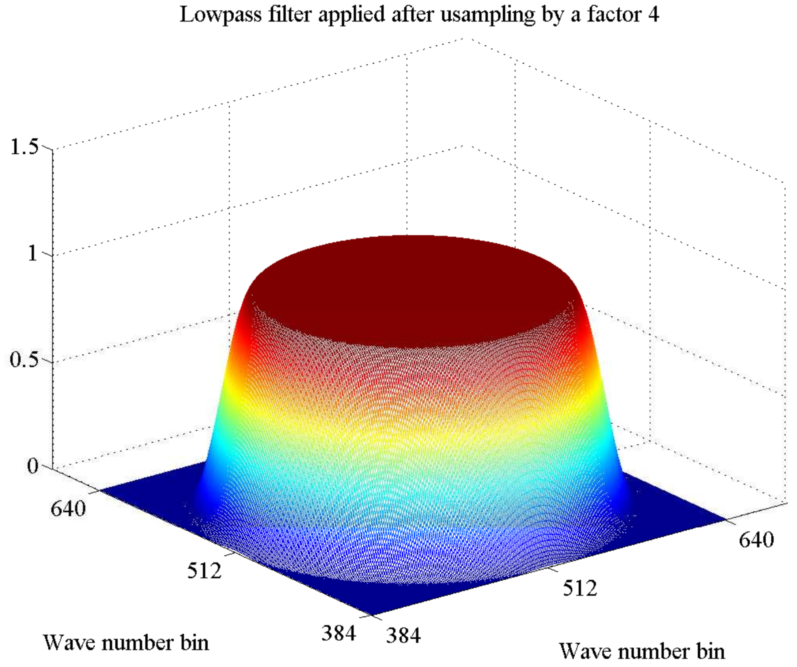

Figure 10: *Low-pass filter. A 1D Tukey window (with a tapering factor equal to* 0.3*) has been interpolated into a 2D signal*

the interpolation procedure is low pass filtering of the spectrum for the removal of image components above π/I. Figure (10) shows the frequency domain low pass filter, $W(K)$; the filter is generated from a 1D Tukey window (with a tapering constant equal to 0.3), and it has been interpolated into a 2D rotational symmetric shape, see figure (11) for the code. The small scale roughness is generated by first creating a full roughness height field that also contains large scale roughness; subsequently high-pass filtering in the frequency domain by the high pass-filter,

$$1 - W(K), \tag{5}$$

is carried out. Figure (12) shows the spectrum after low-pass filtering, i.e., the interpolated height field. The up-sampled and filtered large scale roughness height field can now be added to small scale roughness.

```
% Generate the Tukey-window with a length equal
% to the length, N, of the square matrix divided by the
% upsampling factor, I, and use a taper-ratio of 0.3:
 wt     = tukeywin(N/I,0.3);

% Extract the right part of the Tukey-window:
wt2     = wt(round(length(wt)/2) :length(wt));
% Indices for wt2
x2      = [1 : 1 :length(wt2)];

% Get the piecewise polynomial form of the cubic spline
% interpolant for later use with PPVAL:
pp      = spline(x2,wt2);


% Make a meshgrid of (x,y):
x       = [1 : 1 : length(wt)]-round(length(wt)/2);
y       = x;
[X,Y]   = meshgrid(x,y);

% Convert the (X,Y)-meshgrid into polar coordinates:
[TH,R]  = cart2pol(X,Y);

% The 2D-Tukey window is obtained using PPVAL:
WT      = ppval(pp,R);

% Remove unwated values:
Ind     = find(R>length(wt2)+1);
WT(Ind) = 0;

% The 2D Tukey window, wt, is now obtained:
wt      = WT;
```

Figure 11: *Matlab-code for the generation of the 2D Tukey window shown in figure (10)*

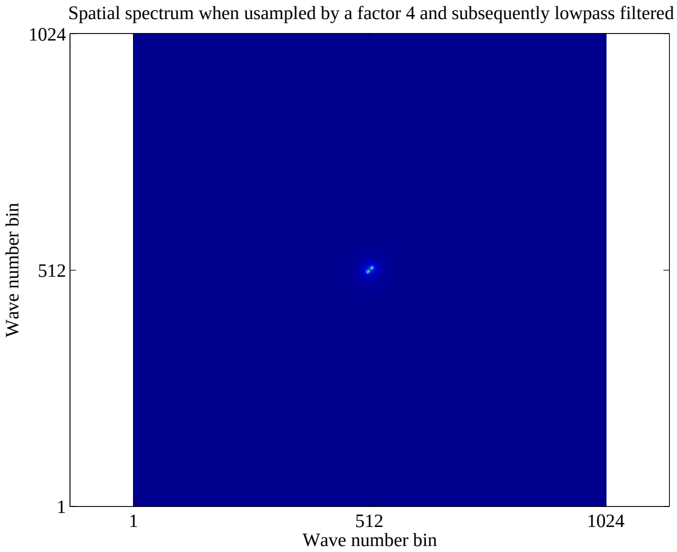

Figure 12: *Frequency spectrum of* h *after up-sampling by a factor* 4 *and subsequently lowpass filter with be filter given in figure (10).*

Figure (13) shows (a) a slice through the original large roughness spectrum before interpolation, (b) the large scale roughness spectrum after interpolation and the spectrum of the small scale roughness height field, and finally (c) the spectrum of the final high resolution height field. Figure (14) and figure (15) shows the resulting height fields.

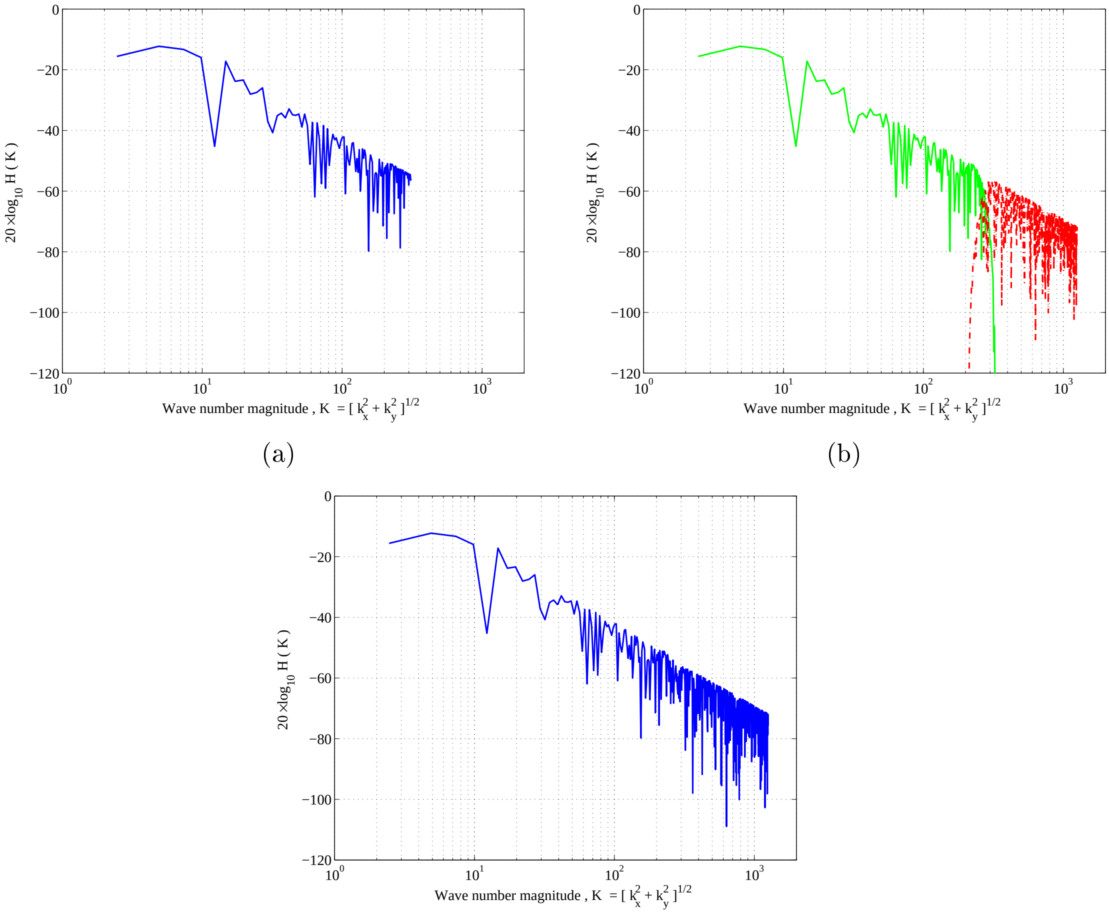

(a)

(b)

(c)

Figure 13: *Slices of spectra. (a) The original large roughness spectrum before interpolation, (b) the large scale roughness spectrum after interpolation and the spectrum of the small scale roughness height field, and finally (c) the spectrum of the final high resolution height field.*

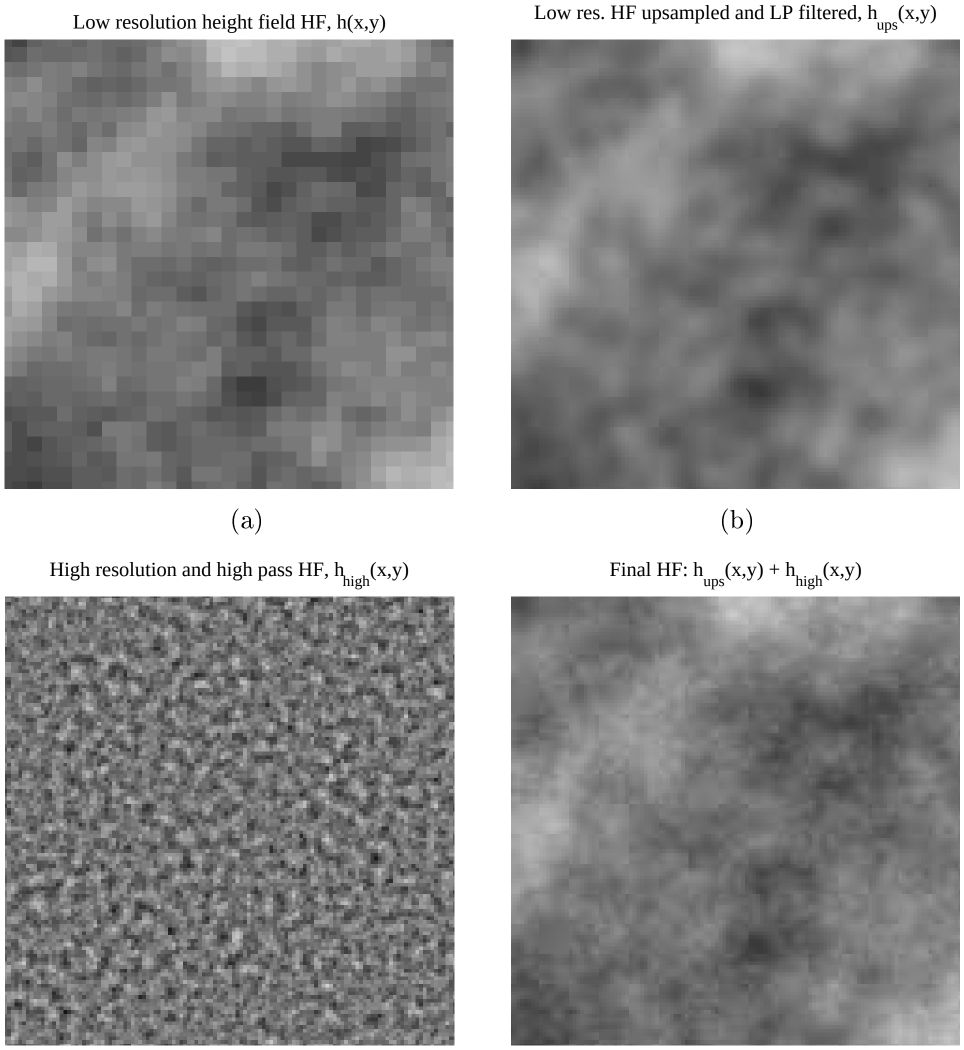

(a) (b) (c) (d)

Figure 14: *The final height field given in (d) is formed by addition of (b) and (c). These figures are zoomed into a limited range in order to visualize the effects of the signal processing*

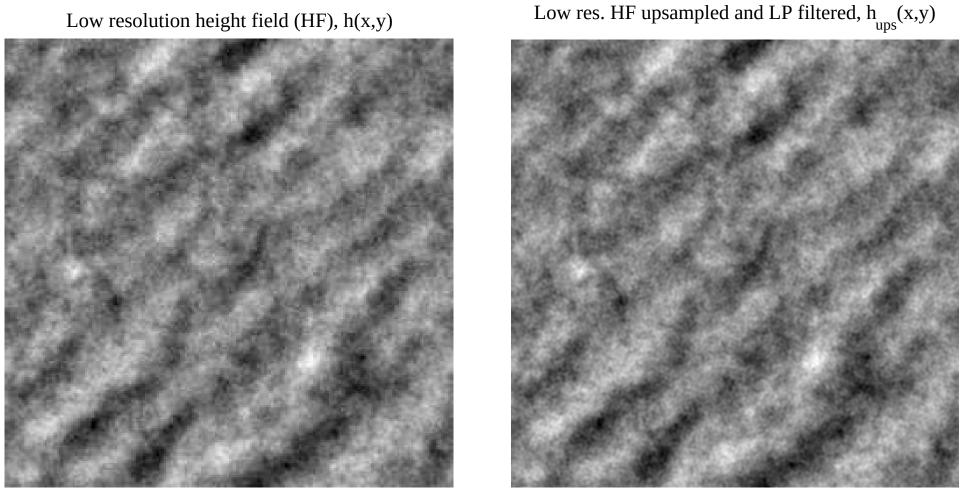

(a) q1 (b) q6

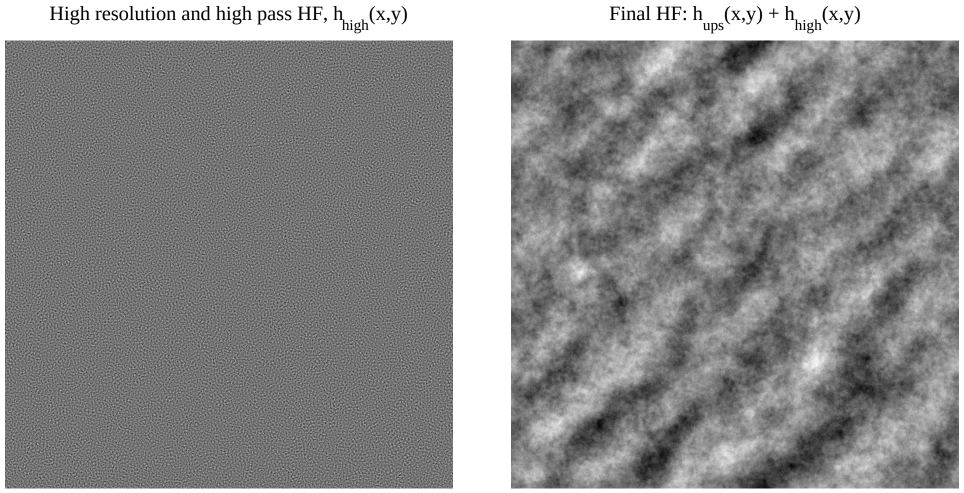

(c) q2 (d) q7

Figure 15: *The final height field given in (d) is formed by addition of (b) and (c). These figures show the full height field.*

4 MIXING DIFFERENT SEABED TYPES

The transition from a non-rippled to a rippled seabed can carried out by adding these two height field with an appropriative windowing method. First, the average path over the matrix must be decided and here only a straight line is considered. Upon the line a random walk is introduced, that is, an AR(1)-process

$$w(n) = \beta w(n-1) + \epsilon(n), \tag{6}$$

where w is the position, β is the weight-coefficient, and $\epsilon(n)$ is Gaussian noise. Figure (16) shows a rippled seabed mixed with a non-rippled one and where $\beta = 0.93$.

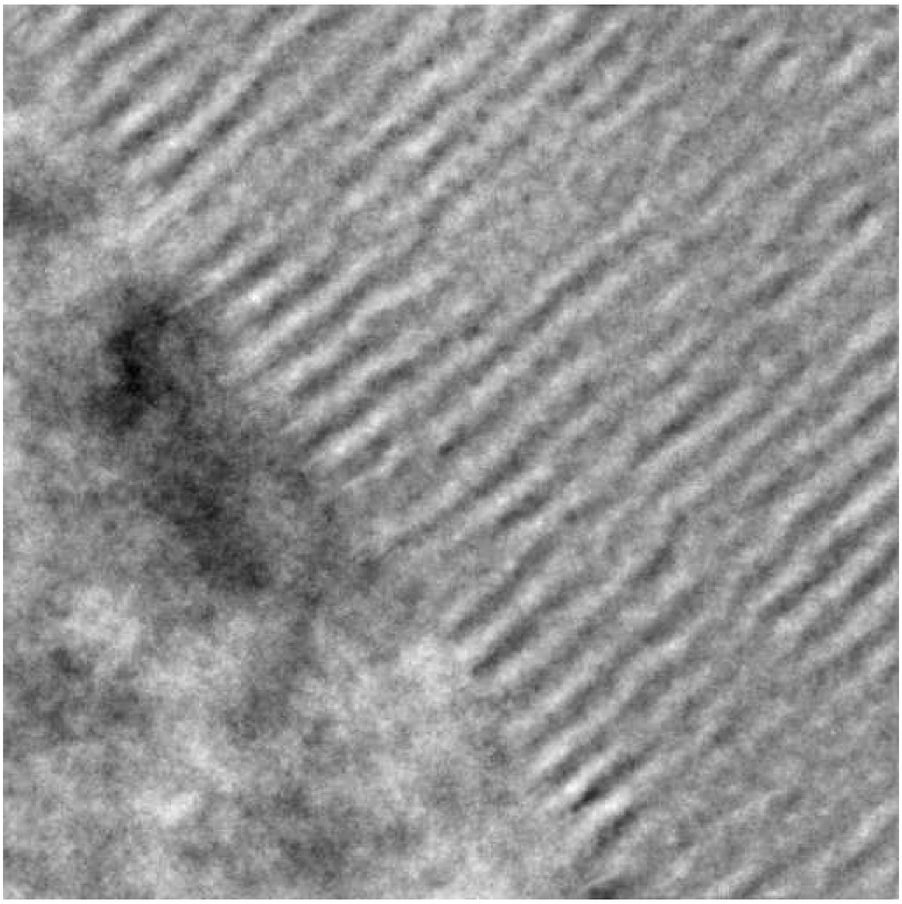

Figure 16: *Mixing two seabed types.*

5 CONCLUSION

Methods involving the generation of synthetic seabeds have been presented. The square-root of the power law spectra whose parameters have been estimated in stereo-photogrammetric experiments are the transfer functions applied. For filtering large 2D-sequences the over-lap-add method, adopted from 1D signal processing, has been applied; the method makes it possible to generate a large continuous synthetic seabed area in sequential steps within the limitations of the PC's workspace. A procedure to superimpose additional small scale roughness onto an existing height field near an object has been presented. Finally, an example of a height field that contains two different seabed types, and where the transition interface has been formed by a random walk, has been presented.

References

[1] K.B. Briggs, "Microtopographical roughness of shallow-water continental shelves," IEEE Journal of Oceanic Engineering Vol. 14, No. 4, pp. 360-367, October 1989.

[2] K.B. Briggs, D. Tang, and K. L. Williams "Characterisation of interface roughness of rippled sand off Fort Walton Beach, Florida," IEEE Journal of Oceanic Engineering Vol. 27, No. 3, pp. 505-514, July 2002.

[3] E. Pouliquen, G. Canepa, L. Pautet, and A.P. Lyons "Temporal variability of seafloor roughness and its impact on acoustic scattering," Proceedings of the seventh European Conference on underwater Acoustics, ECUA 2004 Delft, The Netherlands, 5-8 July, 2004.

[4] J. G. Proakis, D.G. Manolakis, *Digital Signal Processing. Principles, algorithms, and applications*, Third Edition, Prenctice Hall, Inc, 1996.

[5] G. Wendelboe, J.M. Bell, H.B.D. Soerensen, and B. Damsgaard. Simulation of sector sonar images, *Proceedings of the seventh European Conference on Underwater Acoustics, ECUA2004*, Delft, The Netherlands.

[6] G. Wendelboe, F. Jacobsen, and J.M. Bell. Localization of seabed domains ensonified by object reflected sound at very high frequnecies, *Boundary influences in shallow water high frequnency acoustics*, Acoustics 2005, Bath, UK.

Bibliography

[1] G. Wendelboe, J. Bell, H. B. D. Soerensen, and B. Damsgaard, “Simulation of sector sonar images”, *Proceedings of the seventh European Conference on Underwater Acoustics*, ECUA2004, Delft, The Netherlands, 5-8 July, 2004, pp. 857–862.

[2] G. Wendelboe, J. M. Bell, and F. Jacobsen, “Localization of seabed domains ensonified by object reflected sound at very high frequencies”, *Proceedings of Boundary Influences in High Frequency, Shallow Water Acoustics*, Bath, UK, 5th-9th September, 2005, pp. 391–398.

[3] G. Wendelboe, J. M. Bell, and F. Jacobsen, “A numerically accurate and robust expression for bistatic scattering from a plane triangular facet”, J. Acoust. Soc. Am. **119**, 701–704 (2006).

[4] G. Wendelboe, F. Jacobsen, and J. M. Bell, “An equivalent roughness model for seabed backscattering at very high frequencies using a band-matrix”, Conditionally accepted for publication to J. Acoust. Soc. Am., October, 2006. .

[5] G. Wendelboe, “2D signal Processing for Synthetic Seafloor Generation”, Report individual course, Oersted·DTU, DK, April 2005.

[6] L. E. Kinsler, A. R. Frey, A. B. Coppens, and J. V. Sanders, *Fundamentals of Acoustics* (John Wilay and Sons, New York, 1982).

[7] A. D. Pierce, *Acoustics. An introduction to its physical principles and applications* (Acoustical Society of America, New York, 1991).

[8] V. Murino and A. Trucco, “Three-dimensional image generation and processing in underwater acoustic vision”, Proc. IEEE **88**, 1903–1937 (1994).

[9] H. Medwin and C. S. Clay, *Fundamentals of acoustical oceanography* (Academic Press, London) (1998).

[10] J. S. Bolton, “Porus materials for sound absorption and transmission control”, *Proceedings of Internoise, Environmental Noise Control*, Rio de Janeiro, 7-10 August, 2005.

[11] K. L. Williams, J. M. Grochocinski, and D. R. Jackson, “Interface scattering by poroelastic seafloors: First-order theory”, J. Acoust. Soc. Am. **110**, 2956–2963 (2001).

[12] E. I. Thorsos, D. R. Jackson, and K. L. Williams, “Modeling of subcritical penetration into sediments due to interface roughness”, J. Acoust. Soc. Am. **107**, 263–277 (2000).

[13] J. A. Ogilvy, *Theory of wave scattering from random rough surfaces* (IOP Publishing, London, 1991).

[14] R. J. Urick, *Principles of underwater sound. Third edition* (Peninsula Publishing, Los Altos, California, 1983).

[15] E. Pouliquen, G. Canepa, L. Pautet, and A. Lyons, “Temporal variability of seafloor roughness and its impact on acoustic scattering”, *Proceedings of the seventh European Conference on Underwater Acoustics*, ECUA2004, Delft, The Netherlands, 5-8 July, 2004, pp. 583–588.

[16] D. Tang, K. B. Briggs, K. L. Wiliams, D. R. Jackson, E. I. Thorsos, and D. B. Percival, “Fine scale volume heterogeneity measurments in sand”, IEEE Ocean. Eng. **27**, 546–560 (2002).

[17] E. Pouligen and A. P. Lyons, “Backscattering from bioturbated sediments at very high frequency”, IEEE Ocean. Eng. **27**, 388–402 (2002).

[18] K. L. Williams, D. R. Jackson, E. I. Thorsos, D. Tang, and K. B. Briggs, “Acoustic backscattering experiments in a well characterized sand sediment: Data/model comparisons using sediment fluid and biot models”, IEEE Ocean. Eng. **27**, 376–387 (1998).

[19] P. D. Mourad and D. R. Jackson, “High-frequency sonar equation models for bottom backscatter and forward loss”, (1989), iEEE Oceans.

[20] O. H. Jensen, “Detection and tracking of multiple objects in sector-scan sonar images”, Technical Report, DDRE F-41 (2002).

[21] “Special issue papers on underwater acoustic communications”, IEEE Ocean. Eng. **25**, 2–96 (2000).

[22] “Special issue on autonomous ocean-sampling networks”, IEEE Ocean. Eng. **26**, 412–840 (2001).

[23] “Special issue on acoustic communications”, IEEE Ocean. Eng. **21**, 125–192 (1996).

[24] F. Song, P. E. An, and A. Folleco, “Modeling and simulation of autonomous underwater vehicles: Design and implementation”, IEEE Ocean. Eng. **28**, 283–296 (2001).

[25] H. Schmidt, J. R. Edwards, D. P. Eickstedt, T. C. Liu, and M. Montanari, “Integrated autonomous sonar concept for concurrent detection, classification, and localization in littoral MCM”, *Proceedings of Boundary Influences in High Frequency, Shallow Water Acoustics*, Bath, UK, 5th-9th September, 2005, pp. 325–332.

[26] G. Wendelboe, “Nato Expert System Test 2006 (NEST06’)”, Technical Report, DDRE N-09 (2006).

[27] D. R. Jackson, K. L. Williams, E. I. Thorsos, and S. G. Kargl, “High-frequency subcritical acoustic penetration into a sandy sediment”, IEEE Ocean. Eng. **27**, 346–361 (2002).

[28] J. L. Lopez, C. L. Nesbritt, R. Lim, K. L. Williams, E. I. Thorsos, and D. Tang, “Subcritical detection of spheres and elongated targets buried under under a rippled interface: Calibrated levels and effects of large roughness”, *Proceedings of Boundary Influences in High Frequency, Shallow Water Acoustics*, Bath, UK, 5th-9th September, 2005, pp. 145–158.

[29] G. Wendelboe and B. Stage, “Sonar Experimental Testplan”, Technical Report, DDRE A-08 (2002).

[30] O. H. Jensen, “Sonar Experiment Roundup”, Technical Report, DDRE F-21 (2002).

[31] O. H. Jensen, “A Programmer’s Reference to Reson’s SNS-format”, Technical Report, DDRE F-20 (2002).

[32] K. Tornslev, “Large area survey system with forward looking sonar”, Technical Report, DDRE F-32 (2002).

[33] K. Tornslev, “Generation of sonar images”, Technical Report, DDRE F-14 (2002).

[34] T. Aridgides, M. Fernández, and G. Dobeck, “Side scan sonar imagery fusion for sea mine detection and classification in very shallow water”, *Proceedings of SPIE* **4394**, 1123–1134 (2001).

[35] G. Dobeck, “On the power of algorithm fusion”, *Proceedings of SPIE* **4394**, 1092–1102 (2001).

[36] D. C. Ciany, W. Zurawski, and I. Kerfoot, “Performance of fusion algorithms for computer aided detection and classification of mines in very shallow water obtained from testing in navy fleet battle exercise hotel 2000”, *Proceedings of SPIE* **4394**, 1116–1122 (2001).

[37] M. G. Bello, “Comparison of two classifier training methodologies for underwater mine-detection/classification”, *Proceedings of SPIE* **4394**, 1135–1148 (2001).

[38] E. Dura, J. M. Bell, and D. M. Lane, “Superellipse fitting for the classification of mine-like shapes in side-scan sonar images”, *Proceedings of OCEANS’02*, 2002, pp. 23–28.

[39] S. Reed, Y. Petillot, and J. M. Bell, “An automatic approach to the detection and extraction of mine-features in side-scan sonar”, IEEE Ocean. Eng. **28**, 90–105 (2003).

[40] B. Stage and B. Z. Zerr, “Detection of obejcts on the sea bottom using backscattering characteristics dependent on the observation point”, IEEE Ocean. Eng. **22**, 40–46 (1997).

[41] M. J. Chantler and J. P. Stoner, “Automatic interpretation of sonar image using temporal feature measures”, IEEE Ocean. Eng. **22**, 47–56 (1997).

[42] G. L. Foresti, V. Murino, C. S. Regazzoni, and A. Trucco, “A voting-based approach for fast object recognition in underwater acoustic images”, IEEE Ocean. Eng. **22**, 57–65 (1997).

[43] “Personal communication with B. Stage, DDRE”, (2002).

[44] J. Johnson, “Analysis of image forming systems”, *Proceedings of the Image Intensifier Symposium*; ASTIA document AD220160 (1958).

[45] D. E. Schmeider, “Detection performance in clutter with variable resolution”, IEEE Transactions on Aerospace and electromagnetic systems **19**, 622–630 (1983).

[46] G. Aviram and S. R. Rothman, “Evaluation of human detection performance of targets embedded in natural and enhanced infrared images using image metrics”, Optical. Eng. **39**, 885–896 (2000).

[47] J. M. Bell, “Application of optical ray tracing techniques to the simulation of sonar images”, Optical. Eng. **36**, 1806–1813 (1997).

[48] J. M. Bell and L. M. Linnet, “Simulation and analysis of synthetic sidescan sonar images”, IEE Proc. - Radar, Sonar, Navig. **144**, 219–226 (1997).

[49] J. M. Bell, "Sidescan sonar: a directional filter of seabed texture?", IEE Proc. - Radar, Sonar, Navig. **146**, 65–72 (1999).

[50] K. B. Briggs, D. Tang, and K. L. Williams, "Characterisation of interface roughness of rippled sand off fort walton beach, florida", IEEE Ocean. Eng. **27**, 505–514 (2002).

[51] K. B. Briggs, "Microtopographical roughness of shallow-water continental shelves", IEEE Ocean. Eng. **14**, 360–367 (1989).

[52] K. L. Williams and D. R. Jackson, "Bistatic bottom scattering: Model, experiments, and model/data comparison", J. Acoust. Soc. Am. **103**, 169–181 (1998).

[53] Personal communication with J. M. Bell (2003).

[54] G. S. Sammelmann, J. T. Christoff, and J. D. Lathrop, "Synthetic images of proud targets", *Proceedings of OCEANS'94*, 1994, pp. 266–271.

[55] G. S. Sammelmann, "Propagation and scattering in very shallow water", *Proceedings of OCEANS'01*, 2001, pp. 337–344.

[56] T. Capéron, G. Hayward, and R. Chapman, "A 3D simulator for the design and evaluation of sonar system instrumentation", Meas. Sci. Technol. **10**, 1116–1126 (1999).

[57] O. George and R. Bahl, "Simulation of backscattering of high frequency sound from complex objects and sand sea-bottom", IEEE Ocean. Eng. **20**, 119–130 (1995).

[58] E. I. Thorsos, "The validity of the Kirchhoff approximation for rough surface scattering using a Gaussian roughness spectrum", J. Acoust. Soc. Am. **83**, 78–92 (1988).

[59] J. A. Fawcett, "Modeling of high-frequency scattering from objects using a hybrid Kirchhoff/diffraction approach", J. Acoust. Soc. Am. **109**, 1312–1319 (2001).

[60] E. G. Williams, *Fourier Acoustics. Sound Radiation and Nearfield Acoustical Holography* (Academic Press, London,1999).

[61] V. A. Boronikov, *Uniform stationary phase metod* (IEE Electrmagnetic waves series, The institution of electrical engineers, London, 1994).

[62] J. Perez and M. F. Catedra, "Application of physical optics to the RCS computation of bodies modeled with NURBS surfaces", Trans. Anten. Propag. **42**, 1404–1411 (1994).

[63] M. T. V. Nhieu, “Diffraction by plane screens”, J. Acoust. Soc. Am. **97**, 796–806 (1995).

[64] G. M. Jebsen and H. Medwin, “On the failure of the Kirchhoff assumption in backscatter”, J. Acoust. Soc. Am. **72**, 1607–1611 (1982).

[65] A. D. Pierce and R. N. Thurston, *Underwater scattering radiation* (Academic Press, London,1992).

[66] G. B. Arfken and H. J. Weber, *Mathematical methods for physicists. 5th edition* (Academic Press, London, 2001).

[67] L. M. Brekhovskikh and Y. P. Lysanov, *Fundamentals of ocean acoustics. Third Edition* (Springer-Verlag, New York, 2003).

[68] E. I. Thorsos and S. L. Broschat, “An investigation of the small slope approximation for scattering from rough surfaces. Part I. Theory”, J. Acoust. Soc. Am. **97**, 2082–2093 (1995).

[69] S. L. Broschat and E. I. Thorsos, “An investigation of the small slope approximation for scattering from rough surfaces. Part II. Numerical studies”, J. Acoust. Soc. Am. **101**, 2615–2625 (1997).

[70] E. G. Liszka and J. J. McCoy, “Scattering at a rough boundary - Extensions of the Kirchhoff approximation”, J. Acoust. Soc. Am. **71**, 1093–1193 (1982).

[71] S. T. McDaniel, “Diffractive corrections to the high-frequency Kirchhoff approximation”, J. Acoust. Soc. Am. **79**, 952–957 (1986).

[72] S. T. McDaniel and A. D. Gorman, “An examination of the composite-roughness scattering model”, J. Acoust. Soc. Am. **73**, 1476–1486 (1983).

[73] D. R. Jackson, D. P. Winebrener, and A. Ishimaru, “Application of the composite roughness model to high-frequency bottom backscattering”, J. Acoust. Soc. Am. **79**, 1410–1422 (1986).

[74] G. C. Gaunaurd, “Sonar cross sections of bodies partially insonified by finite sound beams”, IEEE Ocean. Eng. **10**, 213–230 (1985).

[75] J. A. Fawcett, “Modeling of scattering by objects on the seabed”, J. Acoust. Soc. Am. **104**, 3296–3304 (1998).

[76] E. Pouligen, A. P. Lyons, and N. G. Pace, “Penetration of acoustic waves into rippled sandt seafloors”, J. Acoust. Soc. Am. **108**, 2071–2081 (2000).

[77] A. Papoulis, *Signal Analysis* (McGraw-Hill, New York, 1984).

[78] M. T. V. Nhieu, "Diffraction by the edge of a three-dimensional object", J. Acoust. Soc. Am. **99**, 79–87 (1996).

[79] P. Y. Umfitsev, "Theory of acoustical edge waves", J. Acoust. Soc. Am. **86**, 463–474 (1996).

[80] J. B. Keller, "Geometrical theory of diffraction", J. Opt. Soc. Am. **52**, 116–129 (1962).

[81] J. G. Proakis and D. G. Manolakis, *Digital signal processing. Principles, alogorithms, and applications. Third edition* (Prentice Hall, London, 1996).

[82] C. H. Chan, L. Tsang, and Q. Li, "Monte Carlo simulations of large scale one-dimensional random rough surface scattering at near-grazing incidence: Penetrable case", Trans. Anten. Propag. **46**, 142–149 (1998).

[83] M. A. Mansour, B. V. Smith, and J. A. Edwards, "PC-based real time active sonar simulator", IEE Proc. - Radar, Sonar, Navig. **144**, 227–233 (1997).

[84] M. I. Skolnik, *Introduction to radar systems. Third edition* (McGraw-Hill, New York, 2001).